



Durham E-Theses

A study of the turbulent flow of a high speed Coanda jet

Cutbill, Sue

How to cite:

Cutbill, Sue (1998) *A study of the turbulent flow of a high speed Coanda jet*, Durham theses, Durham University. Available at Durham E-Theses Online: <http://etheses.dur.ac.uk/4743/>

Use policy

The full-text may be used and/or reproduced, and given to third parties in any format or medium, without prior permission or charge, for personal research or study, educational, or not-for-profit purposes provided that:

- a full bibliographic reference is made to the original source
- a [link](#) is made to the metadata record in Durham E-Theses
- the full-text is not changed in any way

The full-text must not be sold in any format or medium without the formal permission of the copyright holders.

Please consult the [full Durham E-Theses policy](#) for further details.

**A Study Of The Turbulent Flow Of
A High Speed Coanda Jet**

by

Sue Cutbill

**A Thesis submitted for the degree of
Doctor of Philosophy**

The copyright of this thesis rests
with the author. No quotation
from it should be published
without the written consent of the
author and information derived
from it should be acknowledged.

**School of Engineering
University of Durham
1998**



24 FEB 1999

The copyright of this thesis rests with the author. No quotation from it should be published without S. Cutbill's prior written consent and information derived from it should be acknowledged.

Copyright © 1998, S. Cutbill.

Declaration

The work contained in this thesis has not been submitted elsewhere for any other degree or qualification, and unless otherwise referenced it is the author's own work.

Acknowledgements

I am most grateful to my supervisor, Dr. David Gregory-Smith whose guidance, encouragement and supportiveness has been a great help throughout this project.

I would also like to thank Dr. Tony Smith, along with all the other staff of S & C Thermofluids, who have provided me with invaluable advice and guidance on the use of the CFD code PHOENICS. Thanks is also due to Mike Malin of CHAM for his expertise and help in improving my understanding of the CFD code, which enabled me to implement my own modifications to the software.

Thanks must also go to all the staff of the School of Engineering who have provided me with assistance during my time as a research student. In particular, I would like to thank Mr. Ray Mand, the late Michael Page, and Gary Parker in the thermodynamics laboratory, all the technicians in the mechanical and electrical workshops who have built various pieces of equipment for me, and to Trevor Nancarrow for his support in the use of the departmental computer network.

Finally, I would like to thank my fellow research students for their unfailing support, help, and friendship throughout. To my husband, I am eternally grateful for his never ending faith in me, his patience and support, which have made the completion of this thesis possible.

This thesis is dedicated to
my Aunt, Ann Shore, and to
my Grandmother, Mary Smith

A Study Of The Turbulent Flow Of A High Speed Coanda Jet

Sue Cutbill

Abstract

This thesis presents an experimental investigation into a compressible turbulent wall jet issuing from a slot, and flowing over a surface with streamwise curvature, followed by a plane wall recovery region. The purpose of this data was to provide suitable test cases to aid in the design and validation of turbulence models used for curved flow situations in computational fluid dynamics.

The presence of streamwise curvature provides an extra rate of strain to the flow which effects both the mean flow field and the turbulence structure. The effects of curvature are dependent on the ratio of the slot width to the radius of curvature. The effects are increased with the magnitude of this ratio.

Hot film anemometry was used to measure the mean flow and Reynolds stresses under six different flow regimes. Four experiments were performed using a constant slot to radius ratio, and the supply pressure ratio was varied. Two further experiments were performed at a constant pressure ratio, but at differing slot to radius ratios. In all cases, the extra rate of strain was found to increase the jet growth and velocity decay rates beyond those of a plane wall jet. 'History effects' were apparent where there was a change from flow with streamwise wall curvature to that without. The turbulence structure was found to require a finite distance along the recovery section before it reverts to a plane wall turbulence structure.

The presence of the extra rate of strain, and the history effects at sudden changes in surface curvature, make strong demands on any turbulence model. Various turbulence models have been tested, and although no one turbulence model has proved robust enough for all flow situations, a number of models have been identified to provide superior performance under certain conditions. The use of a higher order numerical scheme has also been found to reduce the effects of numerical diffusion, leading to improvements in the predictions of the flow shock cell structure and the breakaway performance of the jet.

List of Contents

1	Introduction	1
1.1	The Coanda effect	1
1.2	Applications of the Coanda effect	3
1.3	Project objectives	7
1.4	Thesis structure	8
2	Review of turbulent flows and measurement techniques	9
2.1	Introduction to turbulence.	9
2.1.1	Predicting turbulence	10
2.1.2	Equations governing fluid flow	11
2.1.3	The time-averaged Navier Stokes equations.	12
2.1.4	Reynolds stresses	13
2.1.5	Transport equations	16
2.1.6	Local equilibrium and self preservation	20
2.2	Free jets in still surroundings	21
2.3	Plane wall jets in still surroundings	22
2.4	Curvature effects	26
2.4.1	Curved wall boundary layers	28
2.4.2	Curved wall jets	30
2.5	Supersonic wall jets	35
2.5.1	Coanda flare flow field	35
2.5.2	Shock waves and boundary layer interactions	37
2.5.3	Breakaway	38
2.6	Flow measurement and visualisation techniques.	39
2.6.1	Schlieren images	39
2.6.2	Pressure measurements	39
2.6.3	Hot wire / film anemometry	40
2.7	Two-dimensionality checks	42

3	Experimental apparatus and instrumentation	44
3.1	Introduction	44
3.2	The experimental rig	44
3.3	Air supply	46
3.4	Calibration rig design	50
3.5	Pressure measurement	55
3.6	Flow measurement and correction	55
3.7	Traverse gear control and data logging	57
4	Hot film anemometry	59
4.1	Introduction	59
4.1.1	The direct calibration technique.	60
4.1.2	Basic equations for determining the Reynolds stresses	61
4.1.3	Choice of probes	66
4.1.4	Calibration	67
4.1.5	Experimental data acquisition and analysis.	70
4.2	Calibration plots	75
4.2.1	Calibration test results	81
4.3	Problems arising from the calibration tests.	83
4.3.1	Torsional twisting of the hot film sensor	83
4.3.2	Noise levels	84
4.3.3	Aliasing	86
4.3.4	Strain gauging effects	88
4.3.5	Electrical interference	96
4.3.6	Setting the frequency response of the hot film sensor.	97
4.3.7	Cleanliness of the air supply.	98
4.3.8	Constant air supply	100
5	Experimental results	101
5.1	Introduction	101
5.1.1	Traverse details	101

5.1.2	Data analysis	104
5.2	Results	104
5.2.1	Mean velocity data	104
5.2.2	Non-dimensionalising the data	109
5.2.3	Normal stresses	123
5.2.4	Shear stresses	130
5.2.5	Kinetic energy and eddy viscosity	134
6	Computational techniques	138
6.1	An introduction to Computational Fluid Dynamics	138
6.2	The structure of the CFD code PHOENICS.	138
6.2.1	Pre-processor	139
6.2.2	Solver	139
6.2.3	Post-processor	140
6.3	The mathematical basis of PHOENICS	141
6.3.1	Pressure correction method	141
6.3.2	Interpolation schemes available in PHOENICS	142
6.3.3	Solution techniques	142
6.4	Turbulence modelling	143
6.4.1	Standard k- ϵ model	151
6.4.2	Chen Kim modification to the k- ϵ model.	152
6.4.3	RNG formulation of the k- ϵ model	153
6.4.4	Hanjalic Launder modification to the k- ϵ model.	154
6.5	Wall functions	155
6.6	Shock waves and predicting transonic flows.	158
7	Modelling results using PHOENICS	161
7.1	Introduction	161
7.2	Initial tests on flow modelling.	163
7.2.1	Grid geometries and generation.	163
7.2.2	Boundary conditions.	163
7.2.3	Convergence criteria	164

7.2.4	Low speed jet flow	165
7.3	General CFD tests on the planar flare model	170
7.3.1	Comparison of various turbulence model performances	172
7.3.2	Velocity profiles	172
7.3.3	Surface pressure predictions	178
7.3.4	Higher order numerical schemes	180
7.3.5	Schlieren images	182
7.3.6	Jet breakaway	183
7.4	CFD predictions for the high speed flow of the planar Coanda model.	188
7.4.1	Grid independency	189
7.4.2	The jet growth and velocity decay rate predictions	190
7.4.3	Velocity profile plots.	197
7.4.4	Kinetic energy and eddy viscosity profiles	205
8	Discussion	213
8.1	Experimental accuracies	213
8.2	Streamwise curvature effects	215
8.3	Assessment of the turbulence modelling	217
8.3.1	Incompressible flow predictions	217
8.3.2	Compressible flow predictions	218
8.3.3	Jet breakaway predictions	221
9	Conclusions and future work	222
9.1	Conclusions.	222
9.2	Suggestions for further work	224
	Bibliography	226
	Appendix A - Equations of motion	237
	Appendix B - Turbulent flow equations	245
	Appendix C - The mathematical basis of PHOENICS	248

List of Figures

1.1	Coanda flow characteristics	1
1.2	(a) Concave and (b) convex wall jets	2
1.3	McDonnell Douglas "NOTAR" (no tail rotor) helicopter	3
1.4	Vacuum cleaner demonstrating the use of the Coanda effect.	4
1.5	Coanda Flare Configurations	5
1.6	Dual purpose HP/LP INDAIR Coanda flare	6
2.1	2-D Turbulent free jet	21
2.2	Nomenclature associated with plane wall jets	22
2.3	Schematic showing the separation angle can be greater than 180° due to the Coanda effect	31
2.4	Schematic diagram of the Coanda flare flow field.	36
2.5	Schematic diagram of an oblique shock interacting with a laminar boundary layer	37
3.1	Traverse Gear	45
3.2	Sketches showing the two modes of traverse available	46
3.3	Air Supply Layout	49
3.4	Calibration rig design	50
3.5	Photograph of the calibration rig	51
3.6	Hot film probe stem design	52
3.7	Subsonic calibration nozzle	53
3.8	Calibration arrangement	54
3.9	Close-up photograph of the calibration nozzle arrangement	54
3.10	Leakage rate versus pressure	56
4.1	Definition of yaw and pitch angles used during calibration	61
4.2	Sensor oriented co-ordinate system	62
4.3	(a) Slanted sensor coefficients, and (b) Straight sensor coefficients	66

4.4	Typical effective mass flux against film voltage plot for a slanted hot film	76
4.5	Raw k^2 and h^2 data for the straight sensor	77
4.6	Raw k^2 and h^2 data for the slanted sensor	77
4.7	Modified k^2 and h^2 data for the straight sensor	78
4.8	Modified k^2 and h^2 data for the slanted sensor	79
4.9	Interpolated k^2 and h^2 data for the straight sensor	79
4.10	Interpolated k^2 and h^2 data for the slanted sensor	80
4.11	RMS variation of h^2 with ρU	80
4.12	Hot film sensor	84
4.13	Sinusoidal input of 10 kHz, with the IFA on standby	86
4.14	Sinusoidal input of 10 kHz, with the IFA in RUN mode	86
4.15	Straight sensor, held normal to 200 m/s flow, with no filter	87
4.16	Straight sensor, held normal to 200 m/s flow, with filtering at 20 kHz	87
4.17	Spectrum of normal sensor output held perpendicular to the flow	88
4.18	Spectrum of normal sensor output held end on into the flow	89
4.19	Spectrum of original normal sensor output held perpendicular to the flow	89
4.20	Slanted sensor @ (a) 40 m/s, (b) 60m/s, (c) 80m/s	91
	(d) 100m/s, (e) 120m/s, (f) 150m/s	92
4.21	Straight sensor @ (a) 40 m/s, (b) 60m/s, (c) 80m/s	93
	(d) 100m/s, (e) 120m/s, (f) 150m/s	94
4.22	Power spectral plot for the normal sensor at 90° round the Coanda surface, $\bar{U}_{eff} = 110\text{m/s}$, $T_i = 15\%$	95
4.23	Apparent temperature fluctuations as a result of electrical interference	96
4.24	Square wave test frequency response for film sensors	98
4.25	Photograph of the planar model, demonstrating the oil contamination	99
4.26	Velocity variation with time at the calibration nozzle, at 145 m/s	100
5.1	Traverse locations round the Coanda flare.	102
5.2	Dimensions required for positioning the traverse gear	103

5.3	\bar{U} versus y ; (a)-(d) $t = 4\text{mm}$; (e) $t = 2\text{mm}$; (f) $t = 8\text{mm}$	105
5.4	\bar{V} versus y ; (a)-(d) $t = 4\text{mm}$; (e) $t = 2\text{mm}$; (f) $t = 8\text{mm}$	106
5.5	\bar{W} versus y ; (a)-(d) $t = 4\text{mm}$; (e) $t = 2\text{mm}$; (f) $t = 8\text{mm}$	107
5.6	Definition of the standard normalising parameters for a typical velocity profile	109
5.7	Alternative normalising parameters.	110
5.8	Normalising parameters for tests in Case (I)	111
5.9	Jet growth rate for the 4mm slot, with variable pressure ratios	111
5.10	Velocity decay rates for the 4mm slot, with variable pressure ratios	112
5.11	Jet growth rate ($y_{m/2}/t$ vs. s/s_{tot}) for a pressure ratio of 0.85, with variable slot widths.	113
5.12	Predicted non-dimensionalised velocity profiles compared to experimental data for the 4mm slot, at 72° , based on two different guesses for \bar{U}_m (a) $\bar{U}_m = 109.5\text{m/s}$, and (b) $\bar{U}_m = 114\text{m/s}$	114
5.13	Jet growth rates for Case (II) using the estimated maximum velocities	115
5.14	Velocity decay rates for Case (II) using the estimated maximum velocities.	115
5.15	Jet growth rates for Case (I) using the estimated maximum velocities	117
5.16	Velocity decay rates for Case (I) using the estimated maximum velocities	118
5.17	Comparison between empirical and experimental growth rates for the 2mm slot	118
5.18	Comparison between empirical and experimental growth rates for the 4mm slot	119
5.19	\bar{U}/\bar{U}_m versus $y/y_{m/2}$; (a)-(d) $t = 4\text{mm}$; (e) $t = 2\text{mm}$; (f) $t = 8\text{mm}$	120
5.20	\bar{V}/\bar{U}_m versus $y/y_{m/2}$; (a)-(d) $t = 4\text{mm}$; (e) $t = 2\text{mm}$; (f) $t = 8\text{mm}$	121
5.21	\bar{W}/\bar{U}_m versus $y/y_{m/2}$; (a)-(d) $t = 4\text{mm}$; (e) $t = 2\text{mm}$; (f) $t = 8\text{mm}$	122
5.22	$\sqrt{u^2}/\bar{U}_m$ versus $y/y_{m/2}$; (a)-(d) $t = 4\text{mm}$; (e) $t = 2\text{mm}$; (f) $t = 8\text{mm}$	127
5.23	$\sqrt{v^2}/\bar{U}_m$ versus $y/y_{m/2}$; (a)-(d) $t = 4\text{mm}$; (e) $t = 2\text{mm}$; (f) $t = 8\text{mm}$	128

5.24	$\sqrt{\overline{w^2}}/\overline{U}_m$ versus $y/y_{m/2}$; (a)-(d) $t = 4\text{mm}$; (e) $t = 2\text{mm}$; (f) $t = 8\text{mm}$.	129
5.25	$\overline{uv}/\overline{U}_m^2$ versus $y/y_{m/2}$; (a)-(d) $t = 4\text{mm}$; (e) $t = 2\text{mm}$; (f) $t = 8\text{mm}$. .	131
5.26	$\overline{uw}/\overline{U}_m^2$ versus $y/y_{m/2}$; (a)-(d) $t = 4\text{mm}$; (e) $t = 2\text{mm}$; (f) $t = 8\text{mm}$. .	132
5.27	$\overline{vw}/\overline{U}_m^2$ versus $y/y_{m/2}$; (a)-(d) $t = 4\text{mm}$; (e) $t = 2\text{mm}$; (f) $t = 8\text{mm}$. .	133
5.28	$0.5q^2/\overline{U}_m^2$ vs. $y/y_{m/2}$; (a)-(d) $t = 4\text{mm}$; (e) $t = 2\text{mm}$; (f) $t = 8\text{mm}$. .	135
5.29	$0.75(\overline{u^2} + \overline{w^2})/\overline{U}_m^2$ vs. $y/y_{m/2}$; (a)-(d) $t = 4\text{mm}$; (e) $t = 2\text{mm}$; (f) $t = 8\text{mm}$. .	136
5.30	Eddy viscosity versus $y/y_{m/2}$; (a)-(d) $t = 4\text{mm}$; (e) $t = 2\text{mm}$; (f) $t = 8\text{mm}$.	137
7.1	Definition of geometry variables	164
7.2	Nomenclature and Co-ordinate System	165
7.3	Typical grid for the Coanda flare geometry	166
7.4	(a) Jet growth rate, (b) Velocity decay rate	168
7.5	Predictions for ENUT : (a) Mixing length model , (b) Standard $k - \epsilon$ model (c) Hanjalic Launder $k - \epsilon$ model, (d) Experimental viscosity levels.	169
7.6	(a) Jet growth rate with varying inlet kinetic energy, and (b) Velocity decay rate with varying inlet kinetic energy	170
7.7	'C' grid used in planar compressible tests.	171
7.8	PHOENICS predictions for the jet growth rate	173
7.9	PHOENICS predictions for the velocity decay rate	173
7.10	Mixing length model predictions for V/U_m vs. $y/y_{m/2}$	174
7.11	Mixing length model predictions for U/U_m vs. $y/y_{m/2}$	174
7.12	$k - \epsilon$ model predictions for V/U_m vs. $y/y_{m/2}$	175
7.13	$k - \epsilon$ model predictions for U/U_m vs. $y/y_{m/2}$	175
7.14	RNG model predictions for V/U_m vs. $y/y_{m/2}$	176
7.15	RNG model predictions for U/U_m vs. $y/y_{m/2}$	176
7.16	Chen Kim model predictions for V/U_m vs. $y/y_{m/2}$	177
7.17	Chen Kim model predictions for U/U_m vs. $y/y_{m/2}$	177
7.18	PHOENICS predictions for the planar model surface pressures	178

7.19	$k - \epsilon$ model pressure plots using the standard and the higher order scheme	181
7.20	Chen Kim model pressure plots using the standard and the higher order scheme	181
7.21	Horizontal Schlieren images(a) Actual photograph, and (b) Artificial image based on the $k - \epsilon$ model using Roe's numerical scheme	182
7.22	Vertical Schlieren images (a) Actual photograph, and (b) Artificial image based on the $k - \epsilon$ model using Roe's numerical scheme	183
7.23	Surface pressure plots from existing experimental data	184
7.24	Surface pressure predictions using the Chen Kim model	185
7.25	Velocity vectors predicted using the Chen Kim model	186
7.26	Differences between (a) predicted, and (b) experimental surface pressure plots	187
7.27	Predicted growth rates for the 4mm slot width performed on three different grids	189
7.28	Predicted velocity decay rates for the 4mm slot width performed on three different grids	190
7.29	Predicted jet growth rates for the 2mm slot at a pressure ratio of 0.85	193
7.30	Predicted velocity decay rates for the 2mm slot at a pressure ratio of 0.85	193
7.31	Predicted jet growth rates for the 4mm slot at a pressure ratio of 0.85	194
7.32	Predicted velocity decay rates for the 4mm slot at a pressure ratio of 0.85	194
7.33	Predicted jet growth rates for the 8mm slot at a pressure ratio of 0.85	195
7.34	Predicted velocity decay rates for the 8mm slot at a pressure ratio of 0.85	195
7.35	Predicted jet growth rates for the 4mm slot at pressure ratios of 0.7 and 0.85	196
7.36	Predicted velocity decay rates for the 4mm slot at pressure ratios of 0.7 and 0.85	196
7.37	Streamwise velocity profiles for the 2mm slot	199

7.38	Streamwise velocity profiles for the 4mm slot	200
7.39	Streamwise velocity profiles for the 8mm slot	201
7.40	Normal velocity profiles for the 2mm slot	202
7.41	Normal velocity profiles for the 4mm slot	203
7.42	Normal velocity profiles for the 8mm slot	204
7.43	Turbulent kinetic energy profiles for the 2mm slot	207
7.44	Turbulent kinetic energy profiles for the 4mm slot	208
7.45	Turbulent kinetic energy profiles for the 8mm slot	209
7.46	Eddy viscosity profiles for the 2mm slot	210
7.47	Eddy viscosity profiles for the 4mm slot	211
7.48	Eddy viscosity profiles for the 8mm slot	212
A.1	Mass flows in and out of fluid element control volume	238
C.1	Grid cell nomenclature.	248

List of Tables

4.1	Mean flow test results	81
4.2	Fluctuating component test results	82
7.1	Summary of CFD test cases	162
7.2	Number of cells used in the grid dependency tests	189

Nomenclature

A	area (m^2)
A_{ij}	coefficients in the hot wire response equation
B_{ij}	coefficients in the hot wire response equation
C_p	surface pressure coefficient = $(P - P_a)/(P_o - P_a)$
C_{po}	driving pressure coefficient (pressure ratio) = P_a/P_o
C_v	specific heat capacity at constant volume (kJ/kgK)
D/Dt	substantive derivative, $\partial/\partial x + \partial/\partial y + \partial/\partial z$
E	wall roughness parameter
\dot{E}_{ij}, e_{ij}	rate of linear deformation by mean and fluctuating velocity components (s^{-1})
e	internal energy per unit mass (J/kg), or an extra rate of strain (s^{-1})
h^2	sensor pitch coefficient
k^2	sensor yaw coefficient
k	Turbulent kinetic energy = $0.5\overline{q^2} = 0.5(\overline{u_1^2} + \overline{u_2^2} + \overline{u_3^2})$ (J/kg) or thermal conductivity (W/mK)
L	characteristic length scale (m)
l_o	mixing length (m)
l_c	mixing length corrected for streamline curvature (m)
l_d	mixing length corrected for streamline divergence (m)
l_t	total corrected mixing length (m)
M	Mach number
n	normal co-ordinate in (s, n, z) system
P	static pressure (Pa), or production rate / unit volume (W/m^3)
P_o	stagnation pressure (Pa)
p	fluctuating static pressure (Pa)
R	surface radius of curvature (m), Universal Gas Constant (kJ/kgK)
R_a	axisymmetric radius of curvature (m)
Re_p	Reynolds No. = $[(P_o - P_a)tR/\rho v^2]^{1/2}$. Incompressible flow, $Re_p = Re_s(R/2t)^{0.5}$
Re_s	Reynolds No. = $U_{slot}t/\nu$
Ri	Richardson number
r	local streamline radius of curvature (m)
S	source term

s	curvilinear co-ordinate in (s, n, z) system
T_i	turbulence intensity = $\sqrt{u^2}/\bar{U}$
t	slot width, (m), or time (s)
\mathbf{U}	velocity vector (m/s)
U, V, W	instantaneous velocity components in (x, y, z) or (s, n, z) co-ordinate systems
$\bar{U}, \bar{V}, \bar{W}$	mean velocity components in (x, y, z) or (s, n, z) co-ordinate systems
u, v, w	fluctuating components in (x, y, z) or (s, n, z) co-ordinate systems
u_τ	friction velocity, $u_\tau = \sqrt{\tau_w/\rho}$, (m/s)
ΔV	finite control volume, (m ³)
V_{film}	hot film sensor voltage, (volts)
x, y, z	rectangular Cartesian co-ordinates

Greek Symbols

α	angle of hot film sensor to the probe axis, degrees
α_1, α_2	constants in streamline curvature correction to l_o
β	factor in Monin-Oboukhov formula
δ	normal thickness of a boundary layer (m)
δ_{ij}	Kronecker delta (equals 1 if $i = j$, or 0 if $i \neq j$)
ε	dissipation rate per unit mass (J/kg)
ϕ	yaw angle (degrees), or a general variable
Φ	dissipation function (s ⁻²)
Γ	diffusion coefficient
γ	ratio of specific heats
κ	Von Kármán constant, equals 0.41
λ	bulk viscosity (Ns/m ²)
μ	dynamic viscosity (Ns/m ²)
ν	kinematic viscosity (m ² /s)
ω	angle between the axis of symmetry and the tangent to the surface, (degrees)
θ	pitch angle (degrees)
ρ	density (kg/m ³)
τ_w	wall shear stress (N/m ²)
τ	shearing stress (N/m ²)

Subscripts

a	ambient or atmospheric
c	calibration
e	experiment
eff	effective
i, j, l	tensor indices
l	laminar
m	maximum
m'	maximum <i>measured</i> value
$m'(3)$	value at 3mm from the surface
$m/2$	half the maximum
$m'/2$	half the maximum <i>measured</i> value
$m'(3)/2$	half the value of the 3mm position
n, t, b	normal, tangential and binormal - co-ordinate system relative to the sensor
r	reference
t	turbulent
w	wall (or surface)
∞	free stream conditions
1, 2, 3	tensor indices for streamwise, normal and transverse directions respectively

Chapter 1

Introduction

1.1 The Coanda effect

Many industrial applications use the skin-adhesion effect, discovered by Henri Coanda, and known as the Coanda effect. The principle is simple yet highly effective. The effect is observed when a jet, blown over a surface of convex streamwise curvature adheres to the surface. The extra strain rates due to convex curvature reduce the turbulent mixing and shear stresses in the near wall region where the angular momentum of the flow increases in the direction of the radius of curvature. However, in the 'jet like' outer layer outside the velocity maximum, these extra strain rates increase the turbulent mixing and the shear stresses are higher.

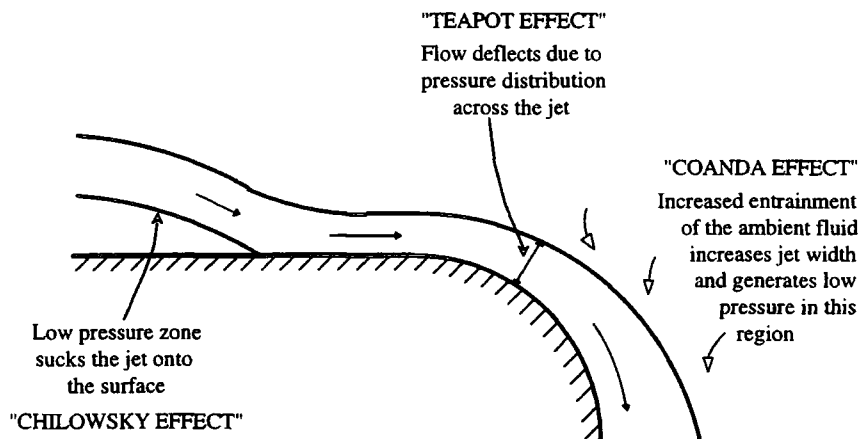


Figure 1.1 : Coanda flow characteristics

Bradshaw (1973) subdivided the Coanda effect into three distinct phenomenon, which are illustrated in figure 1.1.

- The first is a viscous effect whereby a jet whose initial axis does not intersect a solid surface can still attach itself to the surface. This is due to the low pressure region resulting from the acceleration of the fluid that supplies the entrainment. This has been called the 'Chilowsky Effect' by Metral and Zerner (1948). Special effects of streamline curvature on the turbulent mixing are not necessarily involved here.

- The second is an inviscid irrotational effect whereby the streamline pattern induces a sufficiently low pressure at the wall to attach the jet. This was called the 'teapot effect' by Keller (1957).
- The third effect observed is the increased growth of a wall jet on a convex surface compared to one on a plane surface. This intensified mixing at the outer edge of the jet is caused by the influence of the bending of the jet by the wall on the turbulence.

The latter is the single most important effect of streamline curvature on a wall jet. According to Bradshaw, the term 'Coanda Effect' should be exclusively applied to this phenomenon.

Curvature may have either a stabilising or destabilising effect on flow. A simple balance of forces may be used to predict the effects of longitudinal curvature. Von Kármán (1934) considered a fluid element in rotating flow, which is displaced radially by an external force. For a frictionless fluid, this displaced element conserves its angular momentum about the centre of curvature of the streamline. If the angular momentum of the steady flow decreases outwards, the displaced element has a larger circumferential velocity than its surroundings, therefore the radial pressure gradient, $\rho U^2/r$ which keeps the mean flow on its circular path is too small to keep the displaced element in equilibrium, so it moves further out. Alternatively, if the angular momentum of the mean flow increases outwards, the mean pressure gradient forces the displaced element back to a smaller radius, towards its original position about which it will oscillate. Rayleigh (1917) proposed a similar argument for inviscid flows with circulation, showing that curved flows will be unstable if the angular momentum decreases with radial distance i.e. $\partial(\rho U r)/\partial r < 0$ (as in a concave boundary layer, or the outer region of a convex wall jet), and stable if the angular momentum increases with radial distance i.e. $\partial(\rho U r)/\partial r > 0$ (as in a convex boundary layer, or the outer region of a concave wall jet), as shown in figure 1.2

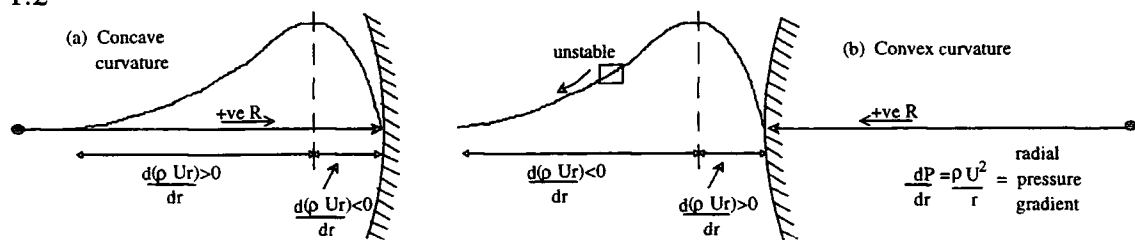


Figure 1.2 : (a) Concave and (b) convex wall jets

1.2 Applications of the Coanda Effect

Many applications make use of the Coanda effect to increase the mixing rate of a jet beyond that obtainable with an equivalent circular jet. Examples of some of these applications are given below. In the aeronautical industry, jets are blown along aerofoil surfaces to re-energise the boundary layer, allowing greater angles of incidence without flow separation. This increases the lift coefficient and allows reduced take off and landing speeds. A second aeronautical use for the Coanda effect is in the directional control for the McDonnell Douglas "NOTAR" (no tail rotor) helicopter, shown in figure 1.3 below. The tail boom of the "rotorless" helicopter requires moderately high pressure air to force through longitudinal blowing slots. This air enters an intake and is driven into the tail boom by a high speed fan. It exists through the pair of fixed slots in the side of the boom producing the Coanda effect. This causes the boom to swing sideways to provide directional control.

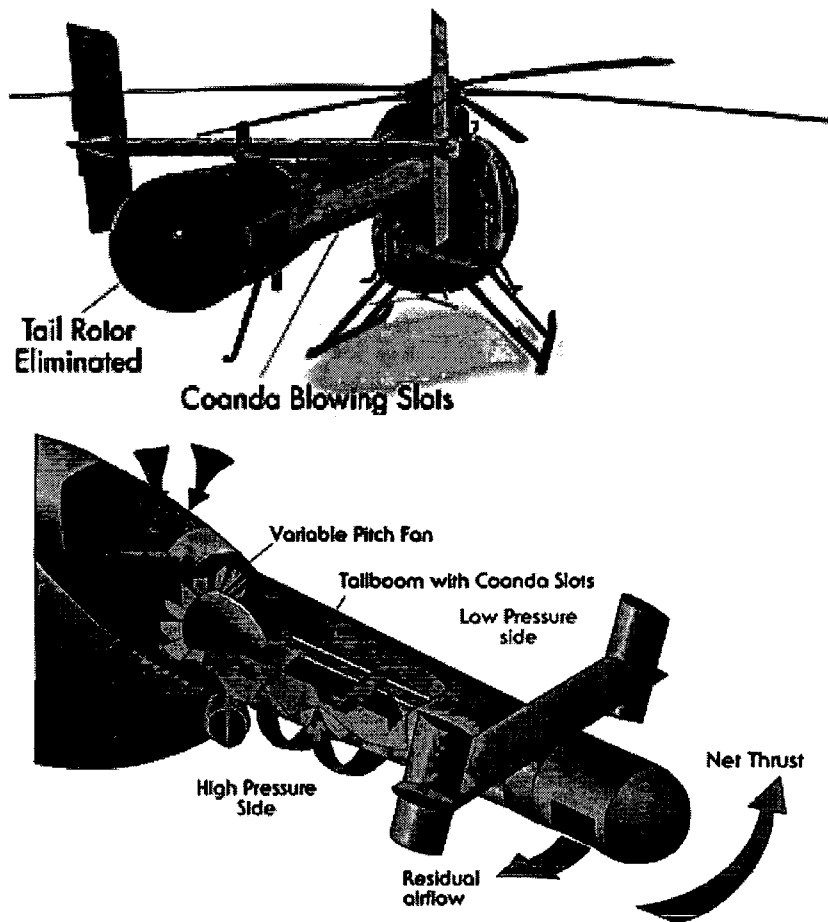


Figure 1.3[⊗] : McDonnell Douglas "NOTAR" (no tail rotor) helicopter

Another example of a use for the Coanda effect is in air cushion vehicles where an annular jet of air is blown inwards around the periphery of the machine and establishes the base pressure which lifts the vehicle off the ground.

Various domestic household devices utilise the Coanda effect, such as the mixing of hot and cold water in shower heads, and in vacuum cleaners, as illustrated in figure 1.4 below. Air is accelerated through the rotor and blown out of an annular Coanda blowing slot. Air passes above the carpet surface, entraining air from under the rim and through the carpet pile. The air spirals out of the fan creating a cyclonic action, throwing dust to the outside. A sucking slot in the passageway divides the air and dirt and air is continually passed back to the fan. The heavier particles such as dirt and dust are deposited in the upper chamber while the remainder is filtered up into the room.

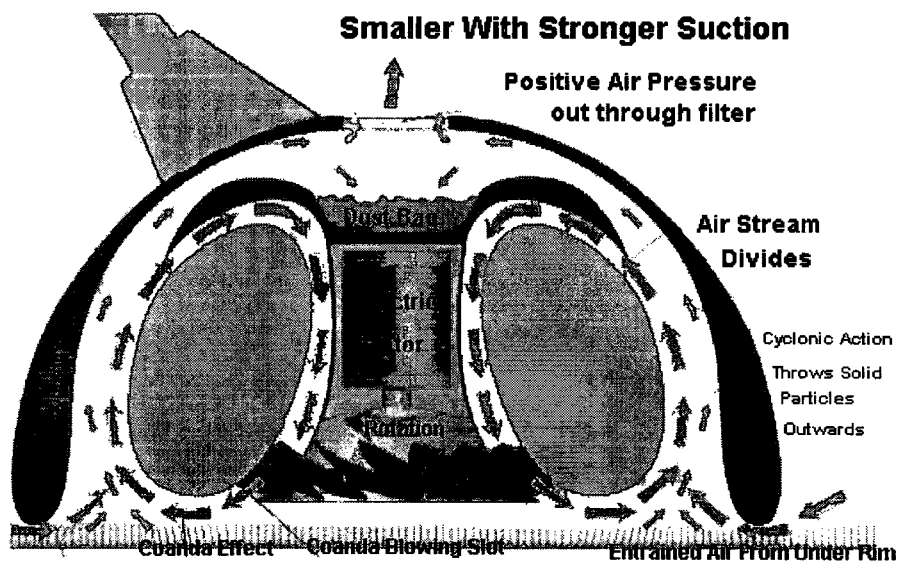


Figure 1.4^{*} : Vacuum cleaner demonstrating the use of the Coanda effect

One further example, which is highly relevant to the current research work, is the development of Coanda flares used by the petroleum industry, as described by Wilkins *et al* (1977). In the past, when markets for the gas were not readily available, the gas was separated and continuously burned as a waste product. More recent economic pressures, and the desire for conservation has led to greater efforts to utilise this gas. Sophisticated gas-transfer installations have been developed, which require safe and efficient flare systems for use during mechanical breakdowns and emergencies. The traditional method

* Pictures obtained from the JETFAN Technology Webpage

of burning gases from the end of an open pipe is no longer adequate to meet today's strict safety and environmental requirements, hence the demand for highly efficient flares has developed. Much of the industry now uses two distinct designs of flare - either an internal or an external configuration, as illustrated in figure 1.5.

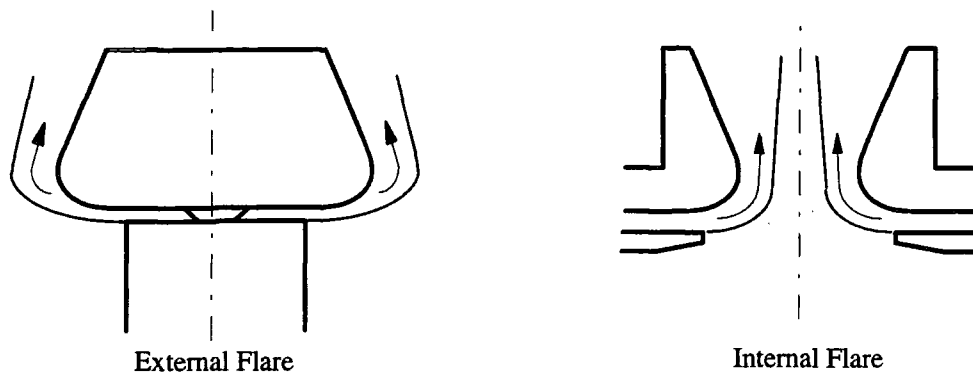


Figure 1.5 : Coanda Flare Configurations

For the external case, high pressure gas ejected from a slot at the base of an axisymmetric flare, adheres to the Coanda profile and rapidly entrains large quantities of air. The flame is initiated near the point of maximum diameter. It burns from the outside inwards, so there is a protective layer of unburned gas which insulates the tip against flame impingement. Turbulence levels are such as to ensure a thorough mixing of gas and air, which leads to far more efficient combustion than from an open pipe.

The flares need to cope with two distinct burning problems - firstly high pressure gases and secondly low pressure, high density gases. It is the latter which pose the greatest problem in terms of pollution due to the high combustion air requirements of the high density gases at or near atmospheric pressure which have insufficient pressure to induce the required volumes of air. A typical INDAIR (INDuced-AIR) flare used by B.P. International plc to overcome this problem is the HP/LP flare, shown in figure 1.6, which simultaneously burns high and low pressure gas. The high pressure gas entrains sufficient ambient air to burn itself, and the low pressure gas bled through the central open pipe of the flare.

Some of the advantages provided by these external waste gas flares are reduced pollution, smokeless combustion, low heat radiation (due to efficient premixing), a shorter flame length, greater wind stability, and increased safety and reliability of operation. There are however some disadvantages associated with using these flares. Their complex design results in high manufacturing costs, and the flow shock structure from the under-expanded jet causes very high noise levels. Their performance is also limited by the undesirable phenomenon of breakaway. Under certain extreme conditions the jet no longer follows the curved surface of the flare, but breaks away and shoots outwards from the flare, so strict safety margins have to be built into the flare design to ensure this does not occur under any operating conditions.

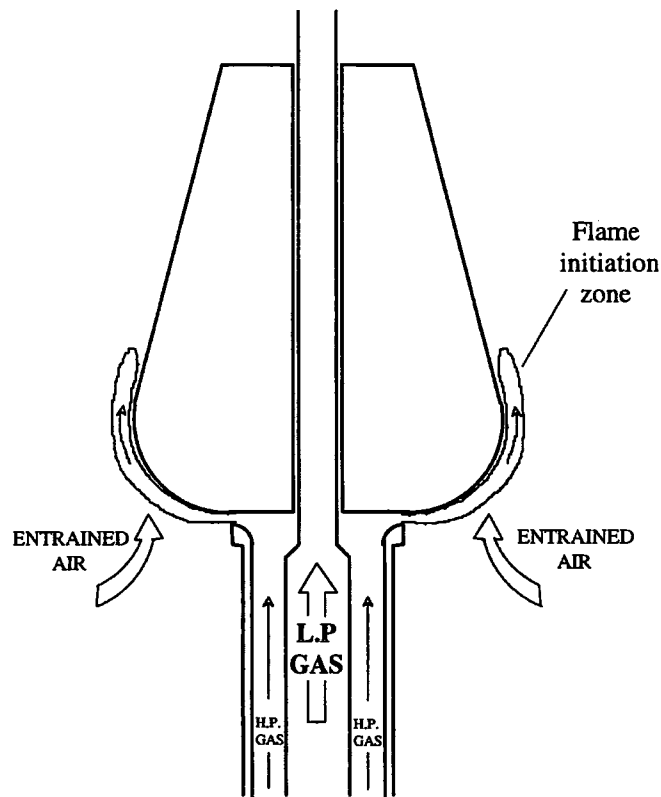


Figure 1.6 Dual purpose HP/LP INDAIR Coanda flare

1.3 Project objectives

The designs for many devices which exploit the Coanda effect have been developed on a 'cut-and-try' basis. Previous work on Coanda flows in Durham has shown that under-expanded high speed jets have extremely complex flow aerodynamics. The turbulence structure in the outer part of the jet, and the shock wave patterns and interactions with boundary layers in the inner part of the jet are all highly complicated.

There are really two important aspects of the Coanda effect flow field which need to be considered if improvements are to be made in future designs. The first is to predict correctly the turbulence structure and entrainment rate of the jet as it goes round a convex surface. The second is to study the effects of compressibility on the flow field. At high blowing pressures the jet is under-expanded and this results in a shock cell structure near the slot. As the blowing pressure is increased the jet eventually ceases to adhere to the surface and breakaway occurs. It is therefore an important aspect of design work to be able to predict the shock cell structure correctly, and determine the critical blowing pressure at which the jet will break away from the surface.

Previous work by Senior (1991) has provided considerable data on the breakaway performance of scaled down planar and axisymmetric models of the INDAIR flare, along with a study of the internal core of the high speed Coanda jet and its interaction with the boundary layer. Work conducted by Hawkins (1988) prior to this was concerned with low speed Coanda flows, with the emphasis placed on studying the outer mixing layer of an axisymmetric flare using Laser Doppler Anemometry (L.D.A.).

The overall aim of this work has been to conduct an experimental investigation into Coanda flows, to gain a better understanding of the flow in general, and to use this information to determine and improve on the best turbulence models and numerical schemes available for modelling the flow using Computational Fluid Dynamics (CFD). All the experimental work described in this thesis has been performed on a 2-dimensional planar model of the INDAIR flare.

The experimental side of this work has been a continuation of the work performed by Senior (1991), who investigated the high speed fluid dynamics of the high pressure

INDAIR flare. Hot film anemometry has been used to measure the mean velocity and turbulence characteristics of the high speed Coanda flow. To permit measurements to be taken over a large portion of the Coanda flare, a traversing gear had to be designed. Software for data acquisition and analysis also had to be developed prior to any experimental work. There were various objectives on the computational side, which involved the use of the CFD code, PHOENICS. These included improvements to the predictions for the jet growth and velocity decay rates, and the turbulence characteristics at low and high speeds, and to accurately predict the conditions when jet breakaway occurs. The data of Hawkins (1988), Senior (1991), Gilchrist (1985), and the experimental results of this current investigation are used to validate the CFD results.

1.4 Thesis structure

A brief introduction to the Coanda effect and some of its applications has been given here. Chapter 2 covers more fundamental aspects of turbulence, streamline curvature and compressibility effects on flows, and past research work is reviewed. The experimental apparatus is described in chapter 3, and the flow measuring technique, hot film anemometry, is described in detail in chapter 4. The experimental results are presented in chapter 5. The computational side of this work is presented in chapters 6 and 7, and a summary and discussion of the findings is given in chapter 8, along with recommendations for future work.

Chapter 2

Review of turbulent flows and measurement techniques

2.1 Introduction to turbulence

At sufficiently low Reynolds numbers, flows are laminar. As the Reynolds number is increased, the flow becomes increasingly unstable, until a critical Reynolds number is reached and the flow becomes turbulent. Almost all flows of engineering importance are likely to be turbulent, so the study of turbulence is one of the most important branches of fluid mechanics. Hinze (1975) defines a turbulent flow as one in which the flow properties show random variations with time and space co-ordinates, and statistically distinct average values may be discerned.

Turbulence can be generated by the shear strain rate produced by velocity gradients, such as those which exist in the region of walls, or by the flow of layers of fluids with different velocities past or over each other. Turbulent motion dissipates kinetic energy by viscous action into heat. If the shearing velocity gradient disappears, this viscous action causes the turbulence to decay.

Turbulent fluctuations are always three dimensional, even if the mean velocities and pressures vary in only one or two spatial dimensions. Turbulent flows contain rotational flow structures, known as turbulent eddies which have a wide range of length scales, ranging from those comparable to the flow boundaries, to intermediate and very small eddies. Turbulent flows involve highly effective mixing, which results in high diffusion coefficients for mass, momentum and heat.

The largest eddies interact with, and extract energy from, the mean flow by a process called vortex stretching. These larger eddies are dominated by inertia effects, and viscous effects are negligible. They are therefore effectively inviscid. The process of vortex stretching creates smaller eddies with shorter time scales, and these smaller eddies are themselves stretched. Thus the kinetic energy is passed down to smaller and smaller eddies in what is called the energy cascade. The smallest scales of motion in turbulent flows are determined by viscosity. At frequencies of typically 10 kHz the viscous effects

become important. Work is done against the viscous stresses by the smallest eddies, and this energy is dissipated and converted to thermal energy. It is this dissipation which results in the increased energy loss associated with turbulent flows.

The largest eddies are highly anisotropic and flow dependent due to the strong interactions with the mean flow. The smaller eddies tend to be more isotropic since the diffusive effects of viscosity tend to smear out their directionality.

Viscosity can in general be neglected in turbulent flows, since the viscous stresses acting on the mean flow are small compared to the turbulent stresses, and the parts of the eddy structure that depend on viscosity are very small and thus weak by comparison to the stress producing parts of the turbulence.

Bradshaw (1975) summarises turbulence as a three dimensional, time-dependent motion, in which vortex stretching causes velocity fluctuations to spread to all wavelengths between a minimum determined by the viscous forces, and a maximum determined by the boundary conditions of the flow.

2.1.1 Predicting turbulence

A brief description of what is meant by turbulence and when turbulent flows may be expected to occur has been given in the previous section. The importance of turbulence, in particular in the numerous applications of the Coanda effect, has been illustrated in Chapter 1. It should therefore be clear that a great deal of engineering design work requires a detailed knowledge of how turbulent flows behave. The design process can be aided by the ability of engineers to model the behaviour of turbulent flows. This can be made possible by the use of Computational Fluid Dynamics (CFD) codes. This method of theoretically modelling flow is discussed in detail in Chapter 6, with specific reference to the modelling methods used in this work. In order to validate the codes used to model turbulent flows, a vast amount of experimental data is required. The majority of this chapter is therefore dedicated to the experimental work which has been conducted in the past, firstly on the more basic flows of free jets, then wall jets, finally leading on to the effects of wall curvature, and compressibility. Comparisons have however been made between these experimental findings, and attempts to model these flows, demonstrating

some of the shortfalls of using CFD. Before a review of experimental work is performed, the equations governing fluid flow are presented, and the significance of the Reynolds stresses explained, along with some other relevant topics crucial to the understanding of the experimental findings.

2.1.2 Equations governing fluid flow

There are five equations which govern all fluid flow, which are based on the underlying principles that mass, momentum and energy are conserved. The full derivation of these equations is given in standard texts, such as Hinze (1975).

The continuity equation, the three momentum equations, and the energy equation are a coupled system of non-linear partial differential equations which are difficult to solve analytically. These five governing equations contain six unknown flow variables, U, V, W, P, ρ and e , so to obtain a closed set of equations, an equation of state such as the perfect gas equation is required. This introduces a further unknown, temperature, so a second equation of state linking internal energy to temperature is necessary.

Historically, the Navier-Stokes equations referred only to the three momentum equations, in honour of the Frenchman M. Navier and the Englishman G. Stokes who independently derived the equations in the early nineteenth century. Nowadays, the Navier-Stokes equations include the complete system of flow equations for the solution of viscous flow. The full set of these governing equations are given below in (2.1(a)-(f)), where all the variables are the instantaneous values. A brief explanation of the derivation of these equations is given in Appendix A.

$$\text{Mass} \quad \frac{\partial \rho}{\partial t} + \text{div}(\rho \mathbf{U}) = 0 \quad (2.1(a))$$

$$\text{x - momentum} \quad \frac{\partial(\rho U)}{\partial t} + \text{div}(\rho U \mathbf{U}) = -\frac{\partial P}{\partial x} + \text{div}(\mu \text{ grad } U) + S'_{Mx} \quad (b)$$

$$\text{y - momentum} \quad \frac{\partial(\rho V)}{\partial t} + \text{div}(\rho V \mathbf{U}) = -\frac{\partial P}{\partial x} + \text{div}(\mu \text{ grad } V) + S'_{My} \quad (c)$$

$$\text{z - momentum} \quad \frac{\partial(\rho W)}{\partial t} + \text{div}(\rho W \mathbf{U}) = -\frac{\partial P}{\partial x} + \text{div}(\mu \text{ grad } W) + S'_{Mz} \quad (\text{d})$$

$$\text{Internal energy} \quad \frac{\partial(\rho e)}{\partial t} + \text{div}(\rho e \mathbf{U}) = -P \text{ div } \mathbf{U} + \text{div}(k \text{ grad } T) + \Phi + S_e \quad (\text{e})$$

$$\text{Equations of state} \quad P = \rho RT \quad e = C_v T \quad (2.1 \text{ (f)})$$

2.1.3 The time-averaged Navier Stokes equations

At sufficiently low Reynolds numbers, flow is totally laminar and the instantaneous velocities used in the governing equations are made up solely of a mean flow component, since there are no velocity fluctuations due to turbulence. Under these laminar conditions, the velocity components, along with pressure and density, are either time independent, or rely very simply on time, so their spatial dependence is also relatively simple.

As the Reynolds number is increased beyond a critical value, the velocities and pressure begin to oscillate about their mean values. These oscillations increase in magnitude as the Reynolds number rises, and there is a gradual change from a simple sinusoidal form to a random motion. At this point the flow is turbulent, and the turbulent fluctuations can occur at frequencies ranging from near zero to 10kHz or more, with an equally wide range of wavelengths. The instantaneous variables for turbulent flow therefore comprise of a mean and a fluctuating component, as shown in equation (2.2), where U is the instantaneous streamwise velocity, \bar{U} is the mean component, and u is the fluctuating component of velocity, and similar notation is used for the other flow variables. Substitution of these components into the Navier-Stokes equations results in a very complex system of equations. A direct numerical solution of these turbulent flow equations would require a very fine finite difference grid both in time, and three spatial co-ordinates. Current computing capabilities mean this is impossible for most flow situations at present.

$$U = \bar{U} + u \quad V = \bar{V} + v \quad W = \bar{W} + w \quad P = \bar{P} + p \quad (2.2)$$

In general, engineers are not interested in the small scale motions of a fluid, only the mean fluid properties, so to simplify the equations, the flow properties are averaged over a time which is long by comparison to the turbulent time scales, but short enough to display any periodic characteristics in the flow. This time averaging results in the 'Reynolds-averaged' Navier-Stokes equations which are presented in full in Appendix B.

The time averaged momentum equations are known as the Reynolds equations, and the tensor form of this equation set is given in (2.3).

$$\frac{\partial(\rho\bar{U}_i)}{\partial t} + \rho\bar{U}_l \frac{\partial\bar{U}_i}{\partial x_l} = -\frac{\partial\bar{P}}{\partial x_i} + \frac{\partial}{\partial x_l} \left[\mu \frac{\partial\bar{U}_i}{\partial x_l} - (\rho\overline{u_i u_l}) \right] + S'_{Mx_i} \quad (2.3)$$

This time averaging results in the appearance of six additional unknown terms, called the Reynolds stresses, which are time-averaged products of fluctuating velocities. Extra unknown terms also appear when scalar transport equations are time averaged. A more complete explanation of what these Reynolds stresses represent is given in the following section.

2.1.4 Reynolds stresses

If the mean values of velocity and pressure are measured in turbulent flow, the mean motion differs from that expected from the action of viscous stresses alone. There are extra 'apparent' stresses which also act on the fluid, and in accordance with Newton's second law, these extra stresses are equivalent to the mean rate of momentum transfer by the fluctuating motion, per unit area.

$$\tau_{ij} = -\rho\overline{u_i u_j} \quad \text{where } i = 1, 3 \text{ and } j = 1, 3 \quad (2.4)$$

These extra stresses are known as the Reynolds stresses, and are given in tensor form in equation (2.4). They appear on the right hand side of the Reynolds equations (the time averaged momentum equations, given in (2.3)). There are three normal stresses (when $i = j$) and three shear stresses (when $i \neq j$). In general, the normal stresses do not differ by more than a factor of 2 or 3, and the shear stresses are of the same order as the

normal stresses. The mean viscous stresses do still act in the flow, but they are generally much smaller.

The Reynolds stresses cannot be thought of as instantaneous stresses like the viscous stresses, despite the fact they have the same effect when considered in terms of the mean values of the flow, since they are in reality a result of the turbulent motions of the fluid. They are generated by the interaction of existing Reynolds stresses with the mean rates of strain, or with the body forces. They may be destroyed by the action of viscous stresses. Pressure fluctuations can redistribute the energy between the Reynolds stress components, but they do not change the overall sum of normal stresses.

From an engineering point of view, it is important to determine the Reynolds stresses, and the other unknown scalar transport terms, since they modify the mean velocity (and temperature) distributions in turbulent flow. There is no direct method of calculating the magnitude of these terms, hence arises the problem of closure. The effects of these terms must therefore be modelled using quantities which can be determined. This involves the use of a turbulence model which consists of a set of equations which, when solved with the mean flow equations, allows calculation of the relevant correlations and permits simulation of the behaviour of a real fluid.

The choice of turbulence model depends on the degree of accuracy, generality and simplicity which is required. The most complex model involves directly obtaining convection equations for the Reynolds stresses. This in turn requires further modelling of higher order terms in order to calculate the Reynolds stresses. Lower order models involve the solution of one or more transport equations for turbulence properties which then allow the Reynolds stresses to be calculated. At the most basic level, Reynolds stresses may be found by simply relating them to the mean field values. Turbulence models are discussed in more depth in chapter 6, but a brief introduction is given here.

Eddy viscosity models

Boussinesq in 1877 suggested that turbulent shear stresses may be proportional to the velocity gradient, just as viscous shear stresses are in laminar flow, but with a factor of proportionality different from the laminar case. This proportionality coefficient is known

as the turbulent 'eddy' viscosity, μ_t . This coefficient may be calculated by solving a simple algebraic expression (as in the mixing length model), or by solving one or two transport equations for parameters. The most widely used type of model involves the solution of two parameters, which define velocity and length scales representative of the large scale turbulence. One example of this is the $k - \epsilon$ model which was developed by Jones and Launder (1972). They solved transport equations for the turbulent kinetic energy, k , and the turbulent energy dissipation rate, ϵ , in order to calculate the local turbulent viscosity. Modified versions of this eddy viscosity model have since been developed by Launder *et al* (1977), Lam and Bremhorst (1981), and Nagano and Hishida (1987), Henau *et al* (1990), and Cheng and Farokhi (1992), amongst others. Various adaptations have been made to the basic model to account for near wall and low Reynolds number flows, and flows involving curvature.

All these models rely on the assumption that the eddy viscosity (which is used to calculate the Reynolds stresses) is isotropic, which is an invalid assumption for many flow situations and can lead to inaccurate flow predictions. The analogy with laminar flow that turbulent stresses are directly proportional to the velocity gradients is a valid approximation for slowly changing shear layers, and in the inner layer of any wall flow, and for flows with similar velocity profiles, i.e. flows in equilibrium or self preserving (these flow types are defined in section 2.1.6). The approximation is invalid however in the outer layer of rapidly changing wall flows, or in rapidly changing free flows. In these cases it is necessary to derive and solve transport equations for the Reynolds stresses themselves.

Reynolds stress models

The transport equations for each Reynolds stress contain diffusion, pressure-strain and dissipation terms which are unknown quantities and difficult to measure. Reynolds stress models require assumptions to be made about these unknown quantities, and the resulting partial differential equations are solved along with the transport equation for the rate of dissipation of turbulent kinetic energy, ϵ .

The process of devising approximations for terms in the Reynolds stress equations is known as 'second-moment closure'. Reynolds stress models have been developed by

various workers, such as Hanjalic and Launder (1972), Launder *et al* (1975), Irwin and Smith (1975), Gibson and Rodi (1981), Gibson, Jones and Launder (1981), and Gibson and Younis (1982).

Algebraic stress models

A simple alternative to solving the full Reynolds stress transport equations is the use of algebraic stress models. These reduce the Reynolds stress transport equations to algebraic equations which are solved alongside the transport equations for k and ϵ . This approach allows a more economical method of introducing eddy viscosity anisotropy into CFD simulations.

The main advantage of the Reynolds stress turbulence model and the algebraic turbulence model over the eddy viscosity model is the ability of these models to account for eddy viscosity anisotropy, and to account for the effects of pressure reflections which occur in wall bounded flows.

2.1.5 Transport equations

Flow variables and turbulent quantities may be determined by solving transport equations. For a general variable, ϕ , the general form of the conservative transport equation may be written as follows :

$$\frac{\partial(\rho\phi)}{\partial t} + \text{div}(\rho\phi\mathbf{U}) = \text{div}(\Gamma \text{grad } \phi) + S_\phi \quad (2.5)$$

where

$\frac{\partial(\rho\phi)}{\partial t}$ is the rate of change of ϕ in the fluid element

$\text{div}(\rho\phi\mathbf{U})$ is the convective term, i.e. net rate of flow of ϕ out of the fluid element

$\text{div}(\Gamma \text{grad } \phi)$ is the diffusive term, and Γ is the diffusion coefficient

S_ϕ is the source term, which contains hidden terms not common to all transport equations

For example, the transport equations for each velocity component (i.e. the momentum equations) may be derived from (2.5) by replacing the variable ϕ with U, V and W respectively, and the diffusive coefficient, Γ , represents fluid viscosity. In this example, solving for the velocity field also requires the continuity equation to be satisfied.

Transport equations for each of the Reynolds stresses may also be derived by considering the technique used to investigate the rate of change of a covariance (i.e. the product of any two fluctuating quantities), e.g. $u_i u_j$. The equation for this rate of change is given by the time averaged sum of ($u_j \times$ the transport equation for U_i) and ($u_i \times$ the transport equation for U_j). The resulting equation describes the transport of the double velocity correlations $\overline{u_i u_j}$ and is called the Reynolds stress transport equation.

The exact transport equation for $\overline{\rho u_i u_j}$ takes the form given in equation (2.6).

$$\frac{\partial \overline{\rho u_i u_j}}{\partial t} + \text{div}(\overline{\rho u_i u_j} \mathbf{U}) = P_{ij} + D_{ij} - \varepsilon_{ij} + \Pi_{ij} \quad (2.6)$$

where

- $\frac{\partial \overline{\rho u_i u_j}}{\partial t}$: rate of change of $\overline{\rho u_i u_j}$
- $\text{div}(\overline{\rho u_i u_j} \mathbf{U})$: transport of $\overline{\rho u_i u_j}$ by convection
- P_{ij} : rate of production of $\overline{\rho u_i u_j}$
- D_{ij} : rate of diffusion of $\overline{\rho u_i u_j}$
- ε_{ij} : rate of dissipation of $\overline{\rho u_i u_j}$
- Π_{ij} : transport of $\overline{\rho u_i u_j}$ due to turbulent pressure-strain interactions

The Reynolds stress transport equations contain unknown higher order correlations which can be calculated by generating higher order transport equations. However, these higher order equations themselves contain even higher order unknown quantities. At some level these higher order correlations need to be modelled in order to close the system of equations. Closure at the level shown in equation (2.6) requires models for the diffusion, dissipation and pressure-strain correlation terms.

The diffusion term can be modelled by assuming that the rate of transport of the Reynolds stresses by diffusion is proportional to the gradients of the Reynolds stresses. The dissipation rate is usually modelled by assuming isotropy of the small dissipative eddies, and the dissipative term only affects the normal Reynolds stresses. The effect of the pressure-strain interactions on the Reynolds stresses may be caused by two distinct processes. Pressure fluctuations can result from two eddies interacting with each other, or an eddy interacting with a region of flow of different mean velocity. The pressure-strain term re-distributes energy amongst the normal Reynolds stresses, thus making them more isotropic and reducing the shear stresses.

The terms in transport equations may effectively be divided into production, redistribution, transport and destruction terms, as shown in the Reynolds stress transport equations above. This is further illustrated by considering the transport equation for the turbulence quantity, kinetic energy. Turbulent kinetic energy is defined as half the sum of the mean squared fluctuating components of velocity. The exact transport equation for k is shown below in equation (2.7) (Versteeg & Malalasekera (1995))

$$\frac{\partial(\rho k)}{\partial t} + \underbrace{\text{div}(\rho k \mathbf{U})}_{\text{Transport by convection}} = \underbrace{\text{div}\left(-\overline{p\mathbf{u}} + 2\mu\overline{\mathbf{u}e_{ij}} - \rho\frac{1}{2}\overline{u_i \cdot u_i u_j}\right)}_{\text{Transport terms due to pressure, viscous stresses and Reynolds stresses}} - \underbrace{\overline{\rho u_i u_j} \cdot E_{ij}}_{\text{Production of } k \text{ by turbulence}} - \underbrace{2\mu\overline{e_{ij} \cdot e_{ij}}}_{\text{Dissipation rate of } k} \quad (2.7)$$

where :

$$E_{ij} = \frac{1}{2} \left[\frac{\partial \overline{U}_j}{\partial x_i} + \frac{\partial \overline{U}_i}{\partial x_j} \right] \quad \text{and} \quad e_{ij} = \frac{1}{2} \left[\frac{\partial u_j}{\partial x_i} + \frac{\partial u_i}{\partial x_j} \right]$$

From this equation it is clear that changes to the turbulent kinetic energy are largely governed by turbulent fluctuations. The production term in the above equation is the rate at which the mean velocity gradients do work against the Reynolds stresses,

transferring mean flow kinetic energy to turbulent kinetic energy. The main destructive term is the dissipation of turbulent kinetic energy, ε , by the viscous stress fluctuations and its conversion to heat. A transport equation for the dissipation of kinetic energy is another important equation in turbulence modelling, and the development of such an equation is given by Hanjalic and Launder (1972).

At high Reynolds numbers, the transport by viscous stresses is negligible by comparison to that by the Reynolds stresses, so the second term on the right hand side of equation (2.7) is often ignored. The turbulent transport terms are usually modelled by considering them proportional to the gradient of the mean value of the transported quantity, resulting in a gradient diffusion term. The first term on the right hand side of equation (2.7) is the pressure term which cannot be measured directly, but its effects may be accounted for in the gradient diffusion term.

From the above discussion, it should be clear that transport equations play an important role in determining the turbulent fluid properties. They can be very complex equations containing terms which may not be directly calculable. In such cases, assumptions have to be made, and models developed. Vast amounts of experimental data have been used to develop and validate these models, in order to justify the assumptions that have been made. The objective of this current research was to obtain further experimental data from a high speed curved jet, and compare the data against CFD predictions, with the aim of improving the modelling results.

It is obvious that the design of any device involving fluid flow can be improved through a thorough understanding of the fluid mechanics and the turbulence structure. The majority of the remainder of this chapter has therefore been devoted to reviewing the work of previous researchers to gain further knowledge of turbulent flows in general, and then more specifically, turbulent flows involving curvature. The success of various workers at modelling turbulent flows has also been considered.

2.1.6 Local equilibrium and self preservation

Flow is said to be in local equilibrium when the rate of turbulent energy production equals the dissipation rate. This condition is met in the inner part of a developing boundary layer, where the mean flow convection and the other transport terms are negligible, and the energy production rate equals the dissipation rate. Local equilibrium is also a good approximation for the fully turbulent outer part of a wall boundary layer, where the mean and turbulent transport terms tend to be equal and opposite.

A shear layer may be described as self-preserving if its scaled form remains constant as the layer develops. Self preserving shear layers have dynamically similar profiles. As such, the velocity and Reynolds stress profiles, and other turbulence quantities can all be represented by a single velocity and length scale. Naturally occurring self-preserving flows are rare since they only occur under restricted boundary conditions. However, certain shear layers with sufficiently high Reynolds number can develop near-similar mean velocity profiles when the flow is fully developed. Simple empirical relations between the Reynolds stress components and the mean rate of strain can be found for flows which are self preserving or in local equilibrium.

Numerous workers have performed experimental tests on self preserving flows, and to do so they required stringent boundary conditions or restricted surface shape, both of which rarely exist in nature. For example, a self preserving flat wall jet requires a tailored pressure gradient (Irwin (1973)). Guitton (1967) showed that a curved turbulent wall jet needs a constant ratio of jet thickness to wall radius of curvature for self preservation. To achieve this, the wall radius must be directly proportional to the distance along the wall, which forms a logarithmic spiral. These self preserving flows have a turbulent eddy structure which may be related non-dimensionally to local parameters which do not change significantly with downstream distance.

2.2 Free jets in still surroundings

Newman (1961, 1969) gives a brief description of the theory for undeflected turbulent free jets, and the formation and development of a typical free jet is shown in figure 2.1 below.

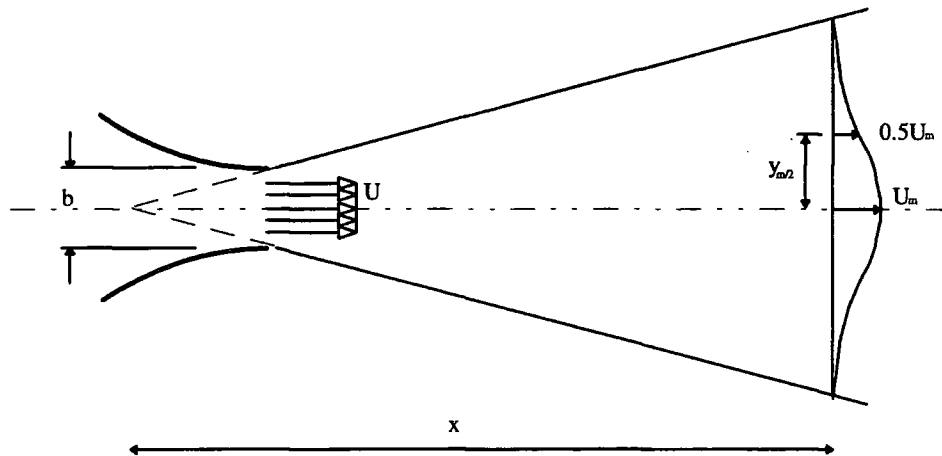


Figure 2.1 : 2-D Turbulent free jet

Providing the contraction ratio at the nozzle exit is sufficiently high, the jet will have very low turbulence levels as it emerges from the slot, with a very thin boundary layer joining the jet to the nozzle wall. Further downstream from the nozzle, the outer edges of the jet mix with the ambient surroundings, and the width of the central core of uniform velocity decreases, as illustrated in figure 2.1. The mean streamlines are straight, except very close to the edges of the flow, where the entraining velocities are comparatively small, so the static pressure throughout the jet may be considered equal to the surrounding atmospheric pressure. The outer mixing layer becomes highly unstable and rapidly becomes turbulent, and the mixing layers gradually grow until they meet. Measurements by Townsend (1956) found the jet to be fully turbulent 10 slot widths down from the nozzle exit. Free turbulent flows often show viscosity independence, or Reynolds number similarity. This has been demonstrated in this case by the angle of spread of the turbulent jet which has been found to be nearly independent of the Reynolds number used to describe the flow.

Newman (1969) describes the basic entrainment mechanism to involve conversion of the irrotational ambient surroundings to rotational flow through the action of viscous shearing stresses. The entrainment rate of the surrounding fluid is given by Newman to be proportional to $x^{-1/2}$, and is therefore greatest close to the slot.

2.3 Plane wall jets in still surroundings

A wall jet may be defined as a shear flow directed along a wall, where the streamwise velocity at some point within the shear flow exceeds the external stream as a result of the initially supplied momentum. The specific case of a wall jet in stagnant surroundings is shown in figure 2.2. Essentially, this jet consists of an inner boundary layer, and an outer half-jet. As such, turbulent wall jets have a lack of symmetry, and display the characteristics of both a free jet stream, and that of a boundary layer. As a consequence of this, the flow possesses two centres of turbulent production, resulting in free turbulence and wall layer turbulence. These two types of turbulence interfere everywhere, and this has been observed by Alcaraz *et al* (1976) to be most noticeable in the region of the velocity maximum.

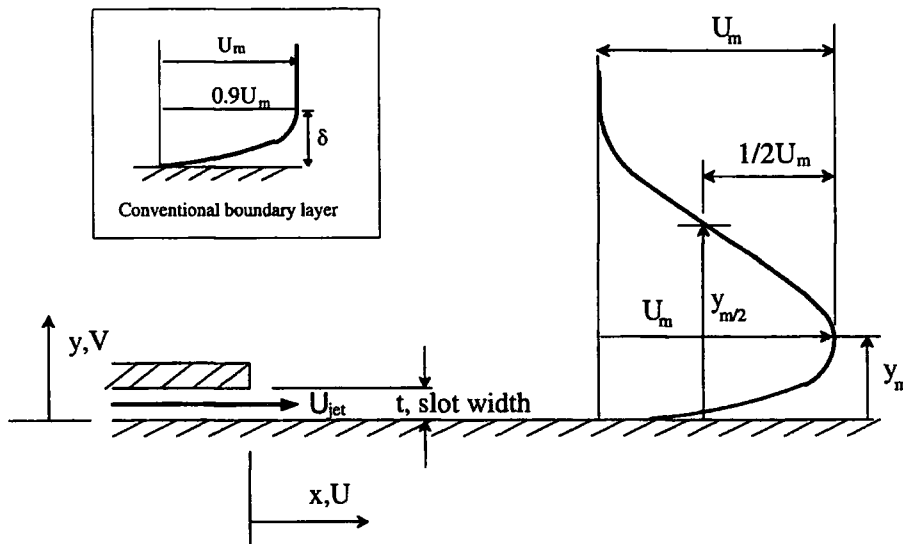


Figure 2.2 : Nomenclature associated with plane wall jets

A review of turbulent jets in general is provided by Newman (1961, 1969), and he, along with Wille and Fernholz (1965) report on the Coanda effect. A comprehensive review of wall jets is provided by Launder and Rodi (1981, 1983).

The turbulent wall jet was first analysed by Glauert (1956), who modelled the flow by considering it to comprise of two regions divided by the velocity maximum. The inner region, lying inside the velocity maximum, was considered to be dominated by wall effects, and to behave like a boundary layer governed by Blasius's pipe-flow formula (i.e. shear stress $\propto U^6$ and velocity $\propto y^{1/7}$). The outer layer, lying outside the velocity maximum, was assumed to behave like a free jet, and a solution for this region was obtained using a constant eddy viscosity proportional to the maximum mean velocity and the width of the shear layer.

The viscous effects in the inner layer were ignored in the analysis. A near-similar solution was sought in which the mean velocity profile (in the outer layer) and the jet growth rate were given by equations (2.8). The eddy viscosity was assumed to vary in proportion to U^6 in the inner layer and to be constant in the outer layer. The two solutions were matched at the velocity maximum, based on the assumption that the shear stress was zero at that point. The values of the constants a and b in equation (2.8) were found to be dependent on the matching procedure used, but were approximately -0.5 and 1.0 respectively.

$$U_m \propto x^a \quad \text{and} \quad y_{m/2} \propto x^b \quad (2.8)$$

Glauert's theoretical analysis was later backed up by the experimental works of Schwarz and Cosart (1960), and Myers *et al* (1963) who experimentally determined very similar values for these constants.

Newman (1961) states that the main effect of changing the Reynolds number (defined for a plane wall jet as $\bar{U}_m (y_{m/2} - y_m) / \nu$), is to alter the proportion of the flow which is occupied by the boundary layer. At high Reynolds numbers the ratio of $y_m / y_{m/2}$ becomes smaller, typically of the order of 0.1. Newman proposes that the inner and outer velocity profiles are nearly independent of Reynolds number. He suggests the

inner profile may be predicted using the method proposed by Glauert, and the outer profile, which is similar to a free jet, may be predicted using the following equation :

$$\frac{\bar{U}}{\bar{U}_m} = \operatorname{sech}^2 \left(0.88 \frac{(y - y_m)}{(y_{m/2} - y_m)} \right) \quad (2.9)$$

Launder and Rodi (1981) performed a very extensive review of turbulent wall jet flows. They discarded any data which failed to meet the two dimensionality checks they applied, and plotting non-dimensionalised mean velocity profiles of the remaining acceptable data they showed the profiles were generally similar, and in close agreement with the predictions of Glauert. Wilson and Goldstein (1976) also found similar agreement.

Launder and Rodi also found that the outer jet growth rate agreed with Glauert's theoretical prediction. They showed that the growth rate of the outer layer of a wall jet in stagnant conditions may be characterised by the formula $\partial y_{m/2} / \partial x = 0.073 \pm 0.002$. This gives a growth rate which is 30% less than that of a plane jet. This has been attributed to the reduction in large eddy length scale due to the presence of the wall, and to the effects of pressure reflections at the wall, which reduce the transfer of energy from the streamwise direction to that normal to the surface. According to Launder and Rodi (1983), in wall bounded flows, the streamwise turbulent normal stress may contain 60% of the total energy, and is about 5 times greater than the perpendicular turbulent normal stress. By contrast, in most free shear flows, such as the free jet considered in section 2.3, less than half the turbulent energy is contained in the streamwise fluctuations, despite the fact that most of the energy from the mean flow enters through this stress component. This theory is in agreement with the findings of workers such as Guitton (1970) and Alcaraz (1977) (as quoted by Launder and Rodi), and Wilson & Goldstein (1976) who measured the normal component fluctuations in plane wall jets to be far less than the streamwise component.

Despite the above agreements with Glauert's predictions, Bradshaw & Gee (1960) pointed out two discrepancies of the theory with real flow. Firstly, they noted that Blasius's pipe flow surface friction formula underestimates the wall shear stress by 25%.

Secondly they found the zero shear stress position does not coincide with the velocity maximum (as it does for a laminar jet), but in fact lies well inside the maximum.

Launder and Rodi (1981) postulated that the skin friction in the wall jet is higher than in a conventional boundary layer (shown in the insert in figure 2.2) due to the increased turbulence levels in the outer part of the wall jet. They also comment on the difficulty of measuring the wall shear stress of wall jets in still air, and reference several workers who have used a variety of different methods to do so. They considered the data of Bradshaw and Gee (1960), obtained using a Preston tube, to be one of the most accurate sets of data. Bradshaw & Gee showed the wall shear stress of a jet in still air can be represented successfully by the formula given in equation (2.10), and Launder and Rodi suggest this is valid in the range $3 \times 10^4 < \frac{\bar{U}_m y_m}{\nu} < 15 \times 10^4$.

$$\frac{\tau_w}{0.5\rho\bar{U}_m^2} = 0.0315 \left(\frac{\bar{U}_m y_m}{\nu} \right)^{-0.182} \quad (2.10)$$

It is clear that the wall region of the flow is highly dependent on the outer flow, and likewise the outer jet-like flow is strongly influenced by the wall. The large scale eddies of the outer shear layer bear a shear stress of opposite sign to that of the wall, and the incursions of these eddies strongly affect the inner region. As a direct result of the influence of the outer shear layer, the shear stress in the wall region decreases far more rapidly than in a boundary layer with no pressure gradient. The shear stress as a consequence does not equal zero at the velocity maximum, and has been found to fall to zero at about 60% of the distance to the velocity maximum. At the position of maximum velocity the shear stress has been measured to be of about the same magnitude but of opposite sign to that at the wall. Mathieu (1959) (as quoted by Launder and Rodi, 1981), is thought to have been the first to report on this phenomenon which is due to the diffusion of the shear stress as a result of the highly unequal length scales on either side of the velocity maximum.

To summarise, wall jets display a growth rate which is approximately 30% less than a free jet, and in accordance with this, turbulence levels are lower in the wall jet than the free jet. The skin friction coefficient of a turbulent wall jet is higher by 20-30% than in a

conventional boundary layer. The zero shear stress position in turbulent wall bounded flows lies inside the velocity maximum, whereas in laminar wall flows, the zero shear stress position and the velocity maximum coincide.

Various simple calculation methods, including that of Glauert's, have been based on the assumption that the shear stress is zero at the velocity maximum position. Extensive experimental evidence however shows this is not the case. More complex models are not based on this assumption, and as expected give better predictions. Hanjalic and Launder (1972) were the first to solve transport equations for the Reynolds stresses in order to model a wall jet. They successfully predicted the position of zero shear stress away from the velocity maximum, however the shear stress in the outer shear layer was predicted too high, resulting in a 20% higher jet growth rate. Their calculation failed to model the pressure reflections from the wall, resulting in unrealistically high fluctuations normal to the wall. Launder, Reece and Rodi (1975) introduced wall damping into the model which corrected this deficiency. Gibson and Younis (1982) used a different pressure reflection model with similar success.

2.4 Curvature effects

So far the governing equations of flow have all been presented and discussed in terms of Cartesian co-ordinates. However, when discussing curved flows these equations are often expressed in terms of curvilinear (s, n) co-ordinates, where s follows a curved reference line (usually a solid surface or other streamline), and n is normal to s . The radius of curvature of the reference line, R , is generally a function of s , and the local radius of curvature, r , is related to R by $r = R + n$. Transformation of the 2D incompressible Navier-Stokes equations and the Reynolds stress equations into curvilinear co-ordinates results in extra terms associated with curvature naturally occurring in the equations. The continuity, and the streamwise and normal momentum equations for a two dimensional mean flow are given in equations 2.11(a)-(c) respectively (Bradshaw (1973)). The viscous term in (b) is shown in the simplified form suggested by Bradshaw who applies an order of magnitude analysis to the term. He applied a similar argument to the viscous term in the normal momentum equation and showed the term can be neglected. The viscous term is therefore omitted from equation 2.11(c).

$$\frac{\partial U}{\partial s} + \frac{\partial}{\partial n} \left[\left(1 + \frac{n}{R} \right) V \right] = 0 \quad (2.11(a))$$

$$U \frac{\partial U}{\partial s} + \left(1 + \frac{n}{R} \right) V \frac{\partial U}{\partial n} + \frac{UV}{R} = -\frac{1}{\rho} \frac{\partial \bar{P}}{\partial s} - \frac{\partial \bar{u}^2}{\partial s} - \left(1 + \frac{n}{R} \right) \frac{\partial \bar{uv}}{\partial n} - 2 \frac{\bar{uv}}{R} + v \frac{\partial^2 U}{\partial n^2} \quad (b)$$

$$U \frac{\partial V}{\partial s} + \left(1 + \frac{n}{R} \right) V \frac{\partial V}{\partial n} - \frac{U^2}{R} = -\left(1 + \frac{n}{R} \right) \frac{1}{\rho} \frac{\partial \bar{P}}{\partial n} - \frac{\partial \bar{uv}}{\partial s} - \left(1 + \frac{n}{R} \right) \frac{\partial \bar{v}^2}{\partial n} - \frac{(\bar{v}^2 - \bar{u}^2)}{R} \quad (c)$$

The Cartesian form of these equations, applicable to plane wall jets, is obtained by taking the limit as $R \rightarrow \infty$. The terms U^2/R and \bar{u}^2/R which appear in the normal momentum equation represent the centrifugal force contribution to the radial momentum balance. The Coriolis force contributions to the streamwise momentum balance are provided by the terms UV/R and $2\bar{uv}/R$ in equation 2.11(b).

Simple undistorted shear layers are easily classified since the streamwise Reynolds stress gradients are usually insignificant. More complex, distorted shear layers are harder to classify. Such complex shear layers are described by Bradshaw (1973) as those in which 'extra rates of strain' have a significant effect on the turbulence structure, in addition to that of the simple shear. An 'extra rate of strain' appears as an additional term in the production term of the Reynolds stress transport equation. Bradshaw (1973) gives a detailed discussion of the effects of extra strain rates on turbulence. The most important source is attributed to streamline curvature, however other sources include lateral divergence and bulk compression. Bradshaw describes how the effects of any extra rate of strain are an order of magnitude larger than that expected from the extra terms which appear in the equations of motion. He states that it is almost a universal law that if an extra rate of strain, e , is added to a simple shear layer $\partial u/\partial y$, the Reynolds shear stress will eventually change by a factor of the order $1 \pm 10 \frac{e}{\partial u/\partial y}$.

From the above argument, it may be expected that streamline curvature will have a huge effect on the development of turbulent boundary layers and turbulent wall jets. Numerous practical aerodynamic surfaces have significant curvature, yet despite this, turbulence models are generally very poor at predicting the effects. Bradshaw warns that all models are likely to under-predict these extra strain rate effects by a factor of about

10, unless explicit empirical allowance is made, since standard models only recognise the standard explicit terms.

The effects of convex and concave curvature are totally different, and the differences are such that knowledge of the one cannot be taken as a guide when trying to model the other. For the purposes of this work, only convex flow situations are considered in detail, although comparisons have been drawn with concave curvature.

The next section looks briefly at the effects of curvature on turbulent boundary layers, and the section following this looks in more detail at turbulent wall jets with curvature. The latter has strong relevance to the current field of research.

2.4.1 Curved wall boundary layers

A great deal of research into the effects of curvature on boundary layers has been performed in the last 40 years. In addition to these studies, the recovery process of a boundary layer on a flat plate following curvature has also been investigated.

Many workers have demonstrated how the development of turbulent boundary layers is affected by streamline curvature. In laminar flow, the fractional change in shear stress due to curvature effects is of the same order of magnitude as the ratio of shear layer thickness, δ to radius of curvature, R . In contrast to this, turbulent flow measurements have shown fractional changes in shear stress an order of magnitude higher than this. For example, Meroney & Bradshaw (1975) found that, for constant pressure incompressible turbulent flow over convex and concave surfaces, the skin friction differs from the plane wall value by as much as 10%. Thomann (1968) had observed similar results with supersonic boundary layers under constant pressure flow. He found the heat transfer to be approximately 20% higher than the plane wall value for a concave surface, and 20% less for a convex surface.

Eskinazi & Yeh (1956) used hot wire anemometry to measure the turbulence quantities in a curved channel flow. A significant decrease in the fluctuating components of velocity was noted over the convex surface, and a spectral analysis showed the decrease

was greatest in the large wavelength range. In other words, the size of the largest eddies were reduced by the convex curvature.

Gillis & Johnston (1983) provide a fairly comprehensive review of research performed on the effects of curvature on turbulent boundary layers, so a repetition of this will not be made here. In addition to this review, they investigated how boundary layer turbulence is affected by strong convex curvature ($\delta/R > 0.05$), and how it then recovers on a flat surface following curvature. The shear stress in the outer part of the boundary layer, and the wall shear stress were both found to decrease rapidly following the onset of curvature. The wall and shear stress profiles were then found to recover very slowly to the flat wall conditions once the curvature was removed. They attributed this asymmetrical response of the boundary layer to the action of the radial pressure gradient which acts in such a way to reduce the size of the largest eddies. The explanation given is supported by the findings of many other workers cited by Gillis & Johnston, and by more recent workers, such as Muck *et al* (1985). The larger eddies contain information on the 'history' of the turbulence structure, and if these eddies are suddenly reduced in size (e.g. by sudden convex curvature) then the influence of the upstream conditions on the turbulence is reduced, and the radius of curvature becomes a more important factor in determining the turbulence structure. The upstream conditions still determine the mean velocity flow field, however the above explains why the turbulence structure of dissimilar boundary layers (from separate convex wall experiments by So & Mellor (1972), Gillis & Johnston (1980), and Gillis & Johnston (1983), Simon (1981)) become similar following the onset of strong curvature. When the curvature is removed, the flow does not instantly revert back to the flat wall conditions since the eddy structure needs time to enlarge itself again, in a similar way to the development of the turbulence structure in a developing flat plate boundary layer.

To summarise, convex curvature has been found to stabilise the boundary layer, and concave curvature to destabilise it. Even mild curvature has been found to significantly effect the turbulence and the mean flow. The region close to the wall which obeys the flat plate log-law is effected by curvature, being increased by concave curvature and decreased by convex.

2.4.2 Curved wall jets

Interest in curved wall flows increased in the 1960's, and early tests involved incompressible flows over convex, constant radii surfaces. The flow characteristics of greatest interest at that time were the increased growth rate, the surface pressure distribution, and the conditions for flow separation from the surface. These mean flow characteristics were studied by many researchers, such as Newman (1961), Fekete (1963), and Sawyer (1963), and the findings of these and others have been reviewed by Newman (1969), Launder & Rodi (1981, 1983). Wille and Fernholz (1965) report on the findings of the first European Colloquium on the Coanda effect, and their report covers the findings of experiments on boundary layers and jets on highly curved walls. Following on from this, the turbulence characteristics of these flows have been investigated by Alcaraz *et al* (1976) and Dakos *et al* (1984) for mild curvature. The results of these studies found that the Reynolds stresses are increased by the mild curvature, however, less work has been done involving strong convex curvature. Workers in this field have included Wilson and Goldstein (1976), Fujisawa and Kobayashi (1987), Morrison (1982) and Hawkins (1988). Finally, high speed studies into jets with curvature have been performed by Roderick (1961), Gilchrist (1985) and Senior (1991).

The early work of Newman (1961) studied the flow over a convex surface, and his findings showed that this flow continually entrains ambient fluid, resulting in increasing jet width and decreasing velocity as the fluid progresses round the surface. The pressure at the surface is initially lower than the ambient static pressure, but as a result of entrainment, this pressure rises round the surface until eventually the boundary layer separates from the surface. Newman suggested that the flow may become independent of the slot width and the supply pressure at some distance from the slot, and that it depends instead on the product of the slot width and the supply pressure relative to the surroundings. Newman shows that the surface static pressure at an angular position θ may be related non-dimensionally as follows :

$$\frac{(P_a - P)R}{(P_o - P_a)t} = f[\theta, Re_p] \quad (2.12)$$

where : $\left(\frac{(P_o - P_a)Rt}{\rho v^2} \right)^{1/2}$ - Reynolds number, Re_p

At high Reynolds numbers, the flow becomes independent of viscosity, so the non-dimensional surface static pressure becomes a function of angle only. Newman gives a similar result for the separation angle, θ_{sep} of a fully developed incompressible jet, given in equation (2.13)

$$\theta_{sep} = f(Re) \quad (2.13)$$

This implies that at high Reynolds numbers, the separation angle tends to become constant. Fekete (1963) showed that the separation angle for flows with a constant radius of curvature was indeed approximately constant. For Reynolds numbers greater than 4×10^4 Fekete found the separation angle to be $226 \pm 3^\circ$, as shown in figure 2.3. Wilson & Goldstein (1976) confirmed that for Reynolds numbers greater than this, the separation angle remains constant. At Reynolds numbers less than this, Fekete found separation occurs earlier than 226° due to the increase in skin friction coefficient.

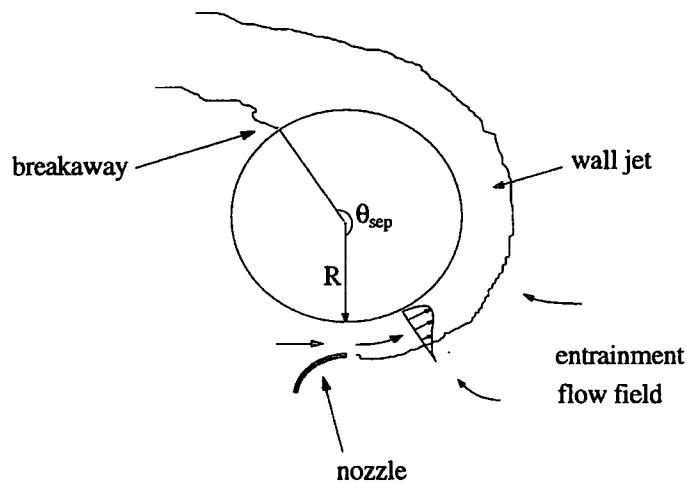


Figure 2.3 : Schematic showing the separation angle can be greater than 180° due to the Coanda effect

When the ratio of slot width to radius is small, the pressure on the surface is less than the pressure of the surroundings by approximately the jet momentum divided by the radius of curvature (from the balance between the centrifugal force and the pressure force, see

equation (2.14)), and since the jet momentum only decays slowly, the pressure on the surface remains almost constant and does not rise rapidly to cause separation of the inner boundary layer. However, once the pressure does begin to rise above the critical value, the inner boundary layer thickens quite rapidly, which raises the pressure even more, so the final approach to separation is quite rapid.

$$\frac{U^2}{Rh} = \frac{1}{\rho} \frac{\partial P}{\partial n} \quad \text{where} \quad h = (1+n/R) \quad (2.14)$$

Launder and Rodi (1981) quote the work of Alcaraz (1977), who measured the triple correlations in curved flow, and normalised them with respect to the appropriate Reynolds stresses. Many turbulence models prior to this work modelled the triple moments by characterising them in terms of the Reynolds stresses and their gradients, so these experimental findings validated these models.

As with the plane wall jet, the pressure reflections at the wall act as a damper, in this case to the radial fluctuations, hindering the transfer of energy from the streamwise to the radial fluctuating component. According to Sawyer (1963) the lateral turbulence intensity, and the large eddy length scales are increased by convex curvature, so the entrainment levels are higher than for a flat wall jet. The converse is true for concave curvature.

The effects of strong convex curvature were investigated by Wilson & Goldstein (1976), Fujisawa & Kobayashi (1987), Hawkins (1988) and Morrison (1982). The latter two performed measurements on an axisymmetric surface, and their findings are discussed further in chapter 5. The two former studies involved measurements of the mean flow and turbulence characteristics on planar two-dimensional surfaces. The Reynolds stresses were found to be much greater than those in a plane wall jet. In particular, strong centrifugal effects were observed on the production of the turbulent fluctuation normal to the surface. They found this production, coupled with the production of shear stress, and the advection of streamwise turbulent fluctuations, increased the interactions between the mean flow and the turbulence, and caused the large growth of the jet width in the strongly convex wall jet.

The restrictive requirement of a logarithmic spiral for self preservation of curved wall jets meant that many experiments have been performed on constant radii surfaces, and early prediction methods relied on empirical formulae to predict the jet growth, for example, Newman (1961) used :

$$\frac{y_{m/2}}{s} = 0.11 \left(1 + 1.5 \frac{y_{m/2}}{R} \right) \quad (2.15)$$

Wilson and Goldstein (1976) demonstrated the non-selfpreserving nature of curved wall jets by examining the velocity profiles of \bar{V}/\bar{U}_m . These were found to be similar for a wall jet on a flat plate, but were non-similar for the curved wall jet. Wilson and Goldstein used equations (2.16) and (2.17) to empirically express the curved jet growth rate and the velocity decay rates respectively.

$$\frac{y_{m/2}}{t} = 0.0787 \left(\frac{s}{t} + 6.0 \right) \left(1 + 2.956 \frac{y_{m/2}}{R} - 0.1599 \left(\frac{y_{m/2}}{R} \right)^2 \right) \quad (2.16)$$

$$\left(\frac{\bar{U}_s}{\bar{U}_m} \right)^2 = 0.0359 \left(\frac{s}{t} + 6.0 \right)^{1.05} \left(1 + 3.354 \frac{y_{m/2}}{R} \right) \quad (2.17)$$

Dakos *et al* (1984) compared the turbulence levels in a heated convex wall jet and a plane wall jet and showed that heat transfer, momentum and turbulence structure are all affected by curvature. Convex curvature was found to increase the displacement of the positions of the zero shear stress and zero streamwise heat flux away from the velocity maximum, towards the wall. The Stanton number for heat transfer from the surface was found to reduce more than the skin friction coefficient. Finally, the stabilising curvature in the inner layer was found to reduce the shear stress, turbulence intensities and turbulent heat flux, whilst the destabilising outer layer increased these properties. The changes due to convex curvature relative to a plane wall jet are proportionally less than those due to concave curvature. This stabilising curvature is far more effective at changing the turbulence structure than the de-stabilising convex curvature. The largest proportional change relative to plane flow recorded by Dakos *et al* was in the triple products associated with the turbulent transport of stress, intensity and heat flux.

The low speed studies of Morrison (1982), conducted on half an axisymmetric model of the Coanda flare, involved measurements at two slot to radius ratios of 0.167 and 0.066. The surface static pressure was found to initially drop due to the curvature, and then gradually rise round the surface to atmospheric pressure. Mean flow properties were measured using a three hole probe and hot wires. The streamwise velocity profiles were found to be similar until 75° round the Coanda surface, by which point the influence of the flat section on the outer layer caused the similarity to break down.

Roderick (1961) investigated the deflection of a compressible jet over a convex surface at stagnation pressure ratios ranging from 0.625 to 0.355, and a slot width to radius ratio range of 0.0156 to 0.0625. There is some doubt as to the two dimensionality of the flow, due to warping of the slot during manufacture, which resulted in variations in slot width of up to 50% at the smallest slot width. Roderick performed an extensive study of the surface static pressure distribution round the surface, and found it to oscillate about a mean negative value just downstream of the slot, and these oscillations became damped out further round the surface. The angular distance between these wave-like peaks and troughs, and their amplitude was found to increase as the stagnation pressure ratio was reduced, and for a given stagnation pressure ratio, the mean value was found to decrease as the slot width was increased. Similar results were obtained in the high speed tests of Gilchrist (1985) and Senior (1991) and are discussed in the following section.

2.5 Supersonic wall jets

The structure of a supersonic jet is dependent on the ratio of the free air downstream to that of the static pressure at the nozzle exit. A ratio of less than unity results in an under expanded jet, and a Prandtl-Meyer expansion occurs at the nozzle exit to reduce the jet static pressure to that of the ambient surroundings. A ratio of unity results in a fully expanded jet, and a ratio of greater than unity implies the jet is over-expanded, and in this situation a compression is required at the nozzle exit, in the form of an oblique shock, in order to raise the jet static pressure to that of the free air.

2.5.1 Coanda flare flow field

The main features of the high speed flare flow field have been determined from the research work of Gilchrist (1985) and Senior (1991). The region of flow establishment downstream of the slot consists of a growing wall boundary layer, an inviscid core, and an outer mixing layer. The growth of the shear layers on the inner and outer boundaries of the jet leads to the eventual elimination of the inviscid core, resulting in a fully viscous flow region further round the flare. Under general operating conditions, the flow is underexpanded at the slot exit, resulting in the development of a shock cell structure.

The experimental findings of Gilchrist and Senior are summarised below. Many of the flow features mentioned here are illustrated on the schematic diagram of the Coanda flow field given in figure 2.4.

- The shock cell structure which exists around the Coanda surface consisting of successive regions of expansion and compression, similar to that of a plane jet. The underexpansion at the slot results in an expansion wave. This becomes reflected from the Coanda surface, and is reflected back from the sonic boundary as a compression wave (waves reflect in a like manner off solid boundaries, and in an unlike manner off free boundaries).
- A sufficiently strong compression wave at the end of the first shock cell causes flow separation. This is characterised by a stagnant pressure region, followed by a region of recirculating flow. A separation shock forms which becomes reflected back as an expansion wave, which aids in the reattachment of the flow.

- The separated region modifies the first shock cell, and the shock wave occurring at the point of separation becomes stronger as the upstream pressure increases. The size of the separated region also increases with upstream pressure.
- As the blowing pressure is increased, a series of separation bubbles form on the Coanda surface, and the growth and amalgamation of these as the pressure rises ultimately causes jet breakaway (described in section (2.5.3) to occur.
- The outer shear layer grows more rapidly than in a plane jet due to the effects of streamwise curvature. The shock cell structure therefore disappears more rapidly than in the plane jet case.
- The axisymmetric jet breaks away from the surface at a higher blowing pressure than the two dimensional jet due to the thinning of the jet by the radial outflow.
- The introduction of a step on the Coanda surface in the exit plane of the slot reduces the shock cell length scale, and hence reduces the size of the separation bubbles which form. This, like the radial expansion effect from axisymmetry, improves the breakaway performance of the Coanda flare.

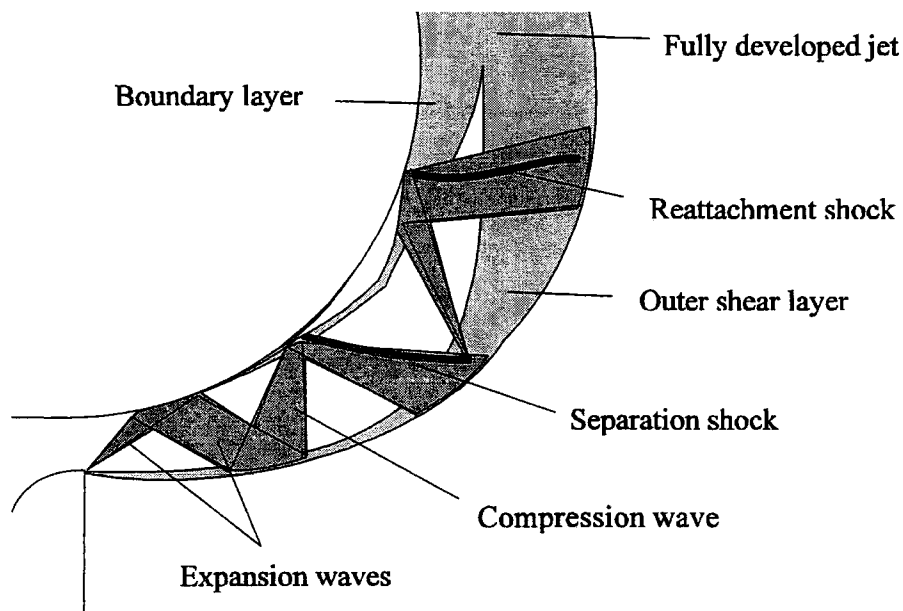


Figure 2.4 : Schematic diagram of the Coanda flare flow field

2.5.2 Shock waves and boundary layer interactions

The shock cell structure which exists in the Coanda flow field results in complex interactions between the shock waves and the boundary layer. Lees and Reeves (1964) describe the interaction between an oblique shock wave and a laminar boundary layer, and a schematic of the flow situation is given in figure 2.5.

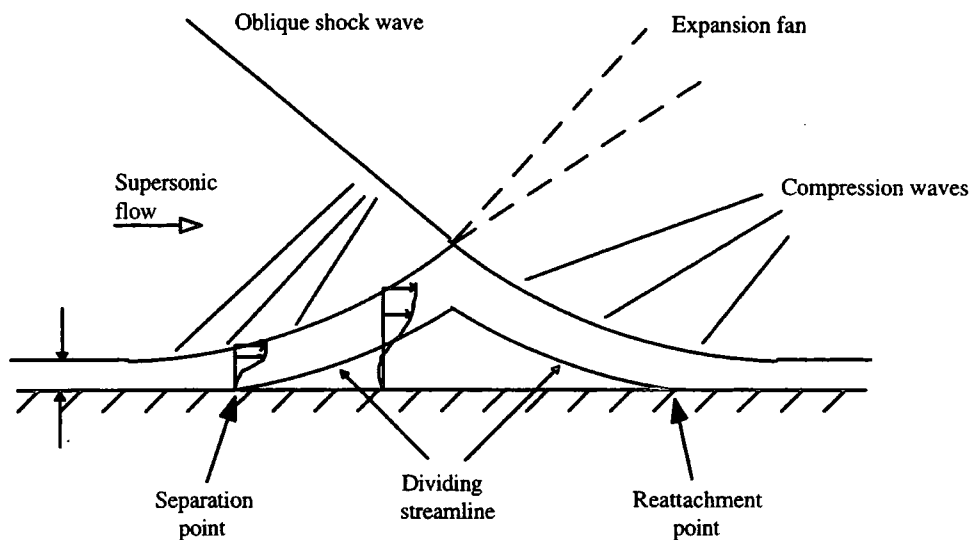


Figure 2.5 : Schematic diagram of an oblique shock interacting with a laminar boundary layer

When an oblique shock impinges on the boundary layer, the subsonic region cannot undergo a localised jump in pressure, so the boundary layer thickens upstream of the shock in order to spread out the pressure rise. Unless the shock is very weak, the adverse pressure gradient which it imposes on the boundary layer results in localised separation. Lees and Reeves quote the findings of Oswatitsch (1958) that the dividing streamline at the separation point leaves the surface at a definite angle. Recirculating flow occurs below this streamline, and a separation shock forms. The thickening of the viscous layer downstream of the separation point results in a reduction in the positive pressure gradient, leading to the region of constant pressure just upstream of the shock impingement - a phenomenon which has been observed by Gilchrist (1985), Senior (1991), and many other workers.

The subsonic viscous layer cannot undergo a sudden pressure rise, so the shock wave becomes reflected as an expansion fan cancelling out the pressure jump across the shock. As a result of this reflection, the flow at the outer edge of the viscous layer is deflected towards the surface, compressing the viscous layer and forcing flow to reverse direction, causing a pressure rise and deceleration of the flow in the viscous layer. Further downstream, increasing amounts of fluid below the dividing streamline are turned back until eventually the fluid on the dividing streamline is also reduced to zero, at which point the flow reattaches to the surface. The growth of the boundary layer generates compression waves which usually come together to form a reattachment shock wave well beyond the outer edge of the layer.

2.5.3 Breakaway

Breakaway refers to the phenomenon whereby a jet no longer follows the curved surface, but 'flips' away to form, in the case of a vertical flare, a horizontal jet. This phenomenon occurs at a critical stagnation pressure, when the separation region on the Coanda surface has grown so large that reattachment no longer occurs.

A hysteresis effect between the breakaway stagnation pressure ratio and the ratio at which the jet reattaches to the surface has been observed by Gilchrist (1985) and Senior (1991). As the stagnation pressure is gradually reduced down from the critical breakaway pressure, the jet progressively deflects towards the surface. Gilchrist notes the jet deflects no more than 10° away from the horizontal before the jet flips back onto the Coanda surface. A complete study of the breakaway performance of the Coanda flare, at a range of slot widths, was performed by Gilchrist and Senior. Reducing the slot width to radius ratio was found to reduce the pressure ratio at which breakaway and reattachment occurred, however the hysteresis between the two was increased.

2.6 Flow measurement and visualisation techniques

In the current investigation, hot film anemometry has been used to measure the mean flow and turbulent fluctuations, however flow visualisation and measurement techniques of Senior (1991) and Gilchrist (1985) have been used to verify some of the CFD predictions discussed in chapter 7. Hence the relevant techniques are described briefly here, but detailed descriptions of the procedures may be found in the above references.

2.6.1 Schlieren images

Schlieren imaging is a flow visualisation technique which was used by both Gilchrist (1985) and Senior (1991) in the study of the Coanda flow field. This, and a similar technique, shadowgraphing, is based on the refraction of light passing through an object with gradients in its refractive index, which in the case of a gas, is caused by density changes in the fluid.

The Schlieren images obtained by Senior and Gilchrist provide qualitative information of the first derivative of the density in the horizontal and vertical directions, via the orientation of a knife edge. A more complete description of the arrangement and method is given in standard texts, and outlined in the thesis of Gilchrist (1985), and also by Gregory-Smith *et al* (1990).

2.6.2 Pressure measurements

Surface pressure measurements round the Coanda surface were obtained by both Gilchrist and Senior, and the results of the latter have been used for comparison with the modelled surface pressures in chapter 7. The pressure tappings used to obtain this surface pressure data were positioned at 3° intervals up to 70° around the curved surface, then at 5° intervals round to the flat surface, and then in 5mm jumps up the flat surface. The positioning of these tappings was staggered, in the central portion of the model surface to avoid side wall effects, and their size was minimised to reduce disturbance to the flow.

2.6.3 Hot wire / film anemometry

A hot wire anemometer is effectively a thermal transducer. The principle behind its operation is the passage of an electric current through a fine filament exposed to a cross flow. As the flow rate varies, the heat transfer from the filament varies, which causes a change in the heat balance, Bradshaw (1975). The filament material has a resistance which varies with temperature, thus by monitoring resistance changes, variations in flow velocity and flow temperature may be observed.

If the hot wire sensor forms one arm of a Wheatstone's bridge circuit, it may be operated in one of two modes. The first is as a constant current anemometer (C.C.A) in which the current through the sensor is maintained constant, and the resistance of the wire fluctuates. This type is rarely used now, and the alternative, a constant temperature anemometer, (C.T.A), is far more common due to its superior frequency response. In this mode a control circuit keeps the wire resistance constant and the current, and hence voltage in the wire fluctuates. Details of the fundamentals of hot wire anemometry are given by Bradshaw (1975), Perry (1982), Lomas (1986) and Bruun (1995).

The hot wire sensors are usually made of platinum or tungsten, with diameters of the order of $5\mu\text{m}$ and about 1mm long. The sensor is soldered or arc welded between the tips of two support needles. They provide a wide frequency response with low noise levels and fine spatial resolution. Due to their small size, they are very fragile, so an alternative to the hot wire is a hot film probe. A variety of configurations of hot film probe are available, including a cylindrical sensor. They are made of nickel or platinum deposited on a thin filament of quartz, and often have a thin protective coating such as quartz deposited over the film. As such, hot film sensors are more robust than hot wires, less susceptible to contamination, and may be used in higher speed flows.

A complex combination of factors determine the heat loss from the hot wire or hot film. They include the effective cooling velocity, the temperature difference between the wire and the fluid, the physical properties of the fluid, and the geometry, and physical properties of the wire. The sensitivity of the hot wire to fluid temperature changes can be minimised by operating the hot wire at a high temperature, and maintaining a constant ratio between the wire temperature and the fluid temperature. The ratio of the heated

sensor operating resistance to the cold resistance is known as the overheat ratio. Setting this as high as possible maintains the sensitivity of the wire to velocity fluctuations, and reduces its sensitivity to ambient temperature changes. In flows involving air, the hot wire overheat ratio is generally set at 1.8, and the overheat ratio for cylindrical hot film sensors is usually about 1.5.

The laser velocimeter is an alternative technique to thermal anemometry, and both have their advantages and disadvantages. The frequency response of the former tends to be poorer, and 'seeding' the flow with particles to scatter the light is a problem, particularly in air. Both can be used over a wide velocity range, however the exclusive sensitivity of the laser velocimeter to velocity fluctuations is an advantage, along with the fact it presents no disturbance to the flow. Despite these advantages, the thermal anemometer is lower in cost, and does not have the problem of flow 'seeding', so this technique has been chosen to study the Coanda flow field. Previous work conducted by Hawkins (1988) into the study of water flowing round an axisymmetric model of the Coanda flare used laser Doppler anemometry, and findings from this work are considered in more depth in chapter 7.

Many workers have used thermal anemometry to measure a vast range of turbulent flows. Numerous techniques have been used, and a comprehensive review of those used in two-dimensional compressible flows is given by Motallebi (1994). From this it is clear that the measurement of high subsonic flows using hot wires presents practical problems which are not encountered in low speed flows. A sufficiently wide pass band is necessary to enable resolution of the highest frequencies of turbulent fluctuations, which increase with air speed. The sensor must also be calibrated over the entire range of Reynolds numbers of interest, and directional coefficients must be determined at different Mach numbers.

The fragility of the sensors, and their sensitivity to contamination mean that an efficient air filtering system is even more important at high speeds to avoid sensor breakage. A simple analysis of the effects of contaminant build up on sensors was performed by Morrow (1972). The effect of dirt particles being deposited on the sensor surface results in a layer of finite thickness building up, which increases the heat transfer resistance and decreases the output voltage. Morrow proposes a correction to the hot wire output in

response to the build up of a dirt layer of finite thickness, and the effects of his modification on the output voltage is similar to that caused by changing the overheat ratio, although there is no physical explanation for this.

Further problems which may occur in higher speed flows are eddy shedding from the support needles, and a phenomenon known as strain gauging. Probes are particularly susceptible to this when introduced with the stem normal to the main flow. Strain gauging involves the vibration of the probe supports or the sensor at their natural frequencies. Hot film probes are more robust and hence less susceptible to strain gauging effects. They are also less likely to break due to contaminants in the air flow, so for these reasons, hot film sensors have been used in this experimental work.

2.7 Two-dimensionality checks

A major problem encountered by many researchers is the establishment of truly two-dimensional flow. Flow may deviate from two dimensionality for two reasons, - either secondary flow effects, or lack of uniformity in the initial flow. The secondary flows which occur at the corners of the side walls can have a significant effect on the displacement thickness of the end wall boundary layers, and effects can encroach on the mid-span flow. Flow uniformity may be affected by disturbances upstream of the flow exit plane, or by slight irregularities in the slot geometry.

A common method used to check two-dimensionality is to compare velocity profiles at various positions off the centre line. Guitton & Newman (1976) suggest a better method is to check that the velocity and length scales which describe the flow vary downstream in a way consistent with the two-dimensional integral momentum equation for the whole flow. Another alternative is to compare the distribution of the measured shear stress with that calculated from the momentum equation using the mean velocity measurements.

Gilchrist (1985) used flow visualisation and total pressure traverses to check the two-dimensionality of a planar model of a Coanda flare under varying operating conditions. The surface oil visualisation technique used also showed up the existence and position of

separation bubbles on the surface. Bands of fluid accumulating on the curved surface were observed, with regions of reverse flow between these bands. As the supply pressure was increased, the bands were seen to gradually move downstream, with the disappearance of bands further round the surface as breakaway conditions were approached. Secondary flows from the side walls were observed after the first separation band, and these flows were amplified by subsequent separation bands. Quite strong evidence was found that fairly strong cross stream vortices form, which are then swept downstream by the main flow, with the effect of narrowing the main jet and reducing the separation zones. Gilchrist found that only the middle third of the flow, in the 8mm slot case, was unaffected by these side vortices. The size of the vortices, and their encroachment onto the Coanda surface was found to increase with slot width. Similar observations using the same technique were made by Senior (1991). The total pressure traverses performed by Gilchrist showed a similar trend. In this, and previous work, the experimental conditions at the slot exit of the Coanda are described using a driving pressure coefficient, C_{po} . This is often referred to as the pressure ratio at the slot, which is equal to the ratio of atmospheric pressure to upstream stagnation pressure, P_a/P_o . With a slot width of 4mm, and a pressure ratio, C_{po} , of 0.662 at 20° round the Coanda surface (measured from the slot exit), Gilchrist found the flow near the surface to be unaffected by the side walls, yet in the outer part of the jet, 40% across the width of the model showed a variation in total pressure. At 40° round the Coanda, 10% of the flow near the surface showed variation in total pressure. The total pressure traverses showed that the effects of the side walls at a given point were increased with a larger slot width or a lower pressure ratio.

Chapter 3

Experimental Apparatus

3.1 Introduction

This chapter describes the apparatus and instrumentation used to obtain the experimental data presented in this thesis. This work is a continuation of previous studies into the Coanda effect at Durham University. The most recent work in this field was conducted by Senior (1991) who investigated the breakaway performance of a high speed jet over a planar model. The model used by Senior was a modification of that used by Gilchrist (1985), involving the introduction of a step at the nozzle exit. The step had the effect of greatly increasing the blowing pressure required to make the jet break away from the surface. Senior also developed a design for an axisymmetric flare, aimed at simulating the flow field of an industrial flare. Due to time constraints, only the planar model has been used for this research work, and only the unstepped case was considered. This planar model had a radius of curvature of 30mm (positioned 25mm away from the base plate / axis of symmetry), and the curved surface extended for 100° from the slot exit, followed by a flat diffuser section of 97mm at 10° to the vertical. Optical and surface flow visualisation techniques were used in previous work to study the flow field around the two models. A different technique, that of hot film anemometry, has been used to obtain the experimental data which is presented in this thesis.

3.2 The experimental rig

To gather data using a hot film, it was necessary to develop a method whereby a probe supporting the sensor could be moved radially out from the curved part of the Coanda surface, and perpendicularly away from the flat section of the model. The requirements for such a traverse were met by the development of the traverse gear shown in figure 3.1. All the slides were supplied by Unislide, and the part numbers for the various traverse components are given on this diagram.

This traverse gear was mounted on an aluminium box section frame that was clamped to the wall at two points, independent of the flare and its supply pipe work to avoid any interference from vibration. The base of the traverse gear was screwed into slots on the

table top of this frame. This allowed adjustment of the traverse gear position, enabling the probe axis to be placed normal to the planar model surface. The manual slide also permitted movement parallel to the planar model surface, and provided a method of checking that the traverse gear was square to the model surface.

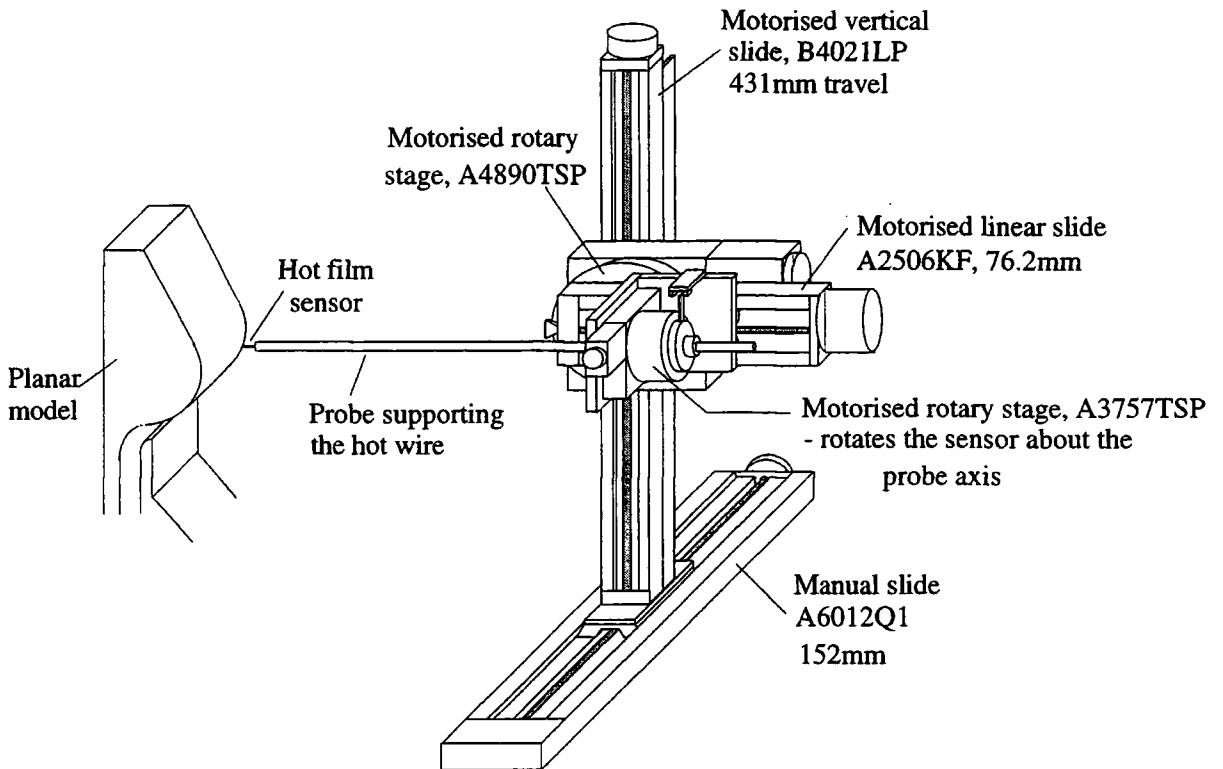


Figure 3.1 : Traverse Gear

The remaining vertical and linear slide, and the two rotational stages were all motorised. The vertical slide and the large rotational stage provided the movement necessary to position the probe stem perpendicular to the flare surface. The smaller linear slide allowed the probe to be taken up to the surface, and then incrementally withdrawn away. The small rotary stage provided rotation about the probe axis. An alternative traverse mode would have been to position the probe axis tangential to the flare surface, so that the axis is aligned in the streamwise direction. In this tangential mode, movement of the vertical and linear traverses is required to move the sensor back from the surface. These two modes of traverse are shown in figure 3.2.

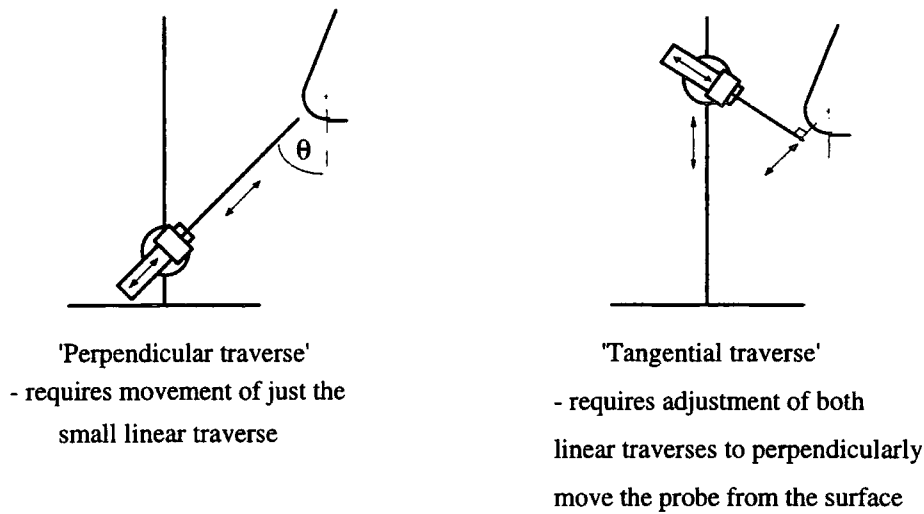


Figure 3.2 : Sketches showing the two modes of traverse available

The range of angles which could be traversed in the two modes was limited firstly by the distance between the vertical traverse and the centre of curvature of the flare, and secondly by the distance between the bottom limit of the vertical slide and the base of the flare. The physical restrictions of the size of the traverse gear, and the side walls of the planar model resulted in the following traverse range restrictions, where the limiting angle of θ is shown in figure 3.2 above :

Perpendicular mode : $\theta_{\min} = 32^\circ$ and 27 mm traverse up the flat section
Tangential mode : $\theta_{\min} = 0^\circ$ and $\theta_{\max} = 37^\circ$

The tangential mode of traverse restricts measurements to only the early part of the jet, whereas the perpendicular mode permits measurements over a much wider range of angles, and more importantly, in the region where the jet is of greatest interest. For this reason, only the perpendicular mode of traverse was used in this work.

3.3 Air supply

The compressed air was supplied by a Reavell CSA9 two stage water cooled compressor which operates at 720 rev/min. It was rated at 30 bar and could supply air at a rate of 434.5 m³/hr F.A.D. into a 5.66m³ welded air receiver, via an air drier. The receiver then

feeds a high pressure line 1.5" diameter B.S.P. which has a number of drop valves situated along its length. It was found however that the compressor could not supply air continuously at the maximum supply rate. This was attributed in part to the fact that solenoid valves on the air drier blew off a considerable quantity of air every minute. Secondly, the supply pressure could not be raised higher than about 28 Bar without blowing a safety valve in the compressor itself.

A problem found in all previous work using this compressor and its associated supply pipework was the contamination present in the air supply. Failure to remove the fine particles in the supply would have led to a greatly reduced operating life for the hot film sensors, since even very small particles travelling at high velocity are likely to damage or even break the film.

A further problem was encountered when running the rig for long periods of time. The pressure, which should be maintained constant by a regulator, was found to drift. The flow rates required for continual operation were considerably lower than those used in previous projects and under such conditions the original regulator was oversized. A new 25 mm Standfast regulator was fitted with a micro flow valve to deal with these lower flow rates. The regulator operation was then found to become oscillatory after short run times. A thorough clean of the regulator revealed large quantities of oily deposit which were clogging up the regulator mechanism.

Examination of the air supply found it to be very damp and oily. Changes were made to the filtration at the air drier. The solenoid valves of the air drier were replaced so they drained correctly, approximately every minute, discharging a white emulsion of oil in suspension.

Despite these changes, problems still existed with the regulator. The air was still contaminated, and running for any period of time resulted in an unpleasant odour. Two options were considered to overcome this problem. The expensive option would have been to place high pressure filters upstream of the regulator to remove particulates, along with an activated carbon filter to eliminate the odour problem. The alternative option, which was adopted, was to make use of an old regulator (large enough to avoid the problems of clogging with dirt) to drop the supply pressure down to just below 10 Bar,

then pass the air through the two existing low pressure filters, then through a new, 0.01 μ filter and finally a new low pressure activated carbon filter before reaching the new Standfast regulator which dropped the pressure from 8 to less than 5 bar. This option required the purchase of two new filters and replacement of the micro flow valve of the Standfast regulator with a standard flow valve due to the reduction in the operating pressure.

A schematic of this new air supply layout is given in figure 3.3. The first stage in the filtration process was the high pressure filter placed upstream of the first regulator. This filter drained automatically and filtered particles down to 25 microns in size. This was followed by an Auld double control high pressure regulator, fitted with a spring to enable the downstream pressure to be varied, which controlled the pressure in the inlet line. The regulator also incorporated a safety blow-off valve to prevent downstream pressures in excess of 10 Bar. This was then followed by a Norgen 30CG-10 filter which performed the second part of the filtration process. It consisted of a 25 micron sintered bronze element and a manual drain to remove water, graphite and some oil. This element was removed and cleaned in an ultra-sonic bath with detergent prior to commencing experimentation. During testing this filter required very regular draining and cleaning due to the high moisture and contaminant levels in the air. The third part of the filtration process was performed by a Balston A15 filter, fitted with a differential pressure gauge and an automatic drain. This filter consisted of a micro fibre disposable element which used collision and static charge effects to remove particles as small as 0.1 micron. This element needed replacing at regular intervals. The fourth part of the filtration process was provided by an OFP195A oil free protection filter. This filter was necessary to prolong the life of the activated carbon filter. It was capable of removing particles down to 0.01 μ . It was supplied with a differential pressure gauge and drained automatically. The final part of the filtration process was provided by an OVR195A activated carbon filter. This operates on the absorption principle, whereby air flows from the inside of the filter element to the outside through a deep bed of activated carbon. A layer of high efficiency filter material then traps any carbon dust which has been released. The operating life of the filter element was supposed to be approximately 100 hours, however, in practise more frequent element changes were necessary in order to keep the odour and vapour problems to an acceptable level. The second regulator was placed after this final filter.

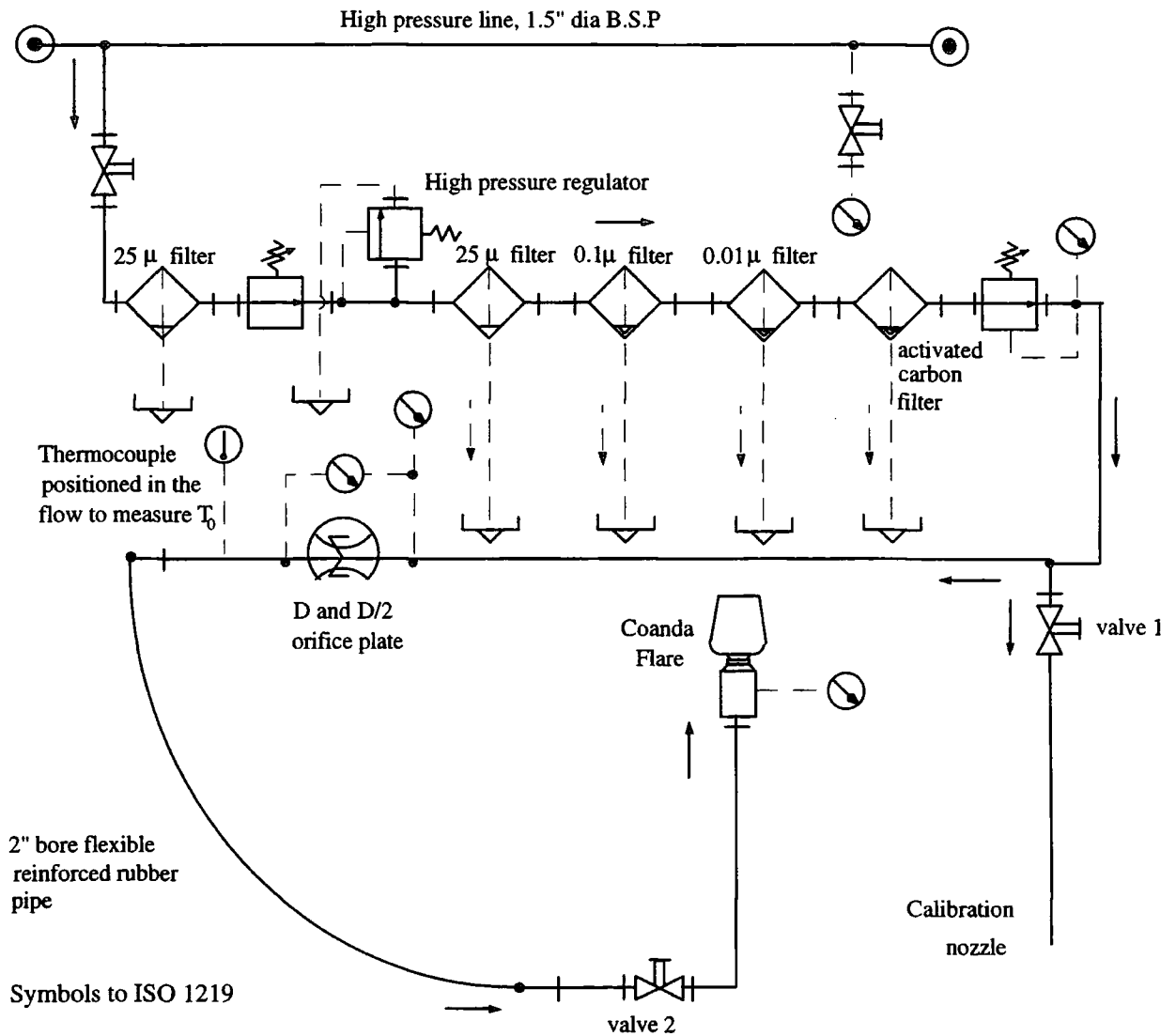


Figure 3.3 : Air Supply Layout

The supply pipework downstream of the filters was quite heavily soiled with deposits of corrosion and carried over oil. The pipework was therefore dismantled and thoroughly cleaned using an electric rotary wire brush. Foam rubber pigs soaked in alcohol were then pulled through the steel pipes. The flexible rubber pipe was washed with a water and detergent mix, then rinsed through with water and allowed to dry. An alcohol pig was then pulled through this pipe to remove the last traces of moisture.

3.4 Calibration rig design

Calibrations were performed by diverting the flow away from the flare and down through the calibration pipe nozzle. This was done by closing valve 2 shown in figure 3.3, and partially opening valve 1. The $\text{Ø}2.5''$ calibration pipe had a subsonic nozzle attached at the end.

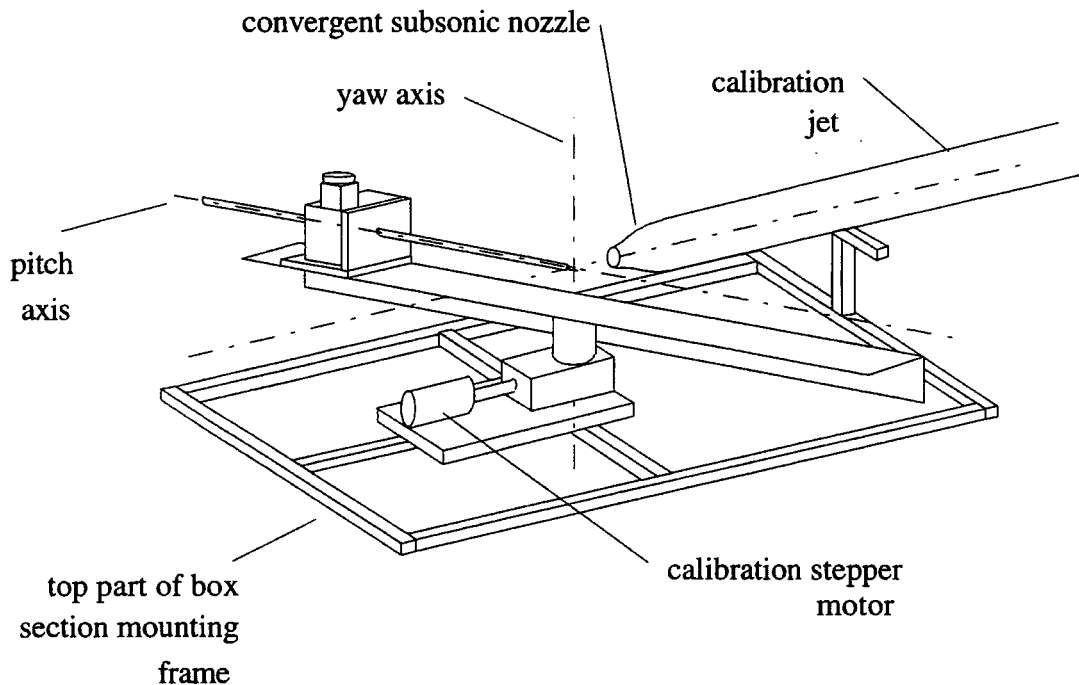


Figure 3.4 : Calibration rig design

The hot film sensor was mounted in such a way that rotations could be made about the probe axis, and also about a vertical axis normal to the calibration jet. This arrangement is shown schematically in figure 3.4. A photograph showing the arrangement is given in figure 3.5 for further clarity. This calibration rig consists of a long arm mounted on a 45:1 gearbox which was driven by a 200 steps / revolution stepper motor. This motor allowed rotation about the vertical axis, altering the sensor yaw angle. Rotation about the horizontal axis to alter the sensor pitch angle was achieved using the same small rotary stage as used on the experimental rig. Both axes pass through the centre of the sensor, thus rotations are about the same point in space, which is so arranged to be at the centre of the calibration jet.



Figure 3.5 : Photograph of the calibration rig

To perform a calibration, the probe stem and the small rotary stage (A3757TSP) had to be transferred intact from the experimental traverse gear rig to the calibration rig, shown above. The rotary stage as a complete unit had to be rotated through 90° to enable it to be bolted to the rest of the calibration rig arrangement using an adapter block.

The length of the probe stem could be altered to suit requirements. A groove along the probe stem, and a locating key on the small rotary stage, ensured that the wire alignment could not alter during a run. Figure 3.6 shows the probe stem design. A collar which fits over the join between the hot film sensor and the probe support supplied by T.S.I. was found to be necessary to prevent the probe from twisting relative to its support once the sensor was introduced into the flow.

The sensor was located in the centre of the calibration jet, approximately 1.5 diameters downstream from the exit. A pitot tube was mounted in the same plane as the hot film sensor allowing calibration jet velocities to be calculated. A 1 Bar pressure transducer was used to monitor the total pressure measured by this pitot tube.

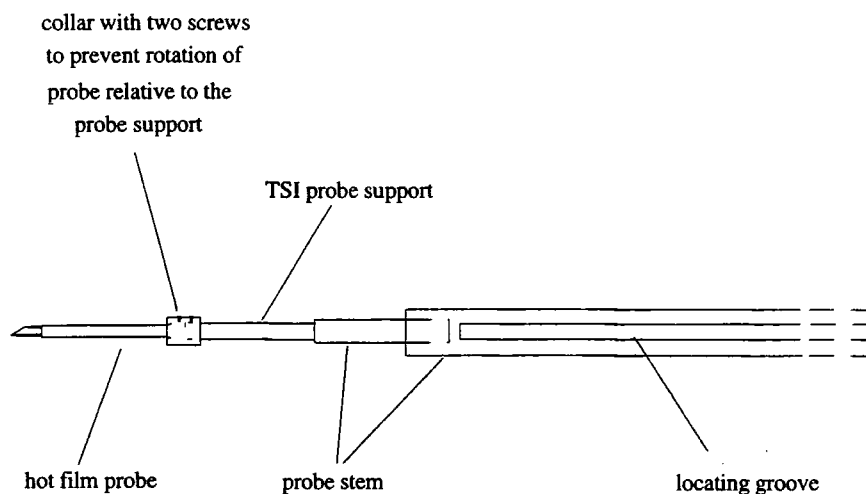


Figure 3.6 : Hot film probe stem design

The temperature of the air supply was expected to vary during the calibration procedure, and differ between calibration and experiment. One option to overcome this would have been to fit a cooler to the supply pipework aimed at maintaining a constant temperature air supply during calibration and experimentation. However, an alternative and cheaper option to this was to monitor the temperature of the flow continually by bleeding some of the flow past the thermocouple in the oil pocket, and correct all voltage readings to a reference temperature. This technique is described in more detail in chapter 4.

The original aim of this work was to investigate flows up to a maximum speed of 0.9 Mach number using a hot film sensor. The calibration procedure, which is described in chapter 4, requires a constant flow to be supplied up to the maximum velocity to be measured during the experiment. The maximum theoretical flow rate which the compressor could supply was 0.143 kg/s, so a subsonic nozzle was designed which required a mass flow rate less than this to provide 0.9 Mach number at exit. The subsonic nozzle was manufactured on a CNC lathe machine. The nozzle design, shown in figure 3.7 was such as to permit the probe to be moved back through an angle of 50° during calibrations, whilst still keeping the probe as close to the nozzle exit as possible, as illustrated in figure 3.8. It was also designed in such a way to minimise the boundary layer thickness at exit, and the acceleration of the flow through a 10:1 contraction reduced the exit turbulence levels.

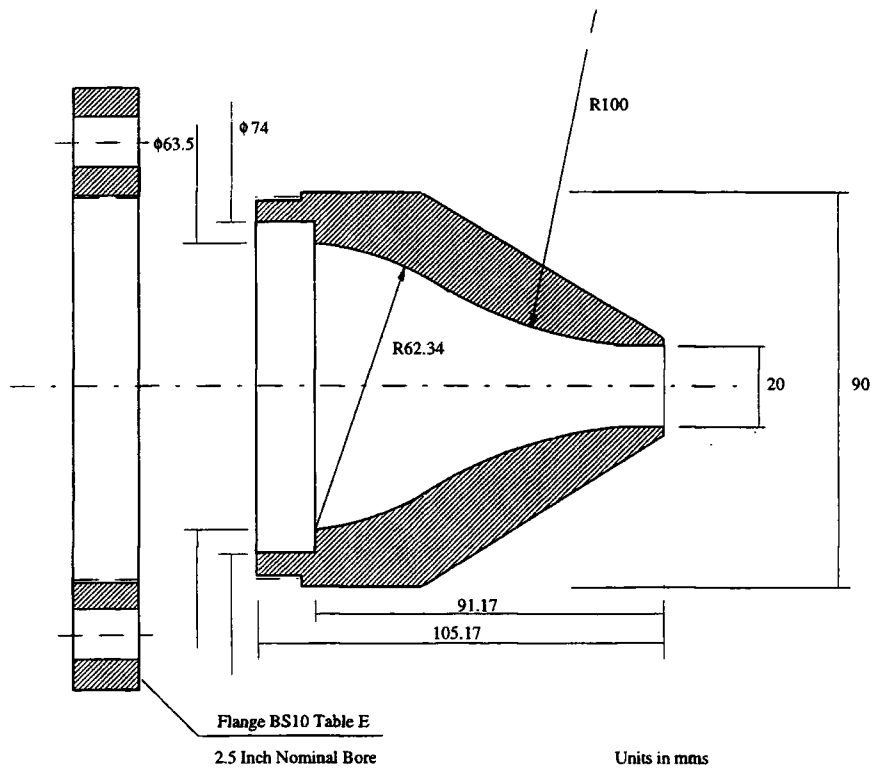


Figure 3.7 : Subsonic calibration nozzle

Finally, figure 3.9 shows a close-up photograph of the calibration nozzle, at a negative angle of yaw, in which the positions of the total pressure probe and the hot film relative to the nozzle can be seen.

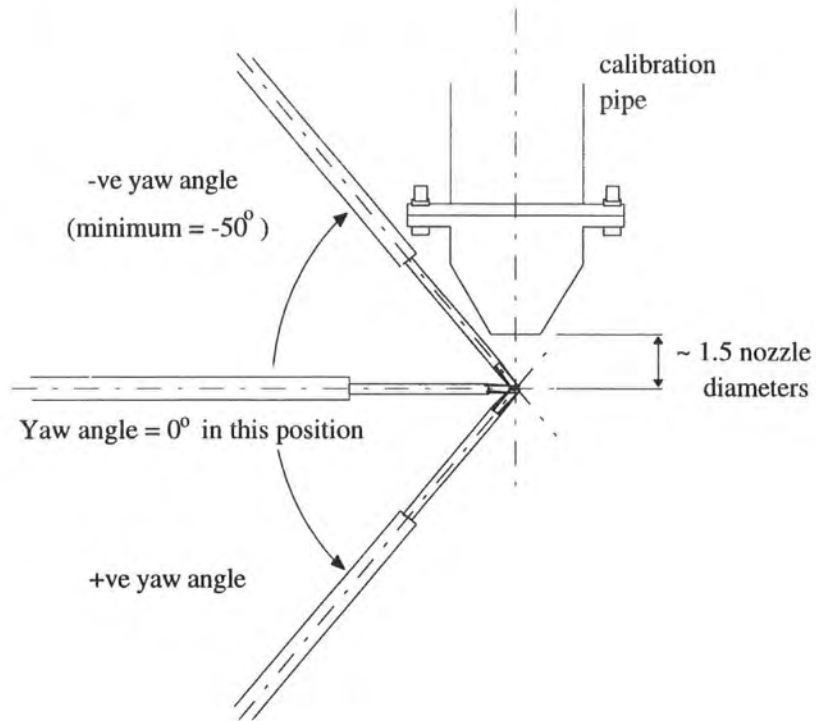


Figure 3.8 : Calibration arrangement

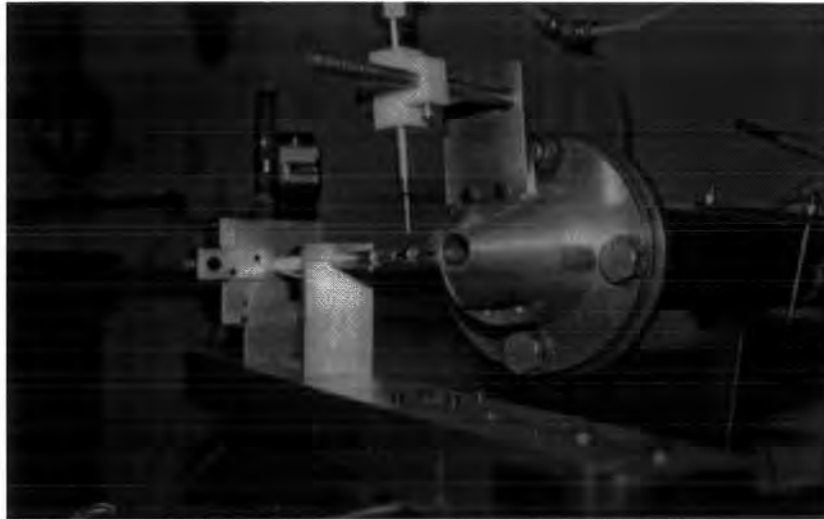


Figure 3.9 : Close-up photograph of the calibration nozzle arrangement

3.5 Pressure measurement

A 1 bar Druck pressure transducer was used to measure the total pressure at the calibration nozzle whilst calibrating, and the pressure difference across the orifice plate during experimental tests. A 35 bar Druck pressure transducer was used to measure the upstream pressure at the orifice plate, and a 7 bar Druck pressure transducer was used to measure the static pressure upstream from the model slot exit. Applying a Mach correction to this static pressure allowed the stagnation pressure, and thus the pressure ratio, P_a/P_o , at the nozzle to be determined. All three pressure transducers were connected to a computer via an A/D converter. The output from the 7 and 35 bar transducers was calibrated against a dead weight tester, and the 1 bar transducer was calibrated against a mercury manometer. The calibrations were then approximated using a third order polynomial.

3.6 Flow measurement and correction

The air mass flow rate was measured using an orifice plate which had D and D/2 tappings, according to BS1042. The 35 bar pressure transducer was used to measure the upstream pressure, and the pressure difference across the plate was measured using the 1 bar pressure transducer.

To ensure accurate measurement of the mass flow rate through the flare nozzle, a correction for leakage losses in the supply pipework was required. Static tests were performed by pressurising the supply pipework with the flare model replaced by a blanking flange. The pipework was rearranged slightly for the purpose of this test. A valve was placed just upstream of the orifice plate, and this valve was closed to isolate the pipework beyond this point from the high pressure main and the filtration pipework. The only leakage of interest was downstream of the orifice plate, and this leakage rate was monitored using the 35 bar differential pressure transducer at the orifice plate.

The leakage rate was calculated from the air density in the pipe before and after the test, the volume of the pipe, and the time taken for the mass loss. The leakage rate was then plotted against the median pressure of the test, and the results from two tests - one with the high pressure valve left open, and one with the high pressure valve closed - are

shown in figure 3.10. The results from both tests are very nearly the same, implying the leakage upstream of the orifice plate had a negligible effect on the test. The average leakage rate was found to be 2.604×10^{-10} kg / sPa .

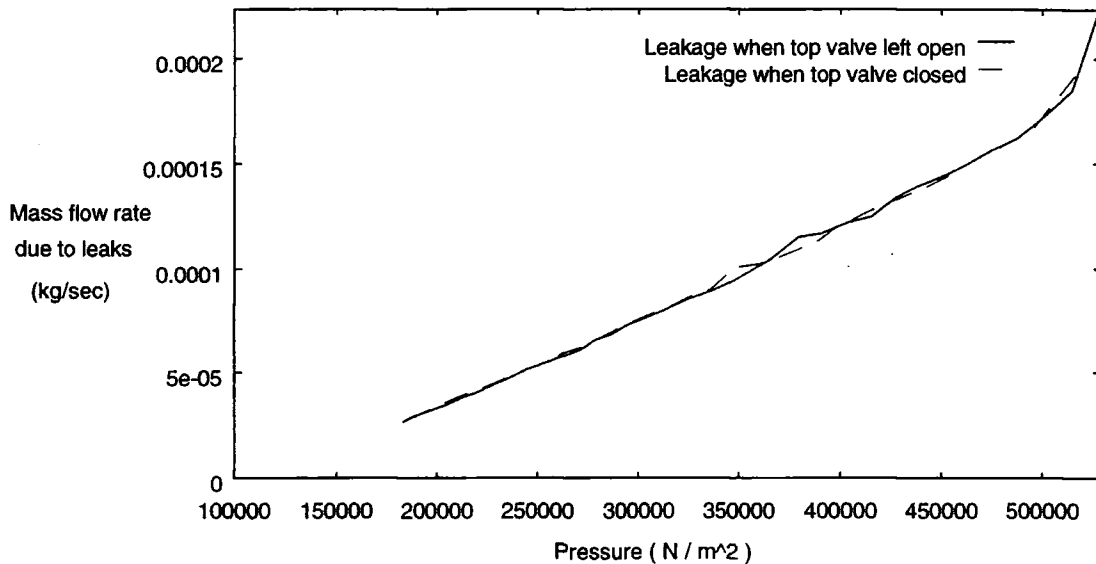


Figure 3.10 : Leakage rate versus pressure

This leakage rate is equivalent to approximately 1% of the total flow rate when the slot width is set at 2mm. At larger slot widths this error is likely to be less if it assumed that the leakage rate is dependent solely on the stagnation pressure of the line. There are likely to be sources of error in determining leakage losses in this manner. Leakage losses from the seals of the flare model cannot be estimated, and in the case of the planar model at small slot heights, this leakage is likely to be significant.

The actual mass flow rate through the flare nozzle at a set slot width and settling tube static pressure was calculated according to BS1042. The two sources of error in determining the flow rate in accordance with this standard, are errors in the measurement of the pressure drop across the orifice plate, and an error in the measurement of the pipe diameter.

The static pressure measured just upstream of the slot by the 7 bar pressure transducer was converted into the stagnation pressure by using a Mach number correction and the

known corrected mass flow rate, i.e. the mass flow rate measured by the orifice plate minus the leakage at that pressure.

3.7 Traverse gear control and data logging

The motorised sections of the traverse gear, shown in figure 3.1, were controlled from a 386 PC. Each stepper motor was driven by a 4 phase bipolar driver board, mounted externally in a driver box placed next to the computer. Each driver board received stepped inputs from a 48 channel Input/Output board (Amplicon Liveline PC14AT) installed in the computer. The motors were all driven in half step mode, and their speeds were ramped up and down to ensure positional accuracy. The positional accuracy of the rotary stages was to $\pm 0.05^\circ$, and a typical linear slide could be expected to return to within 2 steps, or 0.005mm, of its original start position.

The I/O board also received inputs from limit switches on the linear traverses, and optical switches on the two rotational stages. The limit switches were partly a precautionary measure to prevent accidental damage to the slides, but they also aided in the initial positioning of the probe for experimental runs. The optical switches on the rotary stages provided a means of consistently levelling the stages to zero degrees, or moving into the horizontal position.

Data logging was performed using an Analog to Digital (A/D) converter. The A/D board (Amplicon Liveline PC-30PGH) had 12 bit (2.44mV) resolution and accepted inputs of ± 5 volts. The board was capable of logging at speeds of up to 200 kHz. Three channels were used to log the output from the pressure transducers, one was used to log the output from the oil pocket thermocouple, and another was used to record the voltages from the single hot film.

The hot film anemometry equipment itself consisted of a TSI IFA 100 control unit. This main unit consisted of three channels, each with its own MODEL 150 constant temperature anemometer and a MODEL 157 signal conditioner. Only one channel was used however to log the signals from single platinum hot film sensors. The unit allowed cable and probe resistances to be measured, so the operating resistance could be set, and

the frequency optimised. The signal conditioner also applied an offset and a gain to the output signal, so that the maximum and minimum voltages would lie in the range acceptable by the A/D board.

The movement of the traverse gear and the acquisition of data all had to be automated to ensure maximum accuracy, and minimal time for taking experimental measurements. During a traverse, data was processed and reduced to a reasonable degree to minimise storage space on the computer. This generally involved converting the A/D output from a number of steps to either a pressure, or effective mass flux, and calculating the mean and root mean square values of this data, which were written to file for processing at a later date. A typical traverse for each hot film would take between three to four hours.

Chapter 4

Hot film anemometry

4.1 Introduction

Hot wire or hot film anemometers may have a variety of configurations with one, two or three sensors arranged at various angles to each other. Alternatively, hot films may be surface mounted. All these thermal anemometers are ideal for turbulence measurements due to the small size of the sensing element which results in good resolution, minimal disturbance to the flow, and good frequency response. The disadvantages however are a susceptibility to break easily due to contaminants in the flow, and the output from these anemometers requires complex analysis.

One of the most common methods of signal analysis used is based on a technique developed by Jørgensen (1971), who related the three components of velocity to an effective cooling velocity, and hence the sensor voltage. Triple sensor probes can provide instantaneous velocity data using this equation, however, single sensor probes can only provide time averaged velocity data. This is due to the fact that readings must be taken at three different sensor angles using a single sensor, and since these readings are not simultaneous, the equations must be time averaged (which may require some assumptions to be made), thus increasing the complexity of the analysis method required.

There is however an alternative to the Jørgensen equation which involves a method of directly calibrating the sensor over the whole range of flow velocities and angles expected during the experiment. This effectively results in a 'look-up' table which may be used to provide mean flow velocities. The advantage of this sort of technique is that no assumptions are made about the response of the sensor, however large amounts of storage space are generally required in order to obtain the first and second derivatives needed to interpolate between data points. A combination of the direct calibration technique and equation solving may also be used to obtain the mean flow and Reynolds stress data.

The technique used in this work has been based on that developed by Perdichizzi *et al* (1990), using a direct calibration method and two single probes to measure the mean flow and the Reynolds stresses. A similar technique was also used by Moore (1995), but adaptations have been made to extend this technique to high speed flows. Cylindrical platinum hot film sensors have been used in this work instead of hot wires due to their greater robustness. The typical diameter of these sensors is 51 μm , with an effective sensing length of 1000 μm . The maximum velocity which they can withstand (in a contaminant free air stream) is 350 m/s, and the expected frequency response of these sensors is 250 kHz. Single sensors were used instead of the triple sensor arrangement, since the latter type have poorer spatial resolution, and require the probe axis to lie in the direction of the flow.

The following section describes in more detail the basics of a direct calibration technique. The next section then works through the equations which allow the Reynolds stresses to be determined, and an explanation is given for the use of a normal and a slanted probe, instead of just a single sensor. The actual calibration technique used is then briefly described, followed by a full description of the technique used to analyse the experimental data. Some typical calibration plots are examined and the analysis technique tested under known flow conditions. Finally, problems associated with this technique and the experimental rig are discussed.

4.1.1 The direct calibration technique

As described in the introduction to this chapter, a direct calibration technique involves recording the sensor voltage over the entire range of magnitudes and directions of flow to be expected during experimentation. This results in calibration data which is in the form of voltages across the hot film, expressed as a function of the flow velocity, pitch and yaw angle, as defined in figure 4.1, i.e. $V_{\text{film}} = \text{fn}(U, \theta, \phi)$.

The calibration data should provide a set of possible flow velocities that would yield a specific experimental voltage. Since there are three variables, this involves surface fitting techniques and interpolations to obtain the possible values of U , θ , and ϕ . The solution set itself then forms a surface. When a single sensor is used, a minimum of three sensor orientations is required since there are three unknowns for 3-dimensional flow. Placing

the sensor in three different orientations at the same point in space, results in three different experimental film voltages. Each reading should give a set of possible U, θ, ϕ solutions. The intersection of these solution sets should then give a unique solution for the velocity.

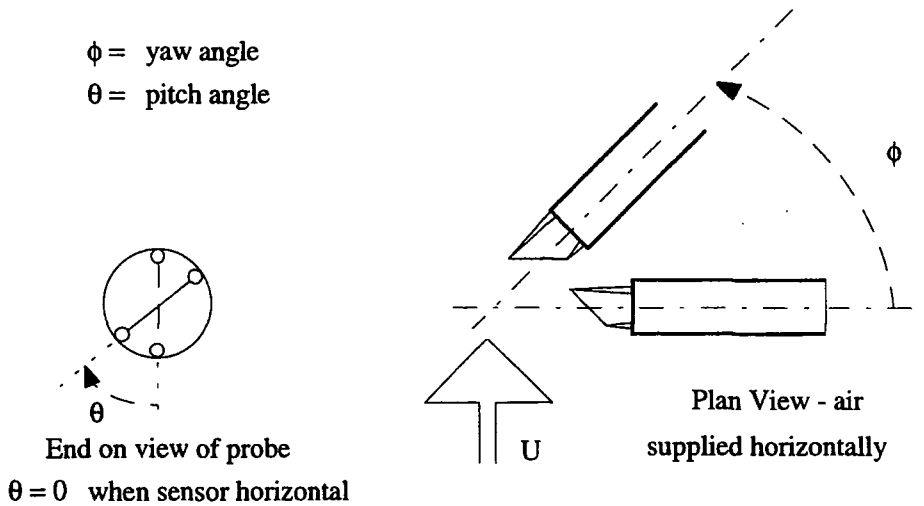


Figure 4.1 : Definition of yaw and pitch angles used during calibration

As previously stated, the solution set for each sensor position forms a surface. Due to the experimental nature of the data, these surfaces will not intersect at a single point, but will instead form the boundaries to a small volume which will contain the solution. A least squares technique must then be used to find the single value which most closely fits all surfaces. By using more than three sensor orientations, an over-determined system is established which should result in a more accurate solution and give an indication of the error in the calculation.

4.1.2 Basic equations for determining the Reynolds stresses

Figure 4.2 shows a slanted hot film of angle α , whose axis lies normal to the main flow direction, i.e. perpendicular to the flare surface. Rotations of the probe are about the U_2 axis. The velocity components in the streamwise, radial and transverse directions from the surface are represented by U_1, U_2, U_3 . This co-ordinate set may be transformed to one relative to the sensor to give the velocity components normal, tangential and bi-normal, U_n, U_t, U_b (see equation (4.6)).

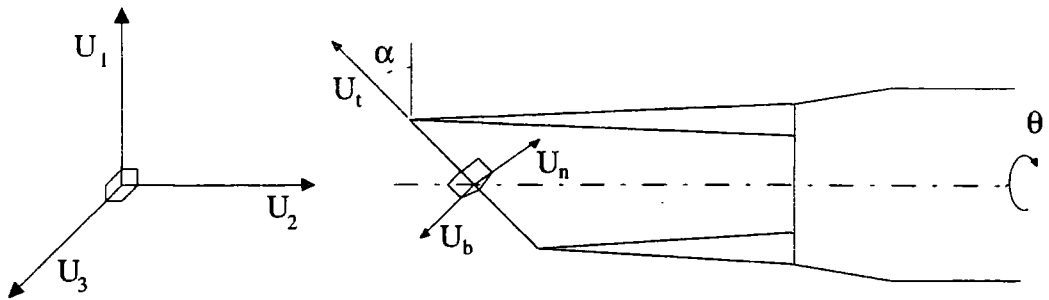


Figure 4.2 : Sensor oriented co-ordinate system

Analysis of any hot film data requires a sufficiently accurate knowledge of the relationship between the voltage across the hot film, and the effective cooling velocity incident on the film. A study of this is conducted by Hinze (1975) and Bradshaw (1975). The heat transfer law given in equation (4.1) is based on that suggested by King (1914), where V_{film_0} is the bridge voltage at zero flow, B and n are empirical constants, U_{eff} is the effective cooling velocity, and ΔT is the difference between the sensor and the fluid temperature.

$$V_{\text{film}}^2 = (V_{\text{film}_0}^2 + BU_{\text{eff}}^n) \Delta T \quad \text{where} \quad n \approx 1/2 \quad (4.1)$$

This equation illustrates the highly non-linear nature of the thermal anemometer response, which requires complex analysis. This analysis is often simplified through the use of a linearising circuit which produces a linearised output voltage, $V_{\text{film}_L} \propto U$. However, linearisers can be prone to drift, noise, and have a limited frequency response. Bruun (1971) studied the accuracy of various linearisation schemes and concluded that none would give good approximations over the entire velocity range 0-150 m/s. It is therefore more accurate to find a direct experimental relationship between the sensor voltage and the effective cooling velocity by fitting a curve through experimental calibration points, and avoiding the use of a lineariser. This direct calibration scheme is discussed in section 4.1.4.

The effective velocity is a function of the magnitude and direction of the flow. The oldest and simplest assumption on the directional sensitivity for a single normal sensor is

the 'cosine law', given in equation (4.2), where φ is the angle between the sensor and the velocity vector.

$$U_{eff} = U \sin \varphi \quad (4.2)$$

Due to the finite length of the sensor, and the disturbances introduced by the prongs, this law was modified by Champagne *et al* (1967) to give (4.3), where k is dependent on the ratio of the sensor length to its diameter, l/d .

$$U_{eff}^2 = U^2(\sin^2 \varphi + k^2 \cos^2 \varphi) \quad (4.3)$$

This equation was modified once more by Jørgensen (1971) to give equation (4.4), where k and h are known as the yaw and pitch coefficients respectively. These coefficients are often considered constant although they are in fact dependent on the magnitude and direction of the flow. For a typical sensor with l/d equal to 250, k is approximately 0.3, and h approximately 1.08. The accurate determination of the yaw and pitch coefficients, along with the relationship between the effective velocity and voltage is dealt with in section 4.1.4

$$U_{eff}^2 = U_n^2 + k^2 U_t^2 + h^2 U_b^2 \quad (4.4)$$

A modified Jørgensen equation, as suggested by Perdichizzi *et al* (1990) may be written, using mass flux components (which take density, and thus compressibility effects, into account) instead of the velocity components. This is given below in equation (4.5).

$$(\rho U_{eff})^2 = (\rho U_n)^2 + k^2 (\rho U_t)^2 + h^2 (\rho U_b)^2 \quad (4.5)$$

The sensor oriented mass flux components, may be written in terms of $\rho U_1, \rho U_2$ and ρU_3 , for a sensor angle of α , as given by equation (4.6)

$$\begin{aligned} \rho U_n &= \rho U_2 \cos \alpha + \sin \alpha (\rho U_1 \cos \theta - \rho U_3 \sin \theta) \\ \rho U_t &= -\rho U_2 \sin \alpha + \cos \alpha (\rho U_1 \cos \theta - \rho U_3 \sin \theta) \\ \rho U_b &= \rho U_1 \sin \theta + \rho U_3 \cos \theta \end{aligned} \quad (4.6)$$

The following expression for the effective cooling mass flux may be obtained by substituting equations (4.6) into (4.5)

$$\rho U_{eff}^2 = A_{11}(\rho U_1)^2 + A_{22}(\rho U_2)^2 + A_{33}(\rho U_3)^2 + A_{12}(\rho U_1)(\rho U_2) + A_{13}(\rho U_1)(\rho U_3) + A_{23}(\rho U_2)(\rho U_3)$$

where

$$\begin{aligned} A_{11} &= \cos^2 \theta (\sin^2 \alpha + k^2 \cos^2 \alpha) + h^2 \sin^2 \theta \\ A_{22} &= \cos^2 \alpha + k^2 \sin^2 \alpha \\ A_{33} &= \sin^2 \theta (\sin^2 \alpha + k^2 \cos^2 \alpha) + h^2 \cos^2 \theta \\ A_{12} &= (1 - k^2) \sin 2\alpha \cos \theta \\ A_{13} &= \sin 2\theta (-\sin^2 \alpha - k^2 \cos^2 \alpha + h^2) \\ A_{23} &= (k^2 - 1) \sin 2\alpha \sin \theta \end{aligned} \quad (4.7)$$

Each component of the mass flux may be split up into a steady, $\overline{\rho U}$, and a fluctuating, ρu , component, where $\rho U = \overline{\rho U} + \rho u$. Substituting this into equation (4.7) gives :-

$$\begin{aligned} (\rho U_{eff})^2 = (\overline{\rho U_{eff}} + \rho u_{eff})^2 &= A_{11} \overline{\rho U_1}^2 + A_{22} \overline{\rho U_2}^2 + A_{33} \overline{\rho U_3}^2 + A_{12} \overline{\rho U_1} \overline{\rho U_2} + A_{13} \overline{\rho U_1} \overline{\rho U_3} + A_{23} \overline{\rho U_2} \overline{\rho U_3} \} \bar{X}^2 \\ &+ 2A_{11} \overline{\rho U_1} \rho u_1 + 2A_{22} \overline{\rho U_2} \rho u_2 + 2A_{33} \overline{\rho U_3} \rho u_3 \\ &+ A_{12} (\overline{\rho U_1} \rho u_2 + \overline{\rho U_2} \rho u_1) + A_{13} (\overline{\rho U_1} \rho u_3 + \overline{\rho U_3} \rho u_1) + A_{23} (\overline{\rho U_2} \rho u_3 + \overline{\rho U_3} \rho u_2) \} \bar{Y}y \\ &+ A_{11} (\rho u_1)^2 + A_{22} (\rho u_2)^2 + A_{33} (\rho u_3)^2 + A_{12} (\rho u_1)(\rho u_2) + A_{13} (\rho u_1)(\rho u_3) + A_{23} (\rho u_2)(\rho u_3) \} z^2 \end{aligned}$$

or more simply :-

$$(\overline{\rho U_{eff}} + \rho u_{eff})^2 = \bar{X}^2 + \bar{Y}y + z^2 \quad (4.8)$$

This is the basic equation describing the response of a sensor to flow. Taking the square root of both sides and then expanding the right hand side using a power series gives equation (4.9)

$$\overline{\rho U_{eff}} + \rho u_{eff} = \bar{X} \left[1 + \frac{1}{2} \frac{(\bar{Y}y + z^2)}{\bar{X}^2} - \frac{1}{8} \left(\frac{(\bar{Y}y)^2}{\bar{X}^4} + \frac{2\bar{Y}yz^2}{\bar{X}^4} + \frac{z^4}{\bar{X}^4} \right) + \dots \right] \quad (4.9)$$

If the terms with triple or higher fluctuating correlations are ignored from equation (4.9) then this yields a new equation (4.10)

$$\overline{\rho U_{eff}} + \rho u_{eff} = \bar{X} \left[1 + \frac{(\bar{Y}y + z^2)}{2\bar{X}^2} - \frac{(\bar{Y}y)^2}{8\bar{X}^4} \right] \quad (4.10)$$

Time averaging equation (4.10) then gives

$$\overline{\rho U_{eff}} = \bar{X} \left[1 + \frac{\bar{z}^2}{2\bar{X}^2} - \frac{(\overline{\bar{Y}y})^2}{8\bar{X}^4} \right] \quad (4.11)$$

If equation (4.11) is then squared and the terms with triple or higher fluctuating correlations are ignored, then equation (4.12) is obtained.

$$\overline{\rho U_{eff}^2} = \bar{X}^2 + \bar{z}^2 - \frac{(\overline{\bar{Y}y})^2}{4\bar{X}^2} \quad (4.12)$$

Time averaging equation (4.8) gives equation (4.13)

$$\overline{\rho U_{eff}^2} + \overline{(\rho u_{eff})^2} = \bar{X}^2 + \bar{z}^2 \quad (4.13)$$

If equation (4.12) is then substituted into equation (4.13) this gives the following equation.

$$\overline{(\rho u_{eff})^2} = \frac{(\overline{\bar{Y}y})^2}{4\bar{X}^2} \quad (4.14)$$

The term $(\overline{\bar{Y}y})^2$ may be multiplied out to give an expression containing 45 terms. This has been rearranged and factorised in equation (4.15) below.

$$\overline{(\rho u_{eff})^2} = \frac{1}{\bar{X}^2} \left(B_1^2 \overline{(\rho u_1)^2} + B_2^2 \overline{(\rho u_2)^2} + B_3^2 \overline{(\rho u_3)^2} + 2B_1 B_2 \overline{\rho u_1 \rho u_2} + 2B_1 B_3 \overline{\rho u_1 \rho u_3} + 2B_2 B_3 \overline{\rho u_2 \rho u_3} \right) \quad (4.15)$$

where :

$$\begin{aligned}
 B_1 &= \frac{1}{2} A_{12} \overline{\rho U_2} + A_{11} \overline{\rho U_1} + \frac{1}{2} A_{13} \overline{\rho U_3} \\
 B_2 &= A_{22} \overline{\rho U_2} + \frac{1}{2} A_{12} \overline{\rho U_1} + \frac{1}{2} A_{23} \overline{\rho U_3} \\
 B_3 &= \frac{1}{2} A_{23} \overline{\rho U_2} + \frac{1}{2} A_{13} \overline{\rho U_1} + A_{33} \overline{\rho U_3}
 \end{aligned}
 \tag{4.16}$$

Equations (4.15) and (4.12) may be solved to give the mean flow velocity and the Reynolds stresses. These equations are not independent so they are solved using an iterative scheme, similar to that used by Moore (1995), which is described in section 4.15.

4.1.3 Choice of probes

The distribution of the 'B' coefficients for the Reynolds stress components against pitch angle for a slanted and a straight probe is shown in figure 4.3. This is for the specific case of zero yaw angle, and $h = 1$ and $k = 0$. The x-axis represents the pitch angle, and the coefficient values for the various stress components are given on the y-axis.

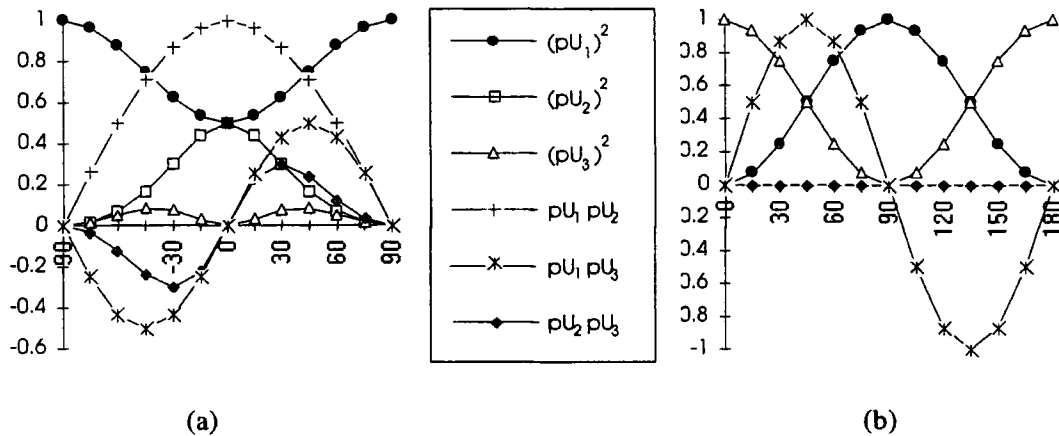


Figure 4.3 : (a) Slanted sensor coefficients, and (b) Straight sensor coefficients

From this it can be seen that the slanted probe is quite insensitive to the $(\rho u_3)^2$ component, so an analysis based on simply slanted probe data would be expected

to give large errors for this component. The straight film can be seen to be insensitive to $\overline{(\rho u_2)^2}$, $\overline{\rho u_1 \rho u_2}$ and $\overline{\rho u_2 \rho u_3}$, but is sensitive to the other three stress tensor components as the pitch angle is varied.

The measuring technique used for the experimental work reported in this thesis involved the use of both a slanted and a straight film probe. Five measurements were taken using the straight probe and this data was used to solve for the $\overline{(\rho u_3)^2}$ component. Nine readings were then taken with a slanted probe and these measurements were used to determine the remaining 5 components. All fourteen readings were used for determining the mean flow conditions. The simultaneous solution of all six Reynolds stresses is not possible using the fourteen sensor angles, since the system of equations which results is very ill conditioned, due to the lack of sensitivity of the various components. The apparently discarded solutions for $\overline{(\rho u_1)^2}$ and $\overline{\rho u_1 \rho u_3}$ from the straight film data are in fact used for comparison against the slanted film solutions for these components to give an indication of the measurement consistency.

4.1.4 Calibration

Calibration of the slanted and straight sensors was performed by holding the probes in a variable velocity jet and rotating them about the ϕ and θ axes (as defined in figure 4.1). The accurate position of the sensor relative to the jet had to be established before any calibration could be performed. This was done by utilising the symmetrical response of the sensors about specific angles. In the case of the slanted sensor, symmetry occurs about $\theta = 0^\circ$ and $\phi = 45^\circ$, as shown by equations (4.17) and (4.18).

When $\alpha = 45^\circ$, and $\phi = 0^\circ$ and θ is varied, the response is symmetrical about $\theta = 0^\circ$:

$$\rho U_{eff}^2 = \rho U^2 \left[\frac{1+k^2}{2} + \left(h^2 - \frac{1+k^2}{2} \right) \sin^2 \theta \right] \quad (4.17)$$

When $\alpha = 45^\circ$, and $\theta = 0^\circ$ and ϕ is varied, the response is symmetrical about $\phi = 45^\circ$:

$$\rho U_{eff}^2 = \rho U^2 \left[\frac{1+k^2}{2} + \left(\frac{1-k^2}{2} \right) \sin 2\phi \right] \quad (4.18)$$

Similarly, for the normal sensor, symmetry occurs about $\theta = 0^\circ$ and $\phi = 90^\circ$. The yaw and pitch angles were positioned by eye close to the angle of symmetry. Eight readings were then taken to one side of this angle, and then sixteen readings were taken at points on the other side and a spline fitted to these points. Interpolations were then made to find the points of equal angle to the first eight readings. The mid point of each pair of voltages was calculated and the average taken to give the point of symmetry. The r.m.s. of the individual mid points was calculated and typically found to be about 0.4° .

As previously described, the calibration data consists of film voltages obtained under specific flow conditions defined by $\rho U, \phi$ and θ . Analysis of experimental results requires a knowledge of the points between the calibration conditions, and for this interpolations must be made in three directions. To simplify and reduce the number of interpolations necessary during the analysis, the data was split up into sets of constant θ , to give $V_{\text{film}}(\theta) = fn(\rho U, \phi)$ and a bi-cubic spline surface fitted for each pitch angle. Intermediate points between the surfaces could then be found by using the same ρU and ϕ on each surface and interpolating linearly between the two.

Calibration data had to be used for two specific tasks before it could be used for analysing any experimental data. Firstly it was used to establish the relationship between the effective mass flux, ρU_{eff} , and the sensor voltage, and secondly it was used to calculate the yaw and pitch coefficients, h^2 and k^2 . For an ideal, infinitely long wire, $k = 0$ and $h = 1$, but applying these values to an actual probe yields poor results, since both coefficients vary with the magnitude and direction of the flow relative to the sensor.

Determining the relationship between mass flux and voltage

The relationship between the voltage and the effective mass flux may be found by placing the sensor normal to the flow, so the ρU_t , the tangential, and ρU_b , the bi-normal components of the flow along the sensor are zero. For both sensors the pitch angle must be zero. The yaw angle must be set at 45° for the slanted sensor, and 90° for the straight sensor. Under these conditions, varying the mass flux gives $\rho U_{\text{eff}} = fn(V_{\text{film}})$. An almost linear relationship exists between V_{film}^2 and $(\rho U_{\text{eff}})^{1/2}$ (King (1914), Perdichizzi *et al*, 1990). Fitting a third order polynomial to this data provides a method for converting any sensor voltage to its corresponding effective cooling mass flux. However, the

relationship is only valid under the exact temperature conditions experienced whilst calibrating. To compensate for any slight temperature variations, all film voltages were corrected to a reference temperature using equation (4.19) proposed by Kanevce *et al* (1973)

$$V_{film,r}^2 = V_{film,e}^2 \left(\frac{T_s - T_r}{T_s - T_e} \right) \quad (4.19)$$

where the suffix 'r' refers to the voltage at the reference conditions, suffix 'e' refers to the voltage either during the experiment or calibration, and T_s is the sensor operating temperature (set at 250°C).

All voltages recorded during the calibration were converted to their corresponding effective mass fluxes before further analysis was performed on the data. Whilst doing this, corrections were also made for any slight variations in the calibration jet velocity, which had a tendency to drift slightly during the course of a velocity run. Once this conversion was complete, the yaw and pitch coefficients, h^2 and k^2 could be determined.

Determining the yaw and pitch coefficients

From equation (4.5) it is clear to see that in order to find k^2 it is necessary to eliminate h^2 , which may be done by arranging for $\rho U_b = 0$. From equations (4.6) it can be seen that this occurs when $\theta = 0^\circ$. Using only the calibration data where the pitch angle is zero, equation (4.20) may be used to calculate k^2 over the range of mass fluxes and yaw angles.

$$k^2 = \frac{(\rho U_{eff})^2 - (\rho U_n)^2}{(\rho U_t)^2} \quad (4.20)$$

By assuming that k^2 is independent of the pitch angle, it is then only a function of two variables, mass flux and yaw angle. A bi-cubic spline surface may therefore be fitted to the data to allow future interpolations.

It is harder to find h^2 , since to do so requires $\rho U_t = 0$ whilst ρU_b may vary. The tangential mass flux equals zero when $\tan \phi = \cos \theta$, so taking readings at values θ and ϕ which satisfy this condition would give $h^2 = fn(\rho U, \theta)$. An alternative, and simpler method is to calculate a value for h^2 for every calibration point using the mass flux, yaw and pitch angles, and an interpolated value for k^2 . This results in h^2 being a function of three variables. This may be simplified by splitting the data according to mass flux, so that at each value of ρU , $h^2 = fn(\theta, \phi)$ and bi-cubic splines are fitted to each of these sets of data. Under known experimental mean flow conditions, a value for the pitch coefficient may be found by interpolating for h^2 at each mass flux using the specific values for θ and ϕ . This provides a value for h^2 at each mass flux. A spline may then be fitted to this data, and interpolation at the required mass flux allows the pitch coefficient to be calculated.

4.1.5 Experimental data acquisition and analysis

In theory, a minimum of only three sensor orientations is required for the mean flow calculation, since there are only three unknowns in 3-dimensional flow. However, three additional readings are required to permit the six Reynolds stresses to be calculated. This therefore results in an over-determined system of equations for the calculation of the mean flow components. In order to obtain further accuracy in the Reynolds stress calculations, an over-determined system of more than six non-linear equations must be solved. Two types of probe have been used - a slanted platinum hot film probe (TSI 1213-20) with a sensor angle, α of 45° and a normal platinum hot film probe (TSI 1210-20) i.e. $\alpha = 0^\circ$. Nine readings taken with the slanted sensor were in the range $\theta = \pm 90^\circ$, followed by five readings using the normal sensor at $\theta = 30, 60, 90, 120$ and 150 degrees.

At each sensor orientation, the voltage was sampled 10000 times at 100 kHz. Before the mean and the fluctuating components of this measurement were recorded to file, each reading had to be corrected for any temperature variations, and converted to its equivalent effective mass flux. It was necessary to perform this conversion before averaging due to the non-linear relationship between V_{film} and ρU_{eff} . Once this conversion was complete the square of the mean effective mass flux, $\overline{\rho U_{\text{eff}}^2}$, and the mean of the square of the fluctuating component of the mass flux, $\overline{\rho u_{\text{eff}}^2}$, could be calculated and saved to file.

For each measurement point in the Coanda flow field, 14 values of $\overline{\rho U_{eff}^2}$ and $(\overline{\rho u_{eff}})^2$ were written to file for later analysis on software run on the UNIX system. These mean and fluctuating values were substituted into equations (4.12) and (4.15) to give two sets of over-determined simultaneous equations which were then solved using the iterative scheme described below.

At each point in the experimental flow field, an initial guess for the mass flux components was made, typically $\rho U_2 = \rho U_3 = 0$ and $\rho U_1 = 100 \text{ kg/m}^2\text{s}$. Using this, values for k^2 and h^2 (determined as described in section 4.1.4) and the 'A' coefficients were calculated. The next step was to solve for $\overline{\rho U_{eff}^2} = \overline{X^2}$ to give a first approximation for $\overline{\rho U_1}, \overline{\rho U_2}$ and $\overline{\rho U_3}$. Using this solution the k^2 , h^2 and the 'A' coefficients were then recalculated, and the 'B' coefficients also calculated using equations (4.16). Equation (4.15) was then solved for the six unknown mass flux correlations $(\overline{\rho u_i})(\overline{\rho u_j})$. Solving equation (4.12) then gave revised values for $\overline{\rho U_1}, \overline{\rho U_2}$ and $\overline{\rho U_3}$. This iterative loop continued to jump back to the point of solving for the k^2 , h^2 , 'A' and 'B' coefficients and solving equation (4.15) until the mean and mass flux correlation solutions converged. Generally 5 loops were required for convergence.

Solution methods

The six mass flux correlations were solved for using the linear equation (4.15). Since more than six readings were taken at each point, the system was over-determined and a least squares solution method was adopted, using a routine from the NAG library, F04AMF. Solving over determined sets of equations improves accuracy and reduces the effects of spurious data. An indication of the accuracy of a solution may be obtained by inserting the solution back into the equation and determining the size of the error.

The solution for the mean flow involves non-linear equations which were solved using the NAG library routine E04FDF. This routine minimises a sum of squares function derived from equation (4.12). The minimised function takes the form of equation (4.21).

$$F(x) = \sum_{i=1}^n [f_i(x)]^2 \quad (4.21)$$

The function is minimised by estimating successive points, based on the curvature of $F(x)$, starting from an initial guess for $\overline{\rho U_1}, \overline{\rho U_2}$ and $\overline{\rho U_3}$. The values for the latter found at the minimum are taken to be the mean flow solution. The residual function, $f_i(x)$ used in the above is found by rearranging equation (4.12), and is given below :

$$f_i(x) = \overline{X}^2 + \overline{z}^2 - \frac{1}{4\overline{X}^2} (\overline{Yy})^2 - \overline{\rho U_{eff}}^2 \quad (4.22)$$

An indication of the accuracy of the solution for the mean flow could be obtained from the value of $F(x)$ using equation (4.23).

$$\% \text{ error} \cong \frac{\sqrt{\frac{F(x)}{\text{No. of wire angles}}}}{\overline{\rho U_{eff}}^2} * 100 \quad (4.23)$$

Solving for the Reynolds stress components

In theory, if the mean total temperature and static pressure are known from separate measurements, and the mean mass flux is approximated with the product of mean velocity and density values, then the velocity components \overline{U}_i , the static temperature \overline{T}_s and density $\overline{\rho}$ can be calculated as follows. The static temperature may be calculated from equation (4.24) which uses the previously determined values of mean mass flux components. The average density may then be determined from the perfect gas law given in equation (4.25). The approximation that the mean mass flux is equal to the product of the mean density and the mean velocity (a valid assumption if the fluctuating Mach number is low) allows the mean velocity components to be determined.

$$\frac{\overline{T}_o}{\overline{T}_s} = 1 + \frac{\gamma - 1}{2} \left(\frac{\overline{\rho U_1}^2 + \overline{\rho U_2}^2 + \overline{\rho U_3}^2}{\gamma \overline{P}_s} \right) R \overline{T}_s \quad (4.24)$$

$$\bar{\rho} = \frac{\bar{P}_s}{RT_s} \quad (4.25)$$

The problem with the above technique lies with the measurement of the mean static pressure. Measurements would be required over relatively short distances, in close proximity to the model surface, and in very high speed flows. A very small, yet highly strong probe would be required for such measurements. In addition to this, further traverse runs were undesirable, in order to minimise exposure to the oil vapours in the laboratory. The mean density was therefore not obtained directly using the simple equations above.

There are several alternative options available for the determination of the density. There is a certain amount of interferometry data which exists from previous projects conducted on the Coanda model. This data would be ideal since interferometry is a direct measure of density contours. Only limited data is available since interferometry measurements were restricted to only low inlet pressures, i.e. flows with little shock structure due to the problems from vibrations in the rig. Another restriction is the data is only available over the initial part of the Coanda surface, and the hot film measurements were taken further round the flare. A second source of density data is the predicted results obtained using the CFD package PHOENICS. This is not a viable option however, since the experimental data is required in order to validate the CFD predictions, and this method would make the experimental results dependent on the computer predictions. Another alternative option was to make estimates of the pressure distribution, based on a knowledge of the surface pressures from experimental results, and the fact that the pressure at the edge of the outer shear layer is atmospheric. This technique has been adopted, based on equation (4.26)

$$\Delta P = \int_{r_1}^{r_2} \frac{\rho U_1^2}{r} dr \quad (4.26)$$

By working from the outer edge of the jet, the change in pressure could be calculated between each streamline, using the local radius of curvature. The total temperature for the flow was very close to the ambient temperature, and hence the density distribution could be calculated using an iterative technique.

For nearly adiabatic flow, where total temperature gradients and therefore total temperature fluctuations are small, the film only senses the mass flux fluctuations. The six mass flux correlations, $\overline{(\rho u_i)(\rho u_j)}$ were determined using the iterative scheme described above. Once the mean velocity and mean density terms were separated using one of the described techniques, the next problem was to separate the mean squared density fluctuations $\overline{\rho^2}$ and the Reynolds stress components $\overline{u_i u_j}$ from the mass flux correlations. *Perdichizzi et al* (1990) describe a method of doing this which is summarised below. The mass flux correlations were approximated in terms of the mean squared density fluctuation, the fluctuating velocity and the density velocity correlations, as shown in equation (4.27).

$$\overline{(\rho u_i)(\rho u_j)} = \overline{\rho^2} \overline{U_i U_j} + \overline{\rho} \overline{U_i \rho u_j} + \overline{\rho} \overline{U_j \rho u_i} + \overline{\rho^2} \overline{u_i u_j} \quad (4.27)$$

They expressed the density-velocity correlations in terms of the fluctuating velocity correlations by using the following relationship between the instantaneous values of total and static temperature.

$$\overline{T_t} + t_t = \overline{T_s} + t_s + \frac{1}{2C_p} \sum_{i=1}^3 (\overline{U_i^2} + \overline{u_i^2} + 2\overline{U_i u_i}) \quad (4.28)$$

By multiplying this equation by u_j and time averaging the resulting equation, and assuming adiabatic flow, a relationship was obtained between the fluctuating temperature-velocity correlations and the Reynolds stress components, as follows.

$$\overline{t_s u_j} = -\frac{1}{C_p} \sum_{i=1}^3 \overline{U_i u_i u_j} \quad (4.29)$$

The relative pressure fluctuations were considered to be small with respect to the static temperature and density fluctuations, and equation (4.29) was combined with the perfect gas law to finally produce equation (4.30).

$$\overline{\rho u_j} = \frac{\overline{\rho}}{\overline{T} C_p} \sum_{i=1}^3 \overline{U_i u_i u_j} \quad (4.30)$$

Substituting equation (4.30) into equation (4.27) results in six algebraic linear equations with seven unknowns - the six Reynolds stress terms and the mean squared fluctuating density. The resultant equation is given in tensor form in equation (4.31)

$$\overline{(\rho u_i)(\rho u_j)} = \bar{\rho}^2 \bar{U}_i \bar{U}_j + \bar{\rho}^2 \overline{u_i u_j} + \frac{\bar{\rho}^2}{\bar{T} C_p} \left[\bar{U}_i \sum_{k=1}^3 \bar{U}_k \overline{u_k u_j} + \bar{U}_j \sum_{k=1}^3 \bar{U}_k \overline{u_i u_k} \right] \quad (4.31)$$

A seventh equation is required for $\bar{\rho}^2$ in terms of $\overline{u_i u_j}$ in order that (4.31) be solved for the Reynolds stress components. Perdichizzi *et al* derives the equation which is given below.

$$\bar{\rho}^2 = \frac{\bar{\rho}^2}{C_p^2 \bar{T}^2} \sum_{i=1}^3 \sum_{j=1}^3 \bar{U}_i \bar{U}_j \overline{u_i u_j} \quad (4.32)$$

4.2 Calibration plots

The raw data from a calibration run consists of an effective mass flux for each of the sensor angles and mass fluxes measured during the calibration. The first use of this calibration data was to establish the relationship between the sensor voltage and the effective mass flux. A typical plot showing this relationship for the slanted sensor is given in figure 4.4. A third order polynomial has been fitted through this data. Two points of note on this graph are the lack of data in the low speed range, and the fact that the maximum mass flux was limited to approximately 200 kg/m²s. An explanation for the latter is two fold, and is discussed in detail in section 4.3. The lack of low speed data is explained below.

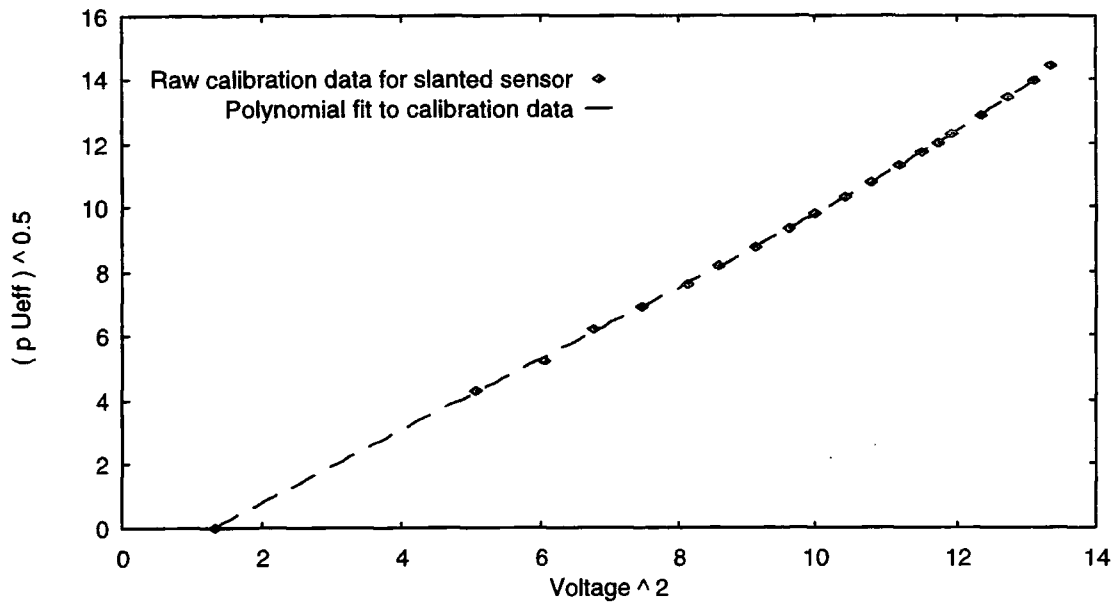


Figure 4.4 : Typical effective mass flux against film voltage plot for a slanted hot film

The yaw coefficient, k^2 , is calculated as a function of mass flux and yaw angle only. The pitch coefficient however is calculated as a function of three variables, $\rho U, \theta$ and ϕ , and then split according to mass flux. To enable this coefficient to be displayed in terms of a three dimensional contour map it has been averaged over mass flux, so that h^2 may be plotted as a function of just (θ, ϕ) .

Typical contour plots for the yaw and pitch coefficients of the straight and slanted sensors are shown in figures 4.5 and 4.6 respectively. The values of the yaw coefficient when the mass flux is zero have been set equal to those at the lowest non-zero mass flux since the coefficient cannot be calculated under zero flow conditions. These plots show the raw coefficient data, and as such, some discrepancies can be seen in this data. Firstly, in the case of the slanted sensor, there are large fluctuations in the value of k^2 as the yaw angle approaches the maximum value of 37.5° . The reason for this lies in the method of calculating the coefficient, as illustrated by equation (4.32) below.

$$k^2 = \frac{U_{eff} - U_n}{U_t} \quad \text{As } \phi \rightarrow 45^\circ, U_n \rightarrow U_{eff}, \text{ and } U_t \rightarrow 0 \quad (4.32)$$

As the yaw angle approaches 45° , k^2 becomes a ratio of two small numbers which is very susceptible to error.

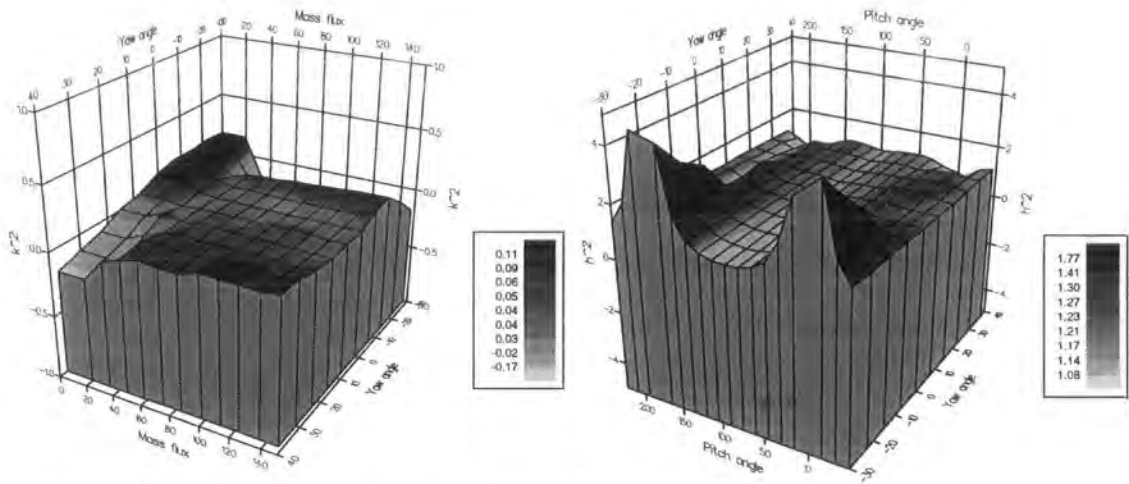


Figure 4.5 : Raw k^2 and h^2 data for the straight sensor

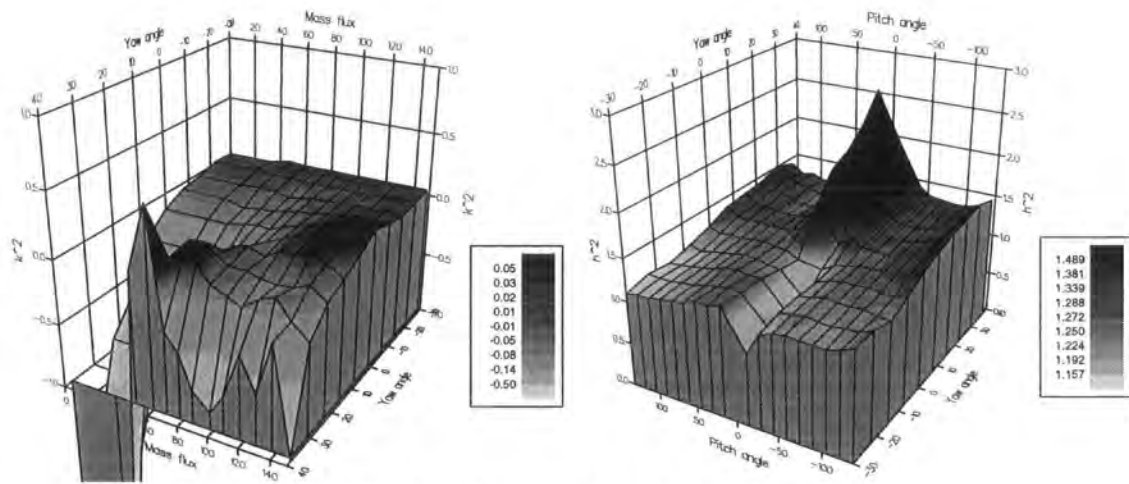


Figure 4.6 : Raw k^2 and h^2 data for the slanted sensor

Secondly, when the mass flux is less than approximately $50 \text{ kg/m}^2\text{s}$, the calculations for k^2 differ considerably from those at higher speed. The reason for this was found to lie with the second regulator in the air supply pipeline which is responsible for dropping the pressure from 8 bar down to below 5 bar. The regulator was sized to cope with the high flow rates necessary for the experimental work, however, at the lower speeds the regulator performance deteriorates and the calibration jet velocity varies considerably

with time. The sensor voltage was corrected to a reference velocity in all cases, but when the mass flux was low, the errors were so great that k^2 could not be calculated with any reasonable accuracy. This lack of accuracy in the low speed range is the reason for the lack of data points at low speeds on the calibration plot given in figure 4.4.

To overcome this problem, the yaw and pitch coefficients were both averaged over all mass fluxes greater than $50 \text{ kg/m}^2\text{s}$ at each angle of ϕ . For mass fluxes less than this, k^2 was then set to its average value for every angle of ϕ . In addition to this, any values of yaw coefficient which lay outside the limit of ± 0.2 were set to the mean value of k^2 for that specific yaw angle. The modified data sets are shown in figures 4.6 and 4.7 for the straight and slanted sensors respectively.

The peak in the h^2 data for the slanted sensor which appears at positive angles of yaw, close to zero pitch angle, seems strange. The h^2 data plots have been averaged over mass flux, and in fact, the height of this 'peak' varies with jet speed. At positive angles of yaw, the k^2 values were quite prone to error. Replacing spurious k^2 values with an averaged value may be an over simplification, and the use of these values in the calculation of h^2 may result in some error, and account for this rise in the h^2 coefficient.

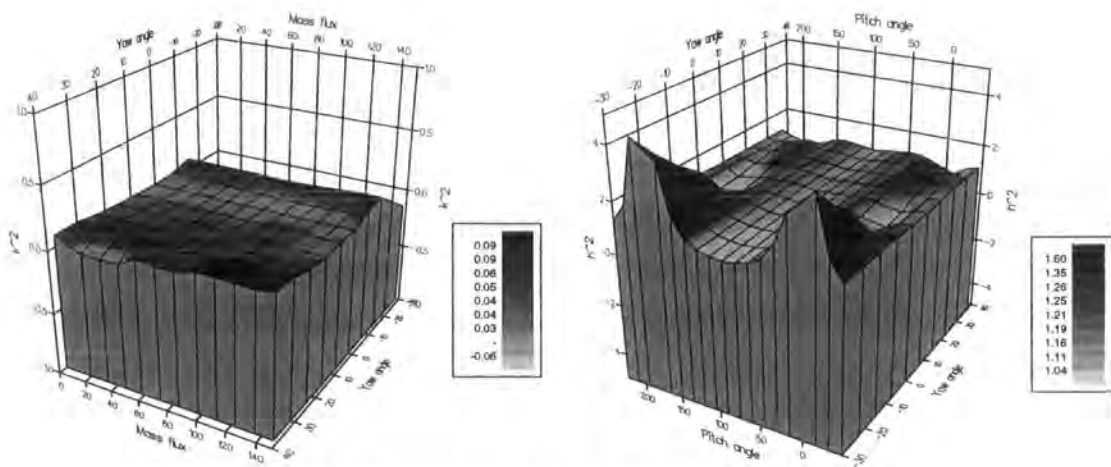


Figure 4.7 : Modified k^2 and h^2 data for the straight sensor

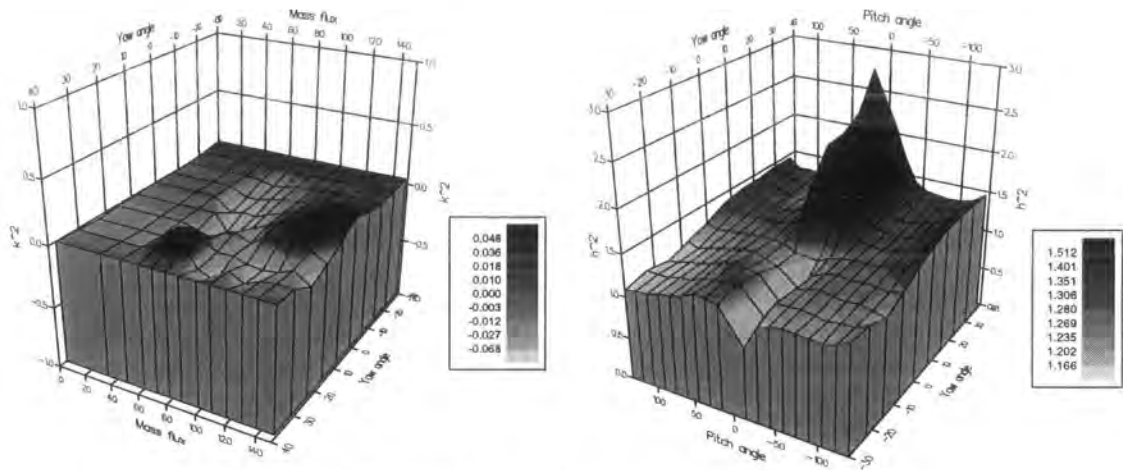


Figure 4.8 : Modified k^2 and h^2 data for the slanted sensor

Surfaces were then fitted to these modified datasets, and points are then interpolated on the fitted surfaces at values that lie between the original data points. The interpolated surfaces, shown in figures 4.9 and 4.10, smooth out some of the discontinuities due to errors in the raw data, and provide quite a reasonable fit.

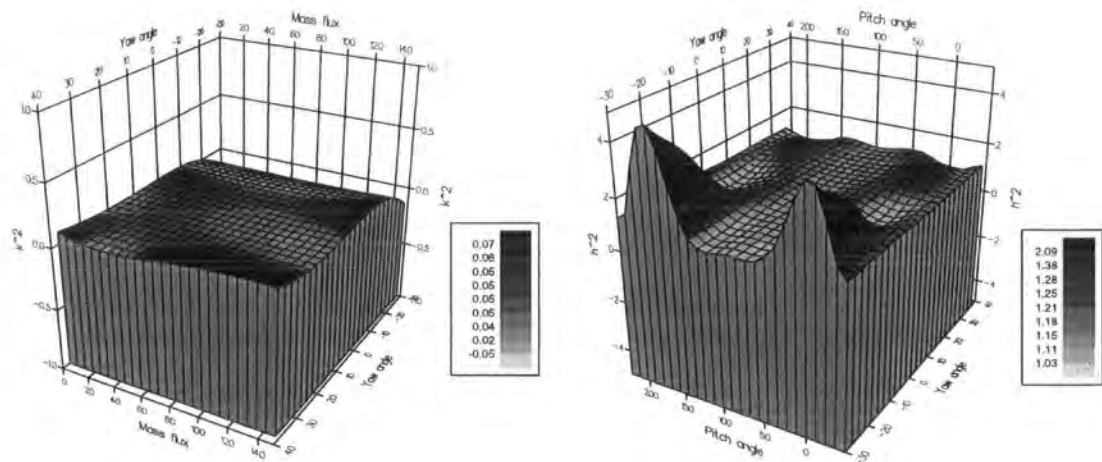


Figure 4.9 : Interpolated k^2 and h^2 data for the straight sensor

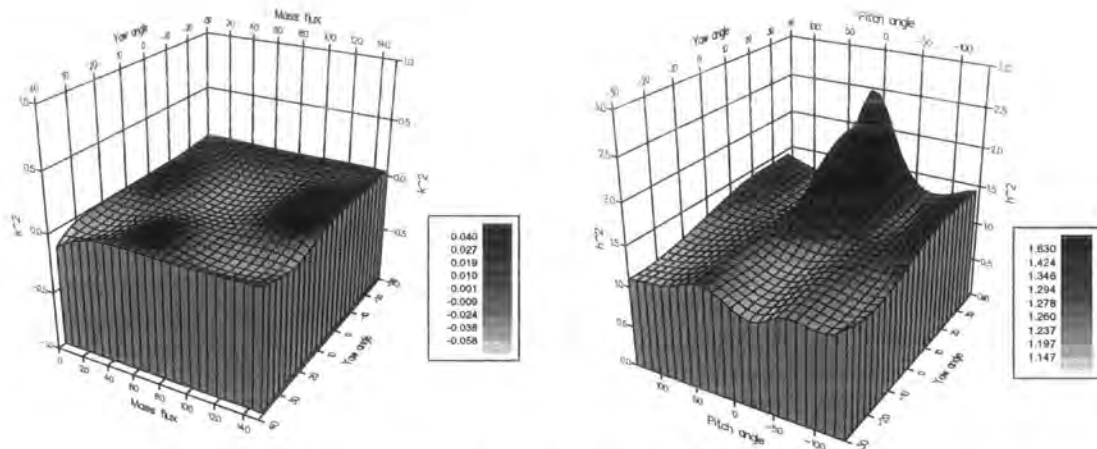


Figure 4.10 : Interpolated k^2 and h^2 data for the slanted sensor

For the purposes of display, the values of h^2 have been averaged over mass flux (the least dependent parameter), hence reducing the data to 3 dimensions. In the experimental analysis, the value h^2 is determined using all three dependent parameters. The root mean square variation of h^2 with mass flux, expressed as a fraction of the mean, is illustrated in figure 4.11 for the normal and slanted sensors. The variation is generally of the order of 3% for the normal sensor, and marginally higher for the slanted sensor. The peaks which occur on the two graphs correspond to when the sensor lies in the plane of the flow, and vortex shedding from the prongs may be occurring.

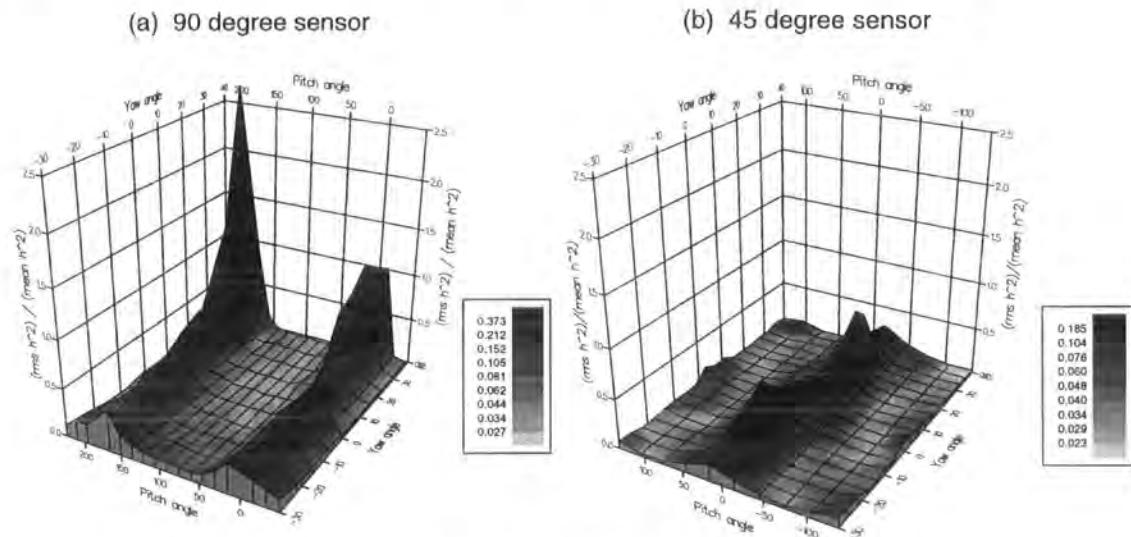


Figure 4.11 : RMS variation of h^2 with ρU

4.2.1 Calibration test results

The calibration data displayed in the previous section was tested by taking a series of 13 readings under known flow conditions at the calibration nozzle, to establish the consistency and accuracy of the proposed hot film technique. The results of the mean flow calculations from the test are summarised in Table 4.1.

Case No.	Actual Flow			Calculated Flow			% error
	ρU	ϕ	θ	ρU	ϕ	θ	
1	76.32	0.0	0.0	73.55	-0.4	-0.8	1.15
2	76.32	0.0	0.0	73.64	0.1	0.8	0.97
3	76.32	0.0	0.0	73.55	0.1	-0.5	1.23
4	76.32	0.0	0.0	74.01	-0.5	-0.1	0.86
5	76.32	0.0	0.0	73.66	0.1	-0.6	1.01
6	76.32	5.0	0.0	74.60	4.5	0.4	1.00
7	76.32	10.0	0.0	74.89	8.6	-0.7	1.97
8	76.32	15.0	0.0	74.57	13.7	0.2	1.47
9	76.32	25.0	0.0	74.21	23.5	-1.0	2.32
10	76.32	35.0	0.0	74.61	33.9	-0.1	1.90
11	76.32	20.0	20.0	74.17	18.6	19.5	1.84
12	76.32	0.0	20.0	73.66	-0.1	20.4	0.67
13	76.32	-20.0	20.0	72.96	-21.2	19.9	1.24

Table 4.1 : Mean flow test results

The first five readings were all taken at the same flow angle to test the repeatability of the results. The last column in the table gives an indication of the error in the result, as calculated using equation (4.23). The errors in the first five readings were all less than 1.25%, and the calculated mass fluxes varied by less than $0.5 \text{ kg/m}^2\text{s}$. However, all the mass fluxes were typically $2\text{-}3 \text{ kg/m}^2\text{s}$ less than that measured using the pitot tube. The angles ϕ and θ were all measured fairly consistently in the first five readings, with typical accuracy of $\pm 0.5^\circ$. The accuracy in the pitch angle remained fairly consistent for all the angular settings tested, however the accuracy of the yaw angle did decrease as the yaw angle shifted away from the zero degrees position.

The results of the fluctuating component calculations from this test are summarised in Table 4.2. The suffixes 1, 2 and 3 correspond to the streamwise, normal and transverse directions respectively.

Case No.	Normal stresses			Shear stresses		
	$\overline{(\rho u_1)^2}$	$\overline{(\rho u_2)^2}$	$\overline{(\rho u_3)^2}$	$\overline{\rho u_1 \rho u_2}$	$\overline{\rho u_1 \rho u_3}$	$\overline{\rho u_2 \rho u_3}$
1	2.712	1.833	2.567	0.507	0.024	-1.418
2	2.678	3.157	3.955	-0.450	-0.549	0.974
3	2.494	1.673	1.724	1.008	-0.262	0.818
4	3.003	7.560	2.977	-2.897	-0.497	0.727
5	2.739	5.231	4.063	-1.102	0.422	-2.118
6	2.438	2.429	3.210	0.329	-0.619	1.103
7	2.359	1.836	2.370	0.810	-0.349	1.660
8	2.757	4.532	2.633	-0.955	-0.495	1.310
9	2.697	3.492	4.988	-0.633	-0.063	-0.520
10	3.103	1.923	4.609	-0.239	-0.789	1.204
11	2.407	2.552	4.079	0.120	0.329	-1.764
12	2.382	3.718	3.349	1.391	0.380	-3.458
13	3.507	1.769	5.081	-0.734	-1.617	1.554

Table 4.2 : Fluctuating component test results

In general, the results show that the normal stresses are small, corresponding to approximately 2% turbulence levels in the calibration jet. In the first five readings, the values for the streamwise normal stress component are consistent. When the yaw and pitch angles are zero, by symmetry, the perpendicular and transverse fluctuating normal components would be expected to be of similar magnitude, and in four out of the five cases, this is true. However, there appears to be a discrepancy in the fourth set of data.

The shear stresses are all calculated to be smaller than the normal stresses, as expected, however there is some variation in the values. Once again, the biggest discrepancy occurs in the fourth set of data which could suggest an error in the fluctuating voltages measured, since there is no corresponding error in the mean flow calculation.

Perdichizzi *et al* (1990) quote acceptable levels of accuracy as $\pm 3\%$ for the velocity (± 2.3 m/s at 76 m/s) and ± 2 degrees in the yaw and pitch angles. The mean flow conditions in these test cases were likely to be as severe as those expected under experimental conditions, hence error levels of no more than these seem quite attainable. However, the turbulence levels are far lower than those likely to occur in the Coanda flow field, so it is harder to estimate the accuracy of the Reynolds stress measurements from these tests. An indication may be obtained by calculating the variations in the normal stresses (excluding the fourth result) which gives values of 3% for $\overline{(\rho u_1)^2}$, 40% for $\overline{(\rho u_2)^2}$, and 30% for $\overline{(\rho u_3)^2}$. The values for the shear stresses are too small for error estimates to be made, and the low turbulence levels mean the error estimates for the normal stresses are likely to be highly inaccurate.

Perdichizzi *et al* perform a sensitivity analysis on the effect of errors in the reading of the hot film fluctuating output on each Reynolds stress component. They illustrate through this analysis that the errors in the transverse normal component, $\overline{(\rho u_3)^2}$, the perpendicular normal component, $\overline{(\rho u_2)^2}$, and the shear stress $\overline{\rho u_1 \rho u_2}$, are all greatly reduced through the use of the straight probe in addition to the slanted sensor, and by using a total of 14 angular positions, they estimate the errors in all components to be less than 10%.

4.3 Problems arising from the calibration tests

Various problems associated with the rig were highlighted by initial calibration tests. Further problems also became apparent once preliminary experimental runs were performed. The majority of these problems originated from the air supply, however vibration problems as a result of high speed flow also had to be addressed. Each of these factors is dealt with in turn under various sub-headings.

4.3.1 Torsional twisting of the hot film sensor

A diagram of the hot film sensor is given in figure 4.12. This shows the locating prongs at the end of the hot film probe which slot into the probe support provided by TSI. These prongs are quite long but not very rigid and allow the probe to twist whilst in the

probe holder. During the course of a calibration, when the probe is exposed to strong velocities perpendicular to its length, the sensor was found to twist. Hence, the zero pitch angle varied throughout the calibration. To overcome this problem, a collar was designed to fit over the end of the probe, and the probe support, and two small screws held the collar and probe assembly rigidly in place. This was illustrated in figure 3.6, and may be seen in the photograph in figure 4.24.

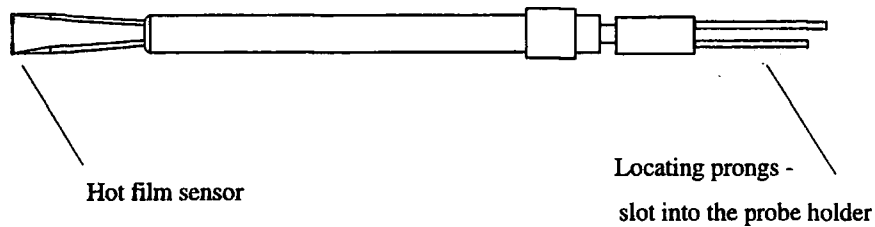


Figure 4.12 : Hot film sensor

4.3.2 Noise levels

The electrical output signal of a thermal anemometer not only indicates the velocity around the sensor, but it also indicates the voltage fluctuations caused by electronic noise from the various electrical components in the anemometer. This electronic noise occurs across the whole frequency spectrum and can affect velocity measurements. The three electronic circuits which contribute to this noise are the hot film itself, the bridge and the amplifier. Two tests were performed in order to obtain a qualitative idea of how large this background noise was.

The signal conditioner, built into the IFA module, allows an offset and gain to be applied to the transducer signal, before it is transmitted to an external device for processing. The signal conditioner can also filter the transducer signal. The two tests described here involved replacing the transducer input to the signal conditioner with a sinusoidal input of 10 kHz, supplied by an external signal generator. The hot film sensor remained connected, but no voltage from this was sent to the conditioner, and there was no flow over the sensor.

In the first test, the IFA was left in STANDBY mode, and in the second test the IFA was in RUN mode. The output from the IFA signal conditioner was analysed from the two tests using Fourier analysis, performed using the MATLAB software, which provided a power spectrum plot of the output voltage. The results from these two tests are shown in figures 4.13 and 4.14. The data logging was performed at a frequency of 200 kHz.

In the first of these graphs, the sinusoidal input is strongly defined by an 18 dB peak, and noise levels lie around -65 dB, with some high frequency peaks extending as high as -40 dB. The IFA unit was in STANDBY mode for this test, and as such all electrical circuitry associated with the bridge and amplifier were switched off. The second graph was obtained with the IFA in RUN mode, and the noise levels with the electronic circuits switched on are significantly higher, particularly in the lower frequency range. At the lowest frequencies, the noise levels are increased to -35 dB, and this gradually drops off to -60 dB at a frequency of 50 kHz.

All thermal anemometers have an upper limit to their frequency response, and a low pass filter is required to cut out any noise above this limit. However, in the above tests no filtering was used, so the full effects of the noise could be observed. Freymuth (1968) analysed the various sources of noise in hot wire anemometers, and predicted signal-to-noise ratios for constant temperature and constant current anemometers, concluding that both may be described by the same equations. Calculating the total output noise involves integration of the equation proposed by Freymuth over the entire frequency range. Only a qualitative analysis of his study is given here. He showed that the signal to noise ratio increases steadily with wire temperature, and so the hot wire should, in theory, be heated to the maximum permissible temperature. The theoretical analysis also showed that in order to maximise the signal to noise ratio, the wire should be made of a material with a high temperature coefficient of resistance, and be as thin as possible to minimise thermal capacity. A review on thermal anemometers is given by Fingerson *et al* (1979) and in this, noise levels with hot film sensors are considered. The larger diameter of the hot film sensors is shown to increase significantly the noise levels between 10 and 1000 Hz, however, beyond this the noise levels approach those of a hot wire.

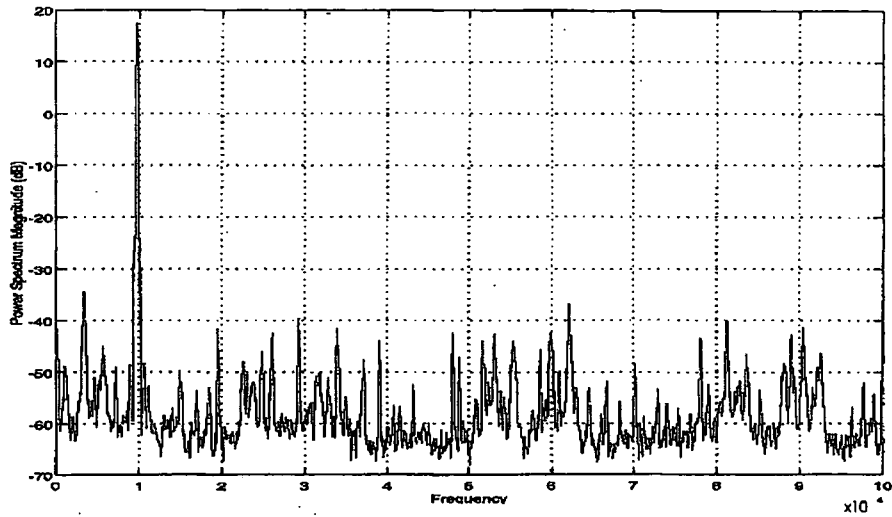


Figure 4.13 : Sinusoidal input of 10 kHz, with the IFA on standby

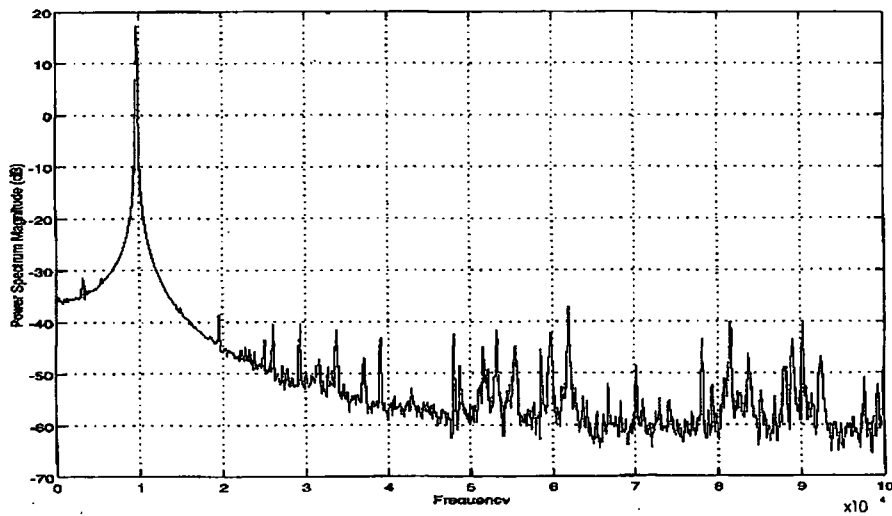


Figure 4.14 : Sinusoidal input of 10 kHz, with the IFA in RUN mode

4.3.3 Aliasing

As previously mentioned, a filtering circuit is built into the signal conditioner of the IFA module. It is a low-pass, third order Sallen-Key type filter (-18dB/octave roll off) with selectable cut-off frequencies. The speed at which the hot film voltage is logged at must be greater than the cut-off frequency when analysing the frequency spectrum, due to a phenomenon called aliasing. The effects of aliasing are demonstrated in figures 4.15 and 4.16. Figure 4.15 shows the frequency spectrum from the straight sensor, held

perpendicular to a flow of 200 m/s, logged at a frequency of 40kHz. No filter was used in this case, and frequency peaks occur at approximately 6kHz, 8kHz, 11kHz and 14kHz. Figure 4.16 shows the results from an identical test, but with the filter set at 20kHz. In this plot, all the peaks except for that occurring at 14kHz have disappeared, despite the fact that they were all apparently occurring at frequencies below the cut-off frequency. The additional peaks which occur in the first plot are in fact due to very high frequencies. These frequencies are higher than the sampling frequency, and are picked up as apparent low frequency signals. This is known as aliasing, and filtering at half the sampling frequency eliminates this phenomenon.

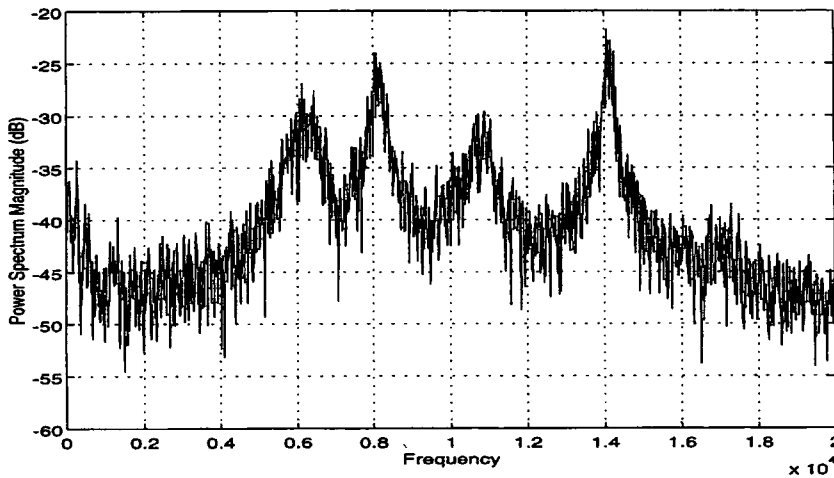


Figure 4.15 : Straight sensor, held normal to 200 m/s flow, with no filter

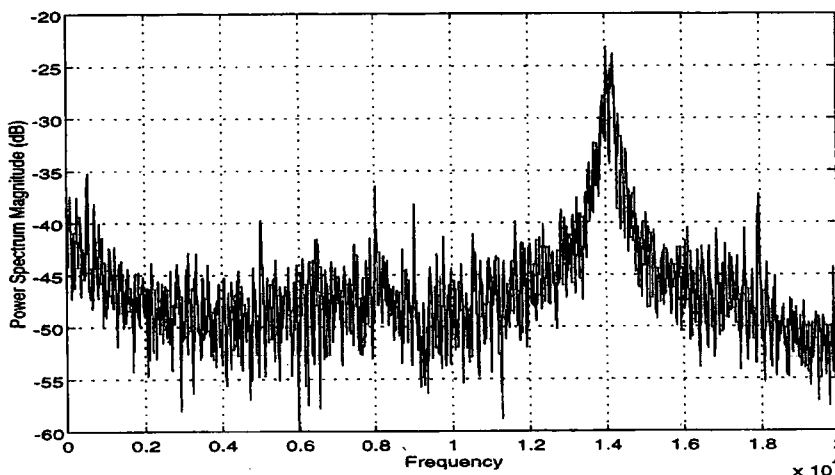


Figure 4.16 : Straight sensor, held normal to 200 m/s flow, with filtering at 20 kHz

4.3.4 Strain gauging effects

It was mentioned in chapter 2 that probes are particularly susceptible to strain gauging or vortex shedding when the probe is introduced normal to the flow. Both sensors were used in this configuration, so it was necessary to establish whether these phenomena were likely to occur. The output voltage from the hot film was once again analysed using Fourier analysis to identify any sharp energy peaks.

The tests were performed at the calibration nozzle, at a moderate speed of 150m/s. A normal sensor was placed perpendicular to the flow ($\phi = 0^\circ, \theta = 90^\circ$), and then end on into the flow ($\phi = 90^\circ, \theta = 90^\circ$). A faster logging rate of 200kHz was used, and the signal was filtered at 100 kHz to avoid aliasing. The results presented in figure 4.17 and 4.18 were obtained using a different sensor from that used in the aliasing tests in section 4.3.3. Results from this original sensor were obtained in just the perpendicular position, since the sensor broke before the second configuration could be tested. The results from this single test are presented in figure 4.19 for comparison.

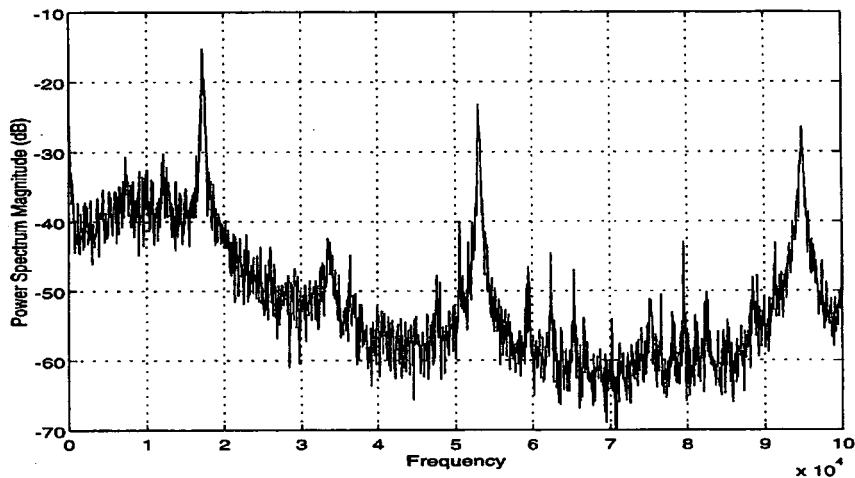


Figure 4.17 : Spectrum of normal sensor output held perpendicular to the flow

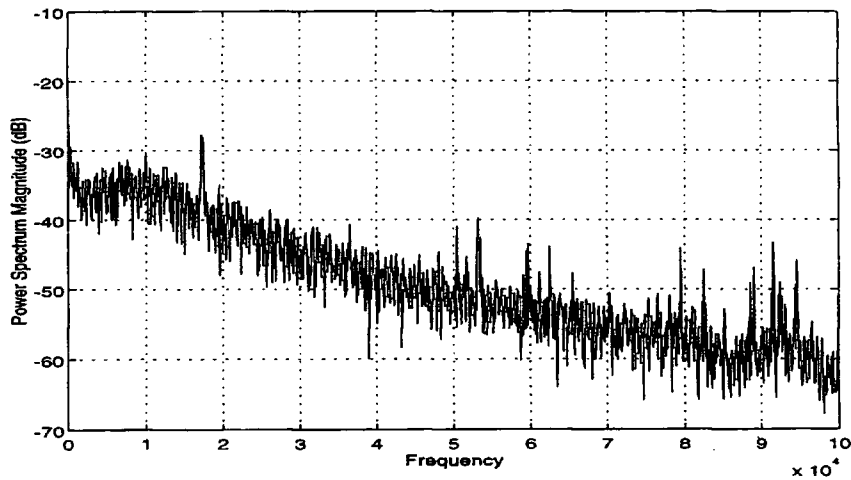


Figure 4.18 : Spectrum of normal sensor output held end on into the flow

In figure 4.17, the probe was held perpendicular to the flow, and sharp peaks of energy can be seen at frequencies of 17.5kHz, 53kHz and 95 kHz. Figure 4.18 shows the power spectrum when the probe was held end on into the flow. These frequency peaks are all greatly reduced in magnitude. The power spectrum obtained using the original normal sensor (in the perpendicular position) is given in figure 4.19. Three distinct peaks in frequency may be seen, at 14kHz, 48kHz and 91kHz, which differ from those in figure 4.17, suggesting the frequency spikes are dependent on the individual sensor geometries, and not caused by the flow, the calibration rig or the probe support.

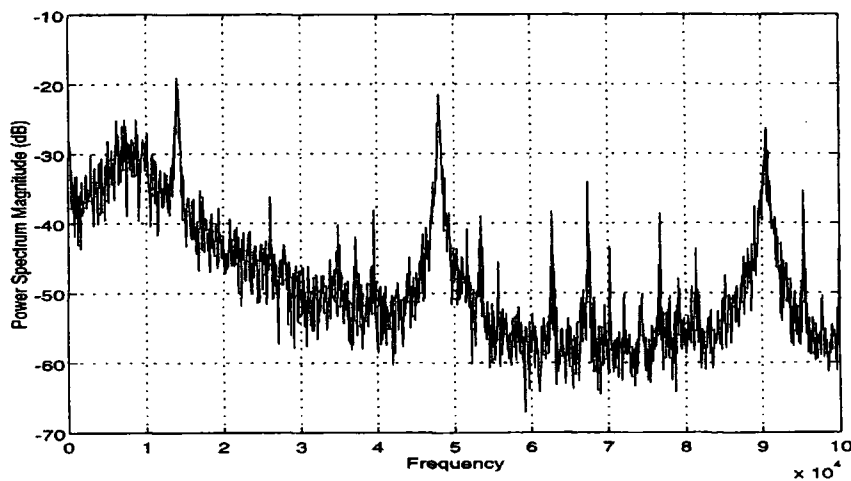


Figure 4.19 : Spectrum of original normal sensor output held perpendicular to the flow

For an infinitely long cylinder, the frequency, f , at which vortices are shed is given by the empirical formula given in equation (4.33) (Massey, (1989))

$$\frac{fd}{u_{\infty}} = 0.198 \left(1 - \frac{19.7}{\text{Re}} \right) \quad (4.33)$$

where fd/u_{∞} is known as the Strouhal number. If the frequency peaks are due to vortex shedding, they would be expected to shift to the right with an increase in velocity. If the mechanical phenomenon of strain gauging is responsible, the resonant frequencies should be independent of flow velocity.

A series of tests were therefore performed using the slanted and normal sensors placed perpendicular to the flow. The velocity was incrementally increased from 40m/s up to 150m/s, the voltage logged at 200kHz, and the signal filtered at 100kHz. The resulting frequency spectra plots for the slanted sensor are given in figures 4.20 (a)-(f), and those for the normal sensor are given in figures 4.21 (a)-(f).

The slanted sensor shows a frequency peak appearing at about 22kHz at a velocity as low as 80m/s. This peak, along with another at 57kHz, becomes far more prominent by 150m/s. The straight sensor also shows peaks starting to appear at speeds as low as 100m/s, at frequencies of 17.5kHz and 53kHz. The peak at 95kHz becomes evident at velocities greater than 100m/s.

These tests confirm that the frequency peaks must be caused by the mechanical vibration of the prongs and the film, rather than due to any vortex shedding effects. A rough approximation for the natural frequency of the hot film may be made by estimating the Young's modulus and density of the sensor to be that of Quartz. The length and diameter are known precisely, and the estimated frequency was calculated to be 97kHz. This is the correct order of magnitude for the resonant frequencies measured. The remaining peaks in frequency may be attributed to the prongs, which are also likely to resonate at high frequencies, due to their conical shape (which provides great stiffness).

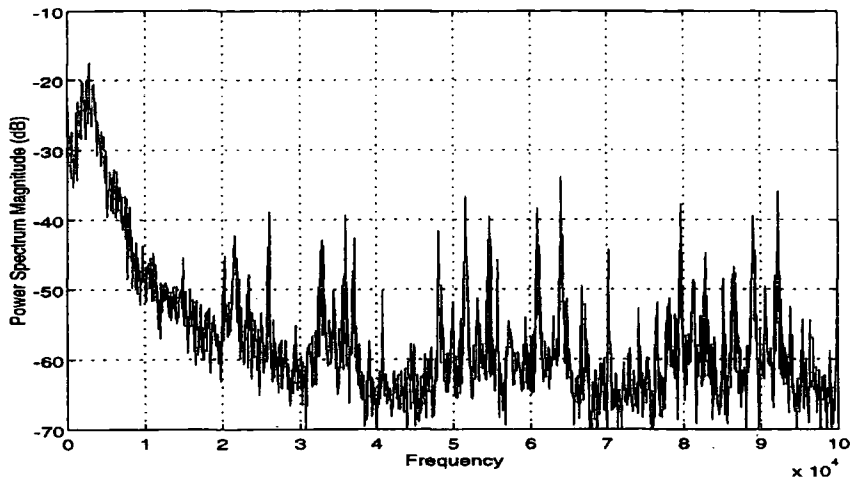


Figure 4.20 (a) : Slanted sensor @ 40 m/s

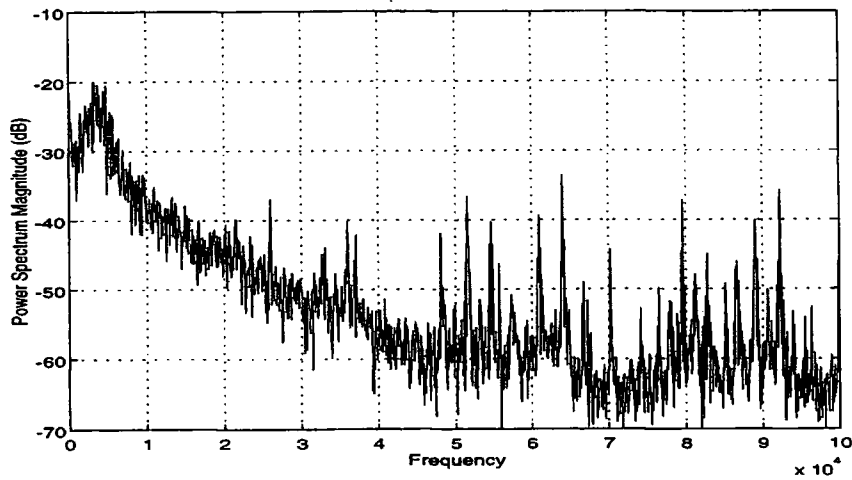


Figure 4.20 (b) : Slanted sensor @ 60 m/s

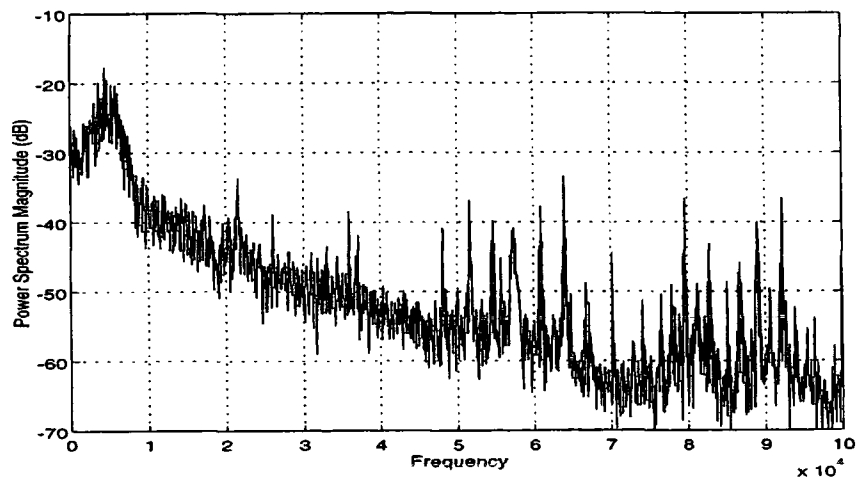


Figure 4.20 (c) : Slanted sensor @ 80 m/s

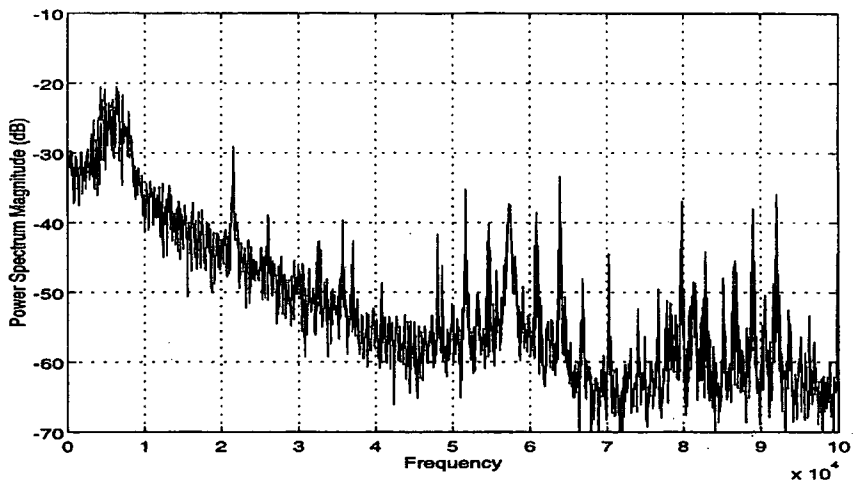


Figure 4.20 (d) : Slanted sensor @ 100 m/s

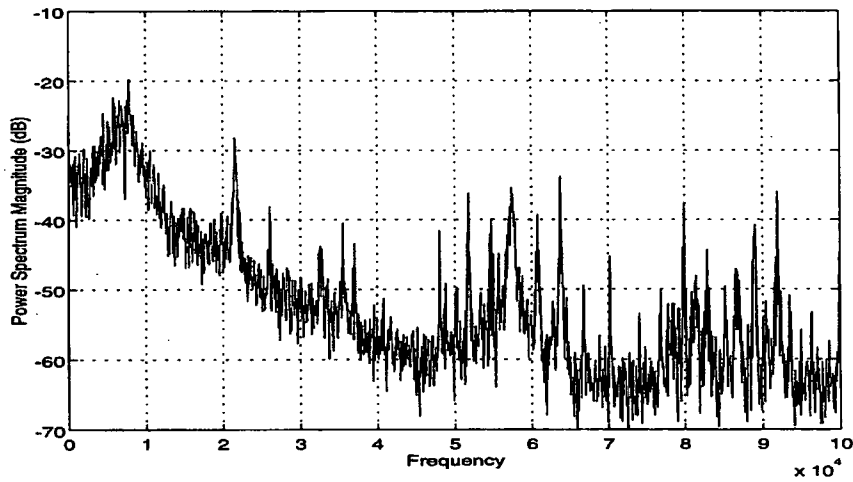


Figure 4.20 (e) : Slanted sensor @ 120 m/s

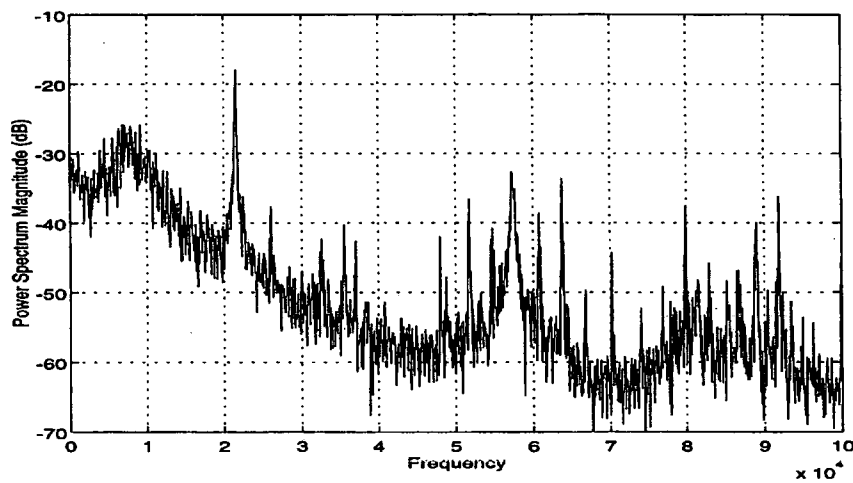


Figure 4.20 (f) : Slanted sensor @ 150 m/s

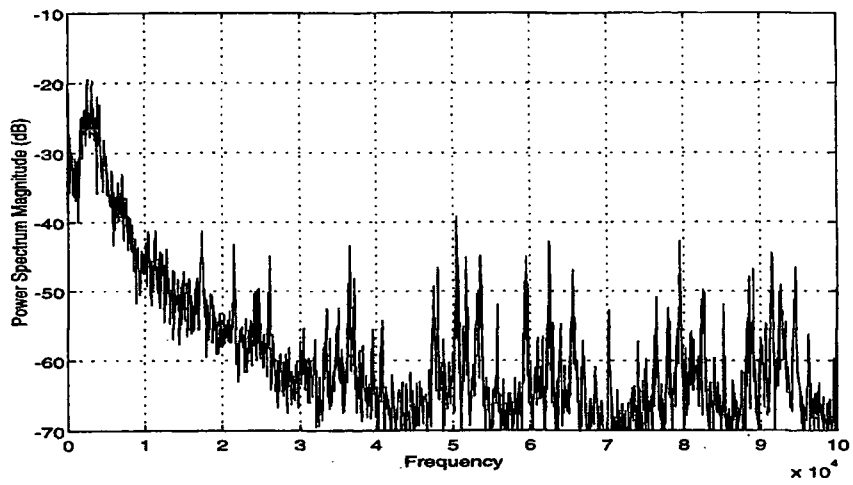


Figure 4.21 (a) : Straight sensor @ 40 m/s

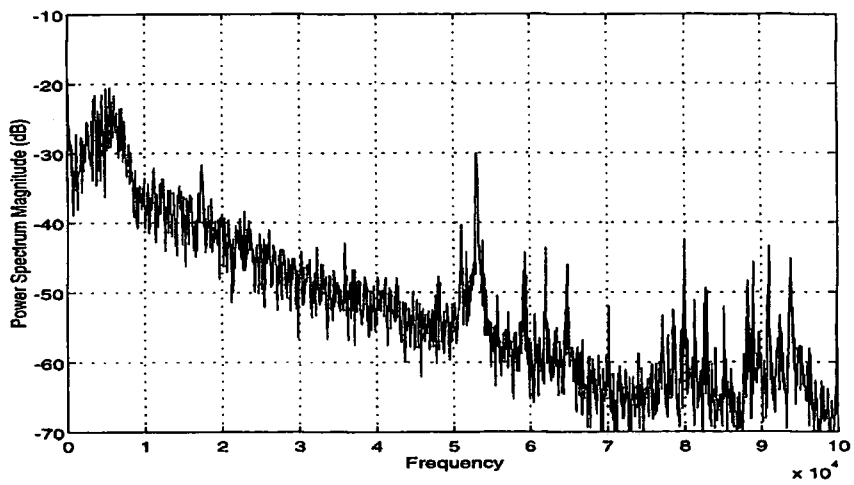


Figure 4.21 (b) : Straight sensor @ 60 m/s

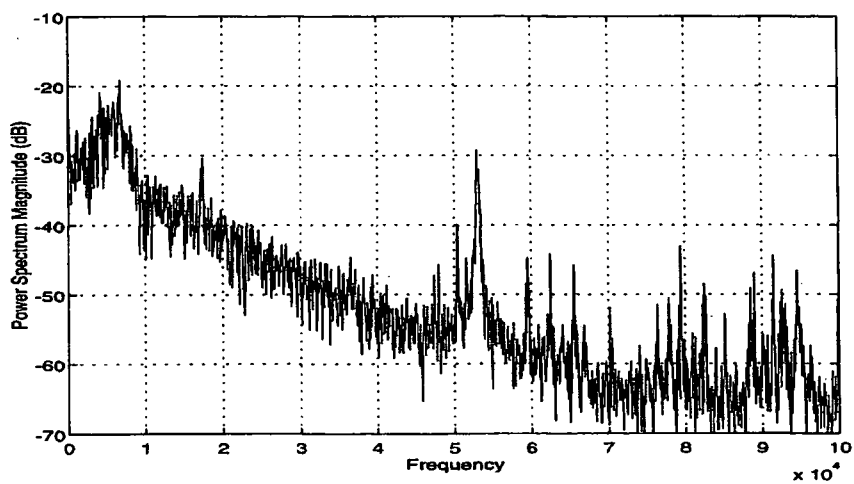


Figure 4.21 (c) : Straight sensor @ 80 m/s

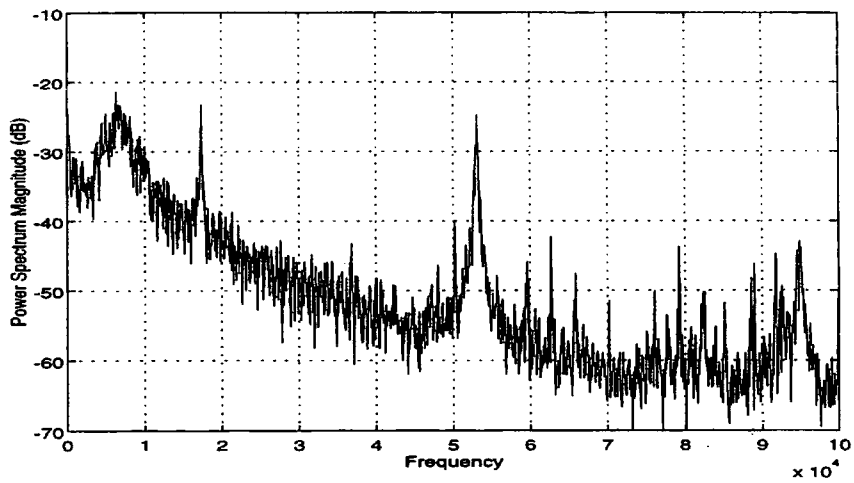


Figure 4.21 (d) : Straight sensor @ 100 m/s

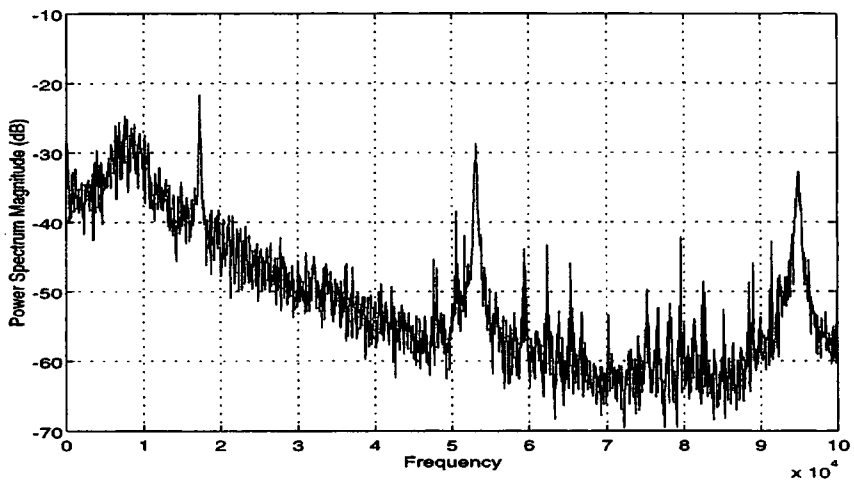


Figure 4.21 (e) : Straight sensor @ 120 m/s

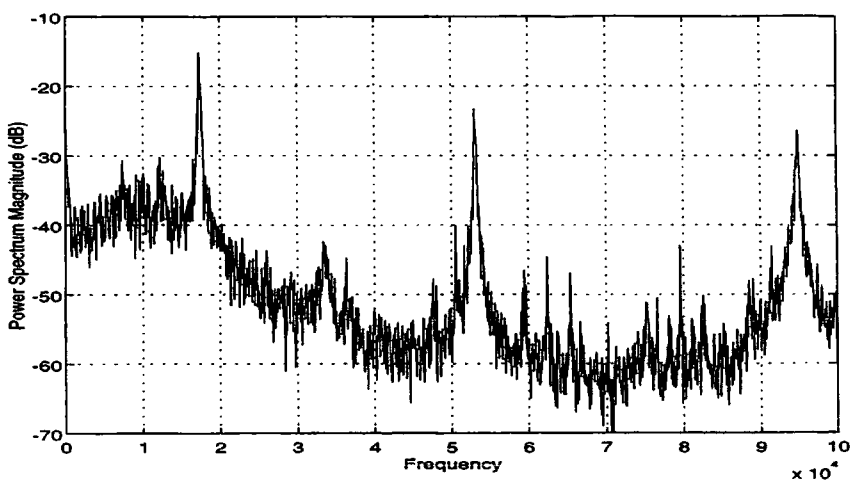


Figure 4.21 (f) : Straight sensor @ 150 m/s

The final spectral plot, shown in figure 4.22, was obtained from the experimental rig rather than the calibration nozzle (where turbulence levels are low). The normal sensor was held (as for an experimental run) with the stem perpendicular to the flow, at 90° round the Coanda surface. The effective velocity over the sensor was 110m/s, and the turbulence level was 15%. The three distinctive frequency spikes are still visible, but the magnitude of these spikes relative to the flow turbulence are quite small. This would suggest that the error, caused by these peaks, in the experimental r.m.s values are likely to be low, particularly since the majority of the Coanda flow is highly turbulent, and the velocities to which the sensor could be exposed to were limited by contamination and sensor breakage problems.

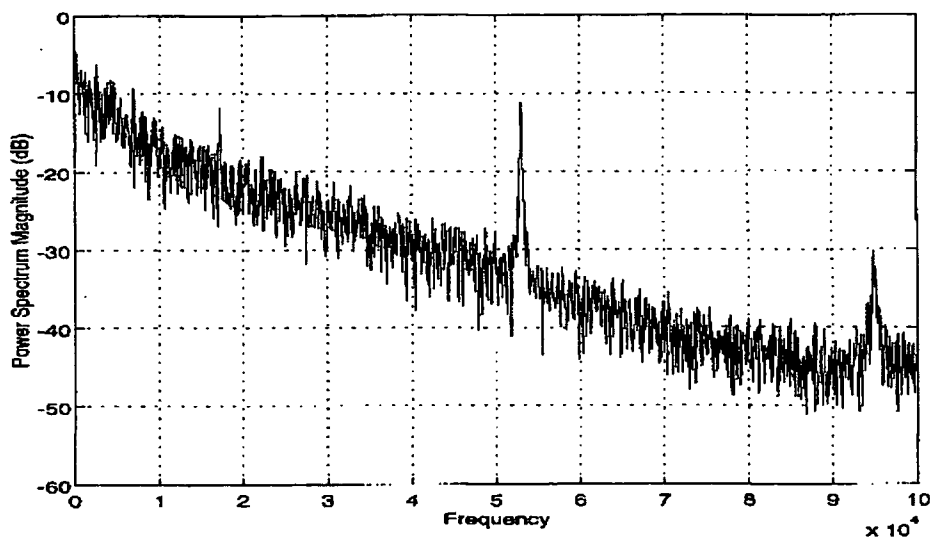


Figure 4.22 : Power spectral plot for the normal sensor at 90° round the Coanda surface, $\bar{U}_{eff} = 110\text{m/s}$, $T_i = 15\%$

4.3.5 Electrical Interference

A minimum distance of 4m was required between the IFA and the computer to avoid electrical interference from the computer affecting the hot film sensor voltage. At distances closer than this, switching the computer on and off resulted in a step changes of up to 0.3 volts in the sensor output voltage.

An additional source of interference was found when certain electrical appliances were in operation in a nearby laboratory. This resulted in the spurious readings taken by the A/D board, as demonstrated in figure 4.23. This graph shows 3000 measurements from the stagnation temperature probe, recorded at a frequency of 1 kHz, and errors of $\pm 5\%$ were recorded. When the source of interference was switched off, the equivalent trace was completely flat, corresponding to the constant temperature. Similar traces were recorded from the hot film anemometer, and the pressure transducers. This problem was overcome by improvements in the electrical earths of the equipment involved.

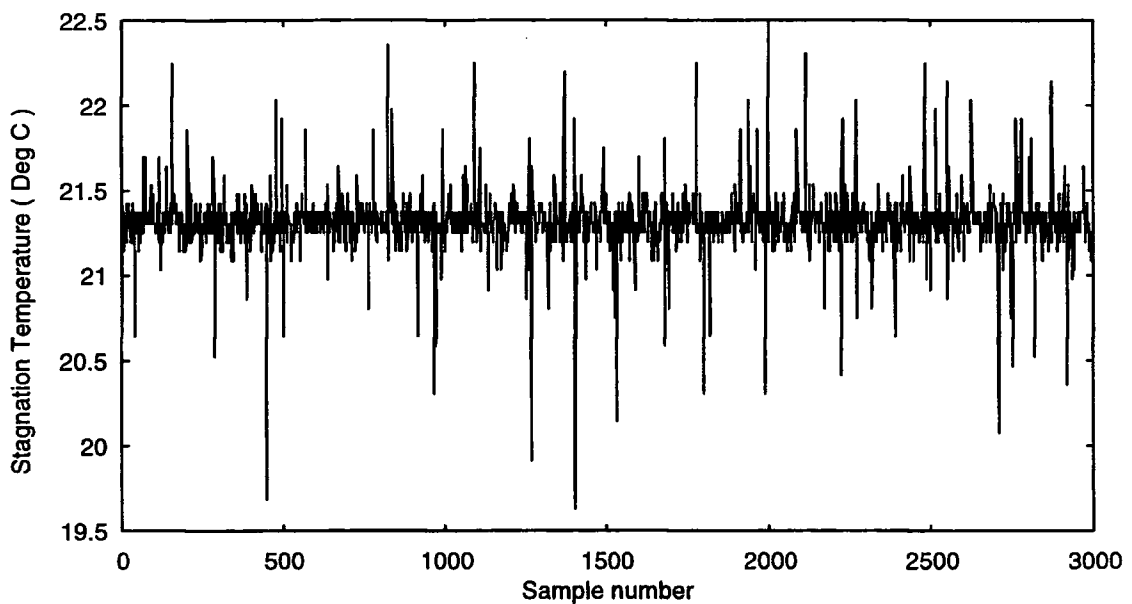


Figure 4.23 : Apparent temperature fluctuations as a result of electrical interference

4.3.6 Setting the frequency response of the hot film sensor

It was necessary to optimise the frequency response of the hot film prior to taking any measurements. This proved to be quite difficult. The aim of optimising the frequency response is to prevent oscillations in the system, to allow fast and small fluctuations to be measured, and to allow the accurate reproduction of small and large fluctuations over a wide range of frequencies.

The optimisation allows an upper limit for the frequency response of that particular sensor, environment, amplifier and bridge to be established, and the system is adjusted so that it gives as flat an amplitude response as possible. An electrical square wave test is used to optimise the system, using a built in square wave generator. Freymuth (1977) describes a detailed theory of sine and square wave testing using a third order linear equation which is consistent with the concept of two adjustable controls for optimising the response of the anemometer.

To obtain as flat an amplitude response as possible, the output from a pulse has to have an undershoot of 13% relative to the maximum, and the cut off frequency for a hot film is given by equation (4.34)

$$f_{\text{cut}} = 1/\tau \quad (4.34)$$

where τ is defined in figure 4.24. Optimisation should in theory be performed at the average velocity expected to occur during measurements, however, where turbulence is likely to be significant it should be performed at the maximum velocity. Incorrect adjustment results in a response curve to velocity which is not flat over the entire frequency range. According to Fingerson *et al* (1979), interpreting the pulse width as defined in figure 4.24 gives a good approximation for the cut-off frequency, however they state that recognising the step response of a film sensor is harder than it is for a hot wire, and this was found to be the case. Turbulence levels, although not particularly high in the calibration jet, tended to completely mask the response to the square wave input, making it hard to determine the degree of overshoot or the frequency response of the system.

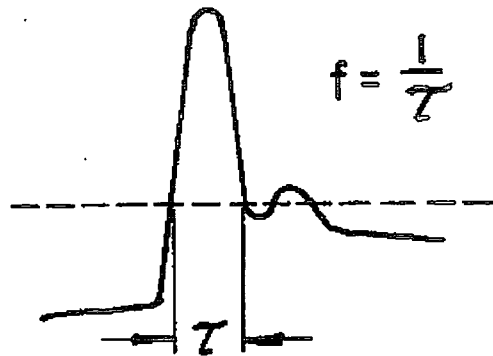


Figure 4.24 : Square wave test frequency response for film sensors

4.3.7 Cleanliness of the air supply

One of the greatest problems faced throughout the experimental work was contaminants in the air supply. Precautions were taken in the form of an extensive filtration process in an effort to eliminate oil and particulates from carrying through into the Coanda and calibration jets. Details of the filtration used are given in chapter 3.

The odours from vaporised oil were a continual problem, despite the presence of an activated carbon filter. Leaks in the rest of the pipework at the numerous junctions led to significant problems in the atmosphere of the experimental laboratory. Frequent filter changes due to oil and water saturation were not the only evidence of the high levels of oil and moisture content in the air. Oil also leaked out of most of the pipework junctions. The pipework was thoroughly dismantled and cleaned prior to starting any experimental work. Despite this, under high speed conditions, particles from inside the pipes were carried through in the air supply, resulting in frequent hot film breakages. The speeds which the sensors were exposed to were limited therefore to approximately 170m/s. The oil contamination was an on-going problem. On several occasions the filters failed, and large quantities of oil carried through the pipework. The operating life of the sensors was considerably shortened by this, since a film of oil rapidly built up on the sensors, dramatically affecting their calibrations.

The presence of the oil in the air can be seen visually on the photograph in figure 4.25. This shows the planar model, with the nearest side wall removed, and the probe

positioned for a traverse run. Part of the rotary traverse gear may be seen in the top right of this picture. The light regions at the top of the side wall and at the bottom of the picture are due to the room lighting. It is difficult to make out the oil film which has been deposited on the side wall, so for clarity the edge has been marked out with a dashed line. The oil film has been wiped off the side wall near the slot, and so the start of the oil 'jet' is sharply defined.



Figure 4.25 : Photograph of the planar model, demonstrating the oil contamination

This oil contamination was yet another limiting factor for the jet speed, and the usable life of the hot films was restricted to only one experimental run, to avoid the sensor performance drifting significantly from the calibration.

4.3.8 Constant air supply

The variation and drift of the calibration jet velocity with time was found to be a problem. This variation is demonstrated in figure 4.26, which illustrates the periodicity of the velocity, and its tendency to drift away from its mean value. This unsteadiness is due to a combination of factors. Firstly the Standfast regulator, despite feedback, is unable to maintain a truly constant mass flow. Secondly, the upstream supply pressure fluctuates since the compressor does not run continuously. The compressor cuts in and out as the pressure in the air receiver varies between pre-set limits. This effect was less evident at very high jet speeds, when the compressor must run almost continuously. The percentage error in the velocity was found to decrease at higher speeds, but even at the relatively high velocity of 145 m/s, shown in figure 4.25, the error is $\pm 3.5\%$ from the initial speed setting.

These readings were taken over an hour. A typical calibration run took approximately 25 minutes at each velocity setting. Thus considerable velocity variation occurred in this time. Before any analysis was performed on the calibration data, the film voltages were corrected to the average mass flux for each calibration setting. However, the errors at low mass fluxes were as high as $\pm 10\%$, and the simple method of correcting the voltages for small deviations in velocity was no longer valid, and was likely to introduce significant errors into the data. As a result, no calibration data was taken below $50 \text{ kg/m}^2\text{s}$.

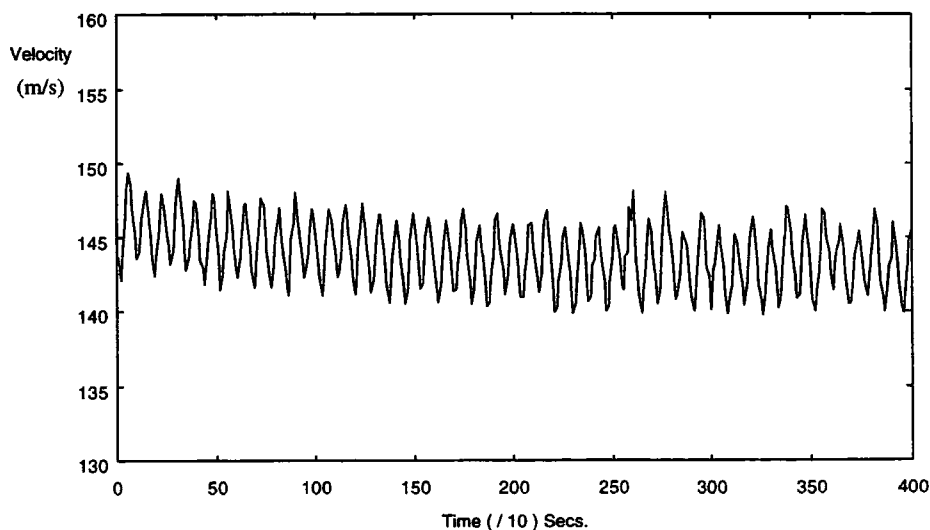


Figure 4.26 : Velocity variation with time at the calibration nozzle, at 145 m/s

Chapter 5

Experimental Results

5.1 Introduction

The experimental tests performed on the Coanda flare may be divided into two sections. The first involved a constant slot width of 4mm, and the pressure ratio was varied. This investigation, referred to throughout this chapter as case (I), was limited to pressure ratios of 0.7 and above. The hot film sensor consistently broke at pressure ratios below this. Time was also a limiting factor, so traverses were only performed at pressure ratios of 0.7, 0.75, 0.8 and 0.85. These correspond to slot Reynolds numbers, Re_p , of 11.5×10^4 , 10.5×10^4 , 9.4×10^4 and 8.2×10^4 respectively. The second set of tests involved maintaining a constant pressure ratio and varying the slot width. This set of tests is referred to as case (II). Measurements were taken at the constant pressure ratio of 0.85, at slot widths of 2mm and 8mm. These correspond to slot Reynolds numbers of 5.8×10^4 and 11.6×10^4 respectively. The corresponding 4mm slot width data from case (I) could then be compared against these two tests.

5.1.1 Traverse details

Each traverse run involved measurements using the slanted, and then the straight sensor at 32° , 45° , 59° , 72° , 86° , and 100° round the curved part of the surface, and at 9mm, 18mm and 27mm up the flat portion of the Coanda model. These traverse locations are illustrated in figure 5.1. Fourteen measurements were taken radially at each traverse location. The spacing between each radial measurement was gradually increased with distance from the model surface, so measurements were concentrated in the region of the jet with the greatest normal velocity gradient.

The streamwise velocity component parallel to the flare surface is defined as U , the normal (or radial) velocity is defined as V , and the transverse (i.e. into the page in figure 5.1) velocity is defined as W . The distance round the Coanda model from the slot is



described using the distance, s , and the total distance traversed around the surface (i.e. from the slot round to 27mm up the flat section of the model) is defined as s_{tot} .

The positions of the first and last traverses were governed by the distance between the limit switches on the vertical traverse. The distance away from the flare surface at which each radial traverse was initiated is defined in figure 5.1 as $y(0)$. This distance was limited to a minimum of 0.9mm by the physical size of the slanted hot film, since the prongs of this sensor are inclined in the plane normal to the wall. Initial experimental runs were performed at a distance of 1.1mm away from the surface, but the air speeds were such that contaminants were a problem and the sensor breakage rate was high. The minimum distance was therefore increased to 1.9mm or more, depending on the slot velocity, to avoid sensor damage.

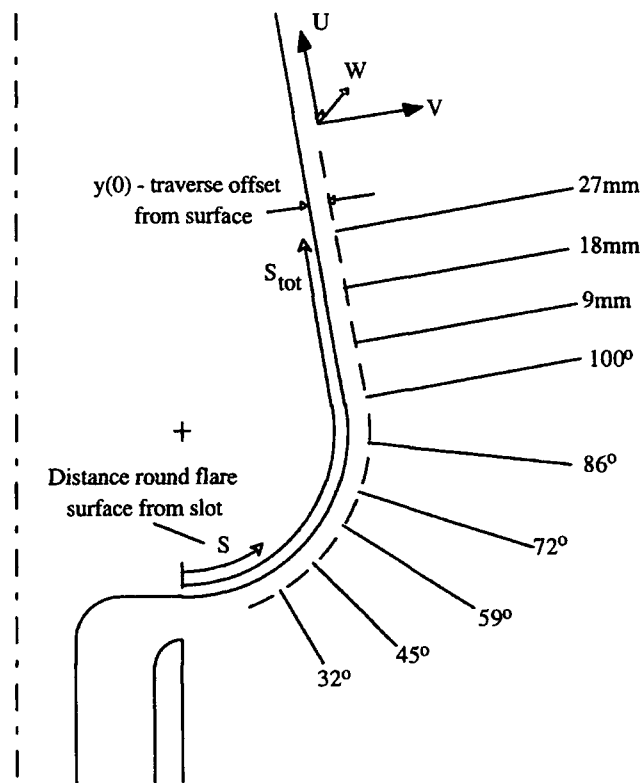


Figure 5.1 : Traverse locations round the Coanda flare

Each traverse run was fully automated. The initial position of the traverse gear was established using basic geometry, requiring a knowledge of the distance between the

vertical traverse axis and the model axis, L_1 , the distance between the base of the vertical axis and the base of the model, L_2 , and the length of the probe, L_3 , as illustrated in figure 5.2. Each distance was measured by taking the relevant traverse to its fixed end limit (sensed automatically using limit switches connected directly to the computer I/O board) and then moving that traverse to a known position relative to the flare. For example, L_2 was measured by initially moving the vertical traverse gear to its bottom limit. The large rotary stage was at 0° , and the probe support held out horizontally. The vertical traverse was then moved vertically till the probe support just touched the flat base of the flare. The distance L_1 was then calculated by recording the number of steps outputted to the traverse stepper motor, and accounting for the thickness of the probe support. Similar techniques were used to measure the distances L_1 and L_3 . The measurement of each of these distances was repeated 5 times before starting a traverse run. The readings were all consistent, and measured to an accuracy of 0.1mm.

At the end of a traverse with the straight sensor, the traverse gear was automatically returned to the start position, in readiness for the second traverse using the slanted sensor. Compensation was made for the slight differences in length between the two probes, which were measured to an accuracy of $\pm 0.01\text{mm}$ using an optical micrometer.

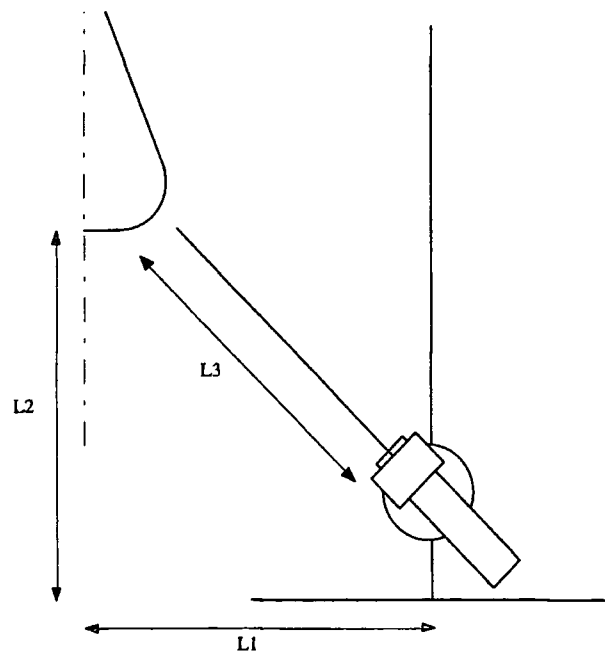


Figure 5.2 : Dimensions required for positioning the traverse gear

5.1.2 Data analysis

A detailed description of the hot film analysis technique has been given in chapter 4. All experimental data was saved to file in the form of mean and fluctuating effective mass fluxes for each angular position, at all traverse locations. This data was then analysed using software written in FORTRAN, and run on the UNIX system. A single data file was output from this routine containing the mean flow and Reynolds stress components at each traverse location. An additional FORTRAN program was then required to extract this data and write it out to individual files in a format compatible for use with UNIRAS. Data files were generated for each of the mean flow and Reynolds stress components, the kinetic energy, and the turbulent eddy viscosity. Graphs of this data were then produced using the graphics packages UNIGRAPH and Excel.

5.2 Results

The first set of results to be examined are the mean flow measurements. These are firstly presented in a raw data format. Methods of non-dimensionalising these plots are discussed in section 5.2.2. This leads on to an examination of the growth rate of the jet as it progresses round the Coanda surface, and the rate at which the maximum velocity of the jet decays with distance. The variation of the Reynolds stress components in the two test cases are then presented in sections 5.2.3 and 5.2.4, and the final section looks at the kinetic energy and eddy viscosities.

5.2.1 Mean velocity data

The three mean velocity components have been plotted against the radial distance away from the model surface, y . These velocity profiles are shown in figures 5.3(a)-(f), 5.4(a)-(f) and 5.5(a)-(f) respectively.

Plots (a)-(d) provide information for case (I). All four sets of data were obtained at a slot width of 4mm, and the pressure ratio was varied from 0.70 to 0.85. Plot (d) also provides information for case (II). The results from this must be compared against the plots in (e) and (f) which were obtained at the same pressure ratio of 0.85, but at slot widths of 2mm and 8mm respectively.

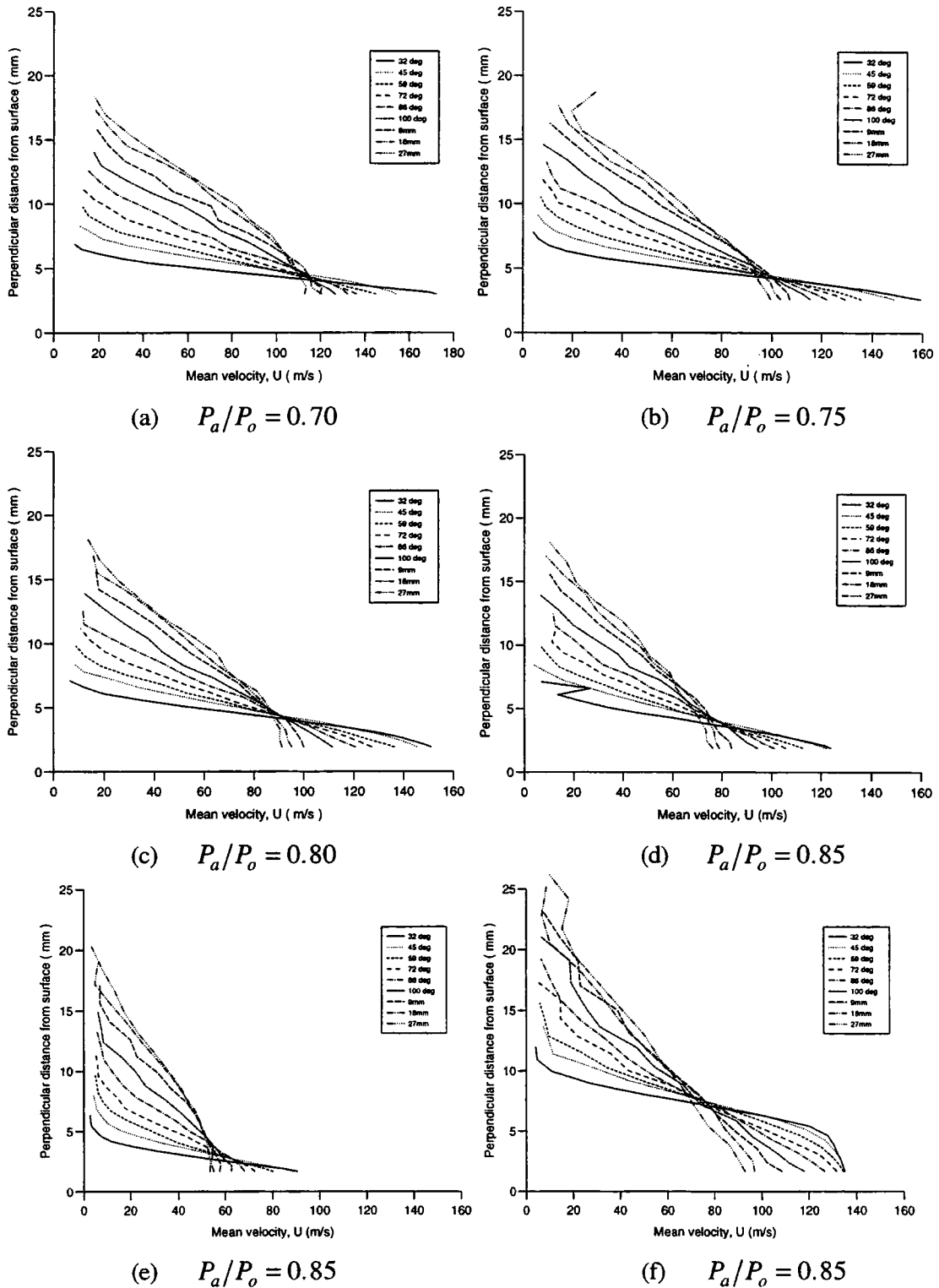


Figure 5.3 : \bar{U} versus y ; (a)-(d) $t = 4\text{mm}$; (e) $t = 2\text{mm}$; (f) $t = 8\text{mm}$

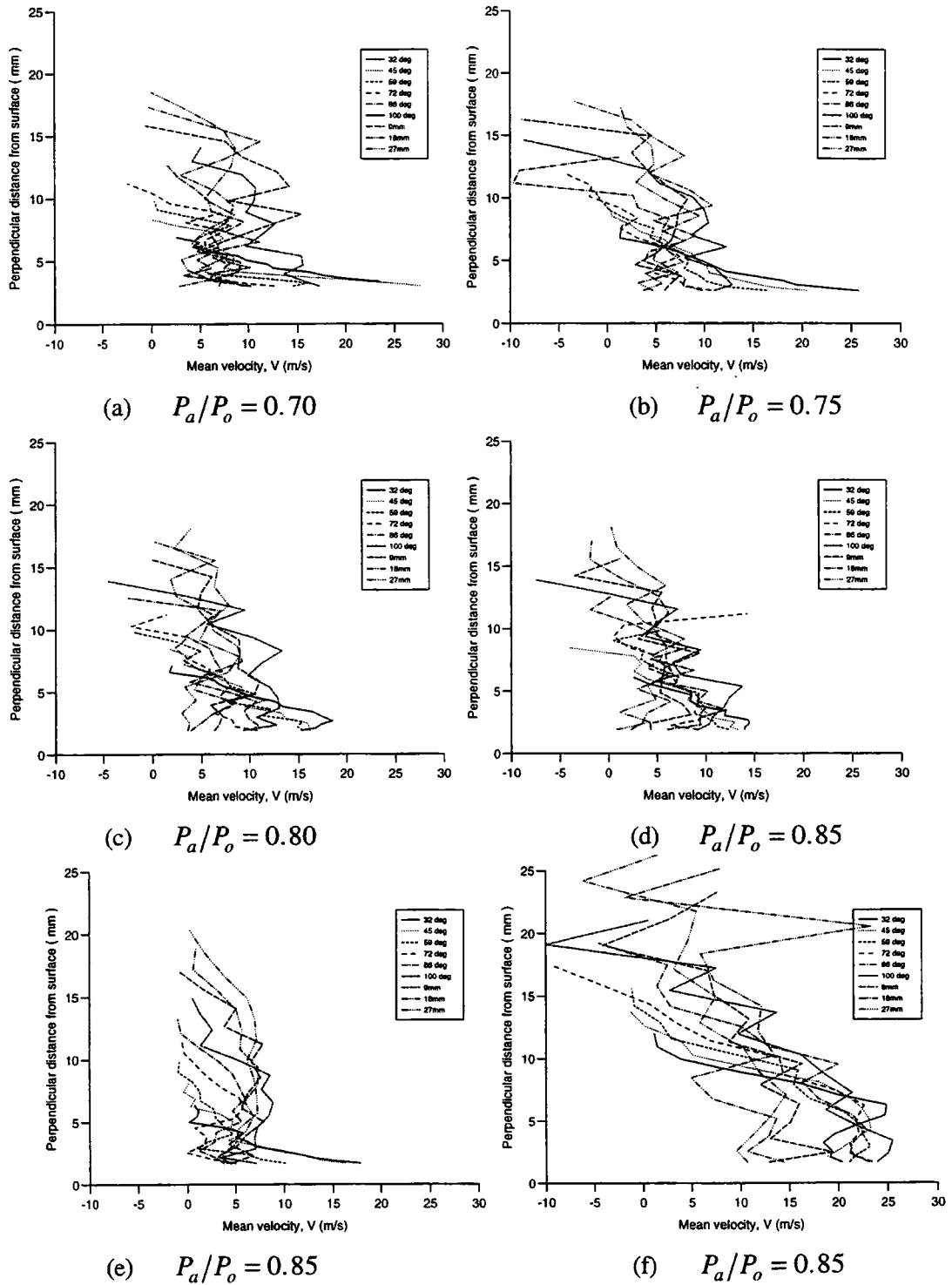


Figure 5.4 : \bar{V} versus y ; (a)-(d) $t = 4\text{mm}$; (e) $t = 2\text{mm}$; (f) $t = 8\text{mm}$

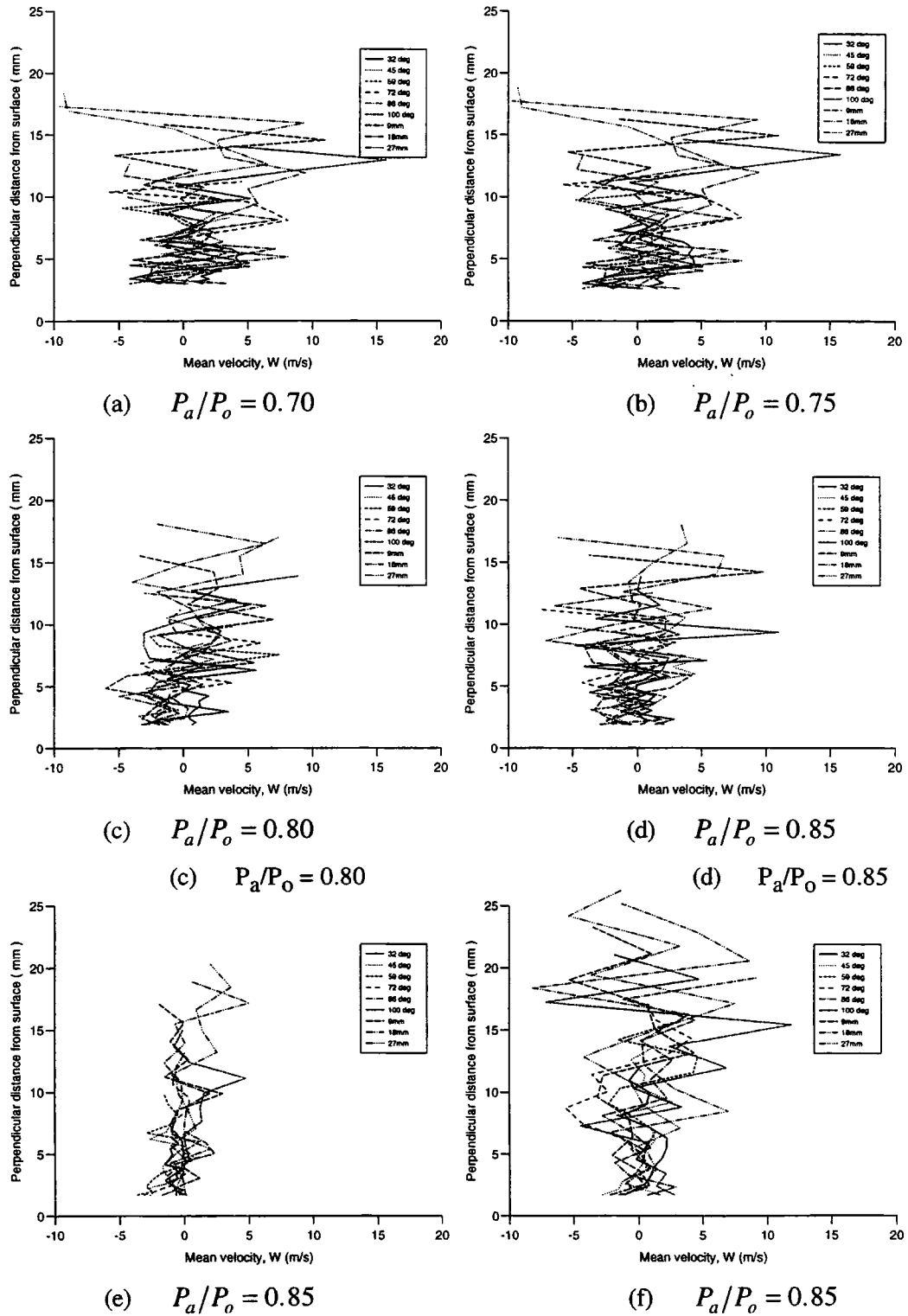


Figure 5.5 : \bar{W} versus y ; (a)-(d) $t = 4\text{mm}$; (e) $t = 2\text{mm}$; (f) $t = 8\text{mm}$

The streamwise mean velocity profiles are fairly reasonable, however the accuracy diminishes in the outer part of the jet. This was to be expected, due to the lack of accurate calibration data in the low speed region. A few spurious velocity values are apparent on the graphs. These points correspond to problems in the analysis routine. In general, 4 to 5 iterations were required to solve the mean flow and Reynolds stresses. However, in a few cases the solving routine became unstable if more than 2 or 3 iterations were performed. In these circumstances, the solution obtained before instability has been used. This is obviously not the fully converged result, and accounts for some of the erroneous points. The reason for this instability in the solving routine seems to be caused by the raw data itself, since the solution stability was unaffected by the choice of yaw and pitch coefficients used.

There is quite considerable scatter in the normal velocity component, \bar{V} . The general trend is for the normal velocity to be positive over the majority of the jet width, due to the radial outflow as the jet thickness grows. The normal velocity only becomes negative at the very outer part of the jet where ambient fluid is being entrained into the jet. The trend in most of the plots appears to be for the normal velocity to be initially quite high at 32° and 45° round the Coanda surface, decreasing further round the surface.

For a true 2-dimensional flow, the transverse velocity component, \bar{W} , should be zero. The plots in figure 5.5 show there is considerable scatter in this velocity component. However, this scatter is about a mean value of 0 which would suggest that the flow is reasonably two dimensional.

The solution process was found to be quite sensitive to the smoothing factors used for generating the surfaces for the yaw and pitch coefficients. Several analyses were performed using slightly different smoothing factors for the k^2 and h^2 coefficients, and the results presented here were those which resulted in the smallest solution errors.

The results from all the tests have been presented alongside each other in figures 5.3 - 5.5. For comparisons to be made between the tests in case (I) involving the constant slot width, and those in case (II) using a constant pressure ratio, the plots need to be non-dimensionalised. This is discussed in the following section. Two different methods of non-dimensionalising are considered for the two cases.

5.2.2 Non-dimensionalising the data

To make direct comparisons between the results in each test case, the velocity profiles needed to be non-dimensionalised. The velocity would normally be non-dimensionalised with respect to the maximum velocity, U_m , in each velocity profile. The usual method of non-dimensionalising the distance from the wall is to use the jet half width, $y_{m/2}$. Both parameters are defined in figure 5.6.

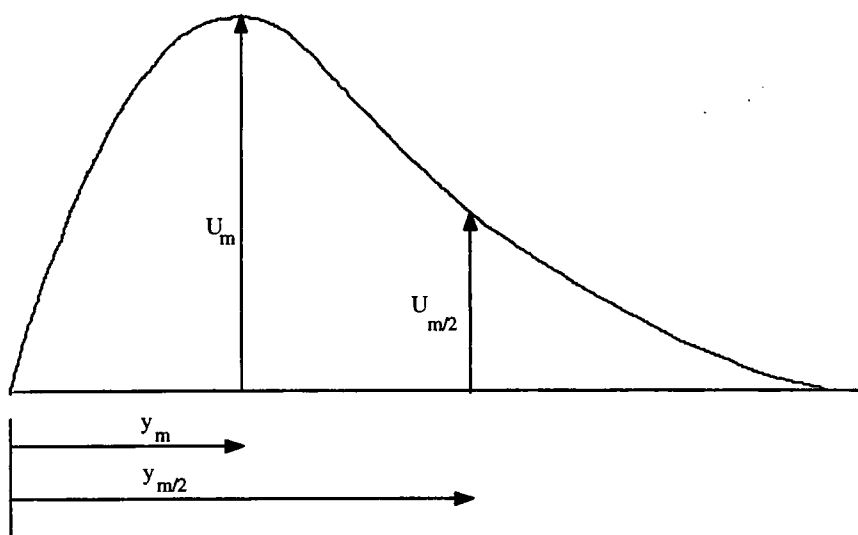


Figure 5.6 : Definition of the standard normalising parameters for a typical velocity profile

Limiting the velocity to which the sensor was exposed meant that traverses were performed in the region of the velocity profile beyond the velocity maximum. Thus U_m was unknown, and the half width could not be determined. An alternative approach would be to use the slot velocity and the slot width to non-dimensionalise the graphs.

A further alternative non-dimensionalising parameter is defined in figure 5.7. The dashed line represents the portion of the velocity profile which was not measured using the hot film. The primes here represent values at the maximum measured velocity. In the case of the 8mm slot width this is likely to be quite a close approximation to the true velocity maximum. By contrast, U_m' at 32° for the 2mm slot is far less than the slot velocity. However, on the recovery section following the curvature, the velocity profiles are quite flat and U_m' is likely to be close to the true U_m .

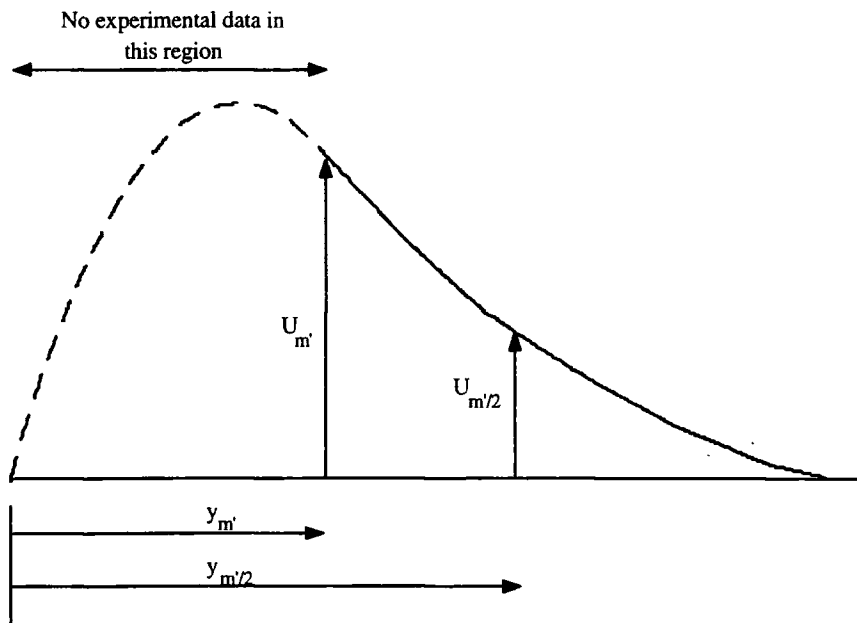


Figure 5.7 : Alternative normalising parameters

The problem with the above is the lack of consistency in the start position, $y(0)$, of the traverses. At the lowest pressure ratio, $y(0) = 3\text{mm}$ to avoid placing the sensors in the high speed region of the jet. At a pressure ratio of 0.75, this distance was reduced to 2.6mm away, and the remaining tests were all performed using a start position of 1.9mm away.

To overcome this, for case (I) the non-dimensionalising velocity may be taken as that measured at 3mm from the surface, referred to as $U_{m'(3)}$, since this data is available for all four tests. The half width is then taken as the distance to half this velocity. This new nomenclature is defined in figure 5.8. The growth rate of a jet is defined as the increase in the half width of the jet round the surface of the flare. The velocity decay rate is simply the rate at which the maximum velocity decreases with distance round the flare.

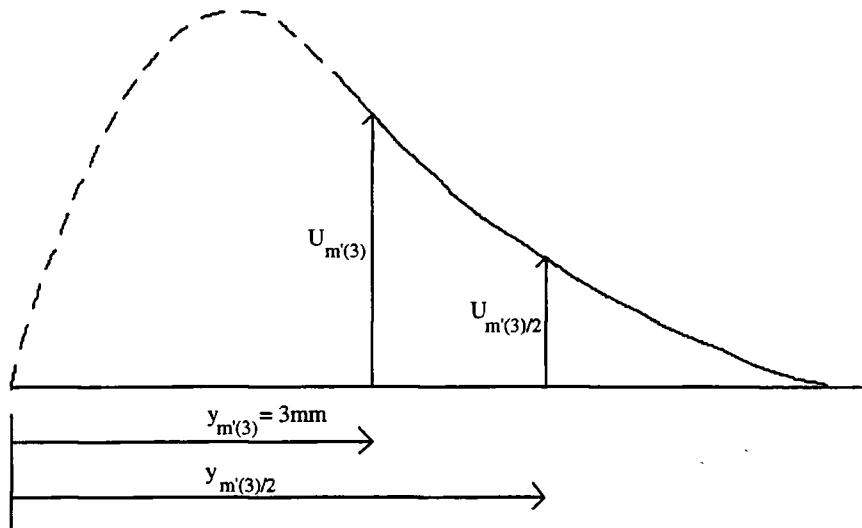


Figure 5.8 : Normalising parameters for tests in Case (I)

The jet growth rate has been produced using the half widths for the velocity at 3mm from the surface, $U_{m'(3)}$, and is shown in figure 5.9. The velocity decay rates for the four pressure ratios are shown in figure 5.10. These have been generated using $U_{m'(3)}$ which has been non-dimensionalised with respect to the slot velocity.

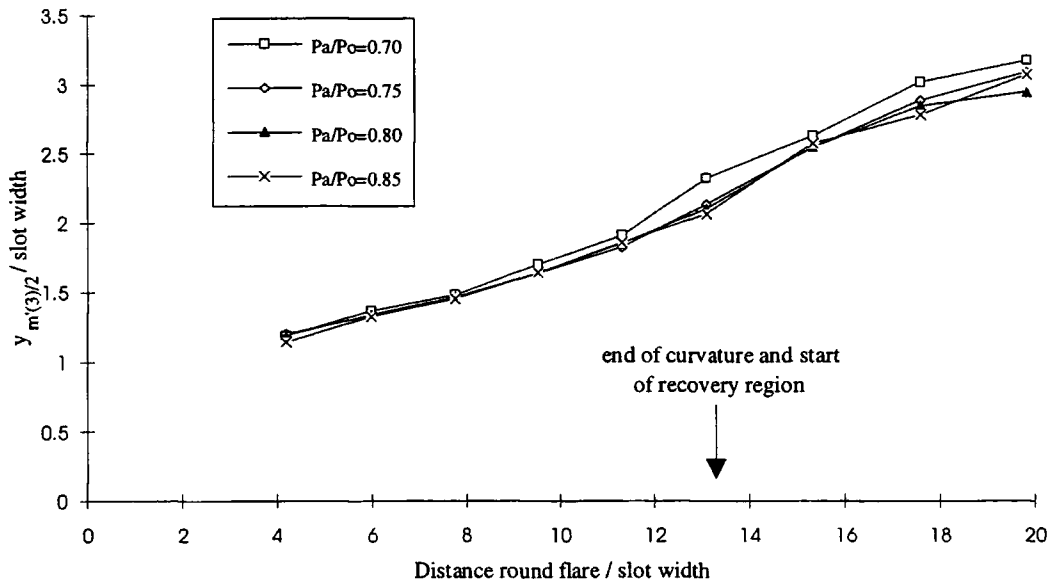


Figure 5.9 : Jet growth rate for the 4mm slot, with variable pressure ratios

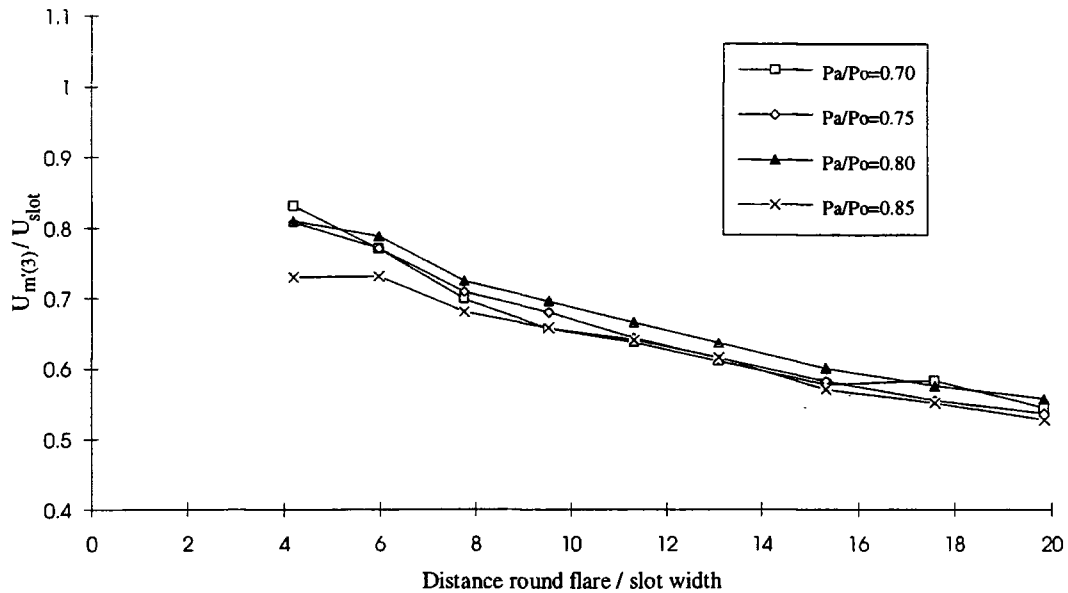


Figure 5.10 : Velocity decay rates for the 4mm slot, with variable pressure ratios

The jet growth rates and velocity decay rates are very similar, so the non-dimensionalising parameters defined in figure 5.8 seem to be reasonable.

The same method cannot be used for the case (II) tests, in which the slot velocity remains the same and the slot width varies. Figures 5.3(e) and (f) are clearly very different, since the jet growth rate is dependent on the slot width to radius ratio. An indication of the relative jet growth rates is shown in figure 5.11 in which the half width of maximum measured velocity at each location (non-dimensionalising with respect to the slot width) has been plotted against s/s_{tot} .

These are obviously not the true jet growth rates due to the lack of near wall data. An attempt has been made to estimate the maximum velocity at each position using the empirical velocity profile equation given by Newman (1961), equation (2.9) in chapter 2. At high Reynolds numbers, the ratio of $y_m/y_{m/2}$ has been taken to be 0.1. Equation (2.9) then simplifies to equation (5.1)

$$\frac{\bar{U}}{\bar{U}_m} = \operatorname{sech}^2 \left(0.88 \frac{(y - 0.1y_{m/2})}{0.9y_{m/2}} \right) \quad (5.1)$$

An iterative method was used to find the best fit approximation to the experimental data. A guessed value of \bar{U}_m provided $\bar{U}_{m/2}$. A value for the half width, $y_{m/2}$, could then be determined from the experimental data. This was substituted into equation (5.1) which was evaluated over a range of y values. As a result, a series of plots of \bar{U}/\bar{U}_m versus $y/y_{m/2}$ were obtained for a number of guessed maximum velocities. Two such typical plots are shown in figure 5.12(a) and (b). Both were obtained for the 4mm slot, at the 72° position, but using different guesses for \bar{U}_m . In most cases the theoretical curve followed the general shape of the experimental data, except at high values of $y/y_{m/2}$ where the mean flow solution was less accurate. The standard deviation of the experimental points from the empirical line was calculated between the points indicated in figure 5.12(a), and the value of \bar{U}_m giving the lowest standard deviation was selected. In this example, the lowest standard deviation, equal to 0.011 occurred at a guess of $\bar{U}_m = 109.5\text{m/s}$. The jet growth rate and velocity decay rate plots, generated using these estimated values for \bar{U}_m , are shown in figures 5.13 and 5.14 respectively.

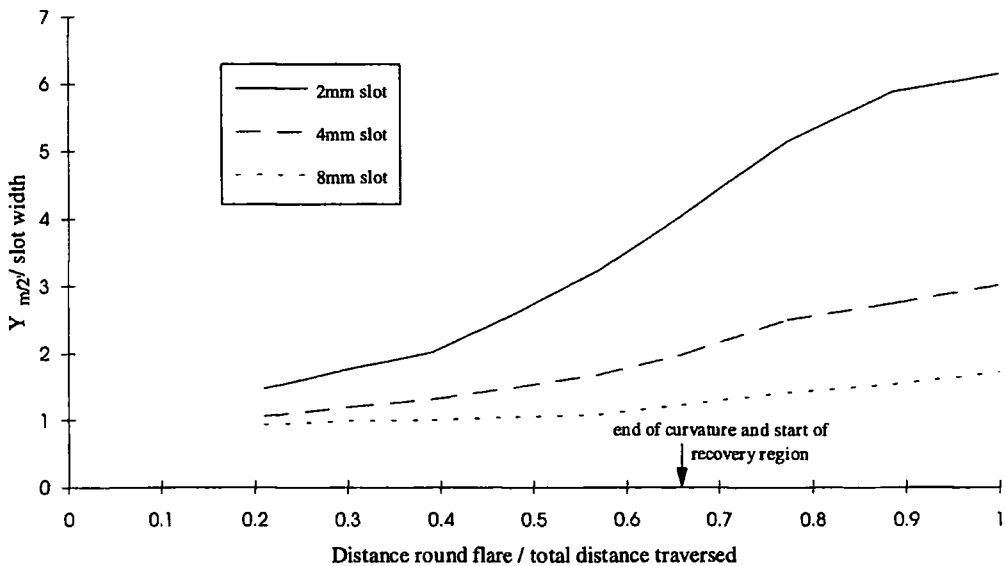


Figure 5.11 : Jet growth rate ($y_{m/2}/t$ vs. s/s_{tot}) for a pressure ratio of 0.85, with variable slot widths

The poorest match between the fitted profile and the experimental profile occurred at the 32° and 45° positions. This discrepancy was greatest with the 8mm slot, and in this case the maximum velocities in the early part of the jet were approximated by extrapolating the velocity profile rather than using the matching procedure. The errors in the maximum velocity and the half width were generally low over most of the Coanda surface, typically 2%. However, the errors in the early part of the jet could be as high as 4%.

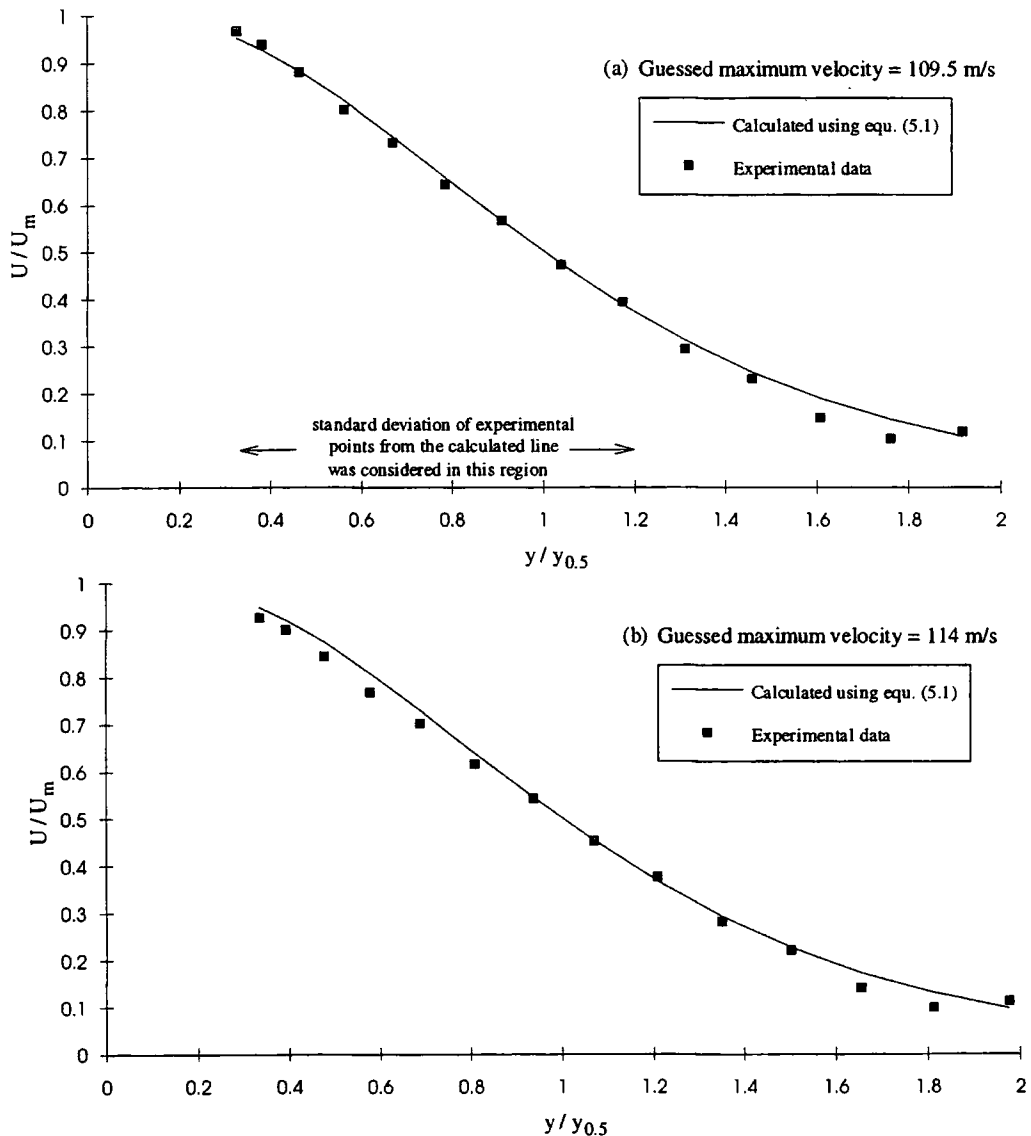


Figure 5.12 : Predicted non-dimensionalised velocity profiles compared to experimental data for the 4mm slot, at 72°, based on two different guesses for \bar{U}_m

(a) $\bar{U}_m = 109.5$ m/s, and (b) $\bar{U}_m = 114$ m/s

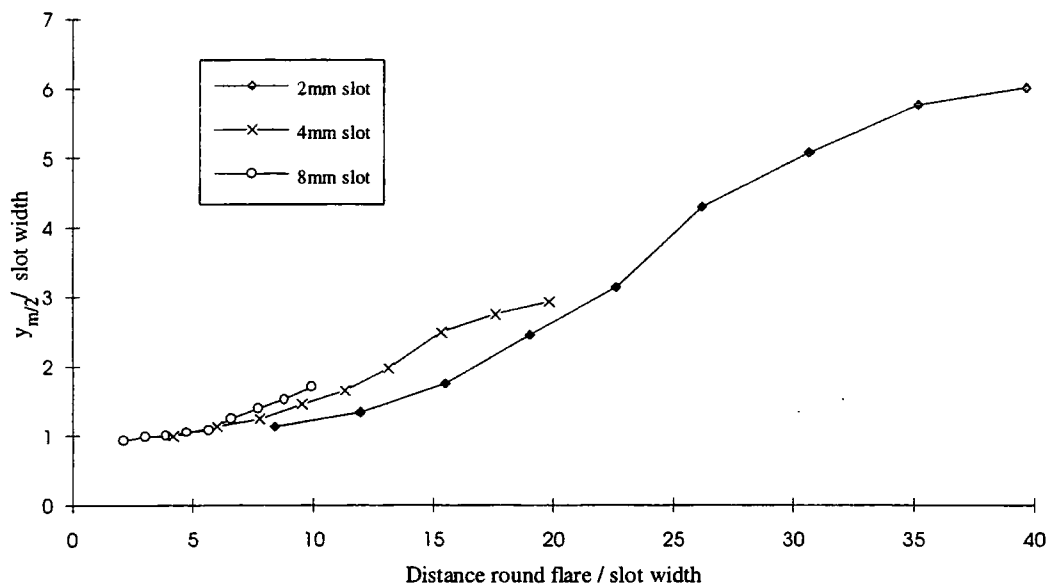


Figure 5.13 : Jet growth rates for Case (II) using the estimated maximum velocities

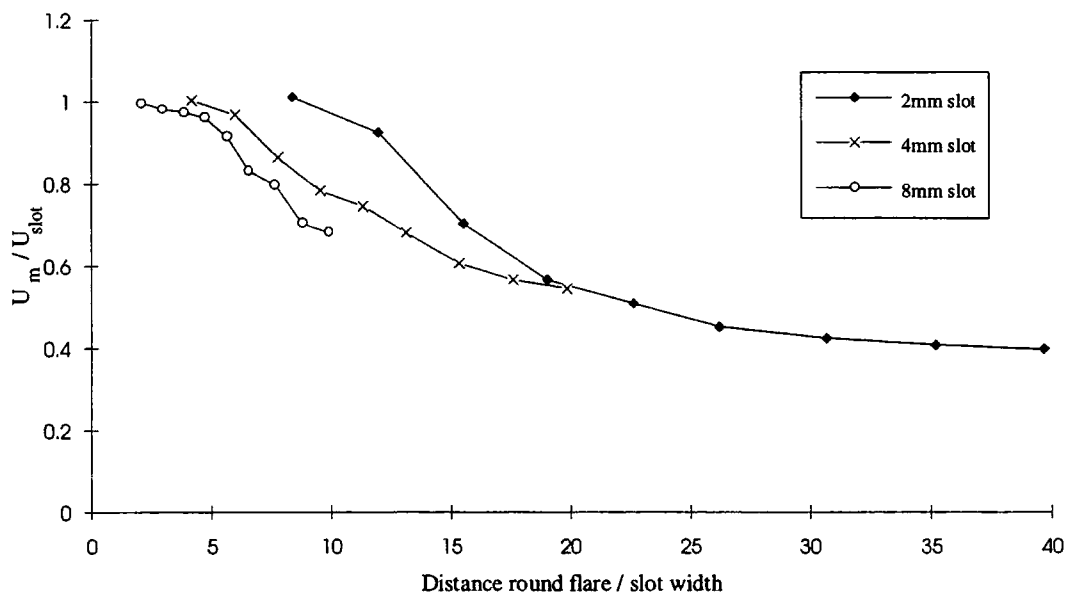


Figure 5.14 : Velocity decay rates for Case (II) using the estimated maximum velocities

These growth rate and velocity decay rate plots may seem a little misleading. From an initial inspection the effects of curvature appear to be greatest for the 2mm slot since the plots for this slot width show the greatest change. The effects of curvature should actually be greatest for the 8mm slot, since the critical ratio which determines the effects of curvature is the slot to radius ratio. This ratio tends to zero as the radius of curvature tends to infinity, and the conditions tend towards those of a flat plate. The effects of curvature increase as this ratio increases, either due to a tighter radius of curvature, or an increased slot width.

The x-axis in graphs 5.13 and 5.14 shows the distance round the flare non-dimensionalised with respect to the slot width. The distance required for the jet to become fully developed, i.e. fully turbulent, is dependent on the slot width. According to Newman (1961), a plane wall jet may be expected to become fully turbulent approximately ten times the slot width downstream of the hypothetical origin. Based on this, the 2mm slot case should become fully turbulent the earliest, after approximately 38° round the flare surface. The 4mm slot case should be the second earliest to develop, at approximately 76° round the flare. Based on this theory, the jet issuing from the 8mm slot would only become fully developed beyond the curved section of the flare. The actual distances required for the jet to become fully developed are likely to be far less than these plane wall values due to the destabilising nature of the convex curvature. The basic trend is that the 2mm slot will become fully developed more rapidly than the wider slot widths. The growth of the jet in the 2mm case therefore is far more apparent than the 8mm slot case, since the distance travelled round the flare relative to the slot width is comparatively large.

The increased effects of curvature with the larger slot width are evident by the fact that the half width of the larger jet starts to grow relative to the slot at a shorter distance round the flare relative to the slot width, than the 4mm and 2mm slot cases. Likewise, the maximum velocity of the 8mm slot case starts to decrease after a shorter distance round the flare relative to the slot width than the 4 and 2mm slot cases.

The agreement between the fitted velocity profiles and the experimental ones was reasonably good, so the idea was extended to the results of case (I). The errors were once again highest at the 32° and 45° positions where the errors were estimated to be as great as 5%. However, in general the matching procedure was successful, and the resulting jet growth and velocity decay plots using the estimated values for \bar{U}_m are given in figures 5.15 and 5.16. These graphs have the same general shape as those obtained using the velocity at 3mm from the surface (figures 5.9 and 5.10). The similarity between the four pressure ratios is also still evident. The agreement between the fitted and experimental profiles was generally good over most of the Coanda surface, and once again the majority of the errors were estimated to be less than 2%, so the approximations for the maximum velocity and the jet half widths have been used as the non-dimensionalising parameters in the remainder of this chapter.

The growth rate data for the 2mm and 4mm slot cases have been plotted against the empirical growth rate for a fully developed jet proposed by Wilson and Goldstien (1976). Figure 5.17 shows reasonable agreement for the 2mm slot case. The agreement for the larger 4mm slot case, shown in figure 5.18 is much poorer. This illustrates the effect of a larger slot width increasing the size of the potential core of the jet. This increases the distance required for the jet to become fully developed, and the growth law is only applicable beyond this point.

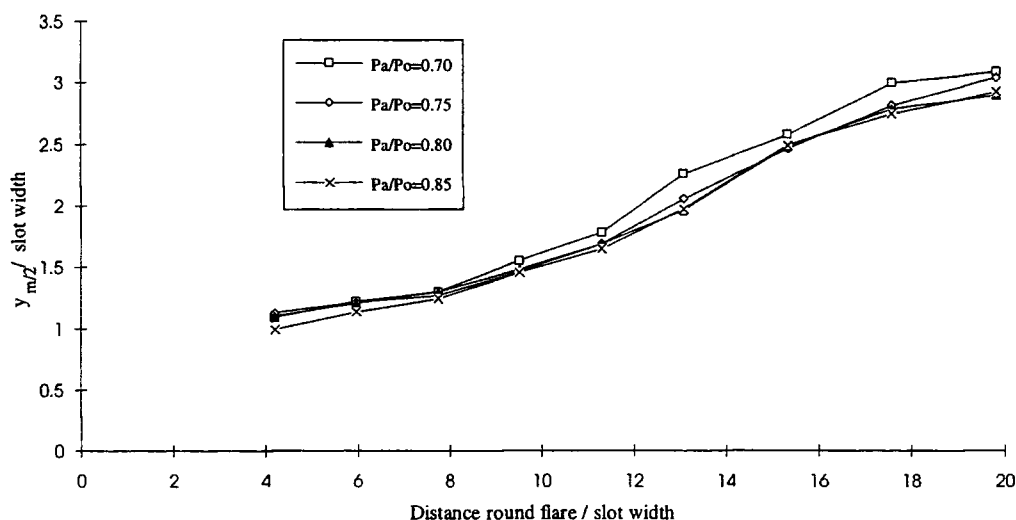
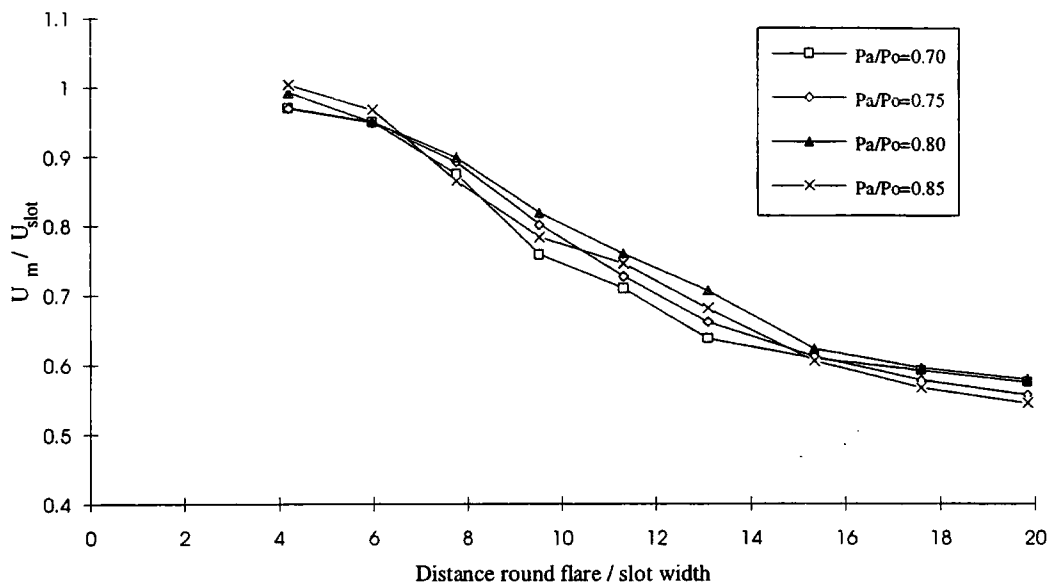
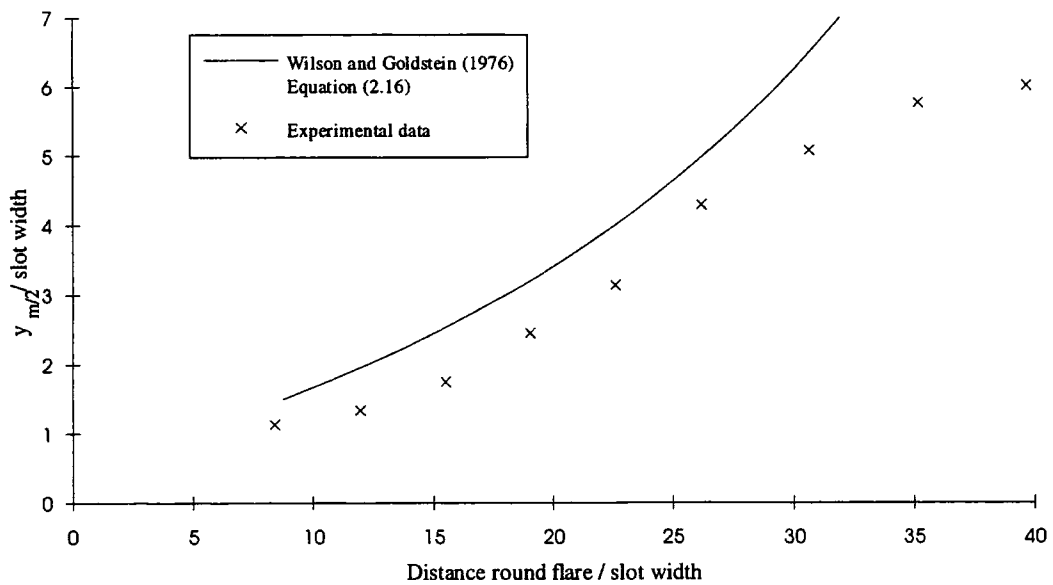


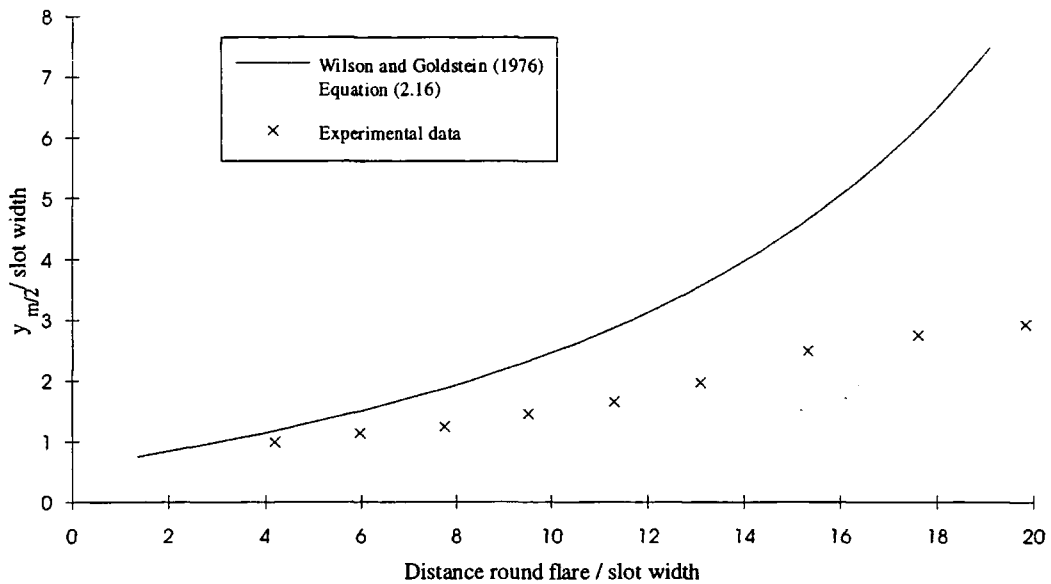
Figure 5.15 : Jet growth rates for Case (I) using the estimated maximum velocities



5.16 : Velocity decay rates for Case (I) using the estimated maximum velocities



5.17 : Comparison between empirical and experimental growth rates for the 2mm slot



5.18 : Comparison between empirical and experimental growth rates for the 4mm slot

Figures 5.19 - 5.21 show the non-dimensionalised mean velocity data. The plots (a)-(d) correspond to case (I) tests in which the pressure ratio varies. Plots (d), (e) and (f) correspond to test case (II) for the 4, 2 and 8mm slot widths respectively at a pressure ratio of 0.85.

Figure 5.19 shows the \bar{U}/\bar{U}_m profiles, and with the exception of the 8mm slot width, the data very nearly collapses onto a single line, giving the impression of similar velocity profiles. A similar result was obtained by Wilson and Goldstein (1976). The larger potential core with the 8mm slot width means the jet is still not fully developed by 59° round the Coanda surface. Beyond this point the profiles do appear to fall roughly on top of one another. There is considerable scatter in the profiles of \bar{V}/\bar{U}_m in figure 5.20. Despite this, there is clearly no similarity in these profiles, and in accordance with the continuity equation, the streamwise velocity profiles must also be non-similar.

The non-dimensionalised plots of case (I) are all similar, suggesting that the flow is independent of Reynolds number, down to a pressure ratio of 0.7.

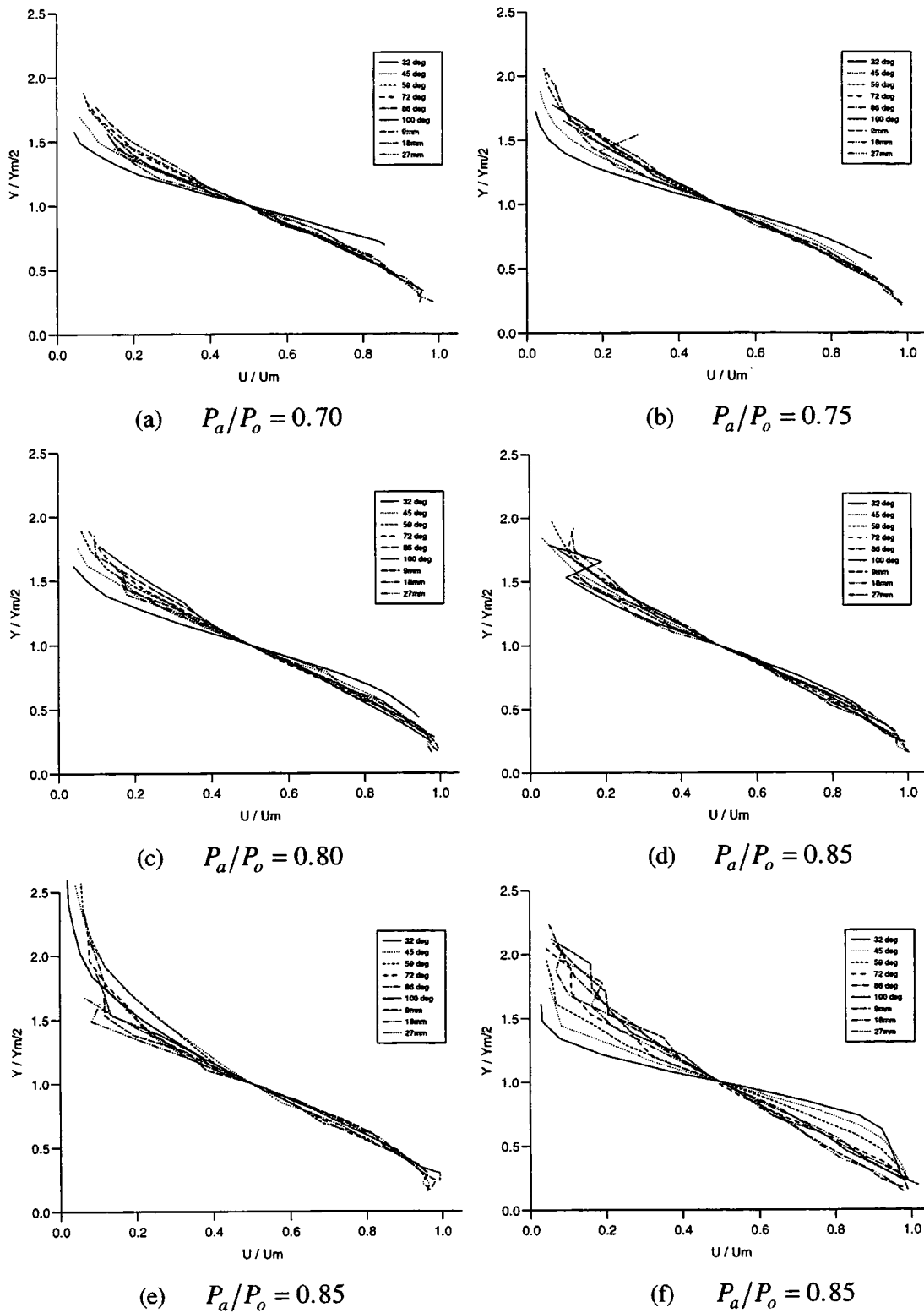


Figure 5.19 : \bar{U}/\bar{U}_m versus $y/y_{m/2}$; (a)-(d) $t = 4\text{mm}$; (e) $t = 2\text{mm}$; (f) $t = 8\text{mm}$

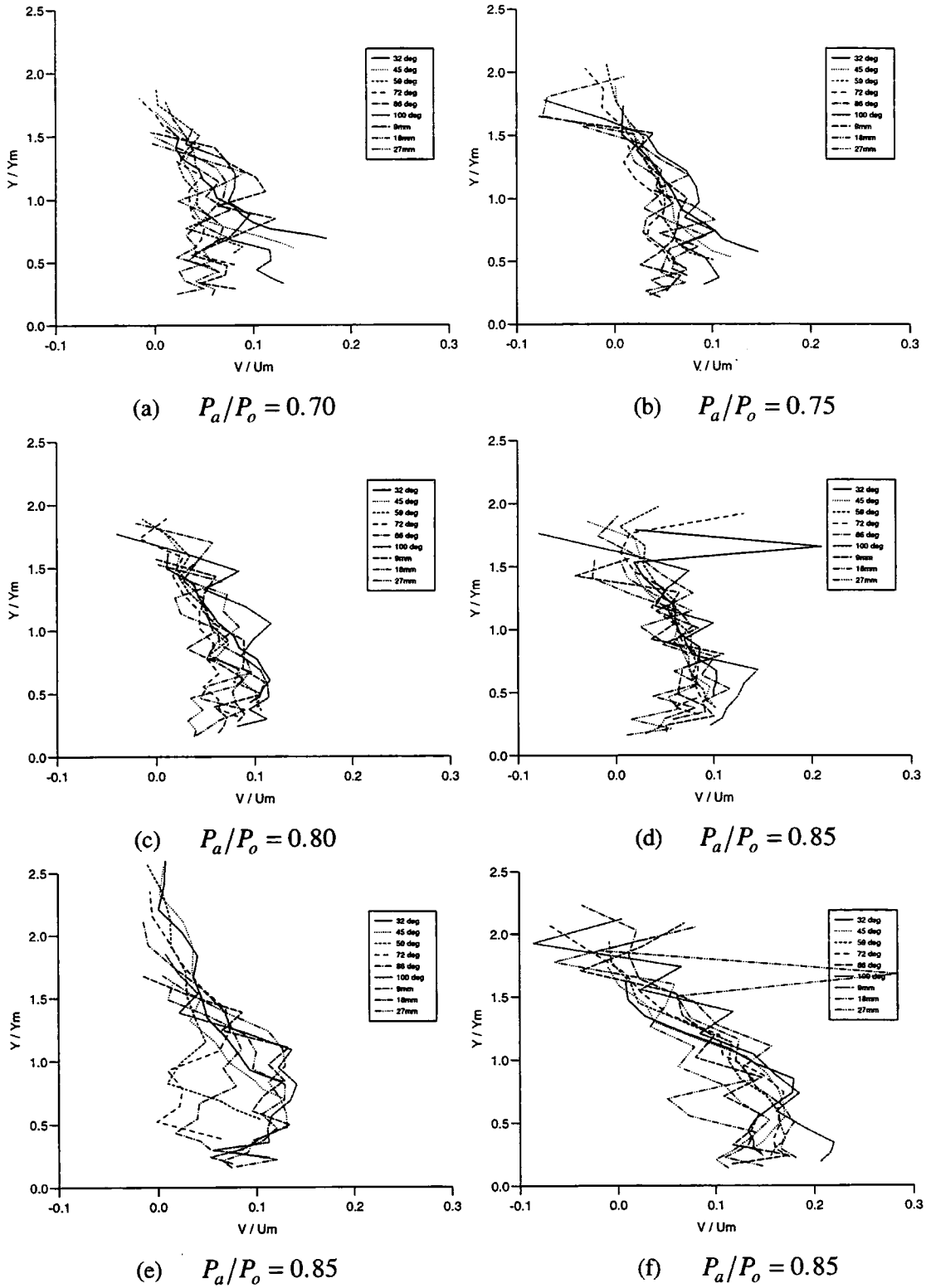


Figure 5.20 : \bar{V}/\bar{U}_m versus $y/y_{m/2}$; (a)-(d) $t = 4\text{mm}$; (e) $t = 2\text{mm}$; (f) $t = 8\text{mm}$

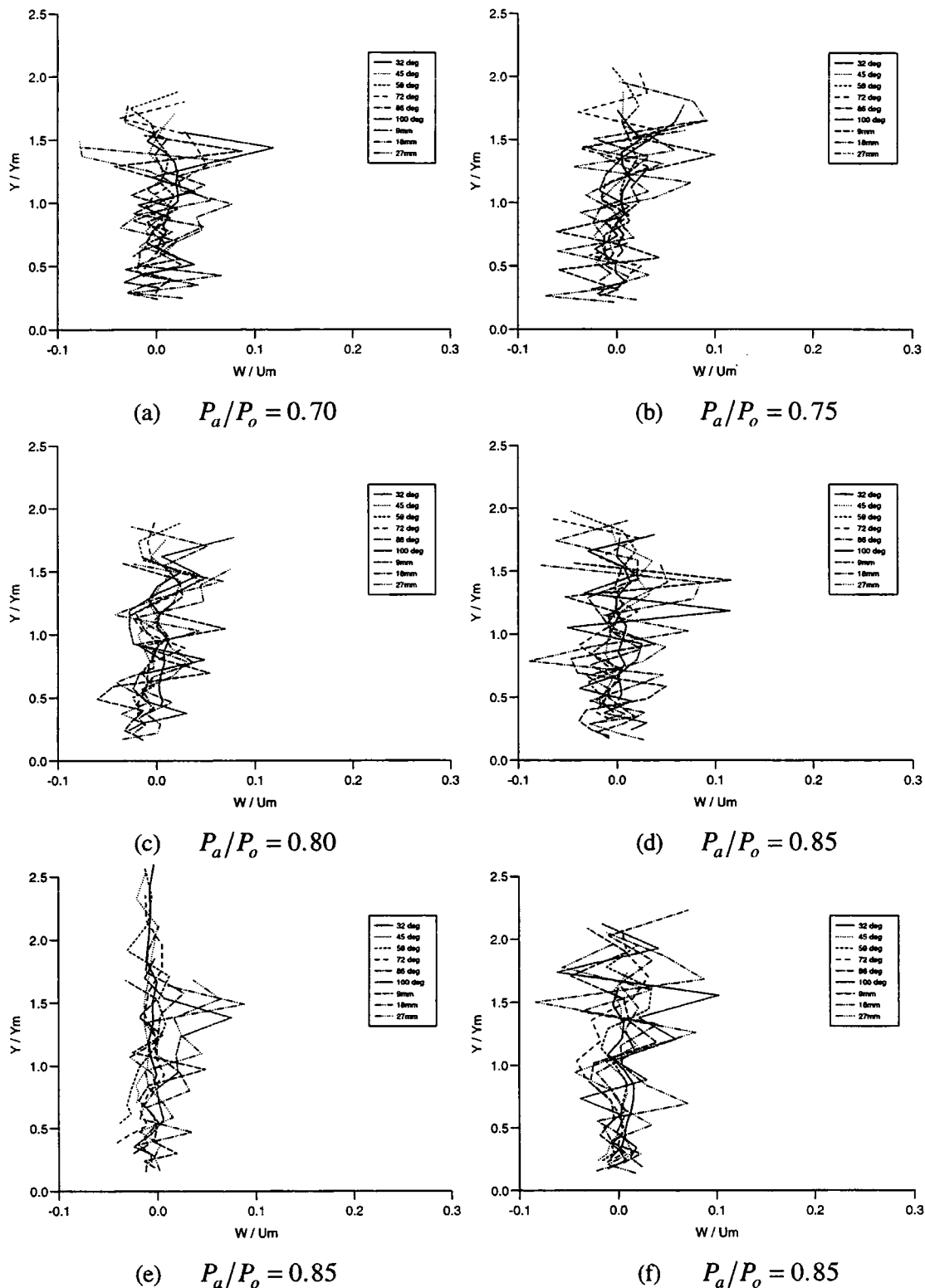


Figure 5.21 : \bar{W}/\bar{U}_m versus $y/y_{m/2}$; (a)-(d) $t = 4\text{mm}$; (e) $t = 2\text{mm}$; (f) $t = 8\text{mm}$

5.2.3 Normal stresses

The normal stress profiles are presented in figures 5.22 - 5.24. They are displayed as turbulence intensities relative to the maximum streamwise velocity. The turbulence intensities are all high, up to 25%. None of the data shows any degree of similarity. As with the mean flow data, the largest degree of scatter occurs in the normal (i.e. the radial) component. Large errors in the solution of the Reynolds stresses were signified by the solution of negative normal stresses, or excessively large stresses, caused by the solution process going unstable. For the purposes of displaying the Reynolds stresses, negative normal stress data points have been ignored, along with any solutions which became unstable and resulted in impossibly large stresses. As a result, some of the graphs contain discontinuities. This is most evident in the 8mm slot case.

The following discussion on the results is generally restricted to the streamwise and transverse fluctuating velocity components, due to the large amount of scatter in the radial fluctuating component profiles. From figure 5.22, the streamwise normal stress may be seen to gradually increase in magnitude round the flare surface from 32° up to 9mm up the flat recovery section. From this point on the recovery region onwards, the normal stress profiles lie approximately on top of each other, which implies no further increase in mixing occurs. In all the test cases, the peak in the normal stress profile at 32° round the flare surface occurs at $y/y_{m/2} \approx 1.1$. This indicates that the jet is only turbulent in the outer shear layer. As the jet becomes more fully developed the profile peak moves inwards to lie between $0.5 < y/y_{m/2} < 1.0$. The transverse normal stress profiles show similar trends, although the peak magnitudes of this stress are lower than the streamwise component, suggesting a lack of isotropy of the turbulence.

Wilson and Goldstein (1976) measured the streamwise and normal fluctuating components of velocity on a plane and a curved wall jet. The slot to radius ratio in their tests was 0.0605. In the current investigation, the slot to radius ratios were 0.067, 0.133 and 0.267 for the 2mm, 4mm and 8mm slots respectively. Hence, the 2mm slot results are the most directly comparable to the results of Wilson and Goldstein. The slot Reynolds numbers are also similar. The slot Reynolds number of Wilson and Goldstein was 5.13×10^4 (calculated using $Re_s (R/2t)^{0.5}$), and in this case the 2mm slot Reynolds number was 5.8×10^4 . Both are above the critical Reynolds number (defined by

Newman as 4×10^4) above which the separation point of an incompressible jet stabilises. The difference is that the experiment of Wilson and Goldstien is incompressible, and the current investigation is compressible, since the slot Mach number is 0.48.

Wilson and Goldstein found the values for the streamwise normal stress to be greater than those for the plane wall jet, for which the normal stress profiles lay on top of one another. By contrast, the magnitude of the peak value of $\sqrt{\overline{u^2}}/\overline{U_m}$ increased with distance round the cylinder, rising to a maximum of 0.24 at $s/t = 38$. The peak value at the equivalent position in the 2mm slot case was slightly lower than this, reaching a maximum of 0.24.

The radial fluctuations measured by Wilson and Goldstein were also found to increase in magnitude with downstream distance, reaching peak values ranging from 0.195-0.26 at values of s/t ranging from 18 to 38. These profiles showed more variation with distance than the streamwise component. Wilson and Goldstein explain that the increase in the radial turbulence intensity is due to the increased production term from the centrifugal forces which acts on the unstable outer region of the jet.

They also explain that the streamwise fluctuations increase is not a direct result of the centrifugal or Coriolis forces. In actual fact, the Coriolis forces act to decrease the production of $\overline{u^2}$ in the outer part of the jet where the shear stress is positive. The increased production of $\overline{u^2}$ is due to an increase in the term $-\overline{uv} \partial U / \partial y$, which represents the production due to the shearing forces, and due to the action of the static pressure fluctuations which couple the radial and streamwise intensities.

The experimental results presented here cannot be compared directly against the turbulence measurements of Hawkins (1988) and Morrison (1982) since both performed experiments on axisymmetric models. The turbulence structures therefore were influenced by an additional rate of strain associated with the streamline divergence, $\partial w / \partial z$. The curvature effect ends abruptly at 100° round the flare surface, when $\partial R / \partial x \rightarrow \infty$. There is no such sudden change in the divergence effect. At 90° the geometry of the axisymmetric model changes from diverging to converging. The ratio of

the axisymmetric radius of curvature to the streamwise distance, $\partial R_a/\partial s$, simply changes sign after passing through zero, and then maintains a constant value.

The slot to radius ratios in the experiments of Hawkins and Morrison were both 0.166, so the effects of curvature are likely to be greater than in the closest equivalent test in the current investigation for the 4mm slot case. The slot Reynolds numbers, Re_s , used in the experiments of Hawkins and Morrison were 2.14×10^4 and 2.17×10^4 respectively. The slot Reynolds number for the 4mm slot case at $P_a/P_o = 0.85$ was 4.2×10^4 .

Morrison and Hawkins both found similar increases in streamwise turbulence intensities with distance round the flare. Morrison found the profiles of $\sqrt{u^2}/U_m$ to peak at $y/y_{m/2} = 0.6$ which coincided with the large positive values of $\partial U/\partial y$. The turbulence intensity was found to drop as the streamwise velocity and the velocity gradient decreased towards the outer part of the jet. Morrison found that $\overline{u^2}$ reached a maximum and was more or less constant across the jet width at 75° and 90° . Hawkins found a maximum at 75° , and reported a decrease at 90° , followed by a recovery to the values at 75° after 20mm beyond the end of the curvature. By contrast, the results from the current investigation showed the turbulence intensity to rise to a maximum beyond the end of the curved section, and to show only a slight decrease in turbulence intensity after 28mm up the recovery section.

Morrison's results showed the radial stress to be very sensitive to the removal of the curvature, whereas Hawkins showed it to be far less sensitive, only showing a response at $100^\circ+20\text{mm}$. Morrison found the profiles of the transverse normal stress, $\overline{w^2}$, to be much flatter and show a consistent increase downstream up to 90° . He found a larger variation in this component in the streamwise direction than the other two stress components. Hawkins found the profiles of this stress component to be very flat, but showed little variation with streamwise distance. Both measured the turbulence intensity of this component to be comparable in magnitude to the other principle normal stresses. The experimental results presented here also show the relatively flat profiles for $\overline{w^2}$, although the magnitude of this stress is smaller than the streamwise component. The maximum turbulence levels reported here are all lower than those measured in the

axisymmetric tests. This can be attributed to the smaller slot to radius ratio and the lack of divergence effects in the planar model.

The results may also be compared against those of Dakos *et al* (1984) who performed measurements on an incompressible jet flowing over a planar convex surface. The slot to radius ratio in this experiment was much smaller, equal to 0.0044, and the slot Reynolds number, Re_s , was 3×10^4 . The turbulence intensities at comparable streamwise distances round the surface relative to the slot height were much lower than those measured in the current investigation. This difference is attributable to the decreased influence of the curvature in the tests of Dakos *et al*, determined by the slot to radius ratio.

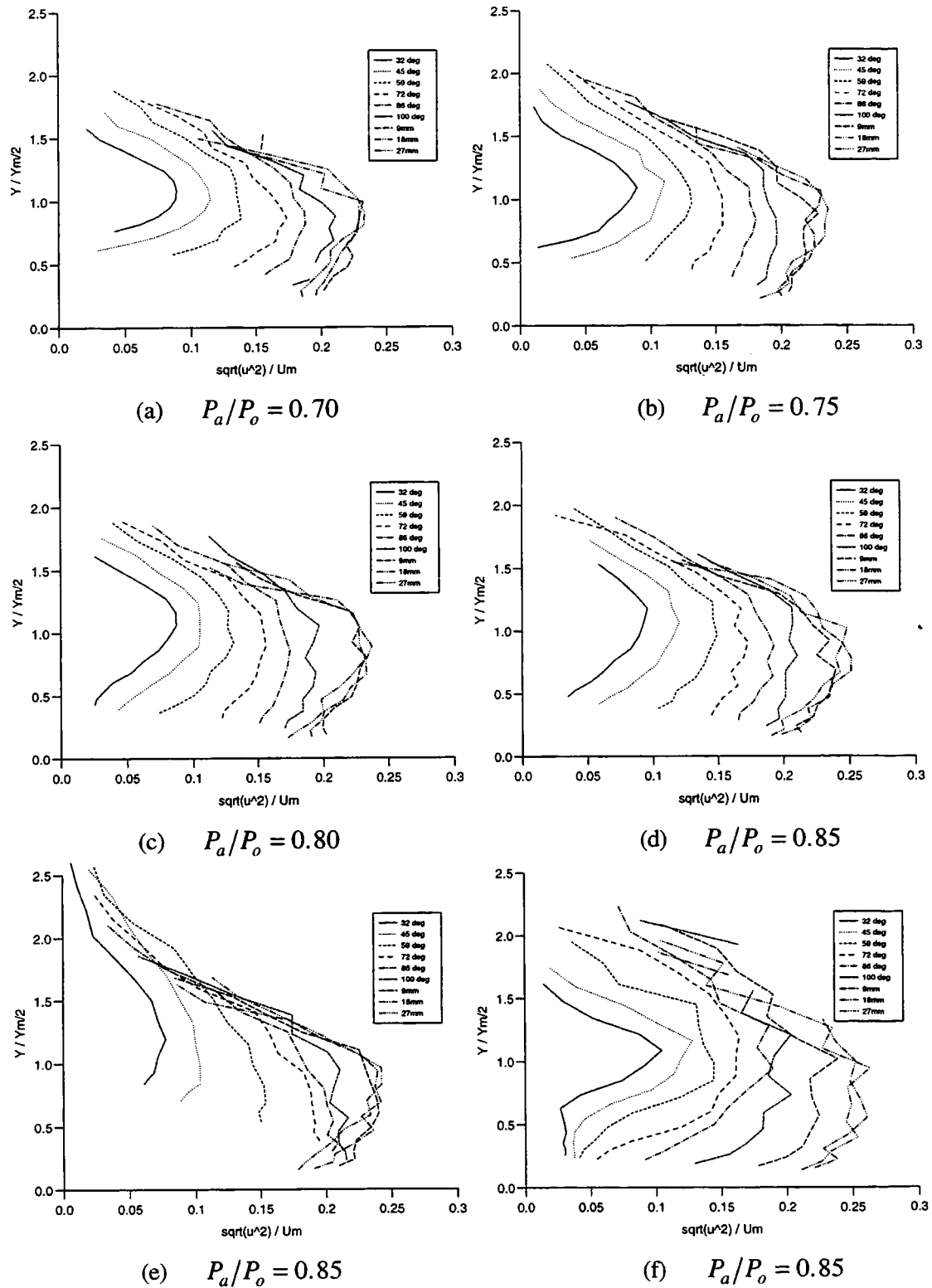


Figure 5.22 : $\sqrt{u^2} / \bar{U}_m$ versus $y / y_{m/2}$; (a)-(d) $t = 4\text{mm}$; (e) $t = 2\text{mm}$; (f) $t = 8\text{mm}$

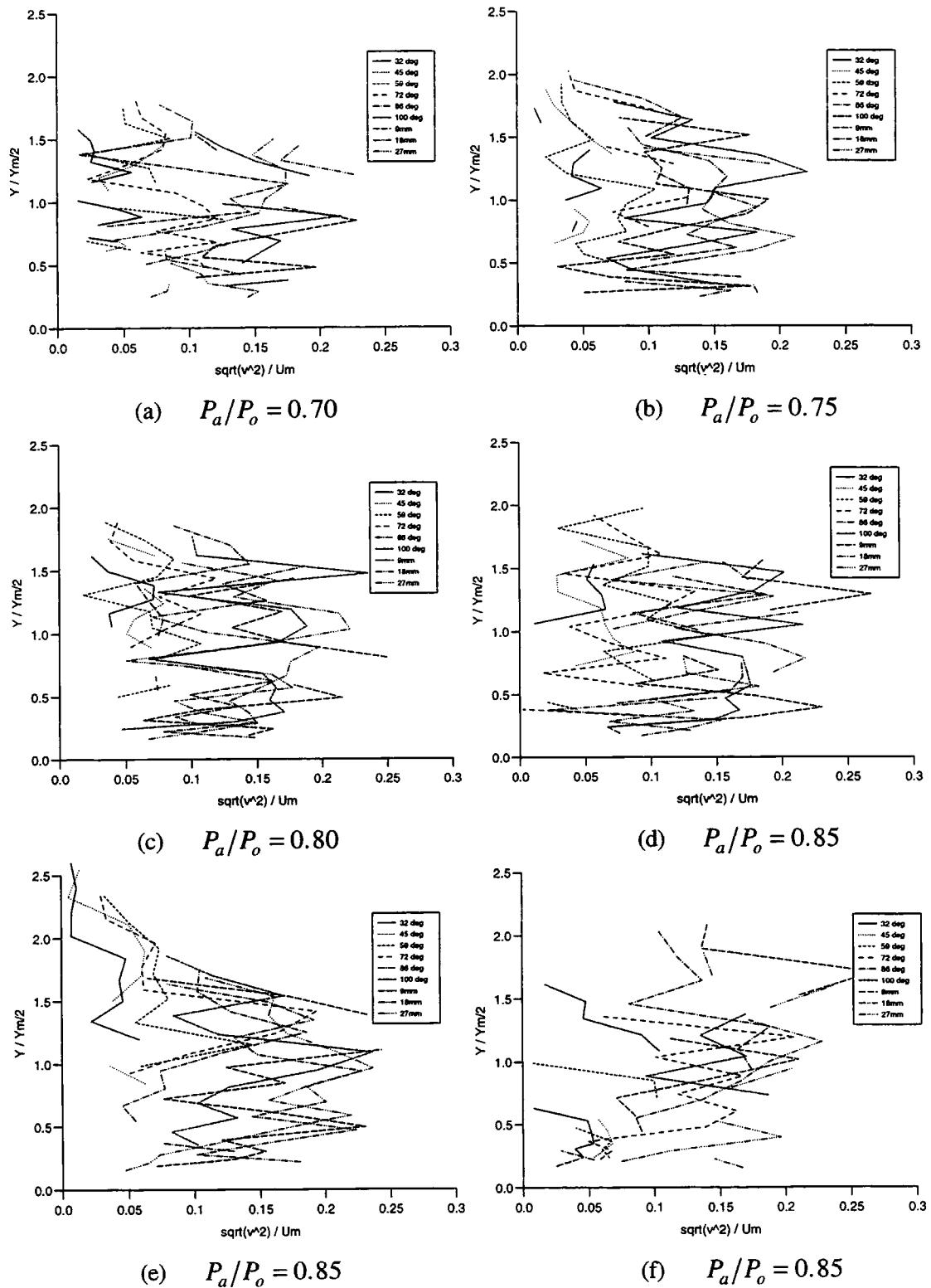


Figure 5.23 : $\sqrt{v^2}/\bar{U}_m$ versus $y/y_{m/2}$; (a)-(d) $t = 4\text{mm}$; (e) $t = 2\text{mm}$; (f) $t = 8\text{mm}$

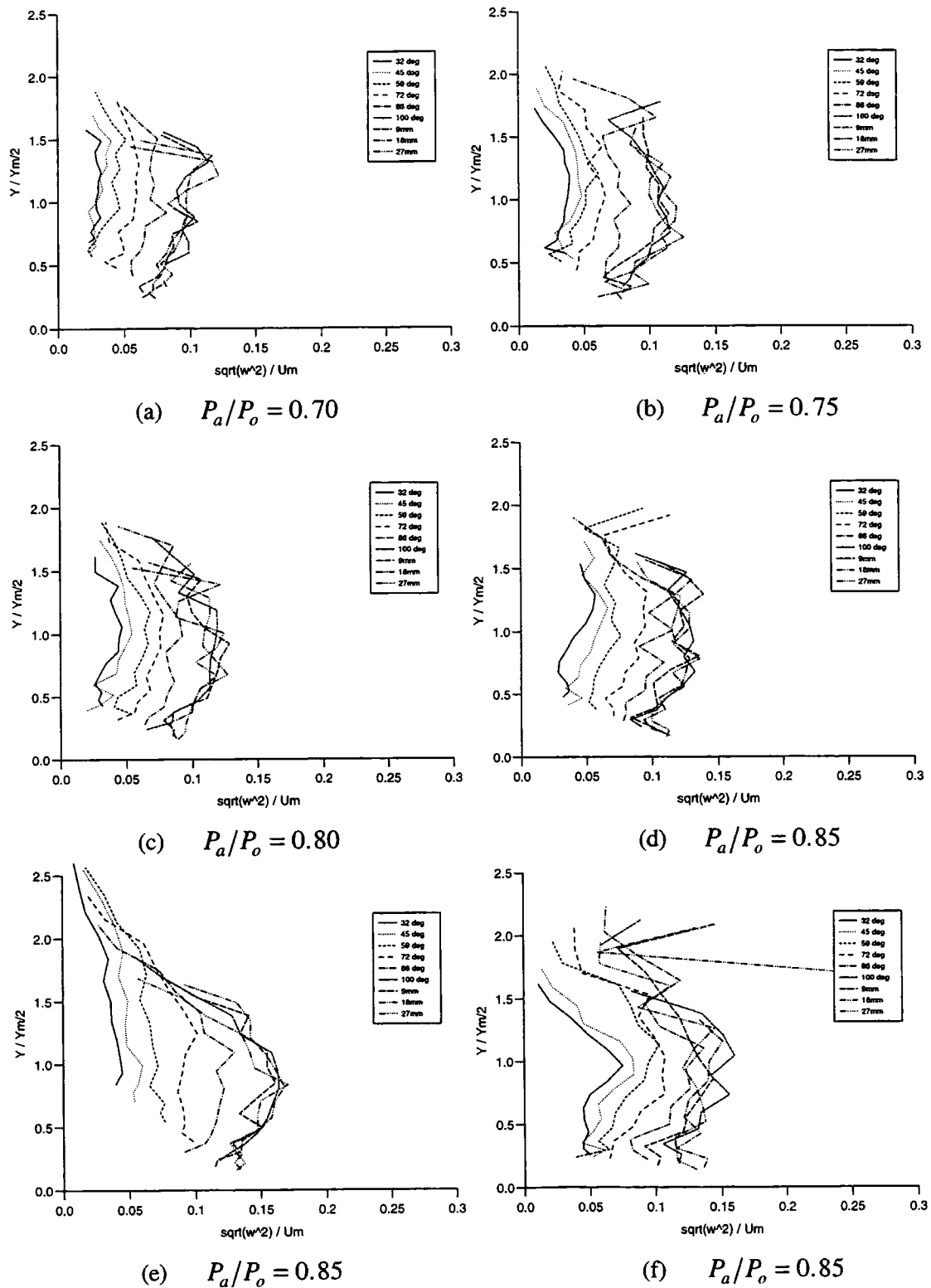


Figure 5.24 : $\sqrt{w^2} / \bar{U}_m$ versus $y/y_{m/2}$; (a)-(d) $t = 4\text{mm}$; (e) $t = 2\text{mm}$; (f) $t = 8\text{mm}$

5.2.4 Shear stresses

The non-dimensionalised shear stress profiles are presented in figures 5.25 - 5.27. Figure 5.25 shows the profiles for the \overline{uv} shear stress. This shear stress contains the fluctuating velocity component normal to the surface. These profiles show the same erratic nature that were observed in the normal stress component profiles for $\overline{v^2}$. The general trend in these profiles is for the magnitude of the shear stress to increase with distance round the Coanda surface, reaching a possible maximum at 100° . The remaining two shear stresses, \overline{uw} and \overline{vw} , are both very small with no discernible variation with distance round the flare surface. For truly 2-dimensional flow these stress components should be zero.

Measurements were not taken sufficiently close to the wall to allow the point at which the shear stress goes negative to be determined. The scatter in the data makes it hard to draw any definite conclusions. The \overline{uv} shear stress levels do appear to be greatest for the 8mm slot case. There is fair agreement between the four cases with the 4mm slot, and all have lower shear stress values than the 8mm slot. The 2mm slot case has the lowest shear stress values early on round the flare surface, but the levels appear to rise above those of the 4mm slot further round the flare. This may be due to the more rapid development of the jet issuing from the smaller slot width. The shear stress is responsible for the entrainment of the ambient fluid into the jet, and the levels of entrainment are enhanced by curvature effects. The highest levels of shear stress for the 8mm slot case are therefore not unexpected.

The shear stress levels of Wilson and Goldstein are slightly higher than those of the 2mm slot case at equivalent positions of s/t , except very early on in the jet where the 2mm slot levels are less than half those of Wilson and Goldstein. By contrast, the results of Dakos *et al* were less than a third of the magnitude of the equivalent 2mm slot measurement, which once again highlights the importance of the slot to radius ratio in determining the influence of the curvature on the flow.

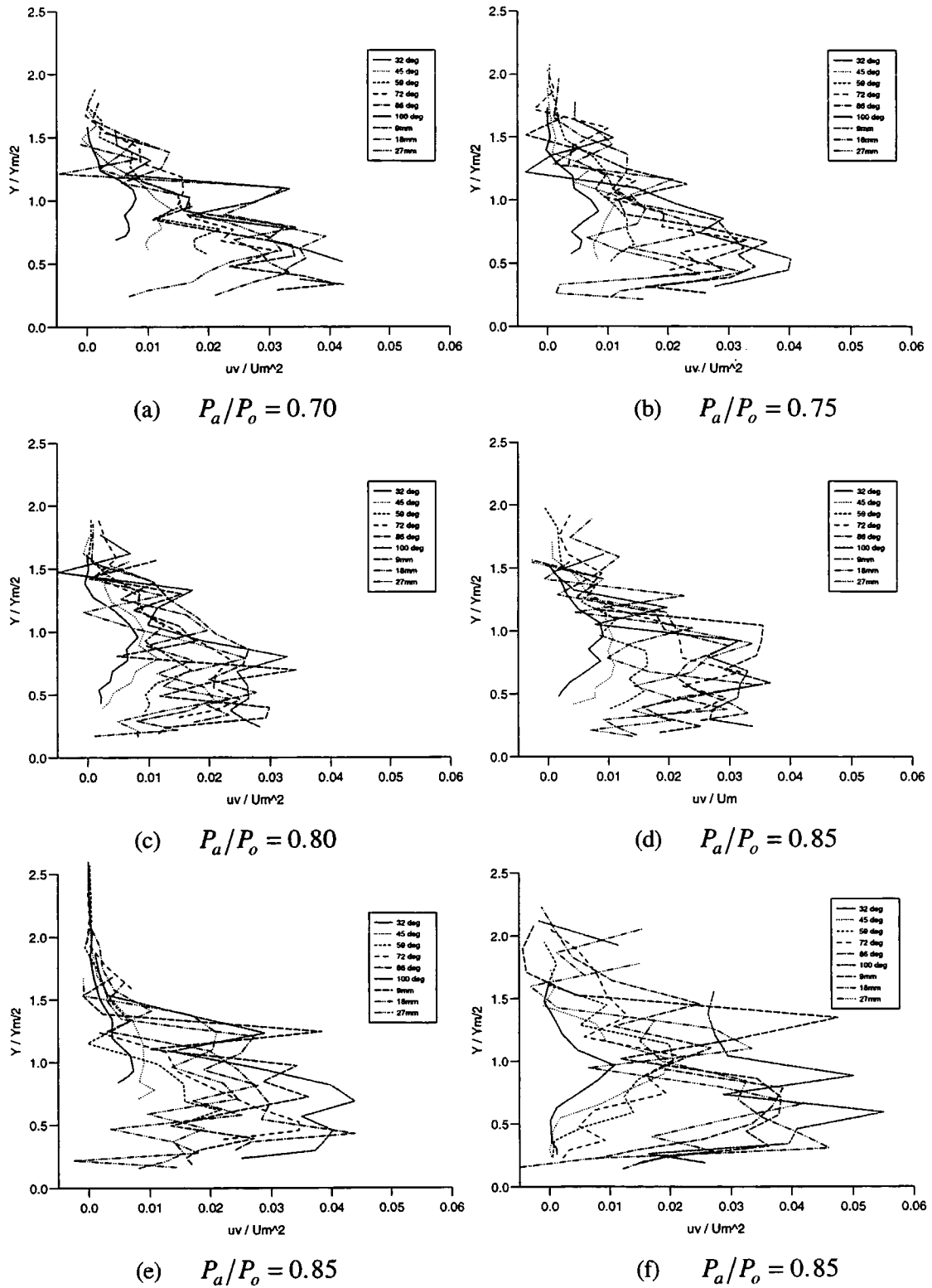


Figure 5.25 : $\overline{uv}/\overline{U}_m^2$ versus $y/y_{m/2}$; (a)-(d) $t = 4\text{mm}$; (e) $t = 2\text{mm}$; (f) $t = 8\text{mm}$

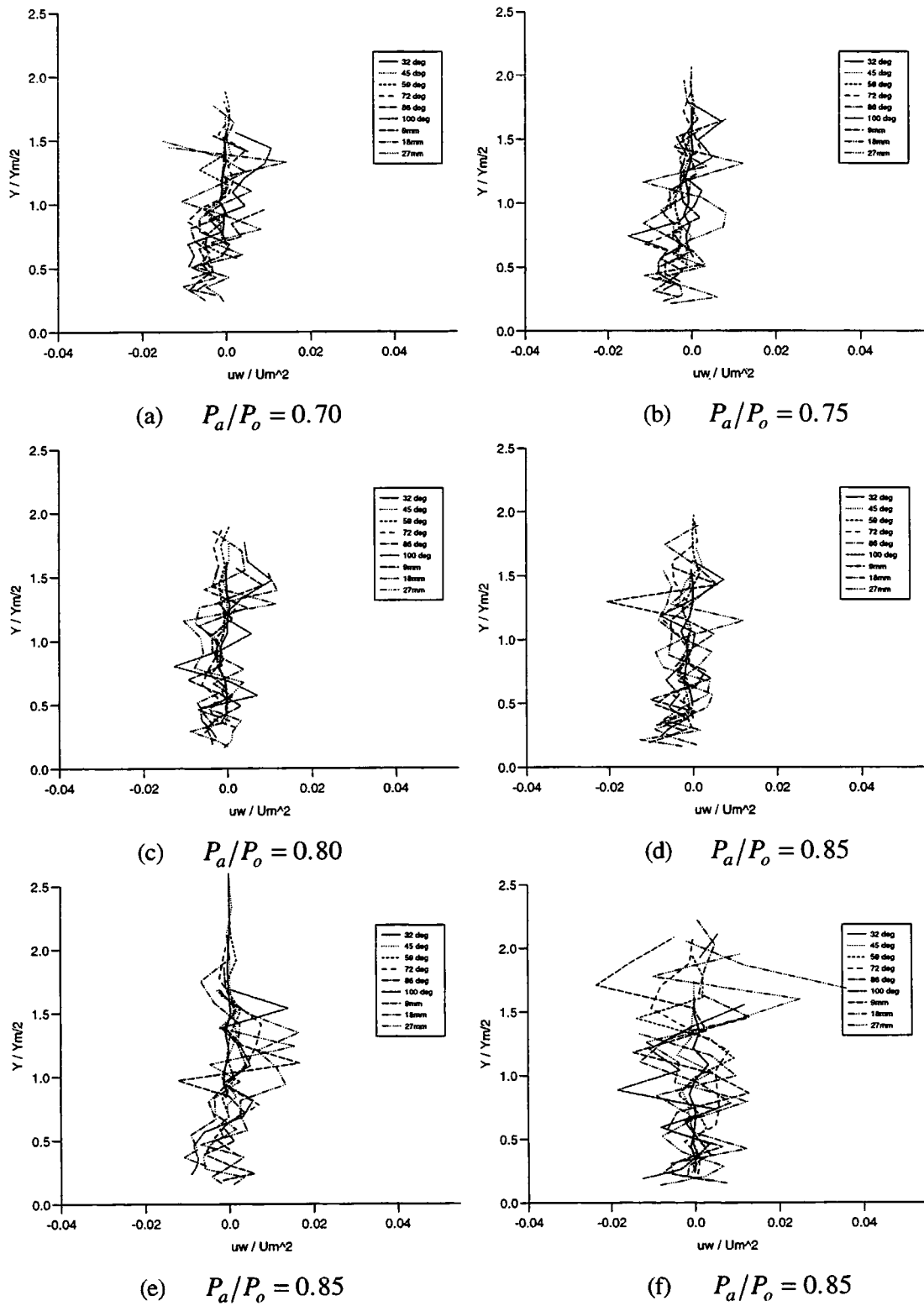


Figure 5.26 : $\overline{uw}/\overline{U}_m^2$ versus $y/y_{m/2}$; (a)-(d) $t = 4\text{mm}$; (e) $t = 2\text{mm}$; (f) $t = 8\text{mm}$

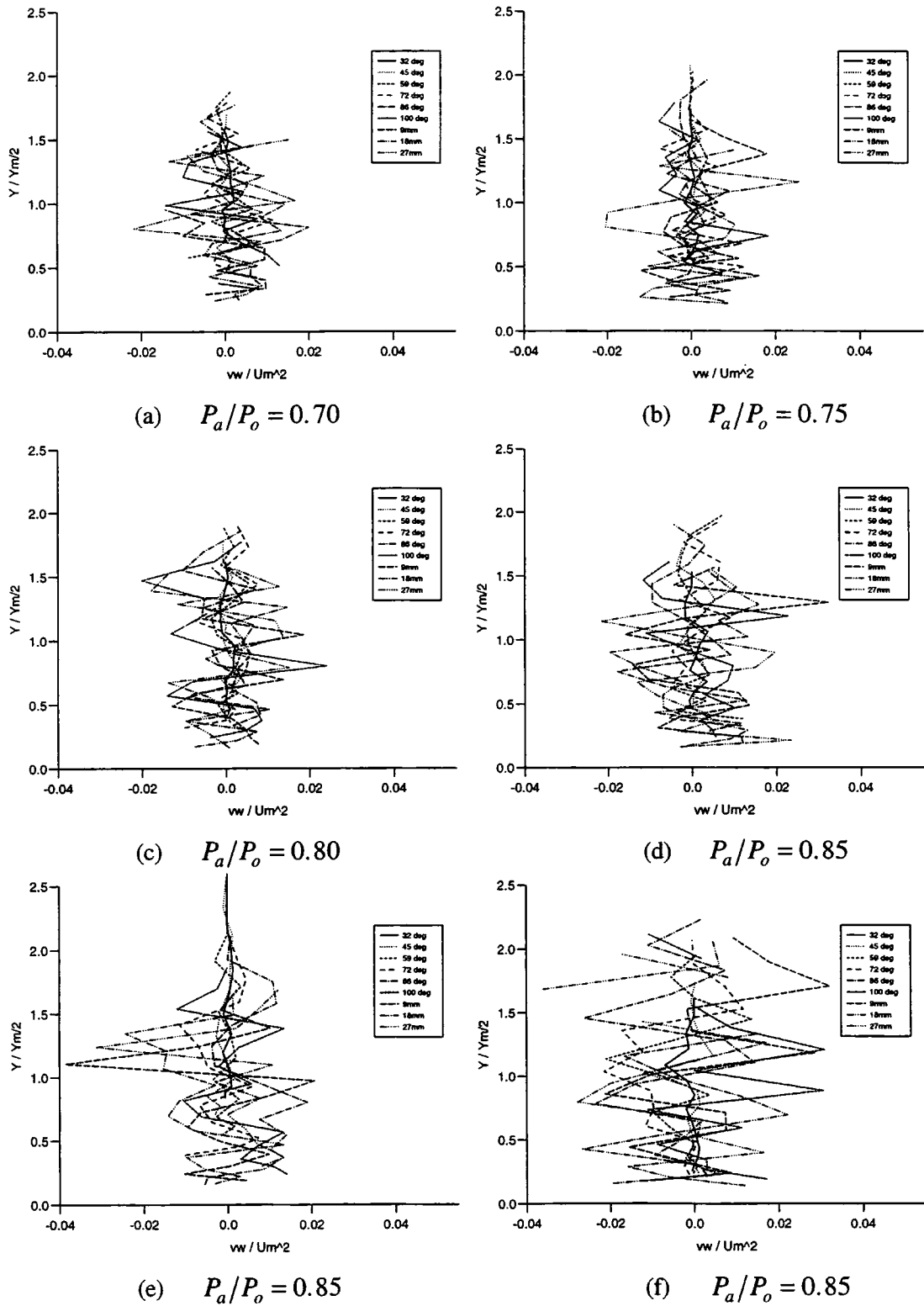


Figure 5.27 : $\overline{vw} / \overline{U}_m^2$ versus $y / y_{m/2}$; (a)-(d) $t = 4\text{mm}$; (e) $t = 2\text{mm}$; (f) $t = 8\text{mm}$

5.2.5 Kinetic energy and eddy viscosity

The kinetic energy has been calculated in two different ways, and in both methods it has been non-dimensionalised with respect to \bar{U}_m^2 . In figure 5.28, the kinetic energy has been calculated using all three of the normal stress components. Where the normal stresses have been calculated to be negative they have been set to equal zero. The scatter in the radial normal stress component is clearly evident in the resulting profiles. To eliminate this spurious data, the kinetic energy profiles have also been generated using only the streamwise and transverse components, and the results are shown in figure 5.29. The resulting profiles are far smoother and, as expected, follow the normal stress patterns (since the kinetic energy is the sum of these stresses). At the first traverse location the magnitude of the peak in kinetic energy increases with the size of the slot width. In all cases, the kinetic energy steadily increases on the curved portion of the Coanda flare, and this increase continues on the flat recovery section. The peak magnitude appears to stay more or less constant between 9mm and 18mm along the recovery section, only starting to decrease slightly at the final traverse location. These experimental results are compared against CFD predictions for the kinetic energy in chapter 7, section 7.4.4. The profiles shown in plots (a)-(d) for the constant slot width vary slightly, showing a slight decrease in kinetic energy as the pressure ratio falls. However, these variations may be due in part to experimental error, and also due to errors in the approximated values for the maximum velocity at each traverse location.

The non-dimensionalised turbulent eddy viscosity profiles are shown in figure 5.30. The eddy viscosity was calculated using the main Reynolds shear stress, and the velocity gradient normal to the surface was determined using the fitted velocity profiles. The eddy viscosity values are highest for the 8mm slot, then the 4mm slot, and least, as expected, for the 2mm slot.

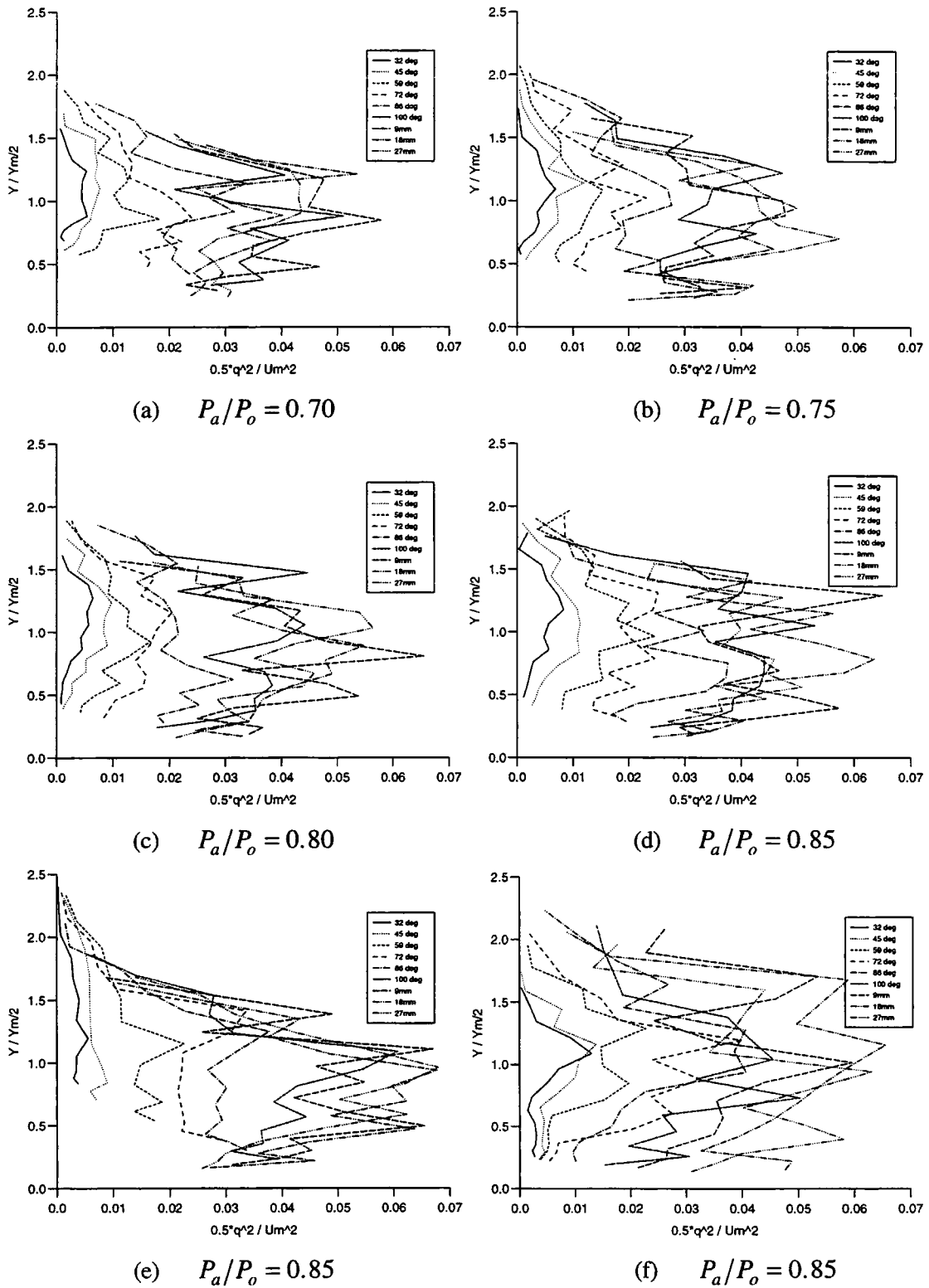


Figure 5.28 : $0.5q^2/\bar{U}_m^2$ vs. $y/y_{m/2}$; (a)-(d) $t = 4\text{mm}$; (e) $t = 2\text{mm}$; (f) $t = 8\text{mm}$

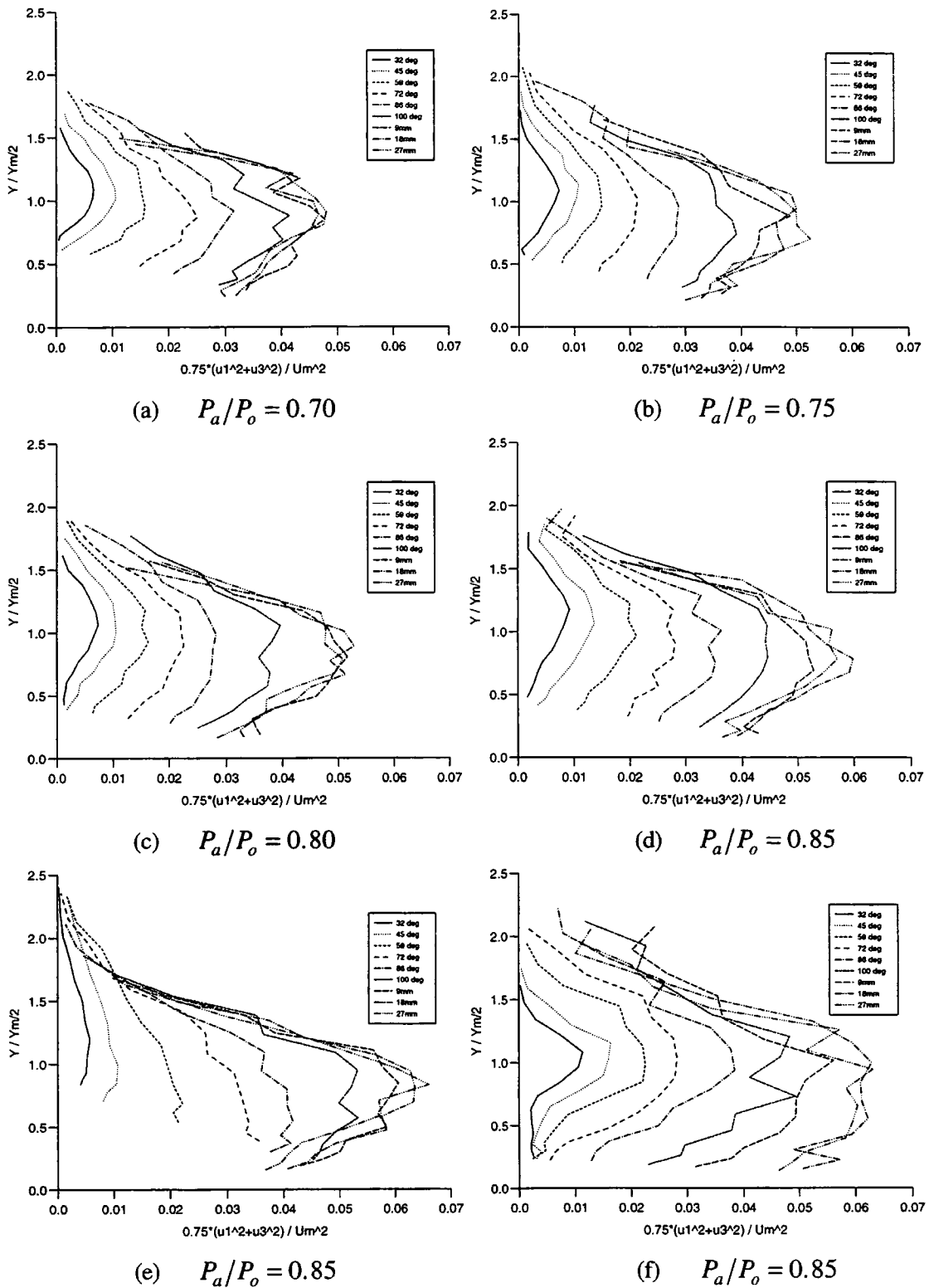


Figure 5.29 : $0.75(\overline{u^2} + \overline{w^2})/\overline{U_m^2}$ vs. $y/y_{m/2}$; (a)-(d) $t=4\text{mm}$; (e) 2mm ; (f) 8mm

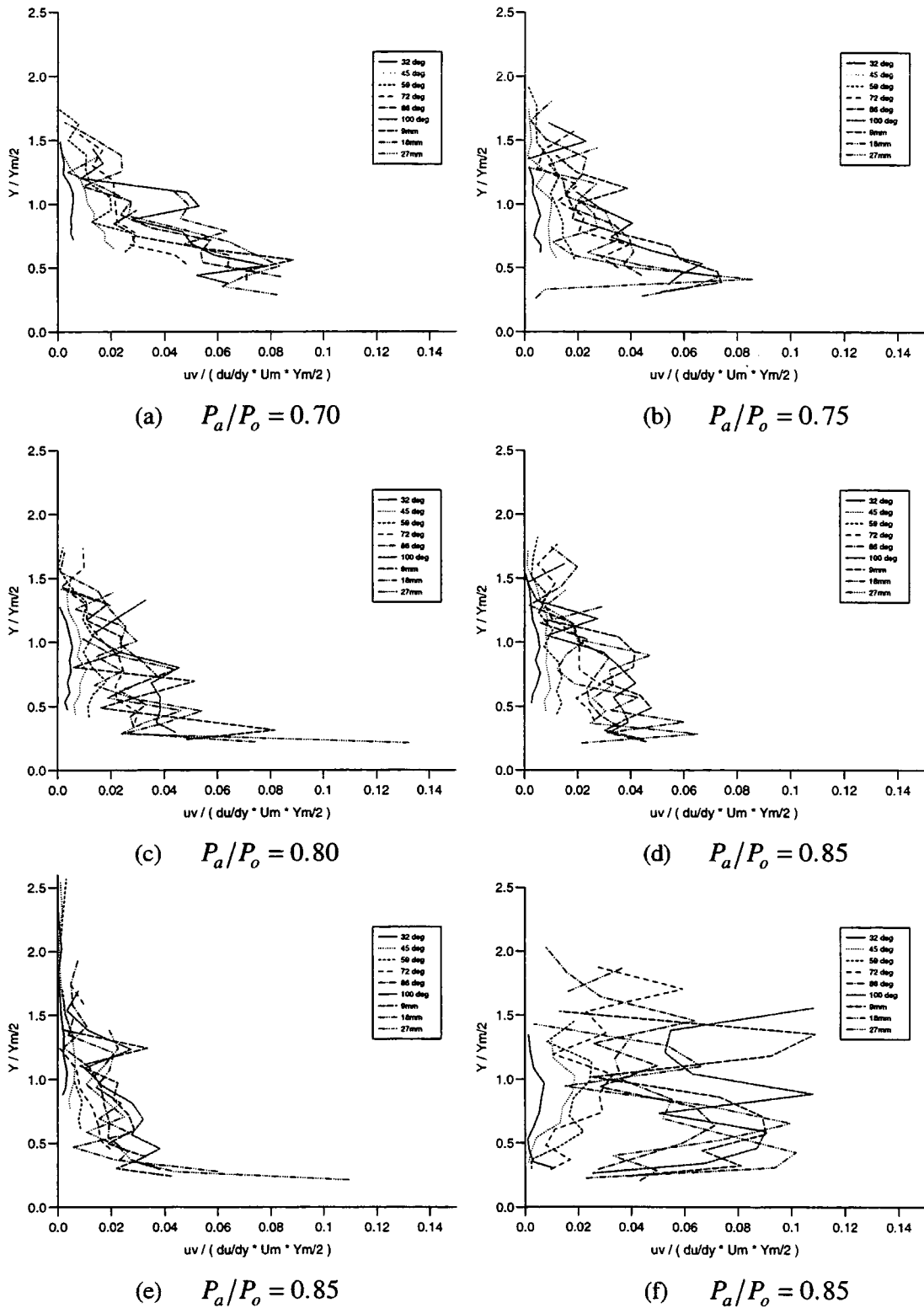


Figure 5.30 : Eddy viscosity versus $y/y_{m/2}$; (a)-(d) $t=4mm$; (e) $t=2mm$; (f) $t=8mm$

Chapter 6

Computational techniques

6.1 An introduction to Computational Fluid Dynamics

There are significant advantages to the engineer in using CFD. Wind tunnel tests do go some way to aiding the engineer and present a more economical approach than full scale testing. However, the use of CFD for design and development presents a faster, and in many cases, more cost-effective alternative to experimental methods. It is however very important that the results of any CFD modelling must be validated using experimental data.

An introduction to the equations which govern fluid flow has been given in chapter 2, along with brief descriptions of the levels of closure available for the solution of these equations. This chapter provides a description of the commercial CFD code used for the computational flow predictions presented in chapter 7 of this thesis. The various turbulence models available in this code are discussed, with specific reference to the models used for predicting the Coanda flow field.

6.2 The structure of the CFD code PHOENICS

The commercial CFD code used in this work is called PHOENICS. This code was designed by the programming firm Concentration, Heat And Momentum ltd. (CHAM). PHOENICS itself is an acronym for Parabolic, Hyperbolic Or Elliptic Numerical Integration Code Series. It is a general purpose code which is capable of simulating single and multi-phase flows, heat and mass transfer processes, and chemical reaction phenomena. The code has been written in ANSI FORTRAN 77 and has been installed on the UNIX system. Versions 2.0 and 2.1 have been used in the tests detailed in this thesis.

There are certain limitations associated with the use of PHOENICS, as with any other CFD code. Firstly, the accuracy of its simulations cannot exceed that of the assumptions on which its use is based. For example, the accuracy of a turbulent flow simulation

depends on the ability of the chosen turbulence model to give realistic approximations to the physical laws. Secondly, the accuracy of any simulation is dependent on the amount of computer time which has been spent. For example, if a coarse grid has been used to simulate a complex flow, the results will be poorer than those obtained from a fine grid, which would require far greater computational time. Finally, there is no guarantee that a converged solution may be obtained for every flow problem without the user making special settings of the solution control switches. This makes any results acquired using PHOENICS somewhat user dependent.

The structure of PHOENICS involves an initial pre-processor, a solver, and finally a post-processor. These are all described in turn in the following sub-sections.

6.2.1 Pre-processor

The pre-processor is known as SATELLITE. It is a data preparation program, enabling the user to define the flow problem. SATELLITE reads in a pre-existing 'quick input' file, known as a Q1 file, and uses this to create a data file which contains instructions which the solver routine, EARTH, can understand and obey. The information in the Q1 file may be modified by the user interactively using a menu, or directly by using the PHOENICS command language, PIL.

The geometry of the problem, i.e. the computational domain, and the grid within this domain must all be defined at this initial stage, along with the physical phenomena that need to be modelled. The fluid properties are also specified, along with all the necessary boundary conditions.

6.2.2 Solver

The solving routine is called EARTH, and this contains the main flow simulating software. This solver may be split into three numerical stages. The first of these involves the approximation of unknown flow variables using simple functions. The second step involves the formulation of finite volume equations (FVE's) (by the integration of the governing equations of fluid flow over all the finite control volumes of

the solution domain), and the final step involves the solution of the algebraic equations which are a result of the discretisation process.

The data file provided by SATELLITE is read in by EARTH and the corresponding computations are executed. EARTH then produces an output file called RESULT which may be examined by the user. A results data file is also produced, called a PHI file, which may be read in by the post-processors.

EARTH possesses FORTRAN subroutines which are accessible to the user. The MAIN program may be modified by the user to re-dimensionalise arrays. Other subroutines which may be user-modified include GROUND and GREX_n (i.e. GROUND example, number n). EARTH calls the subroutine GROUND at pre-set points of the solution cycle.

The main function of GROUND is to supply boundary conditions, sources, fluid properties and output control features that are not contained within EARTH. Coding sequences written by the user can be added to the appropriate points in the GROUND file, and EARTH absorbs these into the solution process. Special communication subroutines allow the user to extract information from EARTH, manipulate it in GROUND and then return new information or instructions to EARTH.

6.2.3 Post-processor

PHOTON is an interactive program which uses the PHI file written by EARTH and allows the user to view the grid, or flow patterns graphically on the screen. AUTOPLOT is another interactive graphics program which may be used to generate plots of any stored numerical data. The flexibility of these packages is somewhat limited, since data from other sources cannot be plotted alongside the CFD results. As a consequence of this, a data extraction program was written, in FORTRAN, enabling the extraction of all the relevant data from the PHI file. This data could then be written out in a form to be used in other graphics packages, namely UNIRAS, in order that comparisons could be made between the experimental and CFD results.

6.3 The mathematical basis of PHOENICS

A brief introduction to the mathematics of PHOENICS is given here. More details of the grid nomenclature, the equation structure, and the method used by PHOENICS to solve the flow equations is given in Appendix C.

PHOENICS uses a finite volume method to discretise the differential forms of the transport equations which, for single phase flow, have the typical form of equation (2.5), given in chapter 2. There are many equations to be solved for each dependent variable, Φ , and these equations are often strongly coupled. PHOENICS solves these in an iterative 'guess-and-correct' method, using an algorithm known as SIMPLEST. This is a derivative of the standard SIMPLE (Semi-Implicit Method for Pressure Linked Equations) pressure correction algorithm for finite volume calculations. Alternative CFD packages may use implicit or explicit time marching schemes instead of the pressure correction method. These marching schemes are generally better for high speed flows, since modifications to the standard pressure correction scheme are necessary to account for compressibility effects.

A solution is obtained if the residuals (which are an overall measure of the conservation of the flow variables) are very small. This is known as convergence. The stability of the solution is associated with the damping of errors as the numerical method proceeds. If the technique is unstable, round off errors in the initial data may cause oscillations or divergence of the solution. To check the grid dependency of a result, a series of grid refinements must be performed, starting with a course grid, until key features no longer change.

6.3.1 Pressure correction method

PHOENICS uses a pressure correction based method to solve the flow equations. An initial pressure field, P^* , is firstly assumed (or the pressure field from a previous time step is used). A velocity field, u^* , is then calculated explicitly from the momentum equations. The pressure correction equation, derived from the continuity equation, is solved to yield a pressure correction factor, ΔP , where the exact solution for P is equal to $P^* + \Delta P$. The velocity calculation is also adjusted using a velocity correction. This solution then repeats until a converged solution is obtained, or the required number of

iterations has been performed. To maintain the stability of the solution, relaxation factors are usually used to limit the changes made by the pressure and velocity correction factors at each iteration.

6.3.2 Interpolation schemes available in PHOENICS

There are various interpolation schemes available in PHOENICS for dealing with the convective terms in the momentum equations. The default is the one sided upwind difference scheme which is first order accurate, equating the velocity derivative to the reference point and its nearest neighbour in the upstream direction. This is the easiest scheme to obtain convergence with, however it can give very inaccurate solutions. Another scheme is the central difference scheme which is second order accurate, and requires the addition of artificial viscosity to stabilise the solution. The hybrid differencing scheme of Spalding (1972) is more accurate and based on a combination of the upwind and central differencing schemes, but will not always converge on all grids.

6.3.3 Solution techniques

FVE's are created for every variable, in every cell. These equations are then solved using one of the built in solvers. The iterative process is a complicated one, involving a multi-stage sequence of adjustments of values, repeated many times. The iterative process can involve slabwise, sweep, whole-field or parabolic solution.

Slabs are arrays of cells having the same Z co-ordinate. Many mathematical operations conducted by PHOENICS operate over a single slab, and many cycles of adjustment may be performed for one slab before moving on to the next. Such a technique is known as a 'slabwise solution'. To permit such a method, the Z axis usually lies in the main flow direction, so the solution proceeds in steps in the streamwise direction.

A sweep is a set of slabwise operations conducted in sequence from the lowest to highest Z slab. Many sweeps are needed before ideally all equations are in perfect balance and no further adjustments are necessary. The number of sweeps which must be made in order to achieve this balance may be decreased by the use of the 'whole field solution', which is usually only applied to the pressure field.

A 'parabolic solution' may be used in situations where higher slab values do not appear in the lower slab equations, although gradients in the solution variables may exist in the low-high direction. In such cases a single sweep through the integration domain is sufficient, thus providing great reductions in computer storage. Several slabwise iterations are most likely needed however to reduce the imbalances in the equations before moving on to the next slab.

6.4 Turbulence modelling

The aim of turbulence modelling is to develop sufficiently accurate and universal computational methods to predict the Reynolds stresses, and other unknown transport terms, to provide a closed set of equations which may then be solved for the fluid flow. Models based on the eddy viscosity hypothesis encompass zero, one and two equation models. The most commonly used and validated of these are the two equation $k-\epsilon$ turbulence model, and the zero equation mixing length model. Both are based on the assumption that an analogy exists between the action of viscous stresses and Reynolds stresses on the mean flow. A brief description of eddy viscosity models, Reynolds stress models and algebraic models was given in chapter 2. The latter two model types are discussed no further, since the aim of this chapter is to describe the turbulence models used in chapter 7 for modelling the Coanda flow.

Zero equation models

Boussinesq (1977) suggested that the Reynolds shear stresses, which appear in the Reynolds averaged Navier Stokes equations, may be replaced by the product of the mean velocity gradient and a quantity called the 'turbulent viscosity', as given by equation (6.1). This is not in fact valid in all situations, as discussed in chapter 2, but in many cases it can give a good approximation.

$$-\overline{\rho uv} = \mu_t \frac{\partial u}{\partial y} \quad (6.1)$$

The turbulent viscosity, μ_t , is not a property of the fluid, but is determined by the local state of the turbulence and varies throughout the flow. To complete the turbulence model, this viscosity must be expressed in terms of known or calculable quantities. This has been accomplished in numerous ways, a few of which are mentioned here. From dimensional analysis, the turbulent viscosity is proportional to the product of a length scale and a velocity scale.

The earliest method of determining μ_t was Prandtl's mixing length hypothesis, which gives the turbulent viscosity to equal the local product of the density, the magnitude of the mean rate of strain, and the square of a characteristic length scale of the turbulent motion. The resulting expression is given in equation (6.2)

$$\mu_t = \rho l_o^2 \left| \frac{\partial u}{\partial y} \right| \quad (6.2)$$

In this model, the length scale is provided by a mixing length, l_o , and the velocity scale by the term $l_o |\partial u / \partial y|$. The mixing length, l_o , is a user-prescribed parameter and calculations by Patankar and Spalding (1967) made use of a ramp function for its determination. This ramp function is given by equations (6.3)

$$\begin{aligned} l_o &= \kappa y & y < \lambda y_e / \kappa \\ l_o &= \lambda y_e & \lambda y_e / \kappa \leq y < y_e \end{aligned} \quad (6.3)$$

where y_e is the location of the 'edge' of the shear layer, and the two constants have the values $\kappa = 0.435$ and $\lambda = 0.09$. This ramp function was successful in predicting conventional turbulent boundary layers. Patankar and Spalding also found that this ramp function predicted the spreading rate of a plane wall jet in still air successfully. This surprising result has been attributed to be due to the linear drop off in the mixing length near the wall which effectively imitates the damping of the normal velocity fluctuations, reducing the shear stress by the correct amount. Radial wall jets however have been found to require very different ramp functions in order to give reasonable predictions. In their review on turbulent wall jets, Launder and Rodi (1983) describe the efforts of Rastogi (1972) to apply the ramp function to curved wall jets, and his findings that the

effects of secondary strain associated with curvature had to be empirically increased by an order of magnitude in order to obtain reasonable agreement with experiments.

The mixing length hypothesis is the most widely used of the zero equation models. As with other models of its type, it is a simple model which requires the solution of no additional differential equations, and providing good mixing length distributions are chosen, predictions of velocity and shear stress distributions of boundary layer flows are good. However, it cannot deal with recirculating flows since the relations between the stresses and the velocity gradients are too complicated. It also ignores the processes of convection and the diffusion of turbulence. From equation (6.2) it can be seen that the model implies, wrongly for a wall jet, that the effective viscosity vanishes when the velocity gradient falls to zero.

Attempts have been made by many workers to take account of the effects of streamline curvature, which are invariably underestimated by all the basic eddy viscosity models. Prandtl tried to take account of the effects of concave and convex curvature in his mixing length model by introducing the curvature parameter given in equation (6.4).

$$l = l_o \left[1 - \frac{1}{4} \frac{U/R}{\partial U / \partial n} \right] \quad (6.4)$$

However, experimental results showed that the mixing lengths in convex boundary layers were far lower than those predicted using this equation.

The combined viscous and turbulent shear stress for a curved thin shear layer, may be written in curvilinear co-ordinates as follows, assuming $V \ll U$

$$\tau = \underbrace{\mu \left(\frac{\partial U}{\partial n} - \frac{U}{R+n} \right)}_{\text{viscous stress}} - \underbrace{\overline{\rho uv}}_{\text{Reynolds stress}} \quad (6.5)$$

The curvature effects appear explicitly in the laminar shear stress term, whereas the turbulent Reynolds stress retains its plane flow form. Sawyer (1963) used Prandtl's

mixing length hypothesis to derive the following expression for the turbulent shear stress in curved flow.

$$-\overline{uv} = l_o^2 \left| \frac{\partial U}{\partial n} \right| \left(\frac{\partial U}{\partial n} - C \frac{U}{(R+n)} \right) \quad (6.6)$$

where C is an empirical constant, and l_o is the mixing length in uncurved flow. Sawyer found the constant C varied from 5 to 9 for curved free jets. The fact that C was not found to equal 1 illustrates the fact a direct analogy between turbulent shear and viscous shear is not appropriate. Secondly, the variation in the value of C required to optimise agreement between predictions and experiments highlights the lack of generality when using a mixing length modification.

Bradshaw (1969) pointed out an analogy between curvature and buoyancy effects, proposing that the Monin-Oboukhov formula (equation (6.7)) for the correlation of the apparent mixing length with small buoyancy effects could be used to model the effects of weak curvature.

$$\frac{l_c}{l_o} = 1 - \beta \text{Ri}_b \quad (6.7)$$

where l_c denotes the corrected mixing length, β is a positive empirical constant, and Ri_b is the 'curvature Richardson number', defined in equation (6.8).

$$\text{Ri}_b = \frac{2U/R}{\partial U/\partial n + U/R} \quad (6.8)$$

This modification has only met with limited success since the mixing length hypothesis is so simple that different mixing length distributions are generally needed for each new geometry under consideration.

Morrison and Gregory-Smith (1984) attempted to model the extra rates of strain associated with longitudinal curvature and divergence using a modifying mixing length model, assuming that the effects of longitudinal curvature and divergence are additive.

The correction to the mixing length formula for longitudinal curvature, l_c , is given below:

$$\left(\frac{l_c}{l_o}\right) = (1 - \alpha_1 Ri - \alpha_2 Ri^2)^{3/2} \cdot (1 - K)^2 \quad (6.9)$$

where the Richardson number is defined by

$$Ri = 2K \frac{1+K}{(1-K)^2}, \quad K = \frac{U/Rh}{\partial U/\partial n} \quad \text{and} \quad h = (1+n/R)$$

which for small curvature reduces to the Richardson number, Ri_b , defined by Bradshaw. The geometric radius of curvature of a streamline is given by Rh , and the values taken by the constants α_1 and α_2 were 3.26 and 3.09 respectively. These constants are not truly universal, but these values were found by Morrison to give satisfactory results.

The equation used to correct the mixing length for divergence effects in the flow is given in equation (6.10)

$$\frac{l_d}{l_o} = 1 - \frac{\sigma(U \sin \varpi + V \cos \varpi)}{R_a \partial U/\partial n} \quad (6.10)$$

where $(U \sin \varpi + V \cos \varpi)$ is the radial outflow velocity component, ϖ is the angle between the tangent and the axis of symmetry (defined in figure 7.2), and R_a is the axisymmetric radius. The empirical constant, σ , was given a value of 9.0. The total corrected mixing length was calculated using equation (6.11), which assumes the effects of curvature and divergence are additive.

$$\frac{l_t}{l_o} = \frac{l_c}{l_o} + \frac{l_d}{l_o} - 1 \quad (6.11)$$

The uncorrected mixing length, l_o , was calculated by separating the jet into inner and outer mixing regions, and using the values of $\kappa = 0.41$ and $\lambda = 0.09$ in equation (6.3). The value for the mixing length in the maximum velocity region was calculated by interpolating the value between the inner and outer regions.

Morrison and Gregory-Smith compared results obtained using this model against seven experimental test cases. The model was found to give good predictions for jet growth and velocity decay rates, but predictions of other flow properties, such as turbulent shear stress, were not so successful due to the simplicity of the model. Gregory-Smith and Hawkins (1989) incorporated this mixing length modification into the PHOENICS solver code. Experimental results obtained for low speed flow over an axisymmetric Coanda flare were compared against these CFD results and reasonable agreement was found. The findings of these tests are considered in more detail in chapter 7.

One equation models

These models involve the solution of one partial differential equation describing the transport of a turbulent quantity. Prandtl (1945) was the first to suggest the solution of a differential equation for the transport of turbulent kinetic energy, which is defined in equation (6.12).

$$k = \frac{1}{2}(\overline{u^2} + \overline{v^2} + \overline{w^2}) \quad (6.12)$$

The transport equation is used to determine the kinetic energy, and then the Prandtl-Kolmogorov relationship, equation (6.13), may be used to calculate the turbulent viscosity.

$$\nu_t = C_\mu k^{1/2} l \quad (6.13)$$

where C_μ is a constant. In this model the velocity scale for the eddy viscosity is provided by \sqrt{k} , and the length scale is provided by l , which is flow dependent and must be determined algebraically. Bradshaw *et al* (1967) adopted a different approach from Prandtl. He also used the turbulent energy equation, but did not use the eddy viscosity concept to calculate the velocity correlations. He assumed the kinematic shear stress to be directly proportional to the turbulent kinetic energy, thus allowing the Reynolds stresses to be determined directly from k . This approach has been used extensively for thin shear layers.

The greatest disadvantage of one equation models is the need to prescribe the turbulent length scale, which results in poor results except in fairly simple wall boundary layers. It is therefore necessary to determine k and l from transport equations, and for the most part, one equation models have been abandoned in favour of higher equation models.

Two equation models

These models involve the solution of two partial differential equations and are more commonly used. These models solve one transport equation for the turbulent kinetic energy, k , (and hence use \sqrt{k} as the velocity scale) and another for the length scale, l , or some other turbulence quantity from which l can be determined.

Several models have been developed, the most well known of which is the $k - \epsilon$ model. Various versions of this model have been developed, by for example, Jones & Launder (1972), Launder and Spalding (1974). All these involve the solution of the dissipation rate transport equation along with the turbulence energy transport equation. The model is based on the relationship proposed by Harlow & Nakayama (1968), given in equation (6.14).

$$\epsilon = \frac{k^{3/2}}{l} \quad , \quad \text{i.e. length scale, } l = \frac{k^{3/2}}{\epsilon} \quad (6.14)$$

The turbulent viscosity may then be expressed in terms of k and ϵ by substituting equation (6.14) into equation (6.13) to give :

$$\nu_t = C_\mu \frac{k^2}{\epsilon} \quad (6.15)$$

In addition to the standard high Reynolds number form of the model, presented by Launder and Spalding (1974), there is the low Reynolds number extension of Lam-Bremhorst, the two scale split-spectrum extension, the Chen-Kim modification, the RNG derived model, along with many other forms. The two equation models used in this research work are described in the sub-sections 6.4.1-6.4.4.

However, before considering the various versions of the model, the fundamental assumptions on which two equation eddy viscosity models are based will be summarised, in order to highlight the advantages and drawbacks of such models. The basic assumptions are :

- turbulent stresses are directly proportional to the mean rate of strain, and the eddy viscosity is considered isotropic
- the eddy viscosity is expressed in terms of two parameters, which define velocity and length scales representative of the large scale turbulence, e.g. velocity scale = $k^{1/2}$, and the length scale = $k^{3/2}/\epsilon$
- the two parameters are obtained from modelled differential transport equations which take account of the history, time and spatial awareness of the local turbulence state

An over simplification of the basic models is that the turbulent stresses are assumed to be directly proportional to the mean strain. The assumption that eddy viscosity is a scalar (isotropic) property means that the models are insensitive to the orientation of the turbulence structure and its transporting and mixing mechanisms. The models are unable to reproduce the eddy viscosity anisotropy. Also, the models are generally limited to only one time or length scale for characterising all turbulence interactions.

These models do have the advantage that they are relatively simple and easy to use. Hanjalic (1994) compares the performance of two equation eddy viscosity models, second order Reynolds stress models, and intermediate 'hybrid' models such as the algebraic stress model. He concludes that the two equation models are still most widely used since they require less computational effort than the Reynolds stress models. He points out that second moment closure models are likely to be used more in the future as knowledge of the physics of the higher order correlations grows, and the degree of uncertainty in their modelling is reduced.

6.4.1 Standard k-ε model

The high Reynolds number version of the $k-\epsilon$ model, presented by Launder and Spalding (1974), is the standard form of the $k-\epsilon$ model used in this research. The transport equations for the turbulent kinetic energy and the dissipation rate of turbulent energy are given in equations (6.16) and (6.17) respectively.

$$\frac{\partial k}{\partial t} + \frac{\partial}{\partial x_j} \left[U_j k - \frac{\nu_t}{\sigma_k} \frac{\partial k}{\partial x_j} \right] = P_k - \epsilon \quad (6.16)$$

$$\frac{\partial \epsilon}{\partial t} + \frac{\partial}{\partial x_j} \left[U_j \epsilon - \frac{\nu_t}{\sigma_\epsilon} \frac{\partial \epsilon}{\partial x_j} \right] = \frac{\epsilon}{k} (C_1 P_k - C_2 \epsilon) \quad (6.17)$$

where P_k is the volumetric production rate of turbulent kinetic energy by the shear forces, and

$$P_k = -\overline{u_i u_j} \frac{\partial U_i}{\partial x_j} \quad (6.18)$$

The empirical constants used above have the following values :

$$C_\mu = 0.09 \quad C_1 = 1.44 \quad C_2 = 1.92 \quad \sigma_k = 1.0 \quad \sigma_\epsilon = 1.314$$

The terms containing σ_k and σ_ϵ in equations (6.16) and (6.17) represent the diffusion rates of k and ϵ respectively. Local values of k and ϵ are determined using the transport equations given above, then a local (turbulent) eddy viscosity may be calculated using equation (6.15). An extended form of the Boussinesq relationship is used to calculate the Reynolds stresses used in the $k-\epsilon$ model, given below in equation (6.19).

$$-\overline{\rho u_i u_j} = \mu_t \left(\frac{\partial U_i}{\partial x_j} + \frac{\partial U_j}{\partial x_i} \right) - \frac{2}{3} \rho k \delta_{ij} \quad (6.19)$$

The extra term on the right hand side involves the Kronecker delta, δ_{ij} , which equals 1 if $i = j$ and equals 0 if $i \neq j$, hence making the term only applicable for the normal stresses.

The equations associated with the transport of k and ε in the $k-\varepsilon$ model are elliptic, and as such require the following boundary conditions to be specified :

- Inlet - k and ε distributions must be specified
- Outlet, or at axis of symmetry - $\partial k/\partial n = 0$ and $\partial \varepsilon/\partial n = 0$
- Solid walls - treatment depends on Reynolds number

Rough approximations for the values of k and ε at inlet can be obtained from turbulence intensity, T_i , a reference velocity, U_r , and a characteristic length scale, L using the following equations (Versteeg and Malalasekera (1995)) :

$$k = \frac{3}{2}(U_r T_i)^2 \quad \varepsilon = C_\mu^{3/4} \frac{k^{3/2}}{l} \quad l = 0.07L \quad (6.20)$$

The log-law may be applied for the boundary conditions at solid surfaces, providing a non-dimensional distance parameter which is grid dependent, known as y^+ , lies within certain limits. This is discussed in greater depth in section 6.5. Under certain conditions the log-law is invalid, and in such flows the $k-\varepsilon$ model needs modifying. Wall damping must be applied to ensure that viscous stresses dominate over the turbulent Reynolds stresses in the viscous sublayer near walls.

6.4.2 Chen Kim modification to the $k-\varepsilon$ model

The standard $k-\varepsilon$ model uses a single time scale, k/ε , to characterise the various dynamic processes occurring in turbulent flows. As a result, the generation, dissipation and transport terms contained in the closed set of model equations all proceed at rates proportional to ε/k . In reality however, turbulence comprises of fluctuating motions with a whole range of time scales, so this single time scale approach is likely to be inadequate in many flow situations.

To try to overcome this deficiency in the standard model, Chen and Kim (1987) proposed a modification which aimed to improve the dynamic response of the dissipation equation by introducing an additional time scale, k/P_k . They also modified some of the

standard model coefficients so that the model gave good agreement with experimental data on classical turbulent shear layers.

The modification they proposed involves splitting the production term for the dissipation equation into two parts. The first is the same as in the standard model, but with a smaller multiplying coefficient. The second part allows the 'turbulence distortion' ratio, P_k/ϵ , to influence the production rate of ϵ . This extra term represents the energy transfer rate from large to small scale turbulence controlled by the production-range time and the dissipation-range time scales.

The overall effect of this modification is to increase the dissipation rate (and hence reduce the kinetic energy) when the mean strain is strong, i.e. $P_k/\epsilon > 1$, and to decrease the dissipation rate when the mean strain is weak i.e. $P_k/\epsilon < 1$. This model is expected to give better results than the standard model when the turbulence is not at local equilibrium, for example in flows with separation. The modified model constants are :

$$C_\mu = 0.09 \quad C_1 = 1.15 \quad C_2 = 1.9 \quad \sigma_k = 0.75 \quad \sigma_\epsilon = 1.15$$

and the extra time scale is introduced into the dissipation equation by the addition of the extra source term $0.25 F_1 P_k^2 / k$, where F_1 is the Lam-Bremhorst (1981) damping function.

6.4.3 RNG formulation of the k- ϵ model

Yakhot & Orszag (1986) derived a $k-\epsilon$ model based on ReNormalization Group (RNG) methods. RNG techniques were used to develop a theory for the large scales, in which the small scale effects are represented by modified transport coefficients. The RNG procedure used by Yakhot & Orszag resulted in a set of equations which have no undetermined constants, and built in corrections which allow the model to be used in high and low Reynolds number flows.

At high turbulence Reynolds numbers, this model is of the same form as the standard $k-\epsilon$ model, except that the model constants are calculated explicitly from the RNG analysis, having the following modified values :

$$C_{\mu} = 0.0845 \quad C_1 = 1.42 \quad C_2 = 1.68 \quad \sigma_k = 0.7194 \quad \sigma_{\epsilon} = 0.7194$$

In 1992, Yakhot and Smith reformulated the derivation of the dissipation equation, re-evaluating the constant C_1 which controls the production of ϵ , and adding an extra production term to the equation which becomes significant in rapidly distorted flows.

RNG methods were unable to close this additional term. However, Yakhot *et al* (1992) developed a model for the closure of this term, and this high Reynolds number form of the RNG $k - \epsilon$ model is reported to give improved predictions for separated flows. Use of the model for plane and free jets however has been found to give poorer results.

6.4.4 Hanjalic Launder modification to the $k - \epsilon$ model

When the describing set of transport equations is transformed to a curvilinear co-ordinate system, the $k - \epsilon$ model greatly under-predicts the sensitivity of the wall jet to streamline curvature (Launder & Rodi (1981)). This is a fundamental fault of all models employing the Boussinesq stress-strain relationship. In simple models such as the mixing length model, it has been shown that curvature may be accounted for by making the local length scale depend on the local mean flow Richardson number. This basic assumption cannot be made in the two equation models since the length scale is not simply prescribed, but calculated using a transport equation. However, the coefficients of one or more of the source terms in the transport equations may be made dependent on a Richardson number. Launder, Pridden & Sharma (1977) adopted just such a modification to the $k - \epsilon$ model to account for curvature, making the destruction term in the dissipation equation a function of the turbulent Richardson number.

Hanjalic and Launder (as quoted by Hanjalic (1982)) also proposed a modification to the $k - \epsilon$ model aimed at improving the model's sensitivity to curvature. Their model has a similar effect on the dissipation term as the Launder-Pridden-Sharmer model (1977). The Hanjalic-Launder model has the added advantage that it is tensor invariant. The sensitivity to curvature of this model is achieved by assuming the extra rates of strain associated with the curvature do not add to the generation of ϵ .

The volumetric production term in the differential equation for the dissipation parameter, P_ε is defined as follows for the standard $k - \varepsilon$ model :

$$P_\varepsilon = \frac{\varepsilon}{k} C_1 v_t \left(\frac{\partial U_i}{\partial x_j} + \frac{\partial U_j}{\partial x_i} \right) \frac{\partial U_i}{\partial x_j} \quad (6.21)$$

By contrast, the volumetric production term in the differential equation for the dissipation parameter is defined as follows for the Hanjalic-Launder model :

$$P_\varepsilon = \frac{\varepsilon}{k} C_1 v_t \left(\frac{\partial U_i}{\partial x_j} \right)^2 \quad (6.22)$$

6.5 Wall functions

There are two physical effects on turbulence to consider in very near-wall flows. The first is the influence of low Reynolds number, which is due to the predominance of molecular viscosity very near to the wall. The second is the effect of wall proximity which results in the damping the velocity fluctuations in the direction normal to the wall. Both phenomenon are very different in nature, but are frequently modelled together since both ultimately result in turbulence damping.

For wall flows, the $k - \varepsilon$ model is usually used in conjunction with wall functions which effectively bridge the gap across the viscous sublayer by using empirical formulae. They therefore provide near-wall boundary conditions for the mean flow and turbulence transport equations. These formulae effectively connect the wall conditions, such as the wall shear stress, to the dependent variables in the grid node nearest the wall, which is presumed to be outside the viscous sublayer in fully turbulent flow. The obvious advantage of using wall functions is that computations do not have to be extended right to the wall, and hence avoid the need to account for viscous effects in turbulence models.

The alternative, integrating right up to the wall, generally involves the introduction of damping functions in terms of turbulence Reynolds number and wall distance, and accordingly, these two effects are then accounted for in the modelled transport

equations. A review by Patel *et al* (1985) concludes that two equation models generally use functions that are dependent purely on viscosity, and do not distinguish between the separate effects of viscosity and wall proximity. Modelling these effects in a combined manner results in poorer flow predictions in cases where the two effects have different relative magnitudes from simple wall flows.

The model of Lam and Bremhorst (1981) takes account of the Reynolds number effects, and the effects of wall proximity. Nagano and Hishida (1987) also proposed a modification to the standard model which accounts for the two factors. Fan and Lakshminarayana (1993) proposed a low Reynolds number modification to the $k-\epsilon$ model for unsteady turbulent boundary layer flows.

The CFD predictions reported in this thesis using PHOENICS have all used the more computationally economical wall functions rather than the low Reynolds number forms of the $k-\epsilon$ models. There are two types of wall function available in PHOENICS, and these are described below.

Equilibrium log law wall function

The turbulent boundary layer adjacent to a solid wall consists of two regions - an inner and an outer region. The inner layer may be further sub-divided into three regions: a sub-layer in which viscous stresses dominate the flow adjacent to the surface; a buffer layer in which turbulent and viscous stresses are of comparable magnitude, and a region in which the Reynolds stresses dominate. The outer region is dominated by the core flow and is free from direct viscous effects.

Outside the viscous sub-layer, yet still in the inner region, a functional relationship exists between the dimensionless groups u^+ and y^+ for $30 < y^+ < 500$. The wall functions in this region are given as follows :

$$u^+ = \frac{1}{\kappa} \ln(Ey^+) \quad (6.23)$$

where $u^+ = \frac{U}{u_\tau} = f\left(\frac{\rho u_\tau y}{\mu}\right) = f(y^+)$, and $y^+ = \frac{y u_\tau}{\nu_l}$

$$\text{and} \quad k = \frac{u_\tau^2}{\sqrt{C_\mu}} \quad \varepsilon = \frac{u_\tau^3}{\kappa y} \quad (6.24)$$

- y - normal distance of first grid point from the wall
 y^+ - dimensionless wall distance

For smooth walls, the wall roughness parameter, E , is equal to 9.8, and values of this parameter for rough walls are given by Schlichting (1979).

This law assumes that the turbulent kinetic energy is in local equilibrium, so it is not really suitable under separated conditions since the turbulent energy diffusion towards the wall is significant, leading to significant departure from local equilibrium. The non-equilibrium log law function was therefore used when modelling the breakaway performance of the Coanda flare.

Non-equilibrium log law wall function

Launder and Spalding (1974) proposed a modification to the equilibrium log law wall function which uses the square root of turbulent kinetic energy instead of the friction velocity as the characteristic velocity scale. Under equilibrium conditions the equation reduces to the conventional law of the wall. This modified wall function is defined below

$$\frac{U\sqrt{k}}{u_\tau^2} = \frac{\ln(C_\mu^{0.25} E\sqrt{k} y/v_l)}{C_\mu^{0.25} \kappa} \quad (6.36)$$

6.6 Shock waves and predicting transonic flows

Flows involving shock waves involve sharp, discontinuous changes in flow variables such as P, ρ, U and T across the shocks. A shock wave cannot physically exist without viscosity, since it is the viscous stress which irreversibly dissipates energy, resulting in the entropy increase across the shock. Despite this, an analytical solution for flows involving shock waves may be obtained by using the *inviscid* Euler equations. If a control volume is considered across a shock wave, the conservation equations are only affected by the flow variables at the boundaries of the volume. Viscous effects are only dominant immediately adjacent to the shock, and are negligible far from the shock, hence the conservation equations for mass, momentum and energy do not require details of the viscous flow within the shock.

There are two common approaches to solving flows containing shock waves, either using shock capturing methods, or shock fitting methods. The first method involves no special treatment for the shock waves, which appear naturally in the solution as a direct result of the general algorithm. The shock waves are therefore 'captured' in the domain by the computational solution of the governing partial differential equations. By contrast, the second shock fitting method involves directly introducing the shock wave into the solution as an explicit discontinuity, and the Rankine-Hugoniot (oblique shock) relations are used to relate the flow immediately ahead of and behind the shock.

The shock capturing method is ideal for complex flows in which the exact location or number of the shock waves is unknown. No special treatment is made for the presence of the shock waves, so it is more computationally economical than the shock fitting technique. The shocks are numerically captured by the addition of artificial viscosity, and the larger this is, the thicker the shock. As a result, the shock is generally not sharply defined, but spread over several grid cells in the computational mesh, so its precise thickness and location are uncertain to within a few mesh points. By contrast, the shock fitting method means the shock location is well defined numerically, but this technique requires prior knowledge of the location and number of shocks present in the flow.

In the past, problems involving only supersonic flow (i.e. only hyperbolic governing equations) were solved using the method of characteristics, which is a shock fitting technique. Gregory-Smith and Gilchrist (1987) used this method to predict the inviscid jet core of the Coanda wall jet with reasonable success. The outer shear layer and the surface boundary layer were ignored in the calculation procedure. Good predictions for the first shock cell were obtained at low blowing pressures. Ignoring the surface boundary layer meant its influence on the flow was also omitted from the calculation and this led to poorer results as the blowing pressure was increased. They managed to improve the predictions for the first one or two shock cells by using experimental surface pressures for the wall condition.

When computing flows involving shocks, the equations are best expressed in conservation form, and discretised in such a way to maintain the conservation form. For steady inviscid flow, the physical character of the flow is elliptic in the subsonic region and hyperbolic in the supersonic region.

Time marching schemes

Explicit schemes are generally used for solving the Euler equations where strong shocks are involved, or the flow is supersonic throughout. For steady flow, the solution can be obtained in one complete sweep. Typically, explicit schemes require a large number of iterations (time steps) to reach convergence due to the limitations placed on the size of the time step to maintain stability. The stability of these schemes is governed by the Courant-Friedrich-Lewy (CFL) number, which must be less than unity. The limiting condition is $(|u| + a) \Delta t / \Delta x \leq 1.0$, where a is the local speed of sound.

Implicit schemes permit much larger time steps, and as a result reach a steady state solution in fewer iterations. A von Neumann (linear) stability analysis indicates whether a solution algorithm is stable. If spatial operators are represented by central differencing then artificial viscosity is generally added. Upwind differencing or the introduction of artificial viscosity in the supersonic region of transonic flow prevents the formation of expansion shocks.

Pressure correction method

Pressure based algorithms involve elliptic equations for the pressure correction, which is not suitable for transonic or supersonic flows which are hyperbolic in nature. Various workers have tried to adapt these pressure based schemes for compressible flow by using the flux linearisation first proposed by Issa and Lockwood (1977). Schemes based on this all have the problem of shock smearing. Improved shock capturing was achieved by McGuirk and Page (1990) using a 'retarded pressure' scheme. The work of Lien and Leschziner (1993) was motivated by the research of Page (1990) who extended the use of the retarded pressure scheme of McGuirk and Page to compute under-expanded turbulent impinging jets.

The following chapter presents the CFD predictions for the high speed Coanda wall jet. Tests were initially performed using the default numerical schemes provided by PHOENICS. As expected, the standard code resulted in considerable numerical diffusion in the presence of shock waves, so Roe's (1982) higher order numerical scheme accessible in PHOENICS was used. This is discussed further in section 7.3.4 of chapter 7.

Chapter 7

Modelling results using PHOENICS

7.1 Introduction

The main objective of this CFD work was to simulate the high speed tests of the experimental work described in chapter 5, and past experimental studies of the Coanda flare. The modifications to the mixing length model, which were proposed by Morrison (1982), and described in section 6.4 of chapter 6, were implemented in a special ground coding routine within PHOENICS. To gain experience in the use of the CFD code, and to validate the results using the modified ground coding, (i.e. information used by EARTH) and Q1 files (input data used by SATELLITE), tests were initially conducted on a previously investigated flow situation. The results of these tests are described in section 7.2 of this chapter. The complete range of flow situations and conditions modelled using CFD are summarised in Table 7.1. The experimental work used to validate the CFD predictions is given in this table, along with the flow conditions at the slot, the turbulence models used to predict the flow, and the methods used to validate the predictions with the experimental data.

The initial test case involved modelling the low speed jet flow over an axisymmetric Coanda flare surface. The Coanda geometry and flow parameters used were the same as those described by Hawkins (1988). The results obtained were compared with those given in Gregory-Smith and Hawkins (1989).

Section 7.3 involves the modelling of flows over the 2D planar Coanda flare, used in the current experimental investigation. The same model was also used by Senior (1991), and the CFD results described in this section are compared against the experimental results of Senior. The experimental data used for comparison includes surface pressures, breakaway performance data, and Schlieren images.

The final section in this chapter deals with the comparisons between the CFD predictions and the experimental findings of this current study.

Experimental work used for validation	Flow medium used	Slot to radius ratio	Conditions at the slot	Turbulence models used	Flow properties considered	Relevant section in chapter 7
Hawkins (1988) (axisymmetric flare model)	water	0.166	velocity = 4.2m/s $Re_s = 21400$	Standard mixing length Modified mixing length Standard k-e model H-L model	Jet growth plots Velocity decay plots Eddy viscosity profiles	7.2.4
—	Air	0.133	$P_a / P_o = 0.324$ $Re_s = 89500$	Modified mixing length Standard k-e model Chen-Kim k-e model RNG k-e model	Jet growth plots Velocity decay plots Velocity profiles - used to compare the performance of the turb. models	7.3.1-2
(planar flare model - no step at slot exit) Senior (1991)	"	"	"	As above, but using a higher order numerical scheme in addition to the standard hybrid scheme.	Surface pressure predictions Artificial Schlieren images Jet breakaway	7.3.3-4 7.3.5 7.3.6
Experimental work presented in chapter 5	Air	0.133	slot = 4mm $Re_s = 59000$ $Re_s = 54000$ $Re_s = 48500$ $Re_s = 42000$	Standard mixing length Modified mixing length Standard k-e model H-L model 'Hybrid' mixing length model	Jet growth plots Velocity decay plots	7.4.2
(planar model, no step)			slot = 2mm $Re_s = 58000$ slot = 8mm $Re_s = 116000$		Velocity profiles Turbulent kinetic energy and eddy viscosity profiles	7.4.3 7.4.4

Table 7.1 : Summary of CFD test cases

7.2 Initial tests on flow modelling

7.2.1 Grid geometries and generation

The streamwise, and in the case of the axisymmetric models, axisymmetric curvature, meant that body fitted coordinates were required. There are three basic types of structured 2-D grids, 'C' grid, 'H' grid, and 'O' grid. The grid type used in these tests is the 'C' grid, which provides the most orthogonal grid for the geometry under investigation. An 'H' grid was also used in preliminary tests, however this sort of grid is less suited to the Coanda geometry, and resulted in highly skewed cells in the early part of the jet.

The grids were all generated using an external program written in FORTRAN. To maintain maximum flexibility, the essential dimensions of the grid were parameterised, so that different Coanda geometries could be modelled quickly. In addition to the flexibility in the physical geometry, the cell structure also needed to be easily changeable, so grid refinements could be implemented. The grid generation program read in all the relevant dimensions and cell densities from the Q1 file, and used this information to generate a file called GRID which contained all the grid coordinates in a format compatible to be read in by EARTH.

The parameterised geometry variables are all defined in figure 7.1. From this it is clear to see that a vast range of Coanda geometries could be created very quickly and easily, simply by changing variables in the Q1 file.

7.2.2 Boundary conditions

The primary inlet flow at the slot was specified as a constant mass flow, and the inlet velocity was specified. The inlet turbulent kinetic energy, and the dissipation rate were specified using equation (6.20). The front and top boundaries were free to entrain and were specified as stagnation pressure boundaries. Wall functions were used to specify the near wall conditions on the Coanda surface.

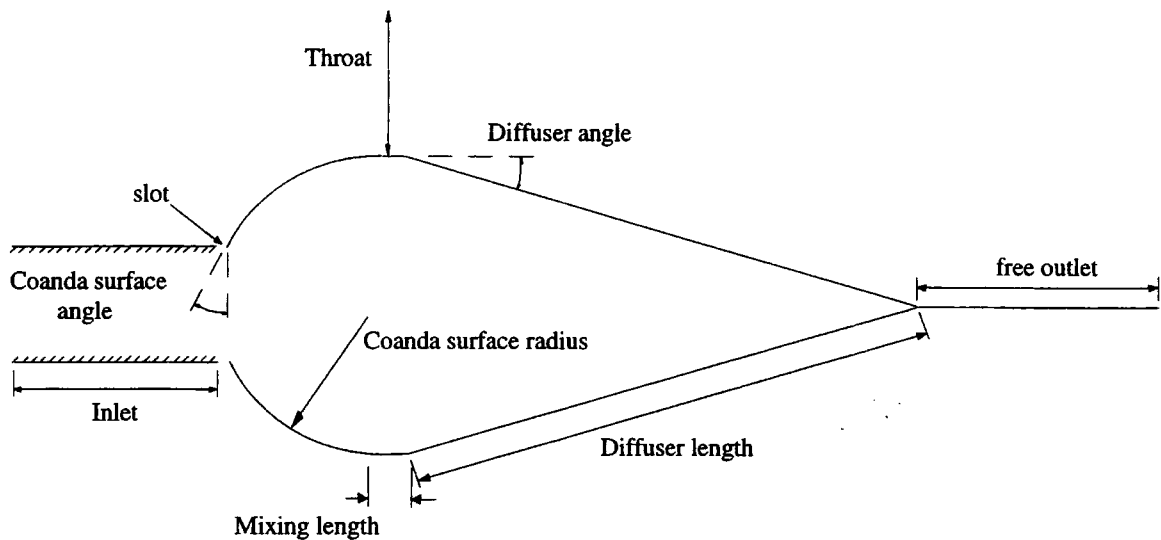


Figure 7.1 : Definition of geometry variables

7.2.3 Convergence criteria

The solution residuals (a measure of the imbalance in the finite volume equations during the solution procedure) were monitored throughout the solution process, and were observed to fall considerably. The solution at a single point was also monitored, and one sign of convergence is when the monitor point values cease to change. The residuals, and the monitor point data could be examined in more detail at the end of a simulation by viewing the file created by EARTH called the RESULT file. This file contains all the information necessary to determine whether a run has converged. The indicating factors are summarised below :

- Monitor point values become constant
- Residuals have fallen several orders of magnitude (typically 4 or 5) since the start of the run
- Mass is conserved, i.e. the total sum of mass leaving the computational domain must equal that entering it. This was typically satisfied to an accuracy of better than 10^{-5} kg.

7.2.4 Low speed jet flow

The full details on which these incompressible tests are based, and which are only summarised here, are given in Hawkins (1988). An axisymmetric Coanda flare model was placed in a closed water tank. Measurements were taken at ten locations round the flare surface using Laser Doppler anemometry. Data was obtained on the mean velocity components and the Reynolds stresses.

Figure 7.2 shows the external flare geometry, and the PHOENICS grid used in the following tests is shown in figure 7.3. This grid was found to give the best convergence performance, and was refined to give near grid independent results. The grid uses a body fitted co-ordinate system, with radial grid lines every 5 degrees around the flare surface, and at 5mm intervals up the conical section. The radial grid spacing varied as a geometric series with an expansion factor of 1.25. The axisymmetric extent was set to 1° .

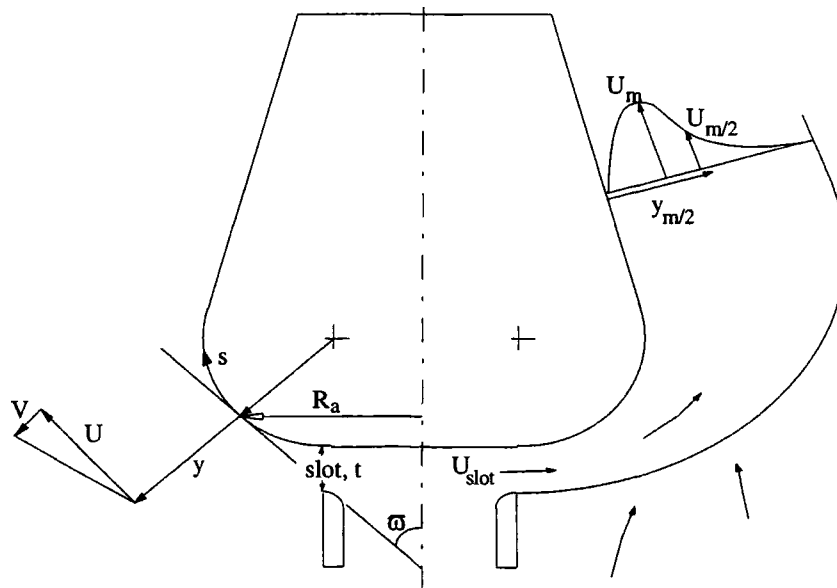


Figure 7.2 : Nomenclature and Co-ordinate System

The experimental conditions were set for an initial jet velocity of 4.2m/s with a slot height of 5mm, giving a slot Reynolds number, $Re_s = 21400$. The Coanda radius was set at 30mm, the diffuser angle at 10° , and the diffuser length was 50mm. The axisymmetric radius was 31.5mm. The variables solved for were the two velocities and

pressure. The latter was solved for using the whole field method since the curvature makes it elliptic. The mixing length was stored and calculated in the special ground file, as was the turbulent viscosity. In the case of $k - \epsilon$ based models, the variables k and ϵ were also solved for.

Three turbulence models were tested on this Coanda geometry. The first involved repeating the tests of Gregory-Smith and Hawkins, using the modified mixing length model developed by Morrison (1985). Tests were also repeated using the standard $k - \epsilon$ model. It has been noted in chapter 6 that this basic model is poor at predicting the effects of curvature, however, the modification to the model by Hanjalic and Launder (1982), has been reported to work much better than the original model in the presence of curvature. Therefore, the third test involved using the Hanjalic Launder (H-L) modification to the $k - \epsilon$ model.

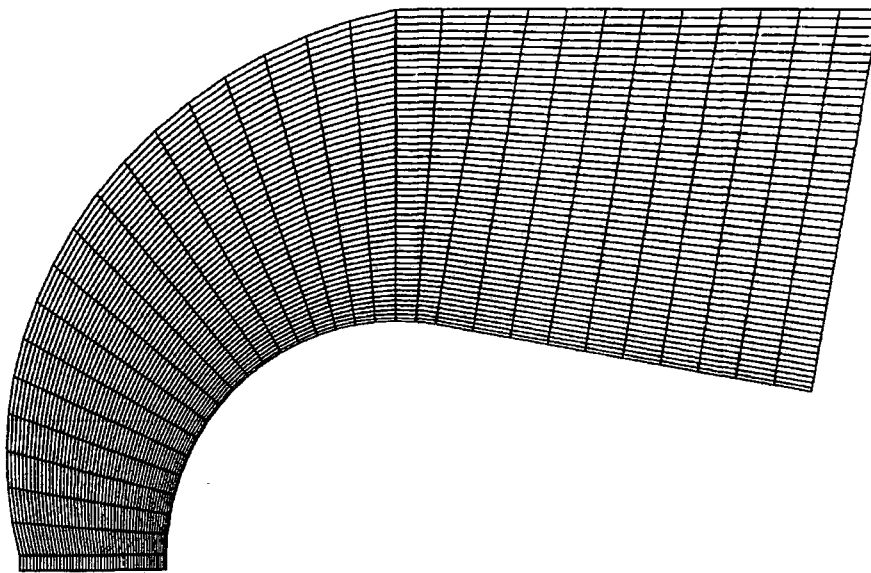


Figure 7.3 : Typical grid for the Coanda flare geometry

Incompressible flow test results

The results from these tests are displayed in the form of jet growth rate and velocity decay rate plots. Plots of eddy viscosity levels at various points around the flare surface have also been generated since the levels of eddy viscosity directly relate to the level of turbulence predicted.

The jet growth rate was assessed by plotting the half width, $y_{m/2}$, against the distance, s , around the flare. Both were made dimensionless with respect to the slot height, t . The velocity decay rate was assessed by plotting the maximum velocity against the distance around the flare and the quantities were once again made non-dimensional. The eddy viscosity levels predicted by the three models were also compared. The viscosity was made dimensionless with respect to the maximum streamwise velocity and the jet half width.

Figure 7.4(a) shows the jet growth rates for the three models, and the dots represent the actual experimental data obtained by Hawkins (1988). Figure 7.4(b) shows the velocity decay rates. Unlike the results reported by Gregory-Smith and Hawkins (1989), there is no initial rise in the maximum velocity, and there is no dip in the jet growth rate plot. Both of these phenomenon are due to the geometry of the upstream passage which causes a vena contractor at the slot. This causes a thinning of the jet and a higher velocity downstream of the slot. None of the turbulence models take account of these upstream effects on the flow, so they fail to show the jet thinning and acceleration close to the slot. The modified mixing length model predictions for jet growth rate follow the experimental results quite closely, showing better agreement round the Coanda surface than the previous predictions by Gregory-Smith and Hawkins. The standard $k-\epsilon$ model predicts little jet growth rate and correspondingly the velocity decay rate is less than in reality. However, it can be seen from these two graphs that the H-L form of the $k-\epsilon$ model is an improvement on the standard model. It predicts a jet growth rate intermediate between that predicted by the mixing length model and standard $k-\epsilon$ model.

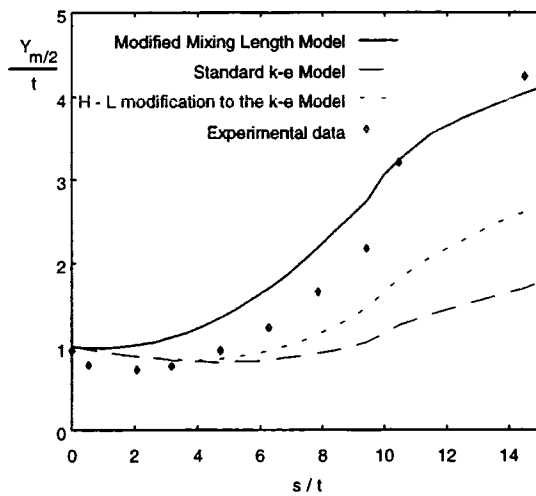


Figure 7.4(a) : Jet growth rate

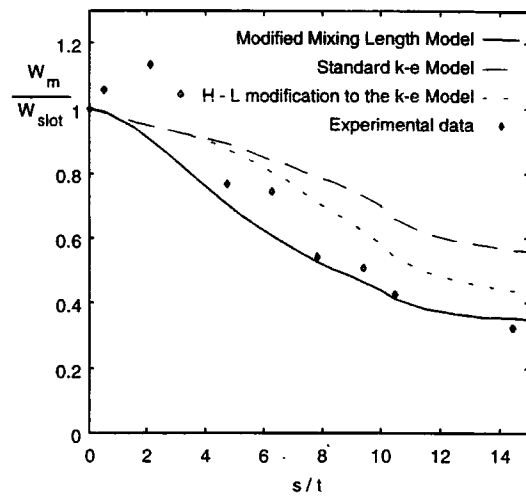


Figure 7.4(b) : Velocity decay rate

Figure 7.5(a)-(c) shows the (non-dimensionalised) values for the turbulent viscosity, ν_t (also referred to as ENUT in PHOENICS), predicted by the modified mixing length model, the standard $k-\epsilon$ model, and the H-L model respectively. These graphs may be compared against the experimental data obtained by Hawkins (1988) and shown in figure 7.5(d). The $k-\epsilon$ model predictions for the eddy viscosity levels can be seen to be far lower than those measured. The modified mixing length model predictions agree quite well in general with the experimental data. The H-L model once again gave intermediate results between the two models. However, the eddy viscosity levels with the H-L model are definitely higher than predicted by the standard $k-\epsilon$ model, indicating this model does predict a higher mixing rate due to curvature.

One approach to try to improve on the predictions would be to use a smaller slot width to mimic the vena contractor. Another option is to try and account for the curvature upstream of the slot. This curvature is likely to result in higher values of turbulence at the exit plane than would be expected from a straight, uniform section. PHOENICS does not take account of this, which may be a further explanation for the $k-\epsilon$ model underpredicting the mixing rate at the slot. To test this theory, the inlet value of turbulent kinetic energy for the standard $k-\epsilon$ model was factored to establish the sensitivity of the result to this parameter. The jet growth rate and velocity decay rate plots, using the standard $k-\epsilon$ model are given below in figure 7.6. The results show

some sensitivity around the standard inlet value, however the sensitivity decreases, as might be expected, at very high values.

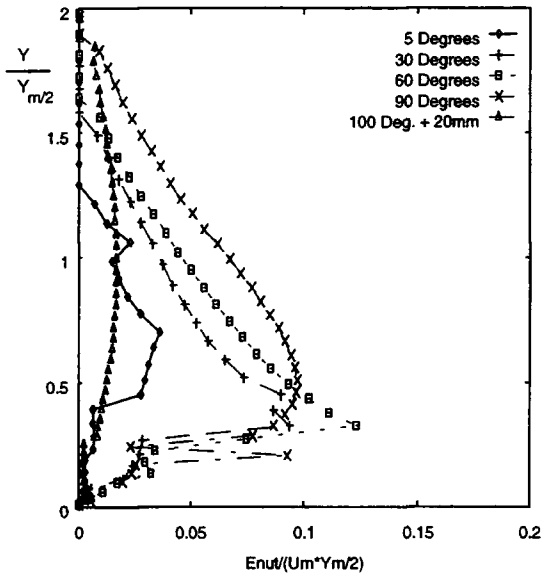


Figure 7.5(a) : Mixing length model predictions for ENUT

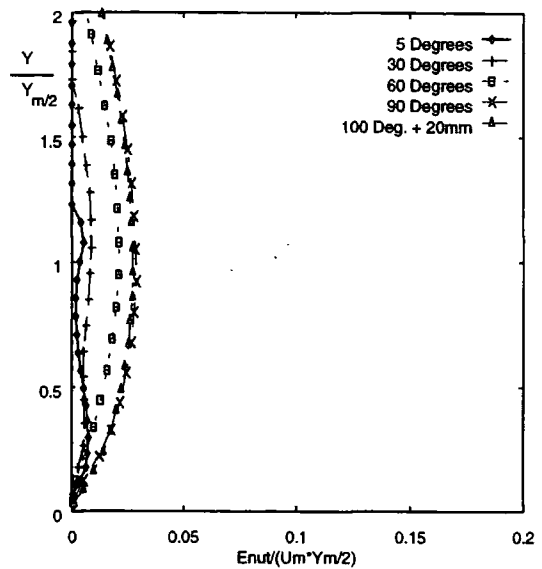


Figure 7.5(b) : Standard k-ε model predictions for ENUT

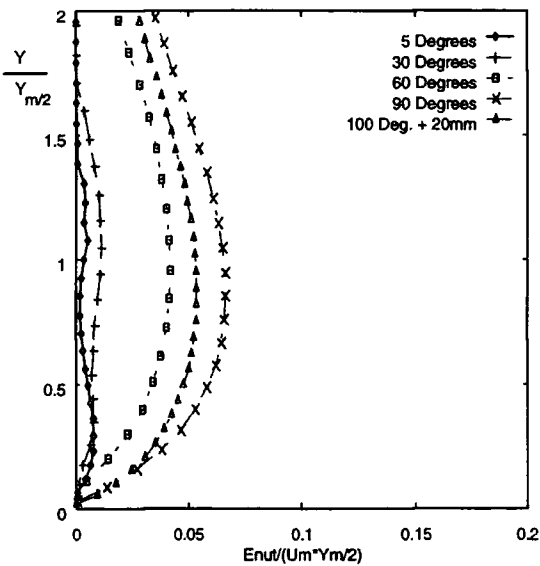


Figure 7.5(c) : Hanjalic Launder k-ε model predictions for ENUT

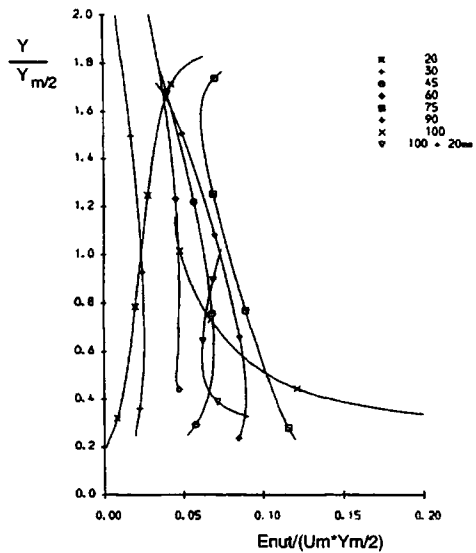


Figure 7.5(d) : Experimental eddy viscosity levels

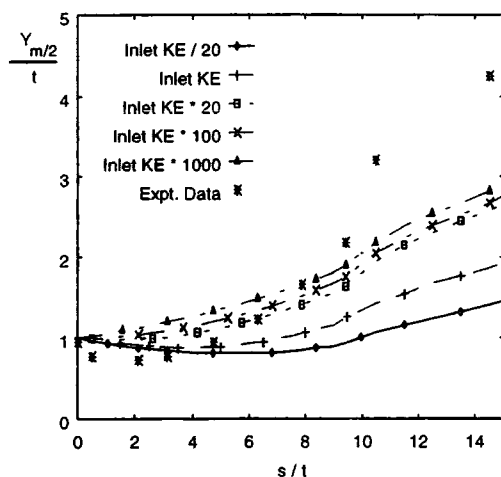


Figure 7.6 (a) : Jet growth rate with varying inlet kinetic energy

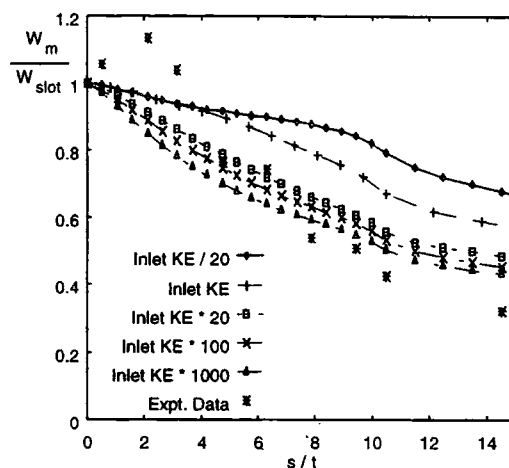


Figure 7.6 (b) : Velocity decay rate with varying inlet kinetic energy

7.3 General CFD tests on the planar flare model

Much of the work performed by Senior (1991) was aimed at studying the effects of a base step in the exit plane of a slot on a supersonic jet blown over a convex Coanda surface. Experiments were performed on both a planar and an axisymmetric model. One of the main aspects of this work was to gain an understanding of the jet structure, and to understand the mechanism which triggers the jet to break away from the curved surface. Tests were performed with and without a base step, and a good understanding of the jet structure was obtained from the results. A summary of these findings may be found in Gregory-Smith and Senior (1994) and full details of the work are reported in Senior (1991).

The work presented in the following sections has considered only the unstepped planar model case. Firstly, a study was made at a moderate blowing pressure, using various turbulence models available within PHOENICS, and the results from these tests were used to produce jet growth and velocity decay rate plots, velocity profiles and surface pressure plots. To establish whether the inviscid core shock structure was predicted correctly, artificial Schlieren images were also generated. The final characteristic of the Coanda flow to be investigated was the breakaway performance.

Various grids were tested before finally settling on the grid shown in figure 7.7. Later in this chapter, Schlieren images (figures 7.21(a) and 7.22(a)) show that very fine details exist in the shock cell structure in the early part of the jet. The grid shown below is unlikely to capture these details in full. A much finer grid would be required in order to resolve all the features of the flow, however attempts to increase the grid refinement resulted in convergence problems. As a result, solutions for the high speed flows are likely to lack complete grid independency. Despite this, use of the grid shown in figure 7.7 permitted predictions of the salient features of the flow, without compromising computation time and avoiding convergence problems. Radial grid lines are placed every 1.82 degrees around the curved surface, and at 1.22mm intervals up the diffuser section. The radial grid spacing varied as a geometric series with an expansion factor of 1.25, with 50 cells in the Y direction. The radius of the planar model was 30mm. The size of the slot used in the following tests was chosen to give a slot to radius ratio of .133 to enable direct comparisons to be made between the theoretical results and those which exist from previous experimental work.

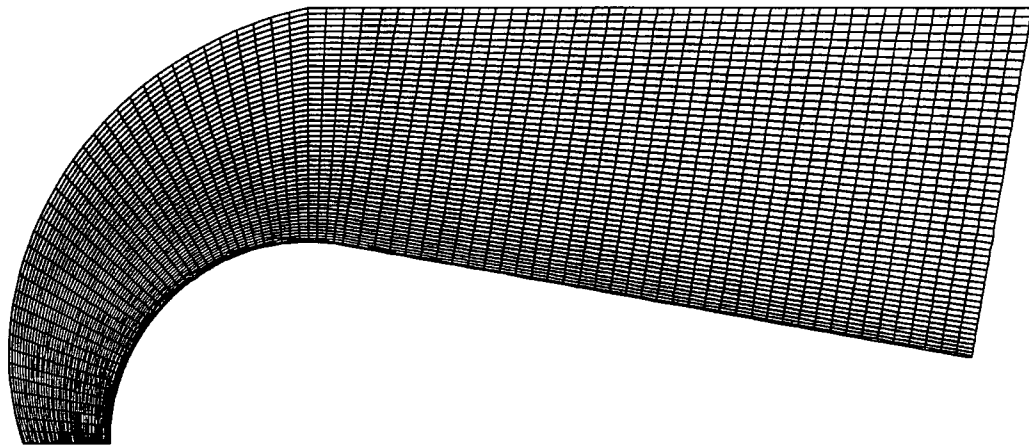


Figure 7.7 : 'C' grid used in planar compressible tests

7.3.1 Comparison of various turbulence model performances

A comparison was made between the modified mixing length model, the basic $k-\epsilon$ model, the RNG model derived from the $k-\epsilon$ model, and the modified $k-\epsilon$ model of Chen and Kim. An additional test was performed with all the turbulence models switched off, thus allowing the solution of the laminar flow case. All the results shown in figures 7.8-7.17 were obtained at the moderate blowing pressure of 3.08 Bar (or a blowing pressure ratio coefficient C_{p0} of 0.324)

7.3.2 Velocity profiles

The jet growth and velocity decay rates were both evaluated in the manner described in section 7.2.4. The PHOENICS predictions for these plots using the various models are shown in figures 7.8 and 7.9. The velocity decay rate has peaks and troughs over the curved section due to the shock cell structure. The initial rise above 1.0 at the slot exit is due to the supersonic expansion which occurs there.

The velocity profiles at various points around the flare surface are shown in figures 7.10 to 7.17. The profiles for the basic $k-\epsilon$ model and the modified $k-\epsilon$ models are all similar which was as expected, due to the similarity between the plots for jet growth rate. There are distinct differences however between these $k-\epsilon$ based models and the mixing length velocity profiles. Figure 7.10 shows that V/U_m settles to a more negative value at large values of $y/y_{m/2}$ with the mixing length model than any of the $k-\epsilon$ based models. This indicates the entrainment velocity is higher with the mixing length model, and this is confirmed by the fact the jet is wider. The smoother, more spread out plots of U/U_m for the $k-\epsilon$ based models appear more realistic than on the mixing length model. However, no experimental data exists at this high pressure ratio, so these CFD results cannot be evaluated with any confidence.

The $k-\epsilon$ based models all show a negative normal velocity profile at the 40° position (figures 7.12, 7.14, 7.16). This corresponds to the position of the first shock cell, as illustrated in figure 7.9 where a dip occurs in the velocity decay plots at $s/t = 5.2$. The rapid jet growth predicted by the mixing length model means the inviscid core vanishes very rapidly, so this first shock cell is not predicted, hence the normal velocity at the 40° position on figure 7.10 is positive.

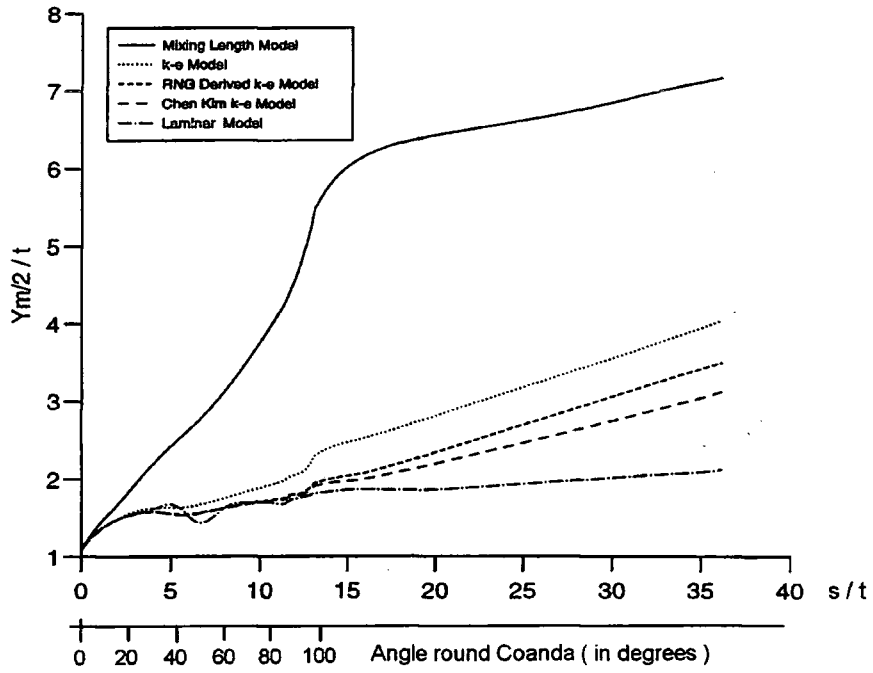


Figure 7.8 : PHOENICS predictions for the jet growth rate

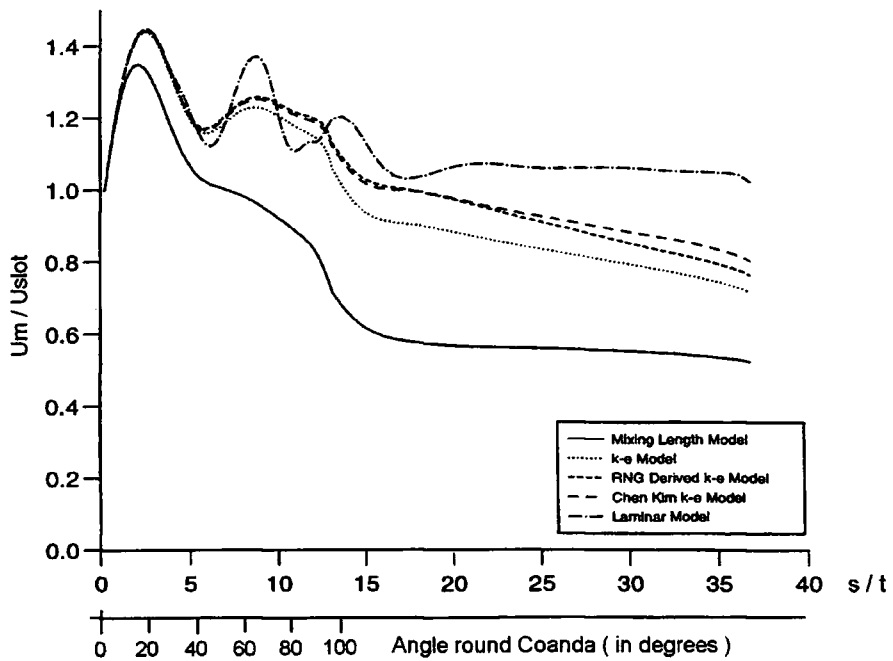


Figure 7.9 : PHOENICS predictions for the velocity decay rate

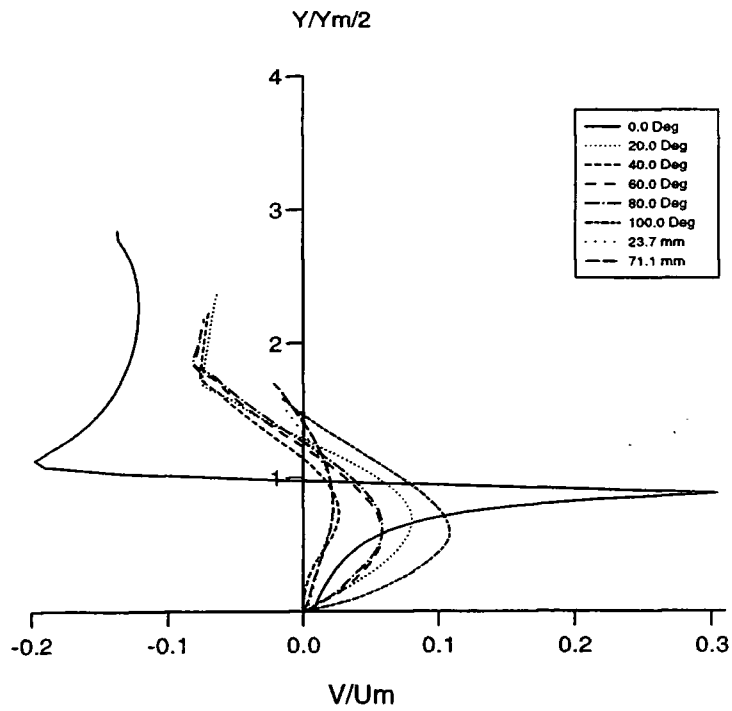


Figure 7.10 : Mixing length model predictions for V/U_m vs. $y/y_{m/2}$

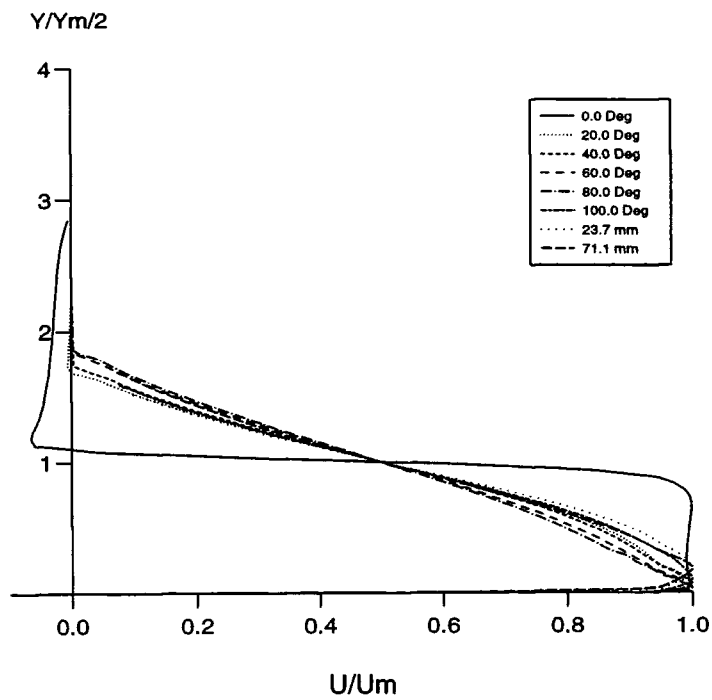


Figure 7.11 : Mixing length model predictions for U/U_m vs. $y/y_{m/2}$

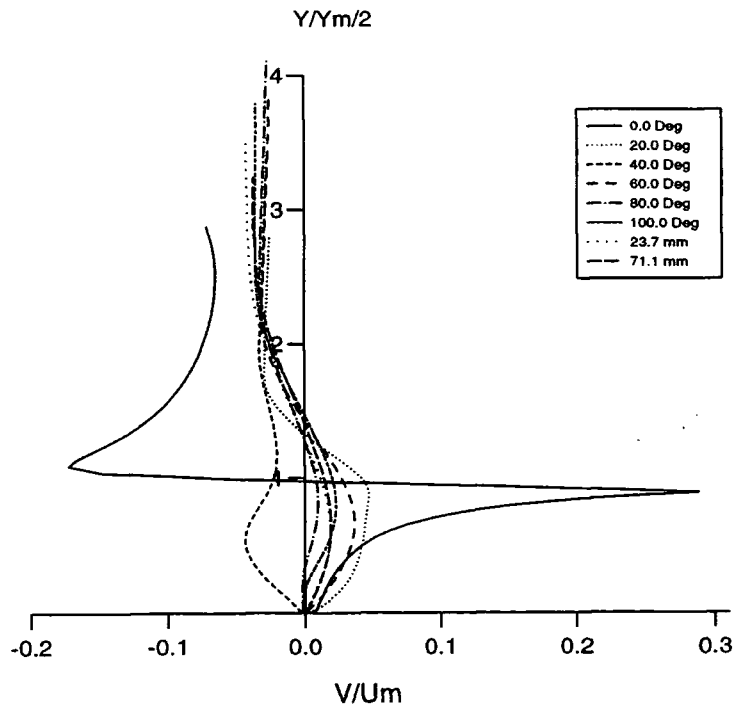


Figure 7.12 : $k - \epsilon$ model predictions for V/U_m vs. $y/y_m/2$

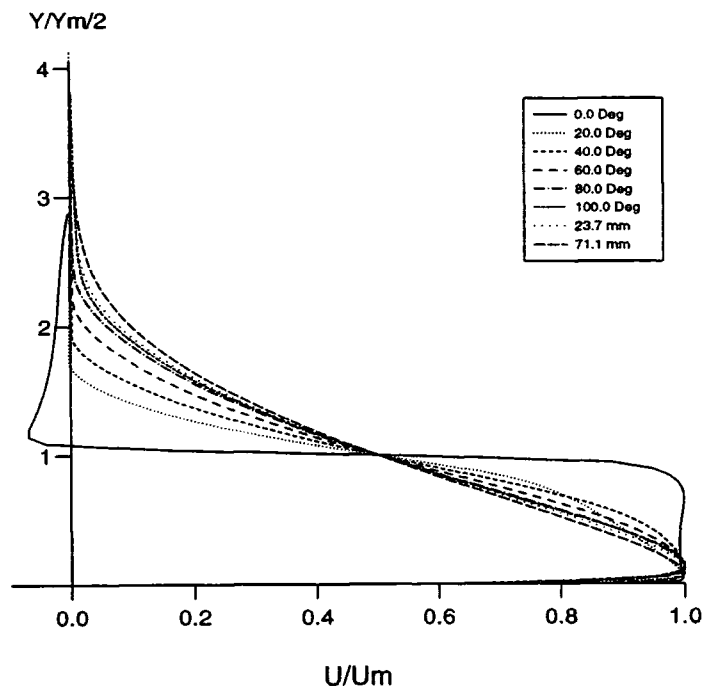


Figure 7.13 : $k - \epsilon$ model predictions for U/U_m vs. $y/y_m/2$

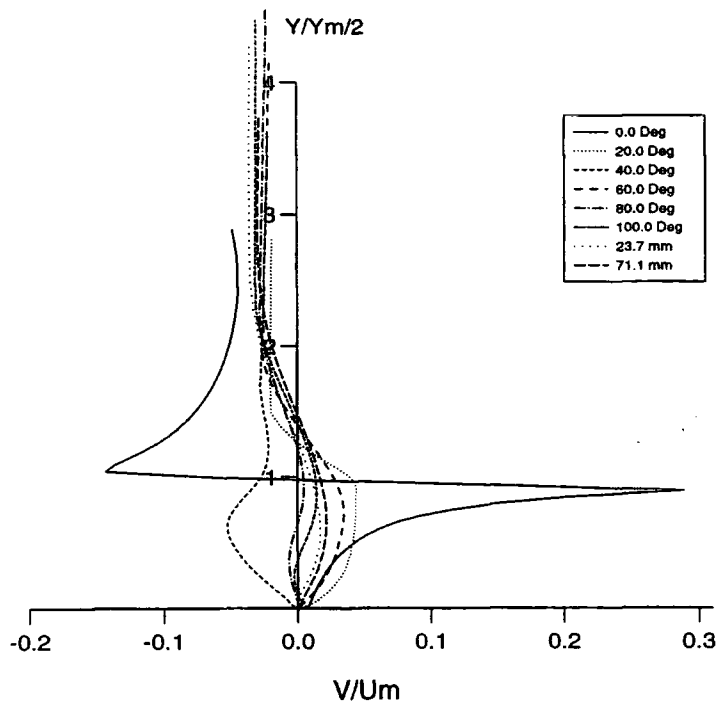


Figure 7.14 : RNG model predictions for V/U_m vs. $y/y_m/2$

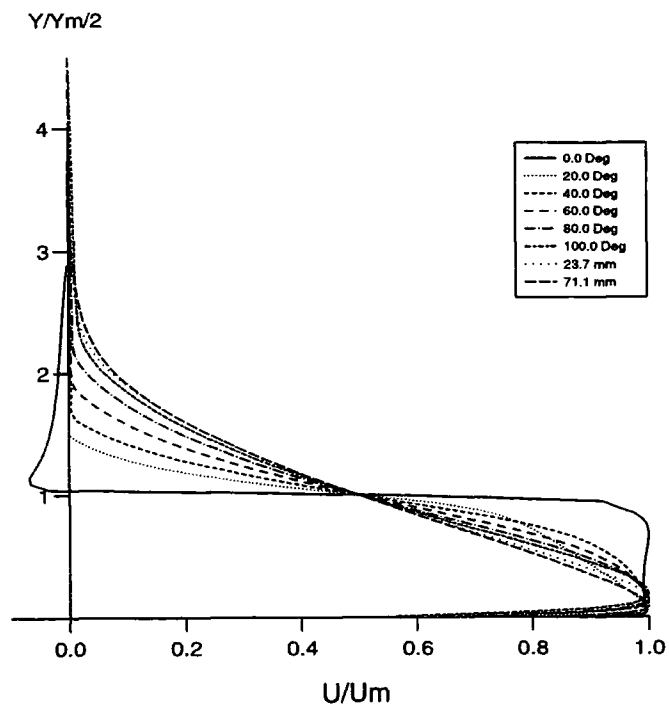


Figure 7.15 : RNG model predictions for U/U_m vs. $y/y_m/2$

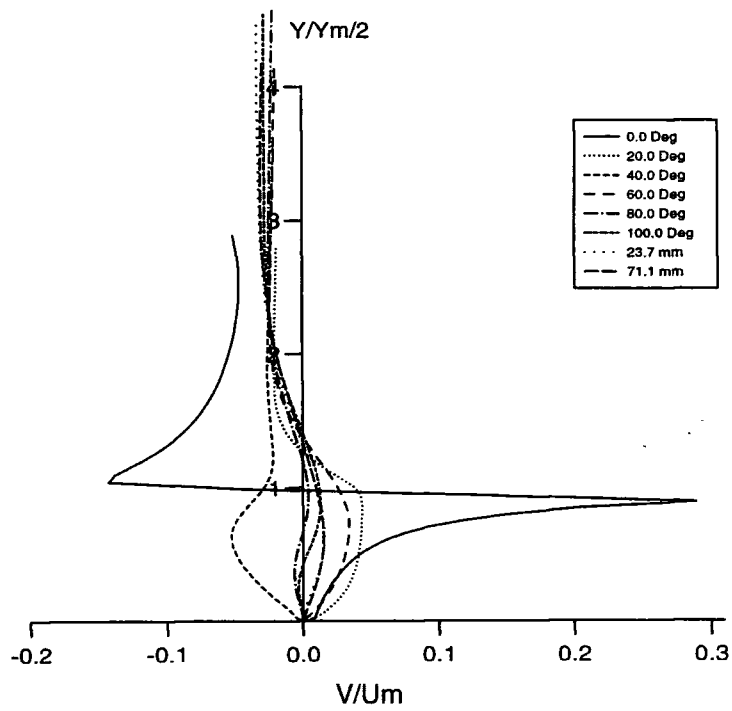


Figure 7.16 : Chen Kim model predictions for V/U_m vs. $y/y_m/2$

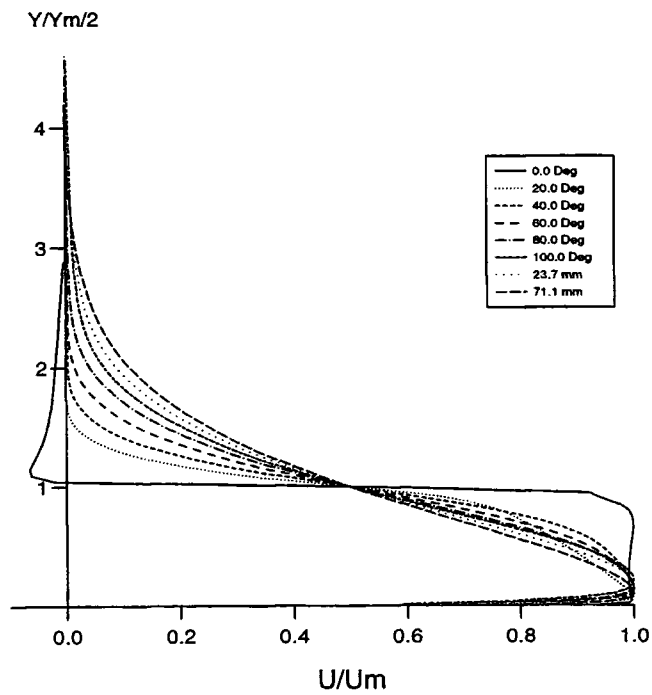


Figure 7.17 : Chen Kim model predictions for U/U_m vs. $y/y_m/2$

7.3.3 Surface pressure predictions

Predictions for the surface pressure distributions (at a blowing pressure of 3.08 bar, which corresponds to $C_{p0} = 0.324$) using the turbulence models under investigation, are all shown in figure 7.18. The results from the RNG model and the Chen Kim model were identical, so only the Chen Kim model result is shown in figure 7.18. The experimental surface pressure data obtained by Senior (1991) has also been plotted on this graph to enable comparisons to be made between this and the PHOENICS results. The graphs show the variation in static pressure coefficient, C_p , round the Coanda surface. The experimental data shows peaks and troughs over the curved part of the flare surface, which correspond to shock cells. The regions of constant pressure in the troughs correspond to separated regions on the surface.

It may be seen immediately from the graph that none of the models tested show any evidence of these separated regions, since no constant pressure zones are present, and this was confirmed by viewing the velocity vectors using PHOTON.

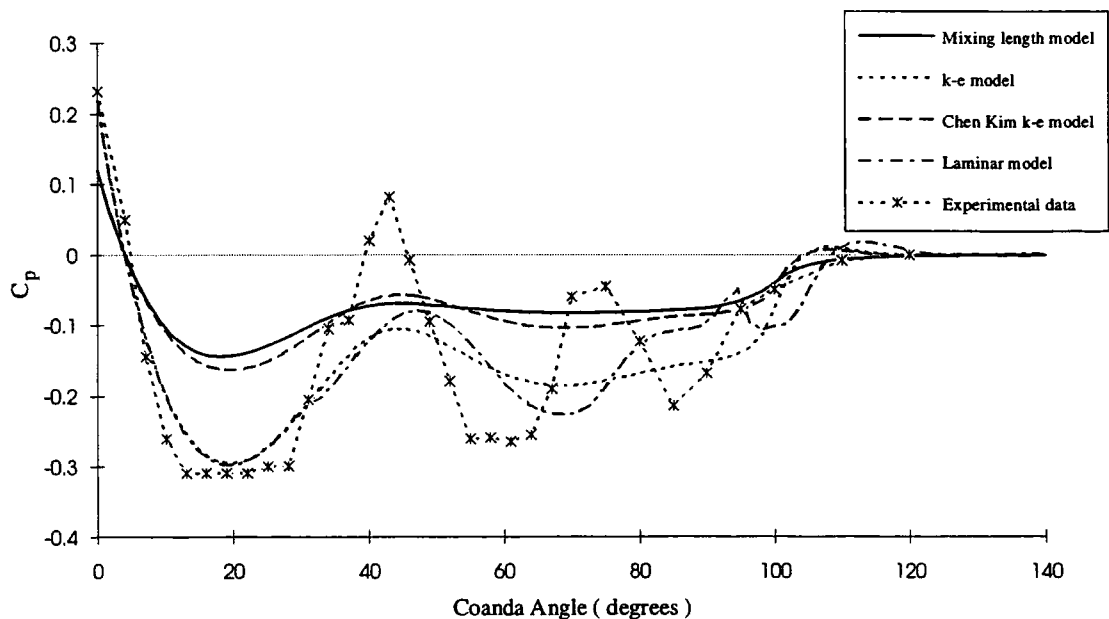


Figure 7.18 : PHOENICS predictions for the planar model surface pressures

It had been expected that the surface pressure plots would be more or less model independent, since the results depend mostly on the inviscid shock cell structure. The predictions of the laminar flow model follow the experimental results shown in figure 7.18 most accurately, but this plot, like the others, lacks the constant pressure zones. However, the peaks and troughs appear at the same points around the surface and they occur at the correct order of magnitude. The mixing length model shows the least variation in surface pressure due in part to the inability of the model to predict separating and recirculating flows. More importantly however, the rapid jet growth rate predicted by the mixing length model would suggest that there is too much viscous damping of the shocks. The $k-\epsilon$ model predictions are similar to the laminar model predictions at the start of the jet, where the outside of the jet has not yet influenced the inviscid core where the shock cell structure exists. Further round the surface, the $k-\epsilon$ model tends to increasingly damp out the effects of the inviscid core. Despite this, the basic $k-\epsilon$ model does predict the surface static pressure coefficient magnitude more accurately than the modified $k-\epsilon$ models. From the experimental data, the surface static pressure coefficient is seen to fall to approximately -0.3 at the first trough. The $k-\epsilon$ model drops to just short of -0.3, whereas the modified version of the model, and the mixing length model, only drop to about half this value.

The results using the Chen Kim and the RNG models coincided, with both models damping out the effects in the inviscid core more than in reality. However, as section 7.3.6 will show, these models are better at predicting breakaway than the basic $k-\epsilon$ model. The standard $k-\epsilon$ model is very poor at dealing with separating flows, but it can predict the inviscid core more accurately, as demonstrated by the deeper troughs on the surface pressure plots.

It was thought that an explanation for the poor shock structure predictions may lie in the numerical interpolation scheme used. A higher order numerical scheme, available within PHOENICS, was therefore implemented in the hope of reducing any numerical diffusion.

7.3.4 Higher order numerical schemes

PHOENICS has built-in options for upwind and hybrid interpolation schemes for the convection terms of the finite volume equations. A series of Non-Linear Convective Schemes (NLCS) are available in PHOENICS which may be used instead of the default upwind scheme.

These schemes can be activated for any variable by introducing a special PATCH with a name starting off with the letters 'NLCS'. This activates NLCS Ground which supports various schemes. The scheme used in the following tests was the fully implicit Monotomic Second Order Upwind algorithm (MSOU) of Roe (1982) which was originally developed for the prediction of inviscid compressible flows.

In addition to applying this higher order scheme, UCONV was set to true. This allows the convection fluxes to be altered in Group 8 of GROUND by calling the routine GXCONV. This routine makes corrections to the convective terms used in the momentum equation so the convective fluxes are then consistent with those used in the continuity equation. To aid convergence in the presence of steep density gradients DENPCO was also set equal to true.

A further correction was applied to take account of the high curvature of the grid lines. This was done by setting WUP equal to true. This causes an upwinding of the contributions of the normal and transverse velocities to be performed in the representation of the grid-line curvature term for the streamwise velocity, for those cells adjacent to the boundaries. This correction should permit streamline separation on a curved boundary to be predicted on coarser grids than would otherwise be possible.

Test results using the higher order numerical scheme

Figures 7.19 and 7.20 show the surface static pressure coefficient plotted against angle round the Coanda surface for a supply pressure of 3.08 Bar. Figure 7.19 shows results using the standard $k-\epsilon$ model, and compares the standard numerical scheme with the higher order numerical scheme of Roe (1982). The experimental data obtained by Senior is also included for comparison. Figure 7.20 also shows the experimental data, along with PHOENICS results using the Chen Kim model obtained using the standard, and the

higher order scheme. Both graphs show an improvement in results when the higher order numerical scheme is employed. The degree of numerical diffusion is reduced and the shocks only start to go out of phase at the second trough.

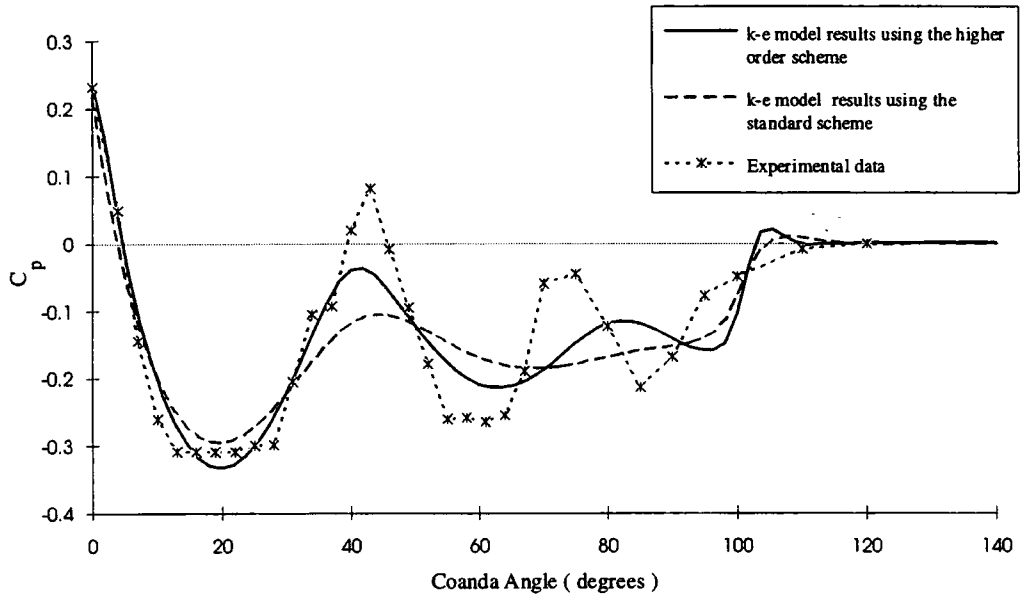


Figure 7.19 : $k - \epsilon$ model pressure plots using the standard and the higher order schemes

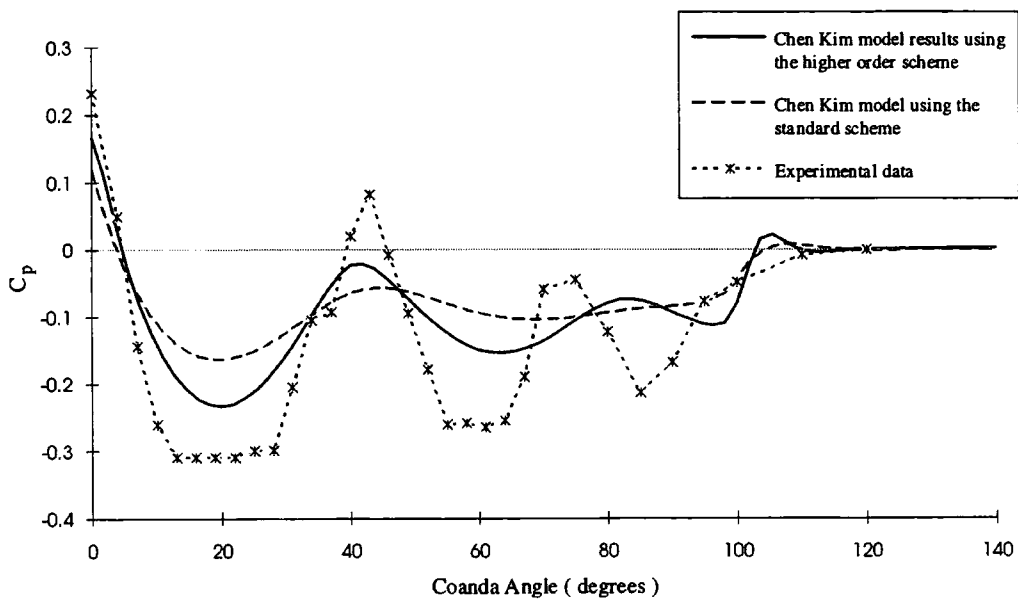


Figure 7.20 : Chen Kim model pressure plots using the standard and the higher order scheme

7.3.5 Schlieren images

The intensity of a Schlieren image depends on the density gradient, so these images are best at showing up regions of compression and expansion. In experimental tests, the orientation of the knife edge determines the spatial direction for the density gradient. Artificial images have been produced from results for the $k - \epsilon$ model using Roe's higher order scheme. The artificial images were generated from information stored in the PHI file by differentiating the density field in either the horizontal or vertical direction.

Figure 7.21(a) shows the actual horizontal Schlieren photograph taken by Senior at a pressure ratio of 0.323. This may be compared to the artificial image in 7.21(b). Dark regions on these images indicate an increase in density from bottom to top (as drawn).

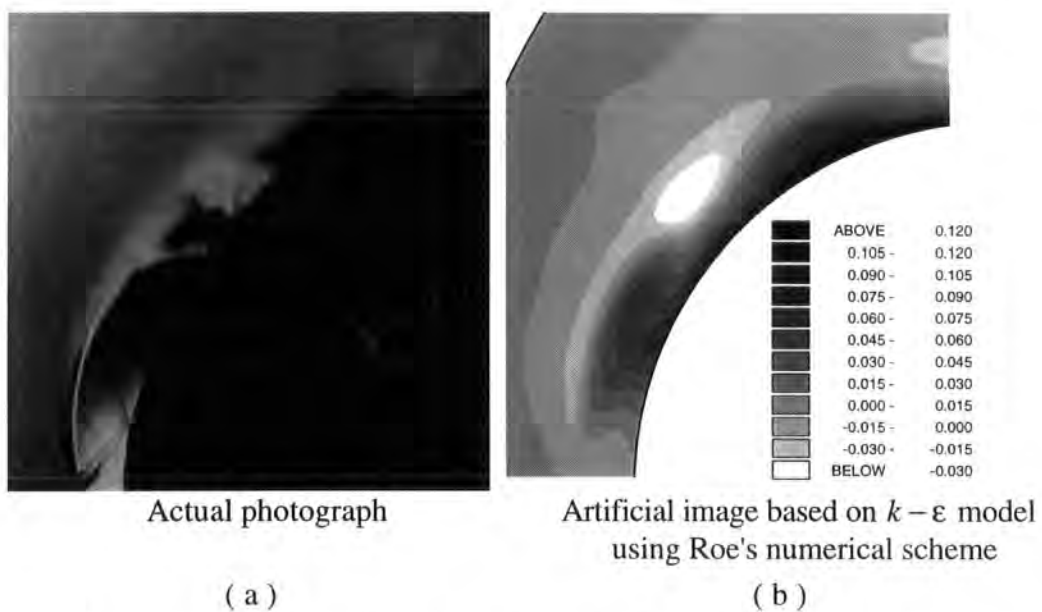


Figure 7.21 : Horizontal Schlieren Images - showing density gradients in the vertical direction, as drawn

The horizontal images have a light region at the slot exit which indicates an expansion fan. The darker region a little further round the Coanda surface corresponds to an incoming compression wave. The repeated regions of expansion and compression indicate the presence of two shock cells over the portion of the Coanda shown in these images.

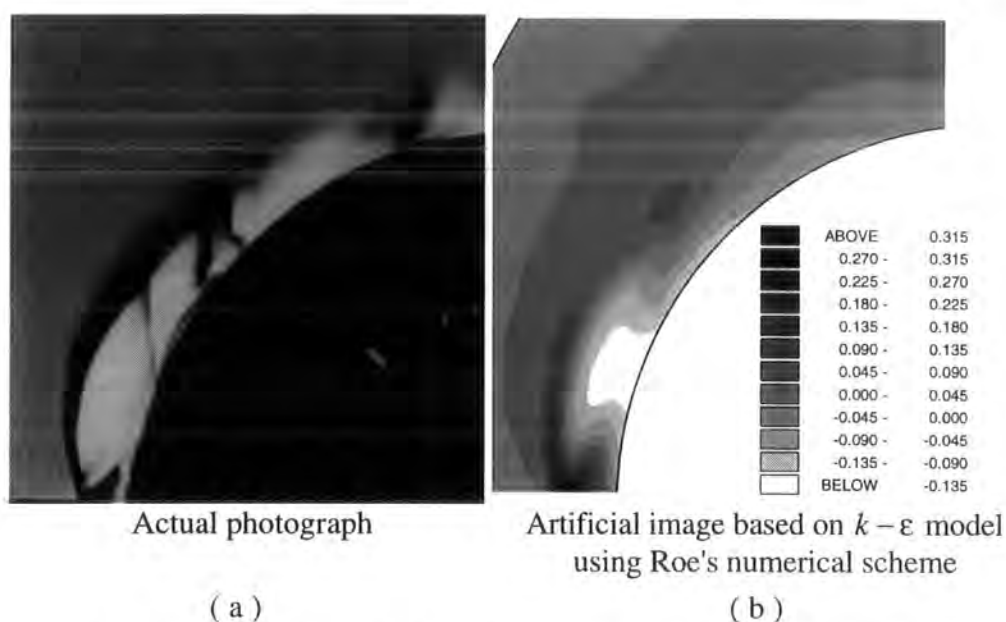


Figure 7.22 : Vertical Schlieren Images - showing density gradients in the horizontal direction, as drawn

Figure 7.22(a) shows the actual vertical Schlieren photograph taken by Senior which may again be compared to the artificial image shown in 7.22(b). Dark regions on these images indicate an increase in density from left to right (as drawn). The dark region extending from the lip of the slot corresponds to the outer shear layer and can clearly be seen on both images. The presence of two shock cells on the artificial image is again visible. The fine details present on the actual Schlieren images are not clear in the artificially generated images, due to the relative coarseness of the grid. Attempts to refine the grid failed due to convergence problems, so, as previously stated, these solutions cannot be assumed to be fully grid independent.

The artificial images generated from runs of the $k-\epsilon$ model using the higher order scheme were found to resemble the actual photographs far more closely than those generated using the standard scheme. Therefore, as hoped, the higher order scheme greatly improved the shock wave definition.

7.3.6 Jet breakaway

The phenomenon of breakaway occurs when the jet no longer follows the curved surface, and this occurs at some critical pressure, which is dependent on a number of

factors. The experimental surface pressure data, published in the paper by Gregory-Smith and Senior (1994) has been reproduced in figure 7.23. These graphs show the surface pressure distributions which were recorded at a range of blowing pressures, with a slot width of 4mm. The plots show the variation in static pressure coefficient, C_p , round the Coanda surface. Even for a moderate blowing pressure of 3.08 bar (which corresponds to $C_{po} = 0.324$) there are peaks and troughs in the pressure distribution over the surface. These correspond to shock cells round the surface. The regions of constant pressure in the first two troughs correspond to separated regions on the flare surface. As the blowing pressure is increased these separated regions grow until they eventually join up, resulting in the breakaway of the jet from the surface at 4 bar.

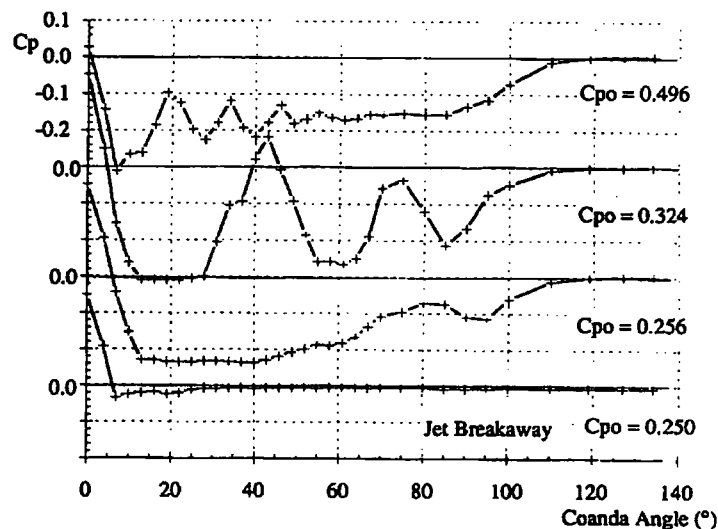


Figure 7.23 : Surface pressure plots from existing experimental data

The Chen Kim form of the $k-\epsilon$ model was used to compare theoretical and experimental surface pressure plots as the inlet pressure was increased up to breakaway. This model was chosen due to its superiority over the standard model where separated flows are concerned. The results from these tests, using the standard numerical scheme, are shown in figure 7.24.

It was noted in section 7.3.2 that the models tested using PHOENICS fail to predict the regions of separation, as indicated by the lack of flat zones in the troughs of the surface pressure profiles. Another important shortfall of these models, which is illustrated in

figure 7.24, is that they over-estimate the pressure at which jet breakaway occurs. In this case, the Chen Kim model predicts breakaway will occur at 4.8 bar ($C_{po} = 0.208$).

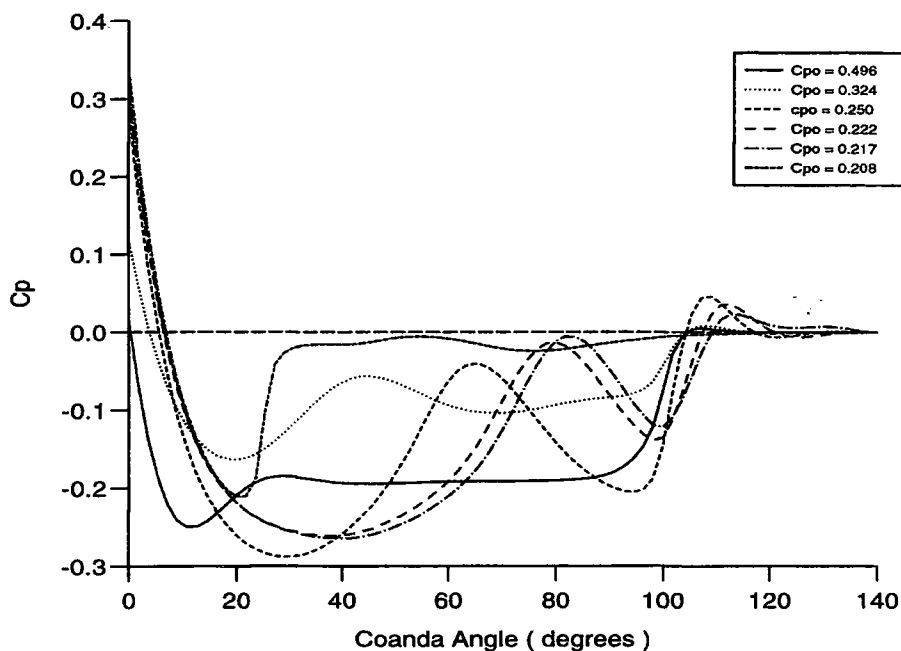


Figure 7.24 : Surface pressure predictions using the Chen Kim model

A brief study of the breakaway performance of the other models was performed. PHOTON was used to view the velocity vectors and identify regions of recirculating or separated flow. The RNG model was found to give very similar results to the Chen Kim model. The basic $k-\epsilon$ model however showed the flow to be still well attached and with no signs of breakaway at a supply pressure of 5.0 bar. The mixing length model was also very poor at predicting jet breakaway and also showed no signs of recirculation zones at 5.0 bar. By contrast, the two modified $k-\epsilon$ models showed significant separated regions with recirculating flow at pressures just below that of jet breakaway. These separated regions were on a far larger scale than those which occur in reality, and they formed further round the Coanda surface.

To summarise, using the standard numerical scheme, neither the mixing length model nor the standard $k-\epsilon$ model were capable of predicting jet breakaway, even when the pressure was raised well above 5 bar. The Chen Kim and RNG models both showed

large recirculation zones at a pressure of 4.7 bar, and in both cases, the jet broke away when the pressure was increased to 4.8 bar.

The use of the higher order scheme significantly improved the ability of the models to predict breakaway. The standard $k - \epsilon$ model showed some recirculation at a pressure of 4.5 bar, and total separation, and hence breakaway, occurred at 4.8 bar. The Chen Kim model predicted the formation of a recirculation zone at 4.15 bar with jet breakaway occurring at 4.3 bar. The corresponding velocity vectors approaching breakaway are shown in figure 7.25(a)-(b). Figure 7.25(c) shows an enlargement of the vectors in the separated region of (b). Figure 7.25(d) shows the velocity vectors at breakaway at a pressure 4.3 bar.

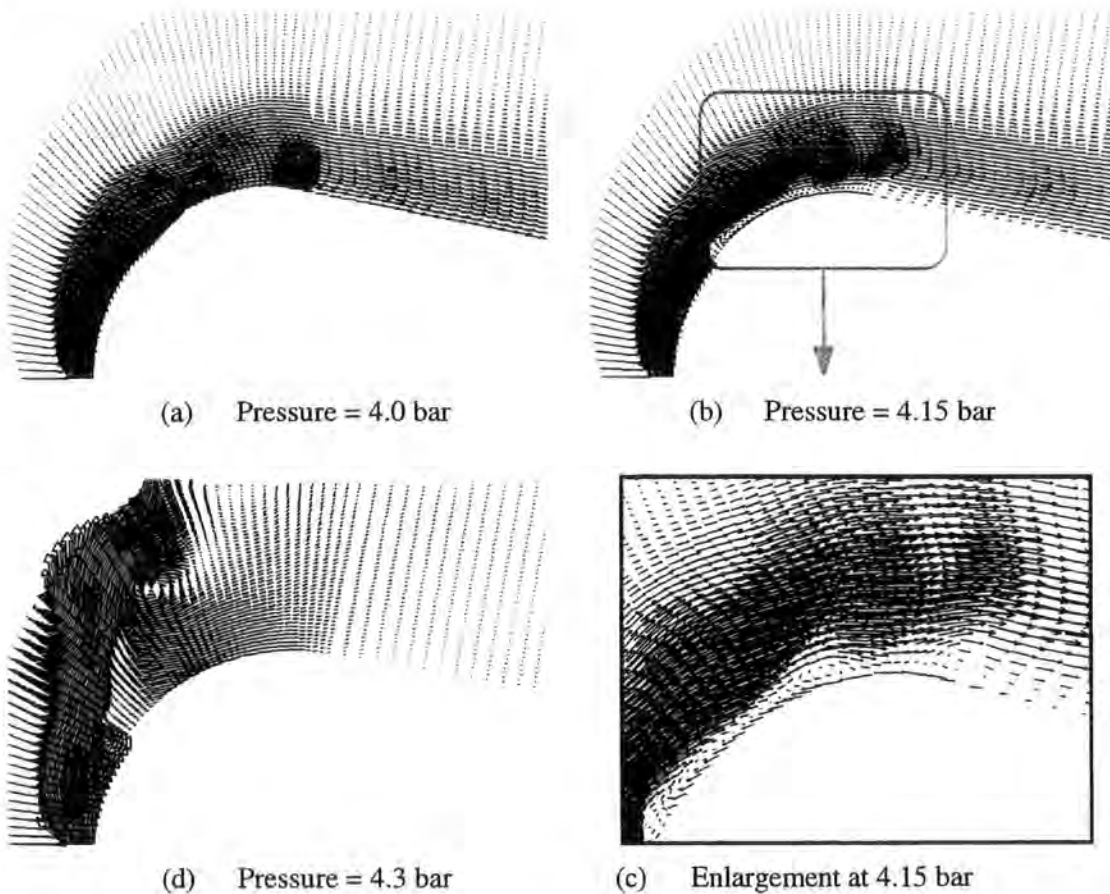


Figure 7.25 : Velocity vectors predicted using the Chen Kim model

It is not really surprising that the $k-\epsilon$ based models were unable to predict the regions of separation and hence breakaway correctly, since they use wall functions and only compute turbulent boundary layers and turbulent separation. In reality the situation is very different. Figures 7.26(a) and (b) aim to explain the shapes of the theoretical and experimental pressure plots. An additional reason for differences to exist is that the theoretical solution assumes a uniform inflow at the slot which is in fact inaccurate due to upstream effects from the slot lip shape.

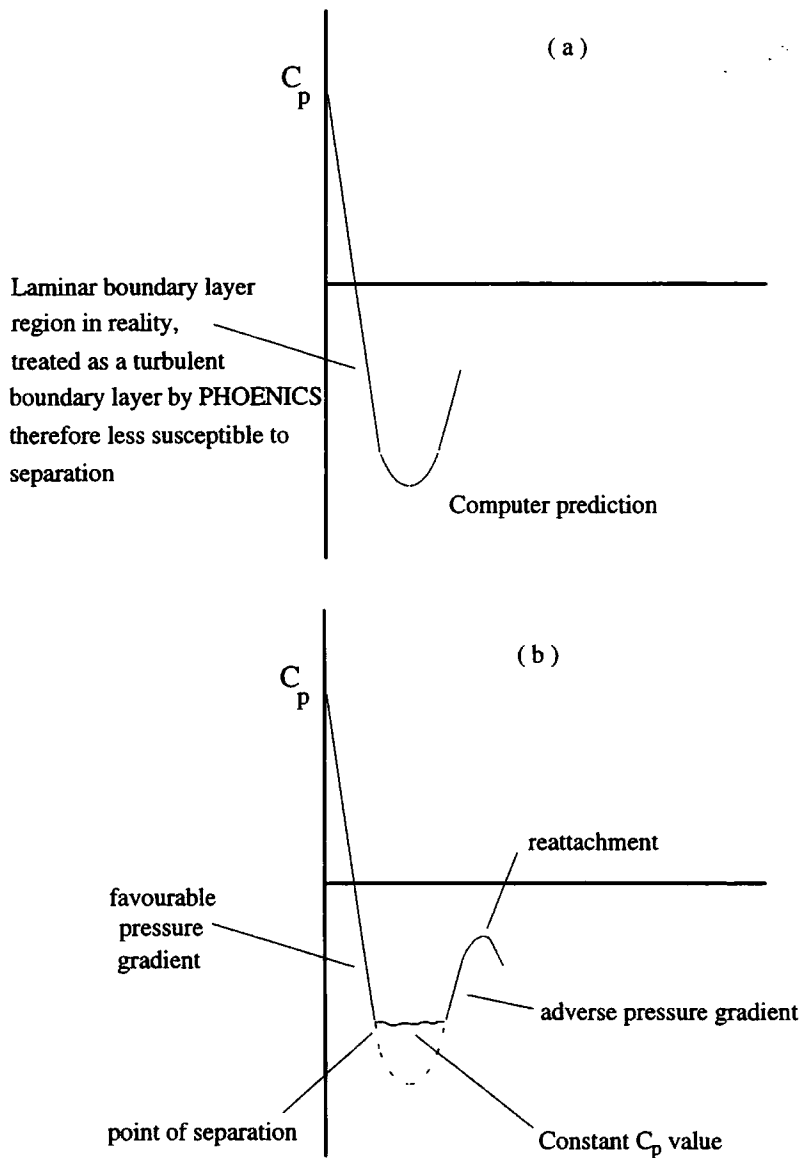


Figure 7.26 : Differences between (a) predicted, and (b) experimental surface pressure plots

Due to high acceleration, the boundary layer round the initial part of the curved surface is laminar, and this laminar boundary layer is more susceptible to an adverse pressure gradient than a turbulent boundary layer. The computer models however assume this is a turbulent boundary layer, which may explain why the predictions for jet breakaway are too high. In reality, the structure of the jet core and the separated regions strongly interact. The expansion fan at the slot exit is reflected back from the free jet surface as a compression wave. This, in the presence of an adverse pressure gradient, causes the initial separation of the laminar boundary layer. This separation causes a separation shock wave to form which modifies the first shock cell, and this shock wave may then travel back upstream, resulting in the separated region indicated by the constant C_p value. The boundary layer is transitional, resulting in a turbulent boundary layer which leads to eventual reattachment at the next peak.

7.4 CFD predictions for the high speed flow of the planar Coanda model

These final tests have been performed on a 2-D grid which represents the planar 2-D Coanda flare model. The conditions used in these tests are the same as those described in chapter 5 so direct comparisons may be made between the CFD predictions and the experimental results. Hence four cases involve a constant slot width of 4mm with the supply pressure ratio varying from 0.7-0.85, and two further cases involve slot widths of 2mm and 8mm at a pressure ratio of 0.85. The turbulence models used in these tests are the standard $k-\epsilon$ model, the Hanjalic Launder modification to the $k-\epsilon$ model, the standard mixing length model, and the mixing length model modified for streamwise curvature. The results are presented in a similar manner to those in the experimental results chapter. Section 7.4.1 demonstrates the grid independency of the CFD tests. The predictions for the jet growth and the velocity decay rate using the four turbulence models under investigation are then presented in section 7.4.2. The velocity profiles, the kinetic energy and eddy viscosity profiles are presented in sections 7.4.3-4.

7.4.1 Grid independency

The grid dependency for the subsonic flow was assessed by examining the predicted jet growth and velocity decay rates. A series of grid refinements was performed, and the results from these tests (with a slot width of 4mm) are presented in figures 7.27 and 7.28. The number of grid cells in each test are summarised in Table 7.2.

	Grid 1	Grid 2	Grid 3
No. of cells on curved portion of Coanda model	20	30	40
No. of cells on the flat diffuser section	20	30	40
No. of cells in the Y direction	30	40	50

Table 7.2 : Number of cells used in the grid dependency tests

The predicted jet growth rates using the standard $k-\epsilon$ model for the three grids are shown in figure 7.27. The results from the coarsest grid, grid 1, differ considerably from the results for the finer grids, 2 and 3, which are almost identical. This would suggest that a near grid independent result was obtained using grid 3. This is further illustrated in figure 7.28 which shows the predicted velocity decay rates. Similar grid dependency checks were performed for the 2 and 8mm slot widths. In all tests, convergence was generally achieved in fewer than 1500 iterations.

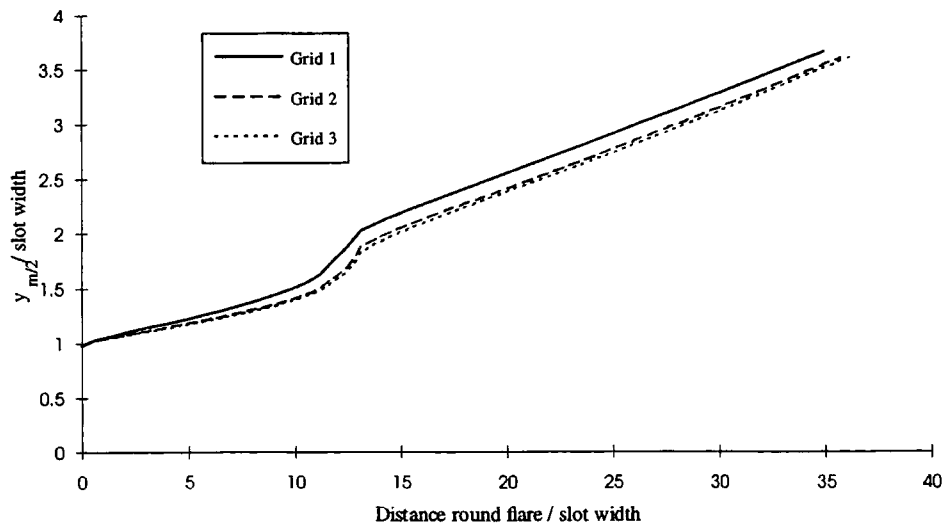


Figure 7.27 : Predicted growth rates for the 4mm slot width performed on three different grids

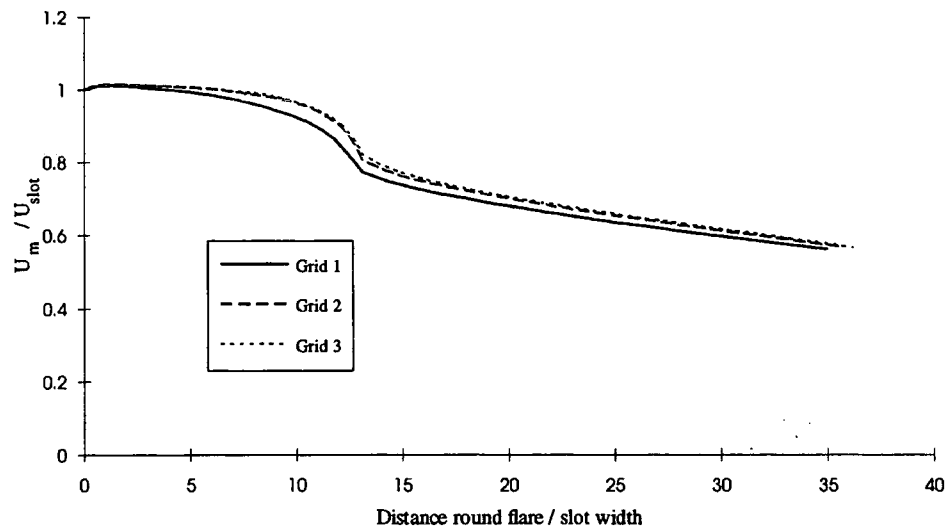


Figure 7.28 : Predicted velocity decay rates for the 4mm slot width performed on three different grids

7.4.2 The jet growth and velocity decay rate predictions

Four turbulence models were used to predict the planar Coanda flow field, namely the standard mixing length model, the mixing length model modified for curvature, the standard $k-\epsilon$ model, and the H-L model. A 'hybrid' of the mixing length model was also used for predicting the 2mm and 4mm slot width cases. This involved using the standard mixing length model on the curved portion of the Coanda surface, for a distance of 10 slot widths, and then switching to the modified mixing length model which enhanced the mixing rate on the remainder of the curved surface. This 'hybrid' could not be applied to the 8mm slot, since the switching distance would lie on the flat section which would produce the same result as the standard model.

The jet growth and velocity decay rate plots for the 2mm slot are shown on figure 7.29 and 7.30, those for the 4mm slot (at $P_a/P_o = 0.85$) are shown in figures 7.31 and 7.32, and the 8mm slot predictions are shown in figures 7.33 and 7.34. The relevant experimental data for each case is also plotted on these graphs for comparison. This experimental data was generated using estimated values for the maximum velocities, obtained using the method described in chapter 5, section 5.2.2. A comparison between

the predictions for the jet growth and velocity decay rate for the 4mm slot at the pressure ratios of 0.85 and 0.70 is also given in figures 7.35 and 7.36.

Different inlet turbulent kinetic energy levels were specified at the slot for the two $k-\epsilon$ based models. Realistic turbulence levels from measurements with a hot film placed at the slot exit found the turbulence to lie between 0.5 - 1%. The growth and velocity decay rates predicted by the standard $k-\epsilon$ model based on 1% turbulence at inlet were found to be very low. The tests described previously in section 7.2.4 (see figure 7.6) showed that slight increases in the inlet kinetic energy resulted in improved predictions for the jet growth rate. For this reason, the inlet kinetic energy was specified based on a higher turbulence level of 5%. This still resulted in growth rate predictions which were too low on the curved portion, however far better agreement was obtained on the plane wall recovery section. The more realistic turbulence levels based on actual experimental measurements were used for specifying the inlet kinetic energy for the H-L model which seems to perform much better than the standard model in the presence of curvature.

At each slot width, the standard $k-\epsilon$ model predicts the least amount of mixing on the Coanda surface, followed by the standard mixing length model, the H-L model, and then the modified mixing length model. On the flat section beyond the curvature, the modified and standard mixing length models predict the slowest growth rate, followed by the standard $k-\epsilon$ model. The H-L model predicts the greatest jet growth rate on the flat recovery section.

Both $k-\epsilon$ based models seem to show no effects of compressibility in the range of pressure ratios from 0.7-0.85, since the graphs for the two pressure ratios shown in figures 7.35 and 7.36 coincide. The mixing length models show slight compressibility effects. A small increase in the jet growth rate, and a slightly more rapid decay in the maximum velocity can be observed from figures 7.35-6 as the pressure ratio falls from 0.85 to 0.7. The experimental data presented in graphs 5.15 and 5.16 in chapter 5 showed negligible compressibility effects in the range of pressure ratios between 0.7 and 0.85.

The $k-\epsilon$ model has a tendency to perform poorly in flows with large extra strains, such as those involving curvature. This is illustrated by the fact the model predicts the least

jet growth rate on the curved portion of the flare surface. The effects of curvature are likely to be greatest in the case of the large slot width, since the ratio of the slot width to radius of curvature is greatest. It therefore may seem a surprising result that there is closest agreement between the experimental data and the predictions using the $k-\epsilon$ model for the 8mm slot. An explanation for this anomaly may lie in the jet development.

The large potential core of the jet issuing from the 8mm slot means the distance required for the jet to become fully developed is greater than that for the 4mm or 2mm slot widths. At the widest slot width, the experimental velocity profile (shown in figure 5.19(f)) shows the jet is not fully developed until 86° or more round the Coanda surface. The outer shear layer in this case grows relatively slowly, and the tendency of the $k-\epsilon$ model to underpredict the effects of curvature leads to the close agreement in the results. The discrepancy between the standard $k-\epsilon$ model predictions and the experimental data increases with a decrease in the slot width. The worst result of all is obtained for the 2mm slot case. The small potential core in the 2mm slot case means the jet is likely to be nearly fully developed by 32° round the flare surface. The inability of the $k-\epsilon$ model to predict the effects of curvature leads to the greatest discrepancy in this case.

The H-L and the modified mixing length models are both better at predicting the effects of curvature. The best agreement between the experimental data and the predictions of these models was obtained for the smallest slot width of 2mm. The H-L model appears to overpredict the growth rate on the flat section, however agreement seems better from the velocity decay plot. The mixing length model seems to overpredict the jet growth rate early on in the jet development, although the predictions are marginally improved using the 'hybrid' model, switching from the unmodified to the modified model after 10 slot widths. As the slot width increases, the modified mixing length model tends to overpredict the growth rate on the curved portion of the Coanda, whilst the performance of the H-L model seems to improve.

The modified mixing length model performs worst for the 8mm slot case. The H-L model performs well, although the results for the standard mixing length model and the standard $k-\epsilon$ model are also reasonable.

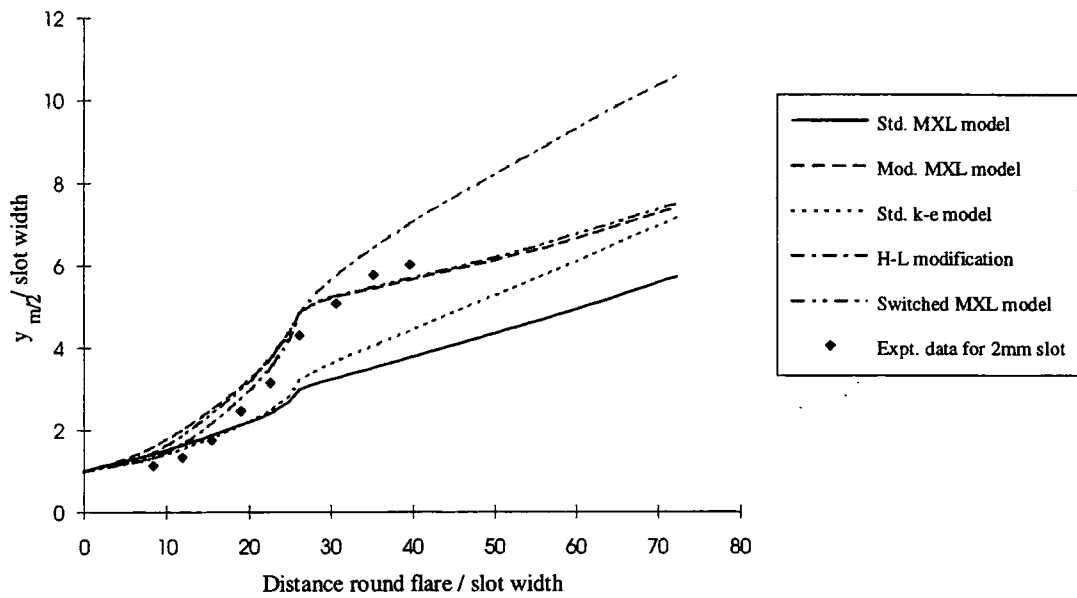


Figure 7.29 : Predicted jet growth rates for the 2mm slot at a pressure ratio of 0.85

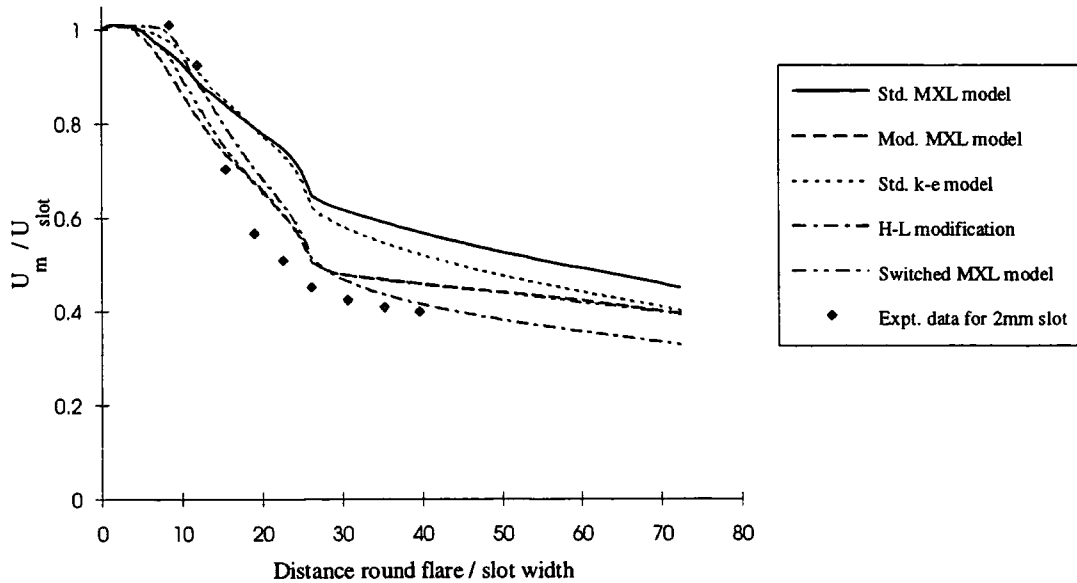


Figure 7.30 : Predicted velocity decay rates for the 2mm slot at a pressure ratio of 0.85

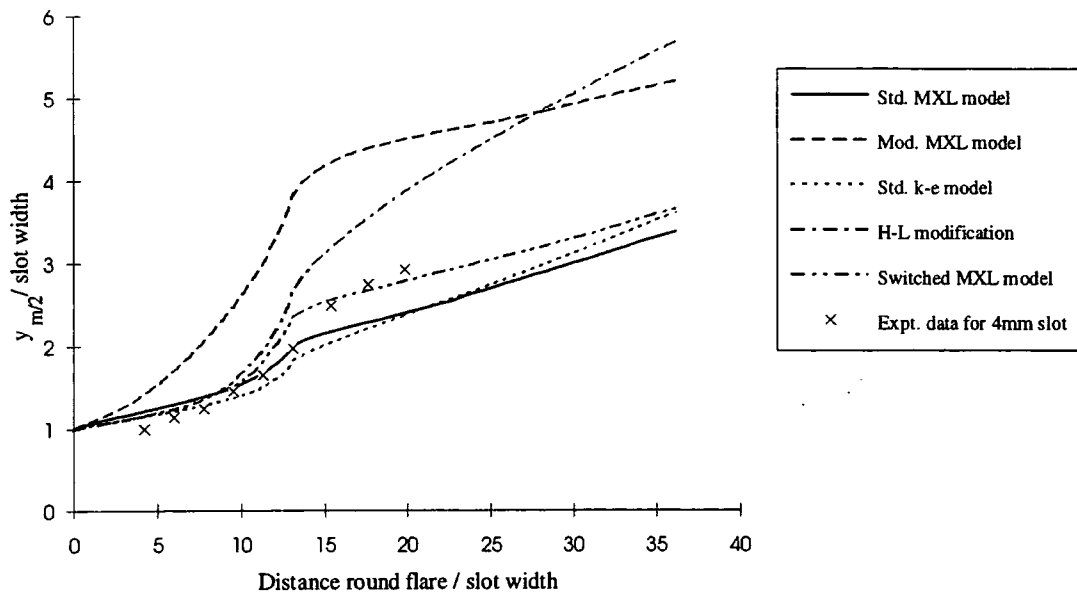


Figure 7.31 : Predicted jet growth rates for the 4mm slot at a pressure ratio of 0.85

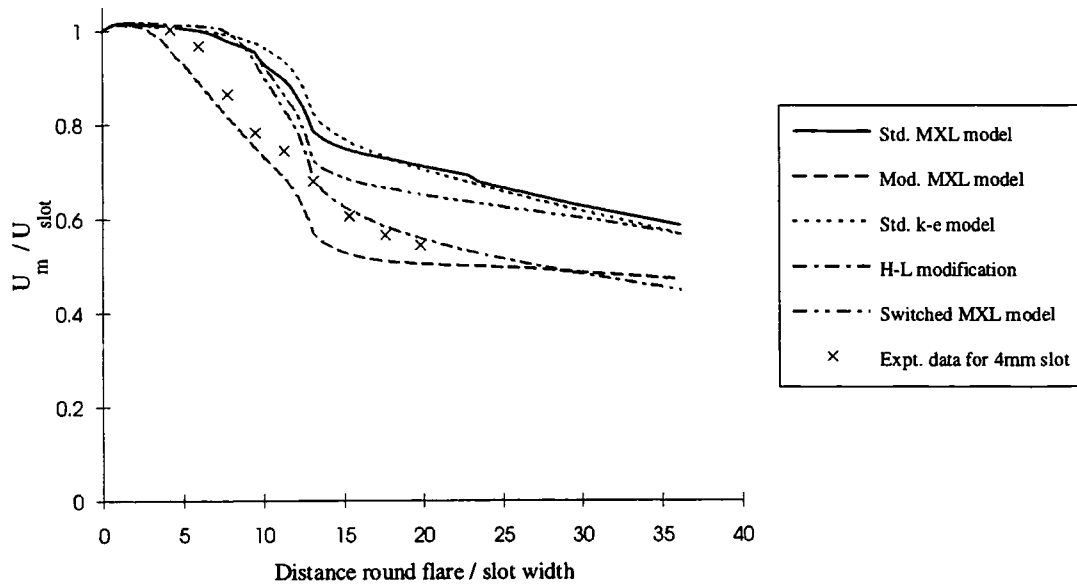


Figure 7.32 : Predicted velocity decay rates for the 4mm slot at a pressure ratio of 0.85

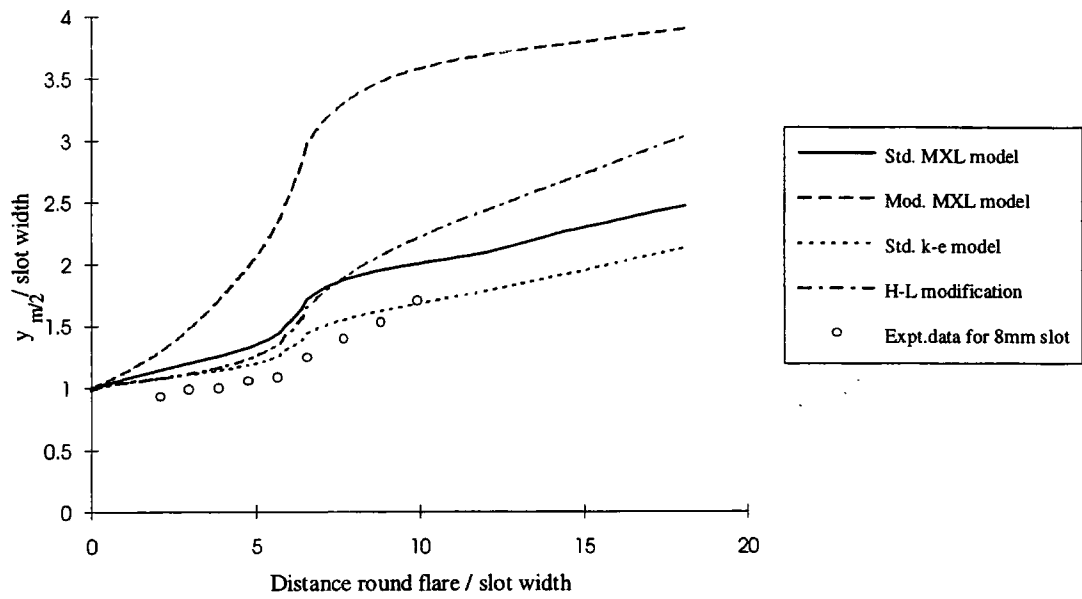


Figure 7.33 : Predicted jet growth rates for the 8mm slot at a pressure ratio of 0.85

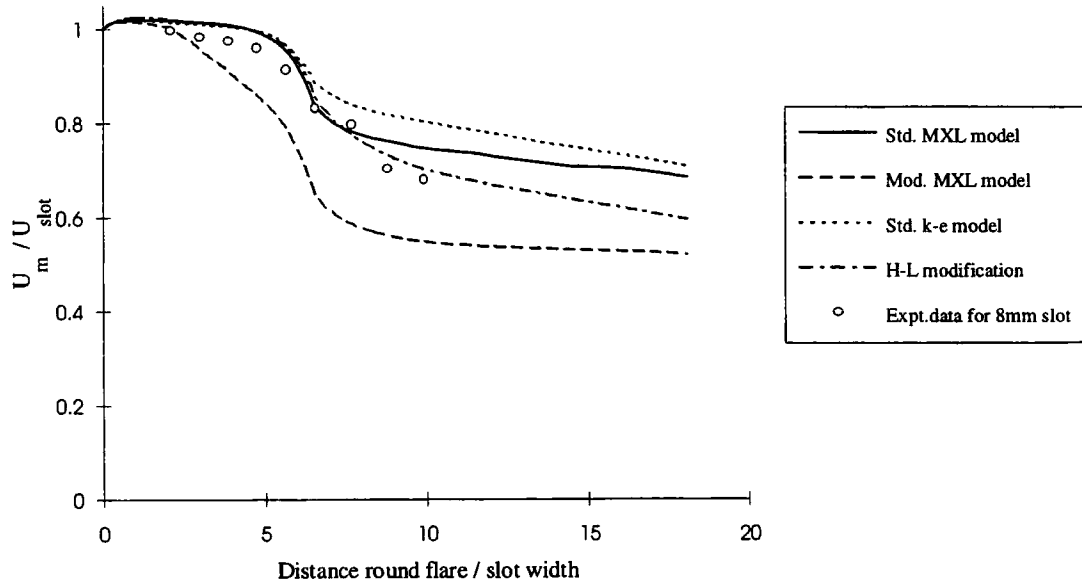


Figure 7.34 : Predicted velocity decay rates for the 8mm slot at a pressure ratio of 0.85

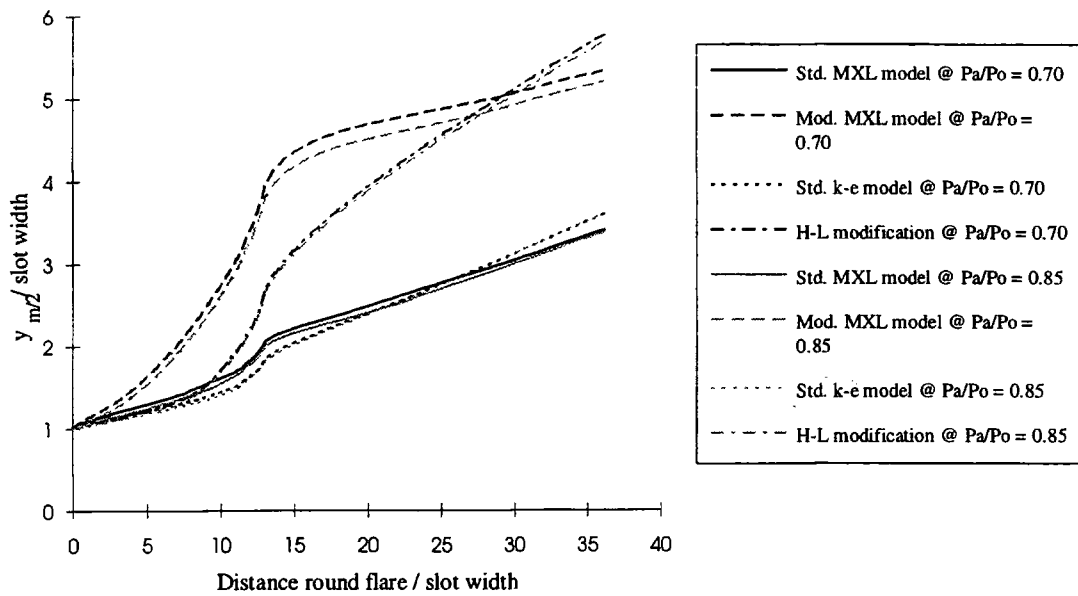


Figure 7.35 : Predicted jet growth rates for the 4mm slot at pressure ratios of 0.7 and 0.85

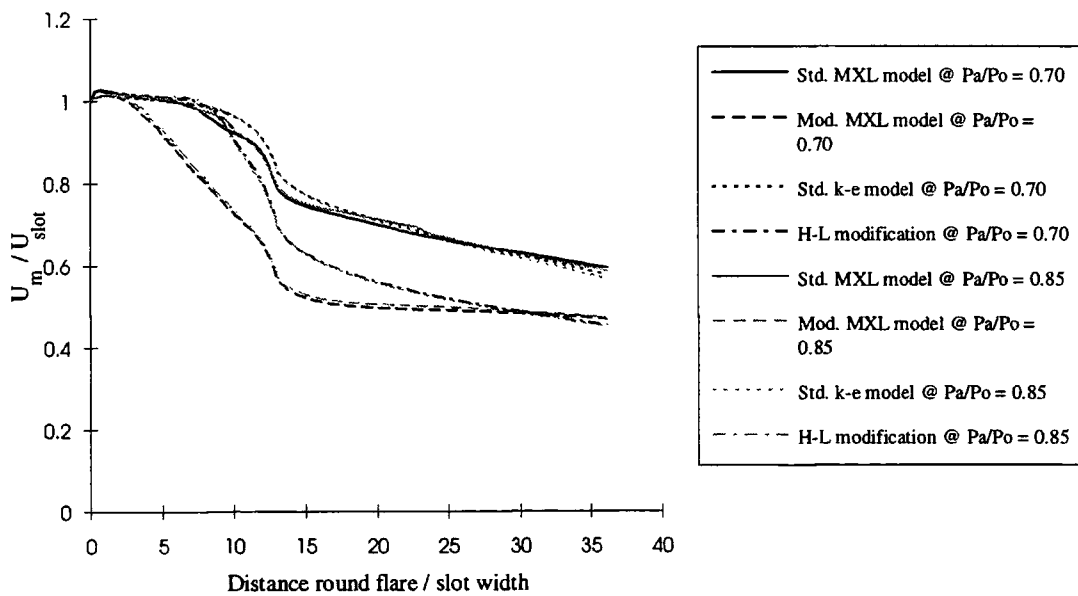


Figure 7.36 : Predicted velocity decay rates for the 4mm slot at pressure ratios of 0.7 and 0.85

7.4.3 Velocity profile plots

The growth rate and velocity decay plots for the constant slot case with a varying pressure ratio were very nearly identical, as shown in figure 7.36. The non-dimensionalised plots of velocity, turbulent kinetic energy and eddy viscosity were also found to be very similar, so the results at only the highest pressure ratio of 0.85 are used for presenting the 4mm slot data in the following sections.

The results of the four turbulence model predictions for the streamwise velocity profiles for the 2, 4 (at $P_a/P_o = 0.85$) and 8mm slot widths are presented in figures 7.37-7.39 respectively. The predictions for the normal velocity profiles for these slot widths are presented in figures 7.40-7.42. The results of the 'hybrid' mixing length model are also given for the 2mm and 4mm slot cases. The experimental data for each slot width is presented in each case for comparison.

The predicted streamwise velocity profiles for the 2mm slot case show apparent similarity from $\sim 59^\circ$ onwards around the Coanda surface. The profiles predicted by the $k-\epsilon$ based models for the 4mm slot case are 'squarer' in shape than the experimental profiles early on in the jet development. The standard model shows similarity from $\sim 86^\circ$ onwards, and the H-L model from $\sim 72^\circ$ onwards round the surface. The experimental profiles for the 4mm slot (figure 5.19 in chapter 5) show similarity in the profiles much earlier in the jet, from $\sim 45^\circ$ onwards. This suggests that $k-\epsilon$ based models are slow to predict the jet development. The velocity profiles for the 8mm slot are quite similar to those observed in the experimental tests. Both show the square profile early on in the jet development. This occurs in reality due to the prolonged existence of the large potential core of the jet.

There is little to choose between the models for the 2mm slot case. The modified mixing length model appears to perform the best for the 4mm slot case, however the H-L model seems to perform best for the 8mm slot.

The normal velocity profiles all consistently show a maximum radial velocity at 100° round the flare surface. For all three slot widths, the standard mixing length model and the standard $k-\epsilon$ model predict little inflow in the outer region of the jet. This was

reflected in the low predictions of entrainment and velocity decay rate using these two models. As the slot width increases, the jet outflow near the surface, and the inflow in the outer part of the jet becomes more exaggerated by the modified mixing length model, whilst the predictions of the 'hybrid' mixing length model and the H-L model are fairly similar and seem more realistic and less extreme.

Comparison with the experimental results is not easy due to the large amount of scatter in the results for this velocity component. However, in all cases the magnitude of the experimental radial velocity component is greater than that predicted using CFD. The discrepancy is greatest in the case of the 8mm slot, where the measured radial velocity is a factor of 2-4 times greater than that predicted. CFD predicts radial inflow occurs beyond $1.2 < y/y_{m/2} < 1.4$, whereas the experimental data appears to show radial inflow occurs beyond $y/y_{m/2} = 1.5$. The lack of similarity between the normal velocity component profiles is greatest in the case of the 8mm slot, which is in accordance with the theory that this case should be most strongly affected by curvature effects.

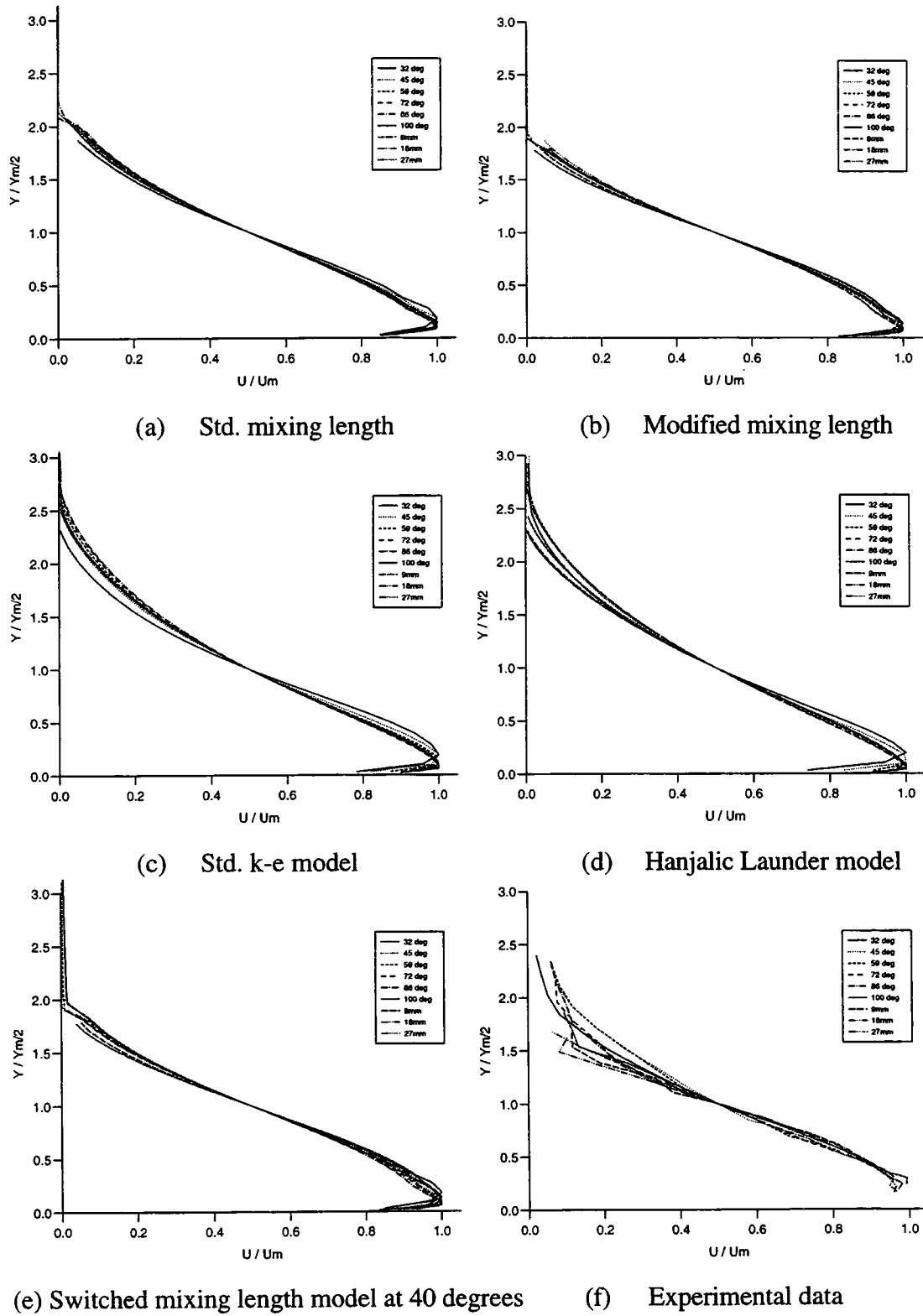


Figure 7.37 : Streamwise velocity profiles for the 2mm slot

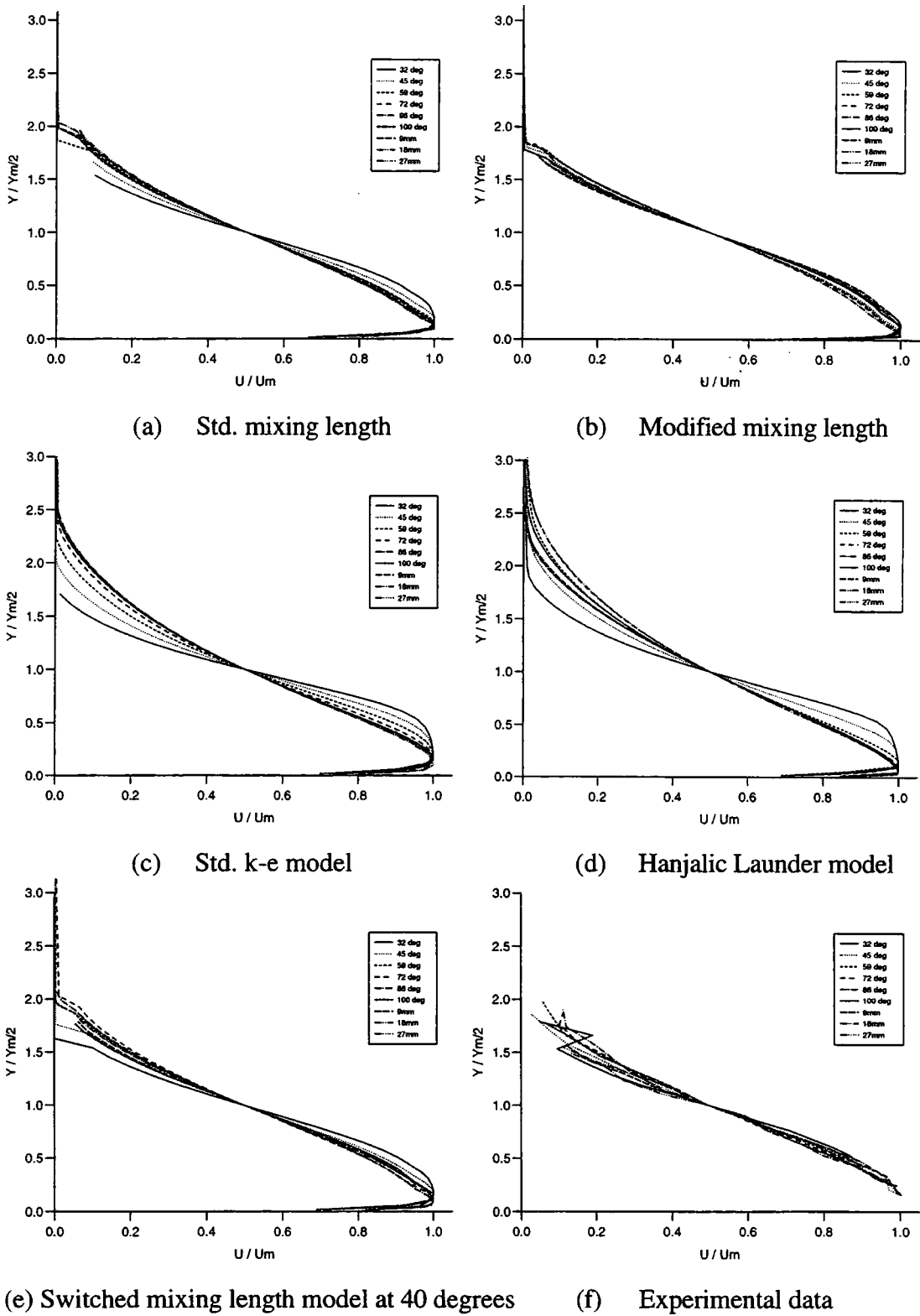


Figure 7.38 : Streamwise velocity profiles for the 4mm slot

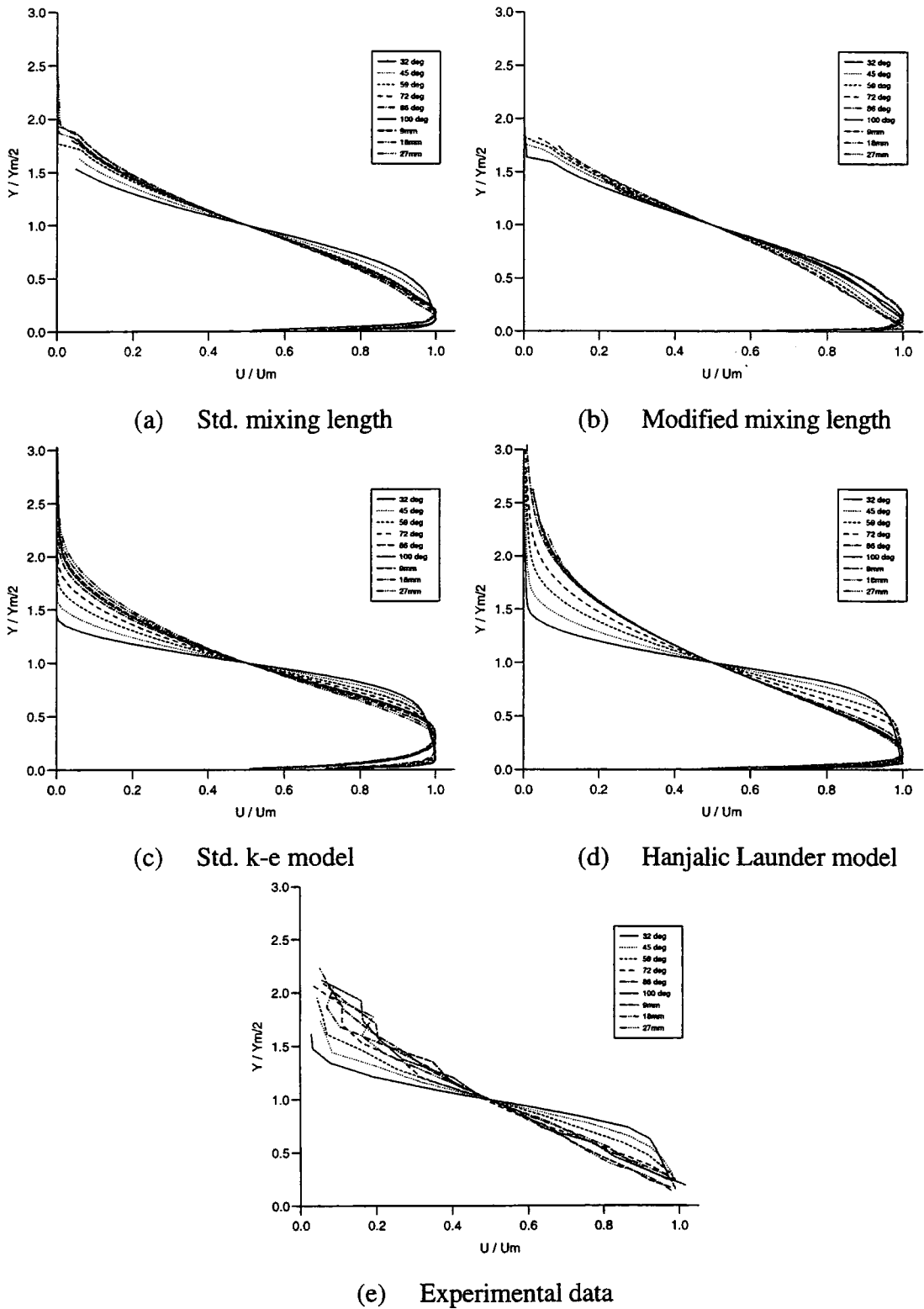


Figure 7.39 : Streamwise velocity profiles for the 8mm slot

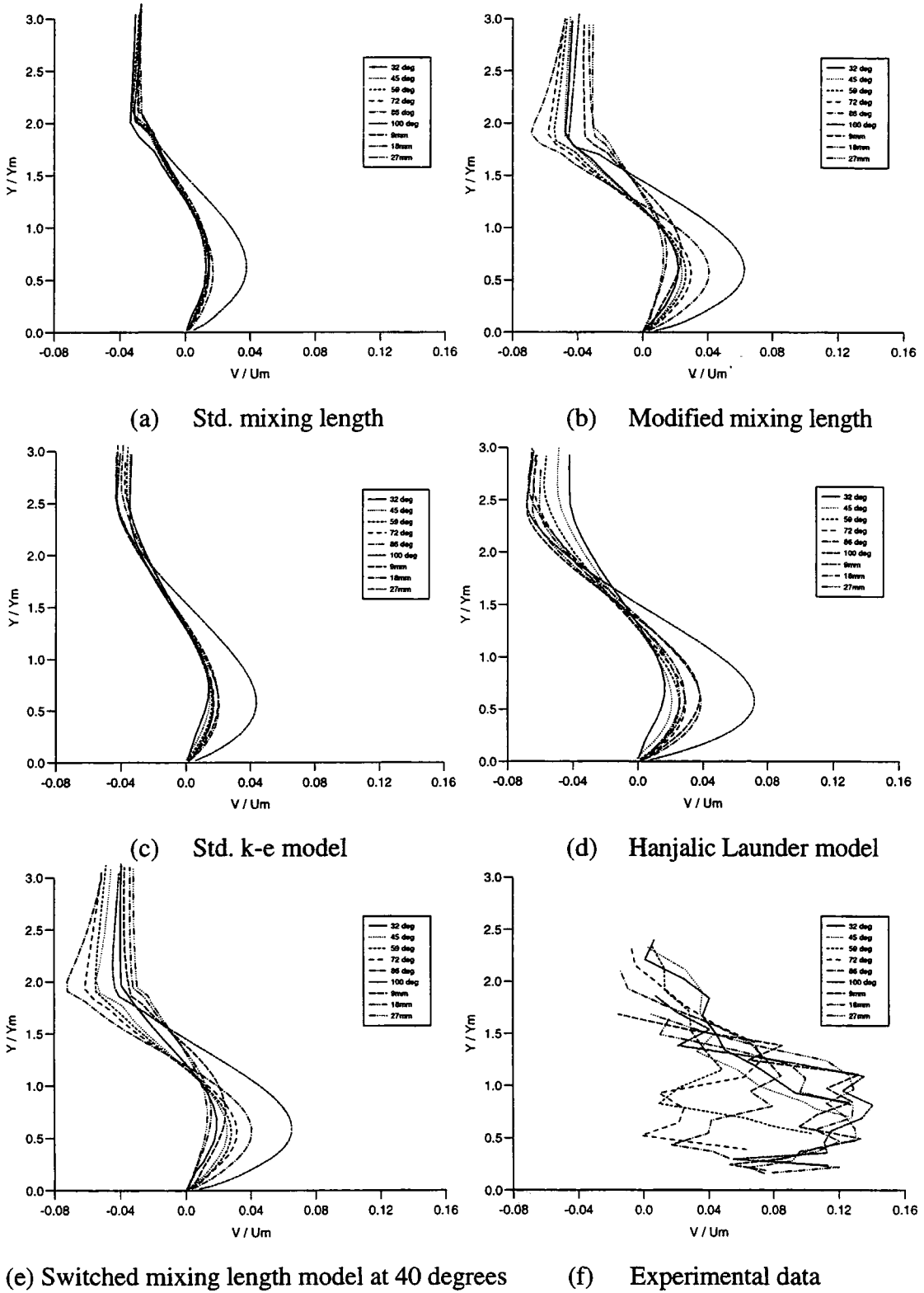


Figure 7.40 : Normal velocity profiles for the 2mm slot

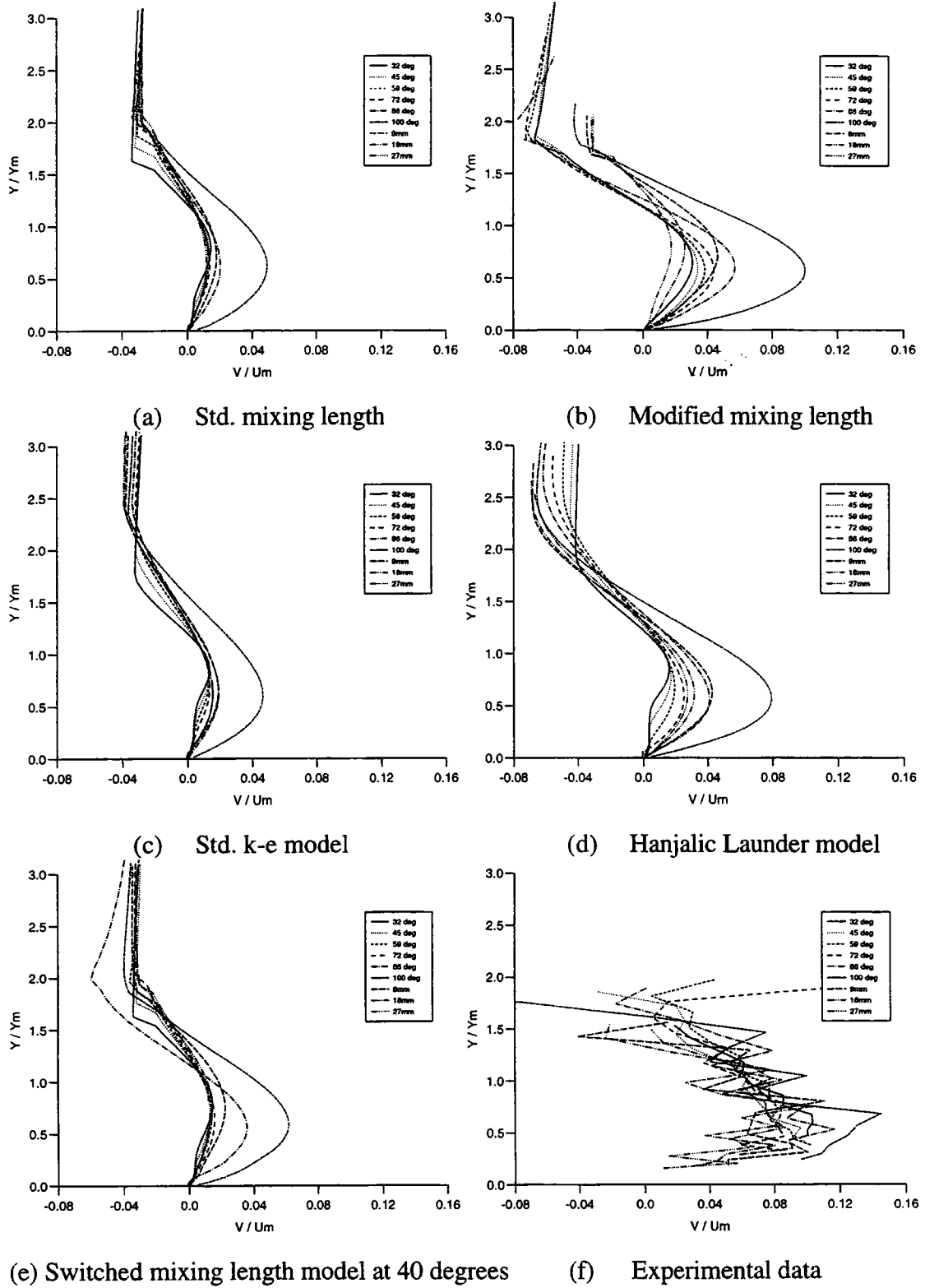


Figure 7.41 : Normal velocity profiles for the 4mm slot

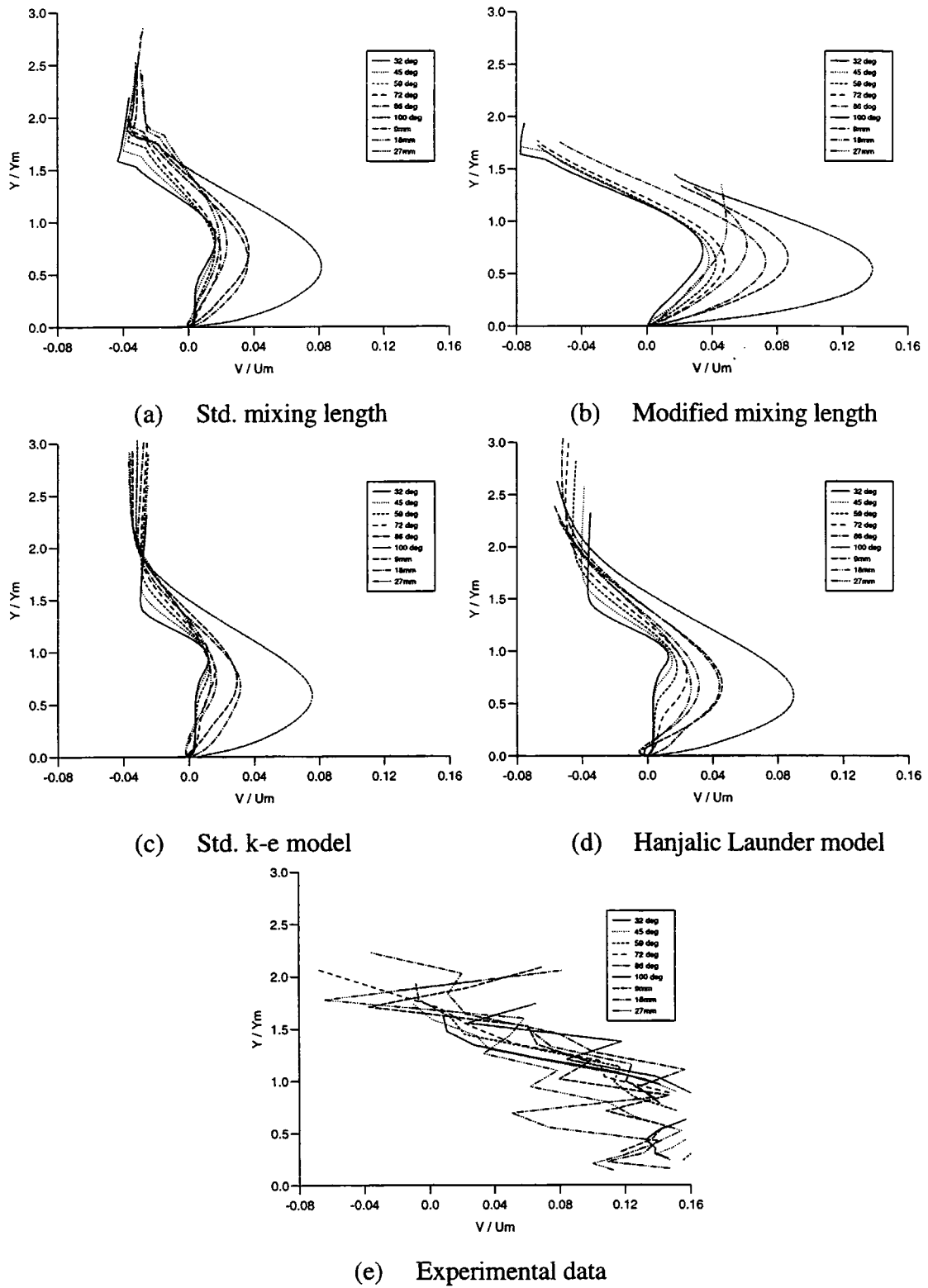


Figure 7.42 : Normal velocity profiles for the 8mm slot

7.4.4 Kinetic energy and eddy viscosity profiles

The kinetic energy profiles for the 2, 4 and 8mm slots widths are given in figures 7.43-7.45. The eddy viscosity profiles for the three slot widths are shown in figures 7.46-7.48. The kinetic energy has been approximated for the mixing length model using the turbulent eddy viscosity and the length scale, using the Prandtl-Kolmogorov relationship, given in equation (6.13).

In all cases, the CFD predicts a rise in the turbulent kinetic energy around the Coanda surface. Both the CFD results and the experimental data show peaks in the profiles close to $y/y_{m/2} = 1.0$ early on in the jet development. Further round the Coanda surface, both show a shift of this peak inboard of 1.0. In the case of the 2mm slot width, a maximum in turbulent kinetic energy is reached at the end of the curvature, at 100° . The turbulent kinetic energy levels are then predicted to steadily fall along the flat recovery section. The $k - \epsilon$ based models predict the kinetic energy level at 27mm up the flat section to be similar to those at the 86° position. The mixing length models predict a more rapid decline in the kinetic energy levels on the flat section, predicting values at the 27mm position which are similar to those at $\sim 59^\circ$. The results for the 4mm slot case differ slightly. The mixing length model still reaches a maximum at 100° , however the $k - \epsilon$ based models predict a maximum in turbulent kinetic energy occurs 9mm up the flat section. In addition, the rate of decline in the kinetic energy along the flat section is less, falling to just 89% of the 100° value. The results for the 8mm slot width follow a similar trend. The mixing length based models in this case reach a maximum at 9mm up the flat section and the decline in turbulent kinetic energy along the recovery section beyond this is only slight. The $k - \epsilon$ based models show a maximum occurring at 18mm along the flat section, and there is very little reduction in turbulent kinetic energy levels by 27mm along the section.

As the slot width increases from 2mm to 8mm, the maximum level of turbulent kinetic at the 32° position is predicted to decrease. By contrast, the experimental data shows a slight increase in the turbulent kinetic energy level at this point as the slot width increases. However, the predicted magnitudes of the turbulent kinetic energy are consistently higher than those measured by experiment. For example, the experimental

data is only 20% of the H-L prediction for the 2mm slot, and 50% of the H-L prediction for the 8mm slot.

The predicted eddy viscosities levels are a better indication of the ability of the turbulence models to predict the levels of mixing in the Coanda jet. The scatter and uncertainty in the experimental data for the Reynolds shear stress \overline{uv} however makes comparisons between the CFD predictions and the experimental measurements difficult.

At each slot width, the eddy viscosity levels predicted by the standard mixing length model and the standard $k-\epsilon$ model are significantly lower than the levels predicted by the modified mixing length model and the H-L model. The mixing length based models all predict a rise in eddy viscosity round to the $\sim 86^\circ$ position, and by 100° the eddy viscosity levels have fallen. For the modified mixing length model, the eddy viscosity levels are predicted to fall well below the levels at the 32° position. This dramatic drop off in v_t is reflected in the jet growth rate predictions, where the jet grows rapidly on the curved portion of the Coanda surface, where the mixing levels are high, and little growth occurs on the flat recovery section. This sudden change in character reflects the inability of the mixing length model to account for history effects in the flow. The $k-\epsilon$ based models predict that, for the 2mm slot case, a maximum in v_t is reached at the 86° position, followed by a gradual decrease in magnitude beyond this. For the 4mm slot case, a maximum is reached at 100° , and for the 8mm slot a maximum occurs at 27° up the flat section.

As with the turbulent kinetic energy, the magnitude of the CFD predictions for the eddy viscosity is too great early on in the jet development, and this discrepancy is least in the case of the 8mm slot. The CFD predictions all show peaks in the profiles to occur around $y/y_{m/2} = 1.0$. Such peaks are not generally evident in the experimental data due to the large amount of scatter.

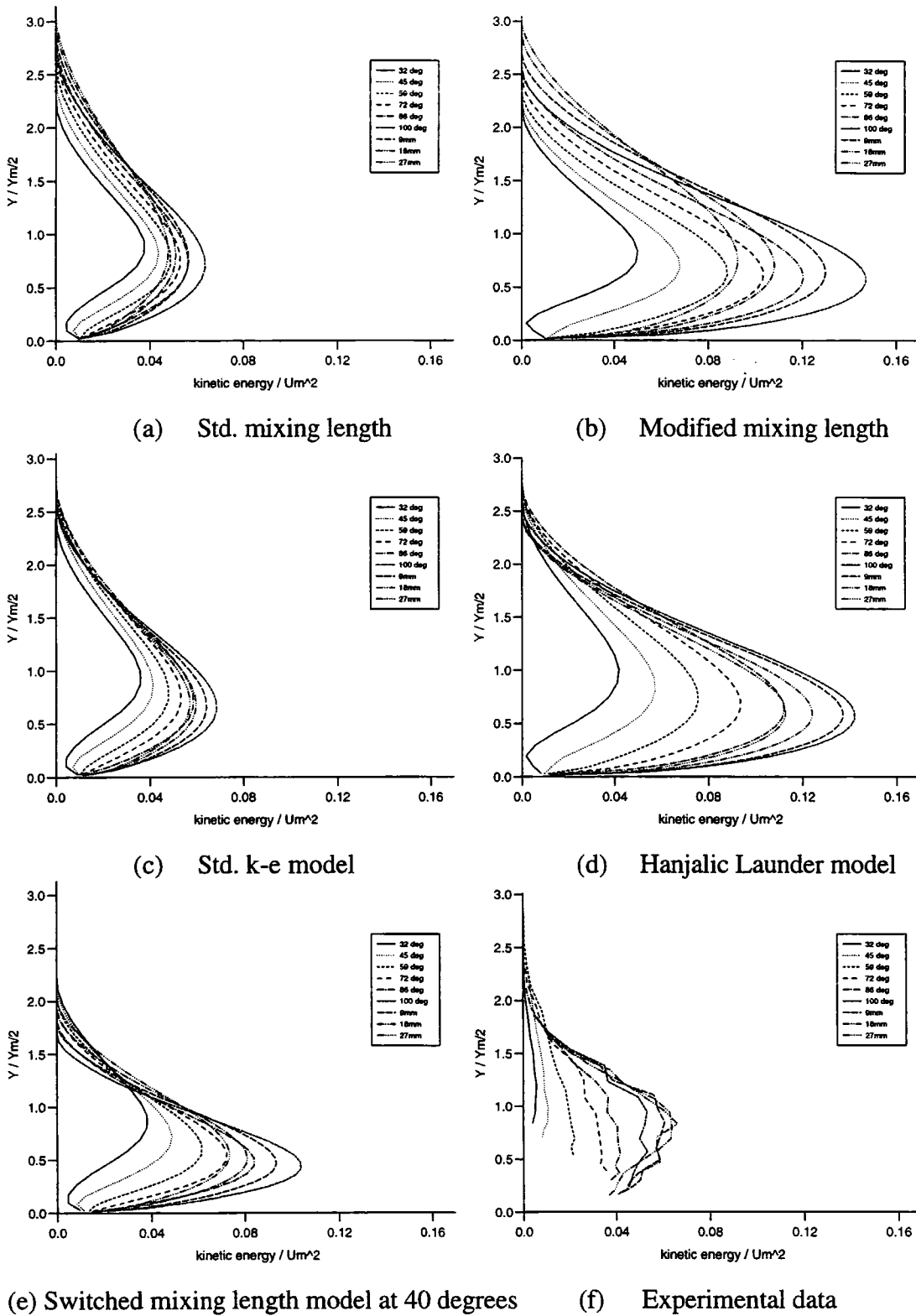


Figure 7.43 : Turbulent kinetic energy profiles for the 2mm slot

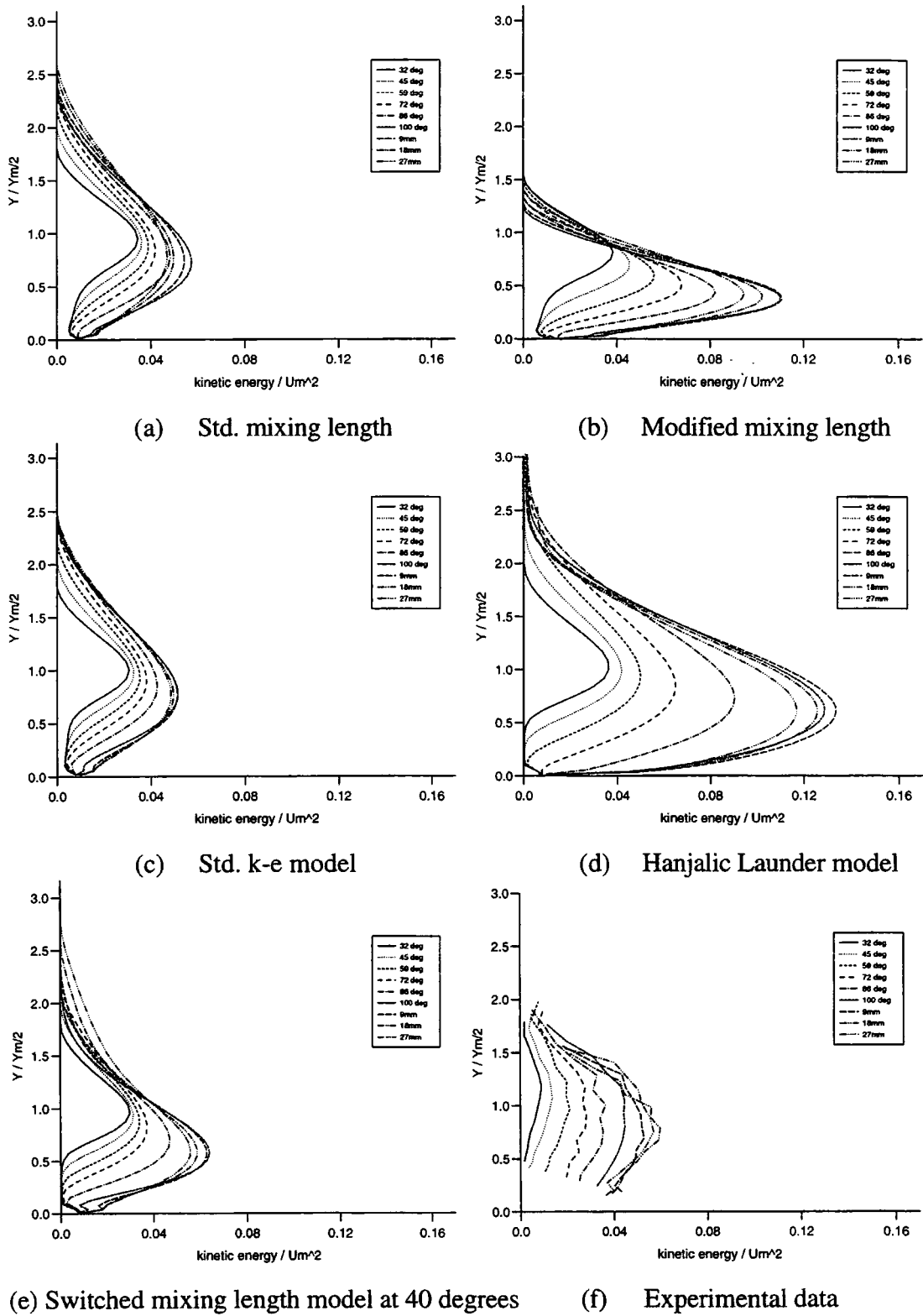


Figure 7.44 : Turbulent kinetic energy profiles for the 4mm slot

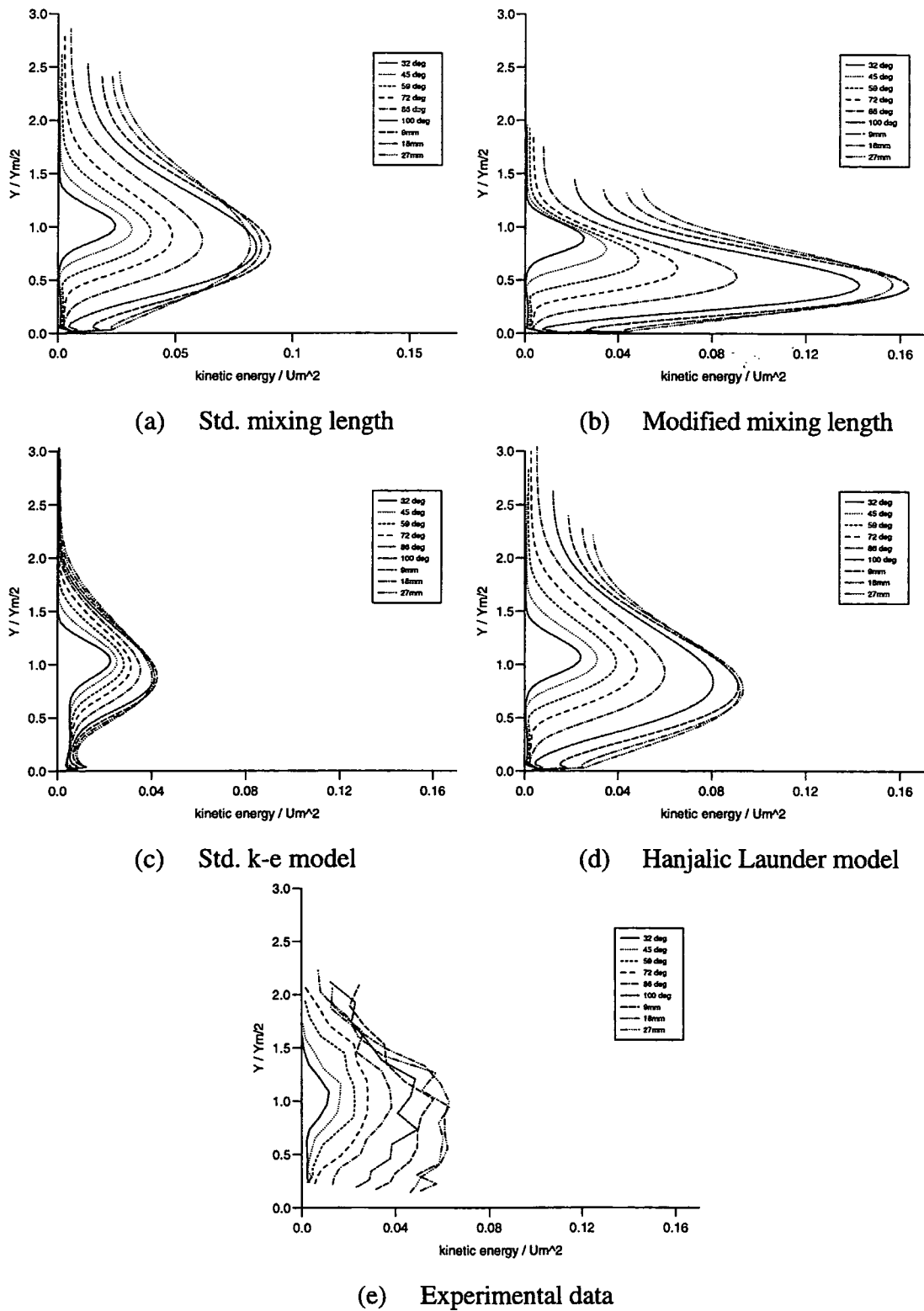


Figure 7.45 : Turbulent kinetic energy profiles for the 8mm slot

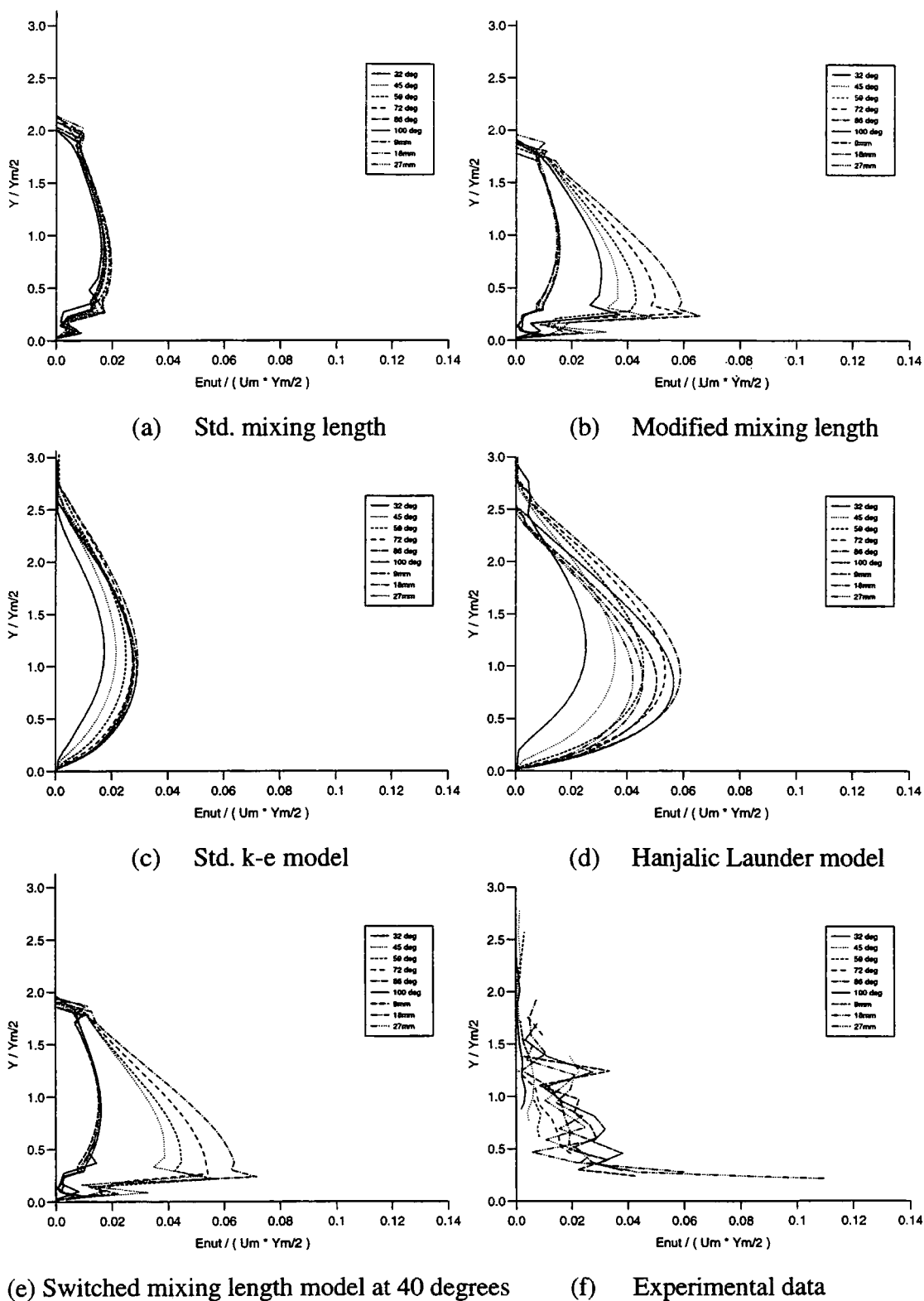


Figure 7.46 : Eddy Viscosity profiles for the 2mm slot

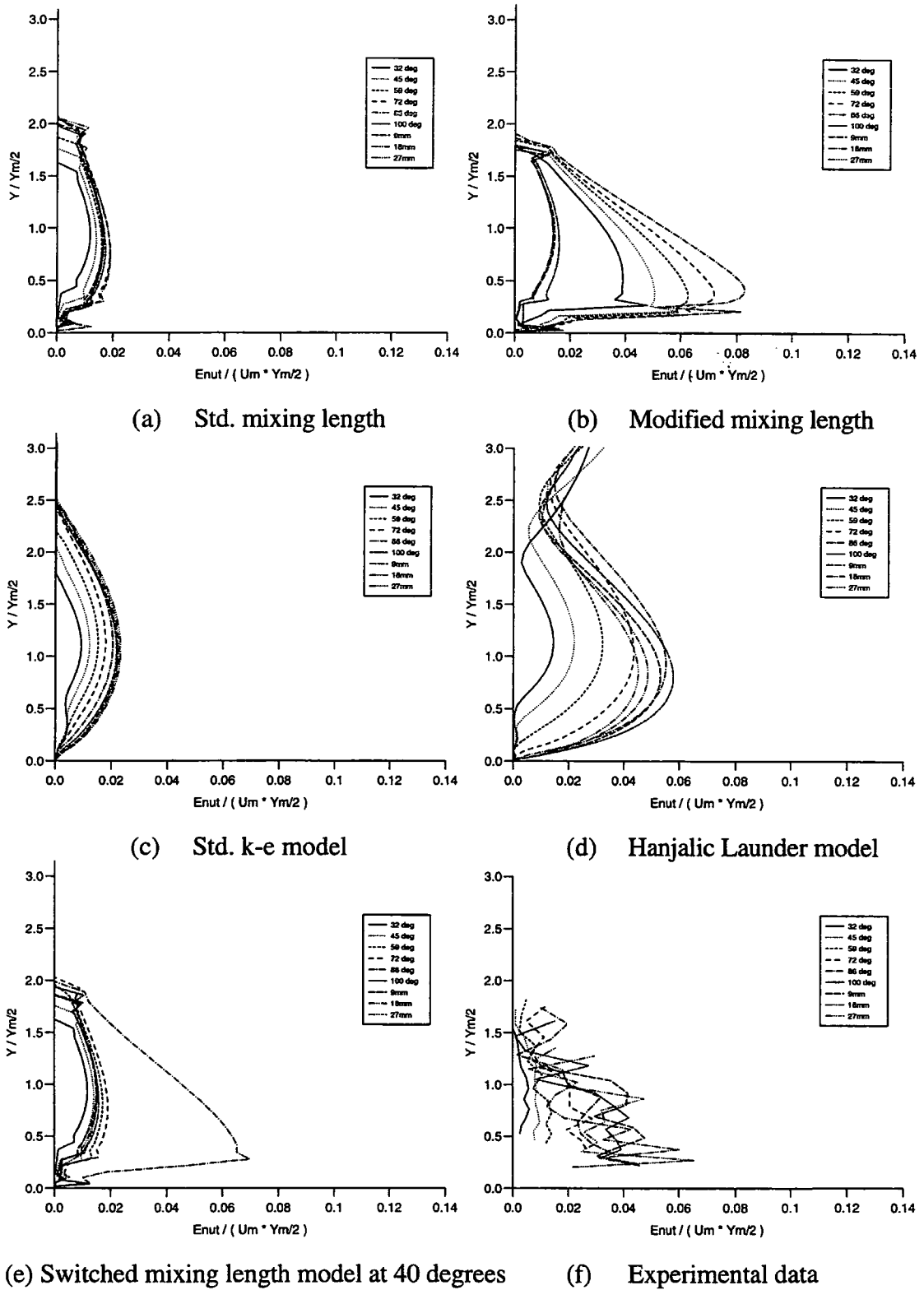


Figure 7.47 : Eddy Viscosity profiles for the 4mm slot

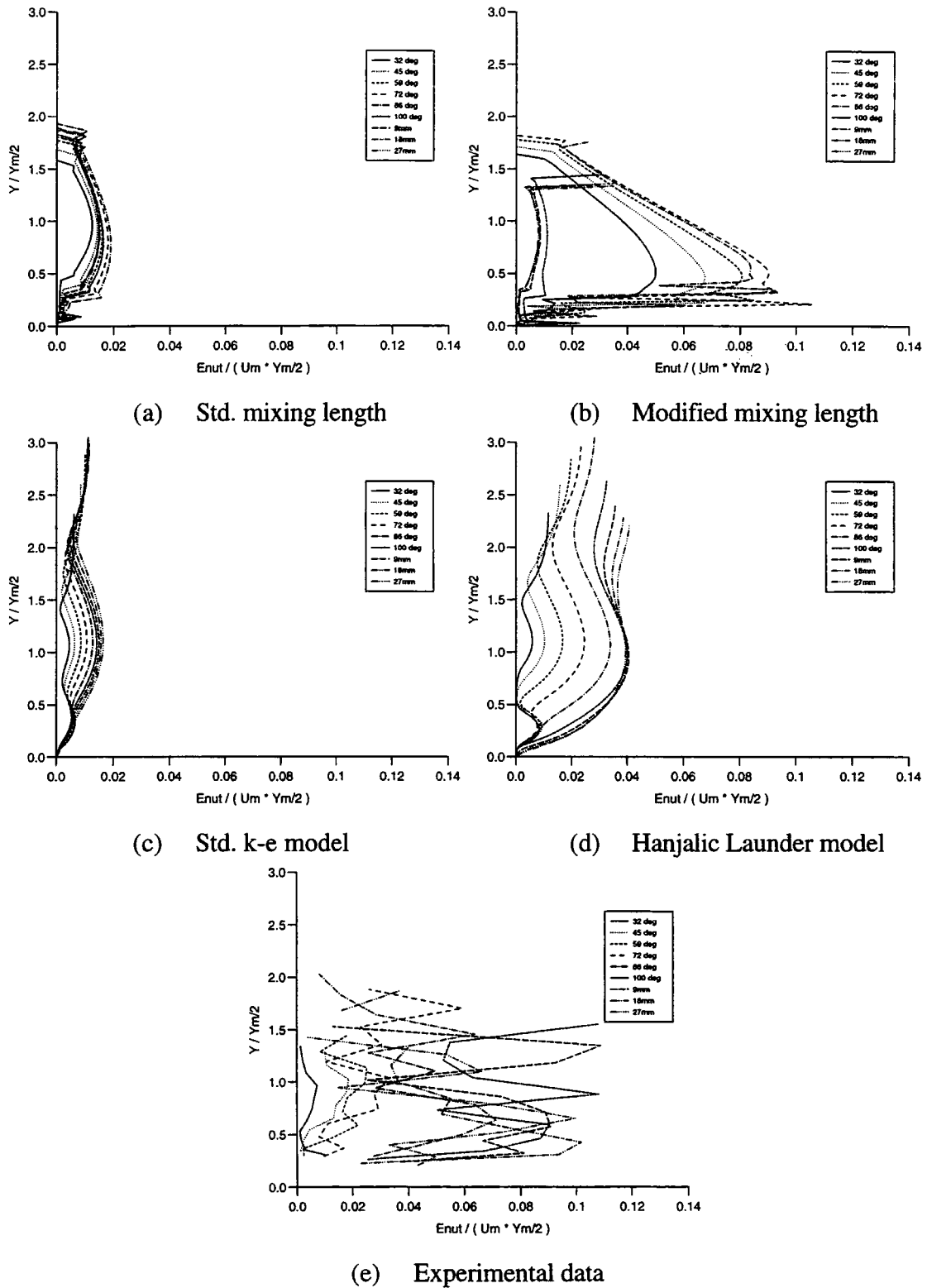


Figure 7.48 : Eddy Viscosity profiles for the 8mm slot

Chapter 8

Discussion

8.1 Experimental accuracies

There are various sources of error in the experimental results presented in chapter 5. These errors result from calibration errors in the low speed region; the positional accuracy of the hot film probes, and drifting of the calibration characteristics of the hot film probes due to oil contamination. The method used to approximate the magnitude of the maximum velocity at each traverse position also introduces an error into the jet growth and velocity decay plots, and the non-dimensionalised profiles for the velocity, turbulent kinetic energy and eddy viscosity.

The critical dimensions used to position the hot film probe, L1, L2 and L3 (defined in figure 5.2), were measured to an accuracy of 0.1mm. This, coupled with the positional accuracy of the rotary stage stepper motor, results in an initial positioning accuracy of $32^\circ \pm 0.08^\circ$. The hot film is therefore positioned within an accuracy of 0.1mm radially, and ± 0.2 mm tangentially. The automated movement of the traverse gear back to the start position after the first probe traverse reduces the positioning errors between probe runs. Any discrepancy in the position of the two probes is likely to be due to errors in the measurement of the probe dimensions, and the positional accuracy of the traverse gear, which should return to within 0.05mm of its initial start position. The probe dimensions were measured using an optical micrometer which gave readings to an accuracy of ± 0.01 mm.

An indication of the accuracy of the mass flux solutions was given by equation (4.23). In general the error was less than 4%. However, in the outer region of the jet where the velocity falls below approximately 50m/s, the accuracy of the solution method deteriorated, with some errors in excess of 30% due to the lack of reliable calibration data in this velocity range. The method used to approximate the density of the flow also introduces an error into the analysis, estimated to be approximately 1%.

The errors due to the hot film sensor contamination were harder to quantify, since the levels of contamination were variable between traverse runs. In the most extreme case, the effective velocity was found to differ by up to 10% from the original calibration value. The data from this traverse run was ignored, and the traverse repeated using newly calibrated sensors. Typically, the calibration was found to drift by less than 2% between the beginning and end of a traverse run. The drift in the calibration characteristics as the traverse progresses results in a gradual underestimate of the effective velocity experienced by the hot film sensor. The net effect is that the maximum velocity appears to decrease more rapidly than in reality with distance round the surface. The jet growth and velocity decay rates may be slightly overestimated round the latter part of the Coanda model.

The positional accuracy, and the drift in the calibration characteristics of the hot film probes may account for the uncertainties in the calculations for the Reynolds stresses. Variations in the air supply to the Coanda model, caused by drifting of the regulator valve, could also be a contributory factor for problems in the analysis of the experimental data. The streamwise normal stress was calculated with reasonable consistency between traverse runs, as was the transverse normal stress, $\overline{w^2}$, which was calculated solely from the straight film data. This straight film data also provided solutions for the streamwise fluctuations, $\overline{u^2}$, and the Reynolds shear stress \overline{uw} . An indication of the consistency between the measurements of the slanted and the straight sensor was obtained by comparing the two solutions for $\overline{u^2}$ and \overline{uw} . Both solutions for the Reynolds shear stress were small, demonstrating a similar degree of scatter about zero. The values for the transverse normal stress calculated from the two sets of data were generally in good agreement, differing typically by less than 7%, although in a few cases the discrepancy was greater than 20%. The largest errors occur in the solutions for the radial normal stress, $\overline{v^2}$, and the Reynolds shear stress, \overline{uv} , and the source of this problem could be attributed to a combination of the factors discussed above.

8.2 Streamwise curvature effects

Convex streamwise curvature has the effect of an extra rate of strain on the flow. From experimental measurements, it has been found to enhance the mixing rate of the jet, resulting in jet growth rates and velocity decay rates which are beyond those of a plane wall jet. The turbulent fluctuations have all been measured to be greater than those in a plane wall jet. Accordingly, the turbulent kinetic energy levels in the curved flow are higher than the corresponding plane wall case. The eddy viscosity levels are also modified by the curvature. The curved wall jet on a constant radius of curvature has also been shown to be a non-equilibrium flow, lacking self-preservation in the turbulence quantities. Apparent similarity was found in the streamwise velocity profiles, however the lack of self-preservation in the mean flow was demonstrated by the lack of similarity in the normal velocity profiles.

The strength of the curvature effect on a flow is determined by the ratio of the slot width to the radius of curvature. The larger this ratio is, the greater the effects on the turbulent eddy structure. It has been observed that the turbulence structure and the mean flow do not return instantly to the plane wall conditions once the curvature is removed, since a finite distance is required for the modified eddy structure to shrink back to that of a plane wall jet flow.

The effects of streamline curvature can best be understood and explained by examining the equations for the production of turbulence energy. These are given by Wilson and Goldstein (1976) as follows :

$$\text{Production rate of } \overline{u^2}/2, \pi_u = -\frac{\overline{u^2}}{1+y/R} \frac{\partial U}{\partial x} - \underbrace{\frac{\overline{uv}}{\partial y} \frac{\partial U}{\partial y}}_{\text{Shear induced production}} - \underbrace{\frac{\overline{u^2}V + \overline{uv}U}{R+y}}_{\text{Coriolis force contribution}} \quad (8.1)$$

$$\text{Production rate of } \overline{v^2}/2, \pi_v = -\frac{\overline{uv}}{1+y/R} \frac{\partial V}{\partial x} - \overline{v^2} \frac{\partial V}{\partial y} + \underbrace{\frac{2\overline{uv}U}{R+y}}_{\text{Centrifugal force contribution}} \quad (8.2)$$

$$\text{Production rate of } \overline{w^2}/2, \pi_w = 0 \quad (8.3)$$

$$\text{Production rate of turbulent kinetic energy, } \pi = \pi_u + \pi_v + \pi_w \quad (8.4)$$

In two dimensional mean flow, the production rate of the transverse velocity fluctuations, $\overline{w^2}$ is zero. The transverse fluctuations are maintained by the static pressure fluctuations which redistribute energy amongst the normal Reynolds stresses. From equation (8.2), the production rate of the radial fluctuations may be seen to be increased by centrifugal forces acting in the outer region of the jet. This increased production accounts for the higher turbulence intensities measured in the radial direction of the Coanda flow. However, the higher levels of turbulence measured in the streamwise direction are not as a direct result of the Coriolis or centrifugal forces. Equation (8.1) shows that the Coriolis force actually decreases the production of $\overline{u^2}/2$ in the outer part of the jet where \overline{uv} is positive. The higher levels of streamwise fluctuations are actually caused by the shear induced production term (indicated in equation (8.1)), and by the static pressure fluctuations which transfer the energy from the augmented radial fluctuations. The shear induced production term is increased in curved flow by the action of the centrifugal forces which increase the production of \overline{uv} , as shown in equation (8.5).

$$\text{Production rate of } \overline{uv}, \pi_{uv} = \frac{\overline{u^2}}{1+y/R} \frac{\partial V}{\partial x} - \overline{v^2} \frac{\partial U}{\partial y} - \underbrace{\frac{\overline{v^2}U}{R+y}}_{\text{Coriolis force contribution}} + \underbrace{\frac{2\overline{u^2}U}{R+y}}_{\text{Centrifugal force contribution}} \quad (8.5)$$

The centrifugal instabilities in convex curved flows are therefore responsible for the rapid mixing of curved wall jets with the surrounding stationary fluid. The curvature also results in sub-atmospheric pressure on the curved surface. Surface pressure measurements were not monitored in this experimental work. However, reference is made in chapter 7 to the findings of Senior who recorded sub-atmospheric surface pressures on the Coanda flare model used in this work. One further effect of the convex streamwise curvature is to shift the position of the zero shear stress from $y/y_{m/2} = 0.5$ to $y/y_{m/2} < 0.1$. This phenomenon could not be measured in this experimental study due to restrictions imposed by the probe geometry and the problems with sensor breakages.

The relative size of the potential core has been found to be important when comparing the jet growth rates and velocity decay rates of different slot widths. The relatively large potential core of a jet issuing from an 8mm slot requires a significant distance round the Coanda surface before the outer shear layer grows to form a fully turbulent jet. The

outer shear layer of a jet issuing from a 2mm slot grows to fill the jet width in a much shorter distance round the flare surface. In the early part of the jet development, the turbulence intensity profiles were found to reach a maximum at $y/y_{m/2} = 1.0$. This maximum has been found to shift towards $y/y_{m/2} = 0.5$ as the jet becomes fully developed.

8.3 Assessment of the turbulence modelling

No single turbulence model or numerical scheme gave accurate predictions under all flow conditions. Three flow regimes have been considered in this work. Initial CFD tests were performed on a low speed axisymmetric model of the Coanda flare. The performance of three turbulence models was assessed by examining the predictions for the jet growth rate and the velocity decay rate, along with values for the eddy viscosity. The results were compared against the experimental findings of Hawkins (1988). This work was then extended to high speed jet flows over a Coanda surface, and comparisons were made against the experimental findings of Senior (1990). In these tests the CFD results were assessed according to the surface pressure predictions, and artificial Schlieren images were generated for comparison against those obtained experimentally. This work also studied the ability of turbulence models to predict jet breakaway. The main emphasis of these high speed tests was to establish whether the shock cell structure of the underexpanded Coanda jet is predicted correctly. The final series of tests involved compressible flow at pressure ratios above those of choked nozzle conditions, so the shock cell structure was absent. In these tests, the CFD predictions were assessed by comparing them against jet growth and velocity decay rates measured experimentally in this work, along with the kinetic energy and eddy viscosity values. The success of these CFD tests are summarised in the sub-sections below.

8.3.1 Incompressible flow predictions

The modifications proposed by Morrison (1982) to the mixing length model to take account of the effects of streamline curvature and divergence were implemented into the GROUND coding of PHOENICS. This model gave quite reasonable predictions for the jet growth and velocity decay rates, and the values for eddy viscosity were far larger than those predicted by the standard $k - \epsilon$ model. The performance of the standard $k - \epsilon$

model was found to be very poor. The modification to the standard $k-\epsilon$ model proposed by Hanjalic and Launder was implemented by modifying the PHOENICS source code. These changes augmented the predictions for the eddy viscosity, and the jet growth rate was also increased, although it was still less than measured in reality. Both this, and the modified mixing length models over-predicted the jet growth rate in the early stages of the jet development. Both models failed to predict the thinning of the jet and the flow acceleration at the slot. The effects of varying the inlet kinetic energy were investigated, and growth rate was found to show some dependency on this inlet condition. Significant increases in the specified inlet kinetic energy did increase the growth rate further round the Coanda surface. However, the result was an even greater overprediction of the growth rate early on in the jet development.

8.3.2 Compressible flow predictions

Compressible flow tests were performed on a planar model of the Coanda flare, and the results were compared against the experimental data of Senior (1991). The turbulence models studied were the modified mixing length model, the standard $k-\epsilon$ model, the RNG and the Chen Kim forms of the $k-\epsilon$ model. Convergence problems prevented the use of the H-L model in these high speed tests. The mixing length model once again predicted a very high jet growth rate on the curved section of the Coanda. The growth rate for the $k-\epsilon$ model was much lower than this, but still exceeded the predictions of the RNG and the Chen Kim forms of the model. No experimental data for the jet growth or velocity decay rates exists at these low pressure ratios, so these results could not be validated.

Experimental data does exist however for the surface static pressures, provided by Gilchrist (1985) and Senior (1991). These experimental studies showed that as the pressure ratio falls, a series of peaks and troughs appear in the surface pressure coefficient. These correspond to the presence of a shock cell system around the Coanda surface. As the pressure ratio drops to a critical value, a flat region appears in the first trough. This corresponds to a separated region on the Coanda surface. As the pressure ratio drops still further, this separated region grows in size, until it eventually joins with a second separated region forming further round the Coanda surface. A large zone of separation exists, which, with a slight decrease in pressure ratio results in the jet breaking

away from the surface - an important phenomenon which requires accurate prediction, known as jet breakaway.

None of the turbulence models investigated predicted these constant pressure regions corresponding to the flow separation. The standard $k-\epsilon$ model predicted the first shock cell with greatest accuracy. However, this and the other models predicted the shock waves to move downstream and go out of phase with the shocks which occur in reality. The mixing length model gave the poorest predictions, possibly due to the excessive levels of mixing predicted, which rapidly damps out the effects of the inviscid core. Improvements to the shock cell structure predictions were obtained by using a higher order numerical scheme which reduced the amount of numerical diffusion. The best results were obtained with the standard $k-\epsilon$ model which successfully predicted the position and magnitude of the first shock cell, and to an extent the second shock cell. This improvement was monitored not only in the surface pressure predictions, but also in the similarity between artificially generated Schlieren images and those obtained through experiment by Senior and Gilchrist.

The final section of chapter 7 presented the CFD predictions for the experimental work described in this thesis. Four different turbulence models were used in these tests, namely the standard mixing length model, the standard $k-\epsilon$ model, the modified mixing length, and the H-L model. A combination of the standard and modified mixing length models, referred to as the 'hybrid' model, was also applied in two of the test cases. The CFD results were validated using the experimental data obtained using hot film anemometry. One set of tests was performed at a constant pressure ratio of 0.85 for 2, 4 and 8mm slot widths, and a second series of tests was performed using a constant slot width of 4mm, at pressure ratios of 0.7, 0.75, 0.80 and 0.85. This second set of tests showed that the compressibility effects appear to be negligible in this pressure ratio range. The velocity profiles, the turbulent kinetic energy and eddy viscosity profiles were found to be very nearly identical at each pressure ratio, hence only the highest pressure ratio profiles were presented in chapter 7.

The standard $k-\epsilon$ model and the unmodified mixing length model were found to underpredict the jet growth rate and velocity decay rate on the curved portion of the Coanda surface. The H-L model and the modified mixing length model were both found

to predict greater mixing than the equivalent standard models. The modified mixing length model was found to overpredict the level of mixing as the slot width increases. On the flat recovery section the modified mixing length model was found to underpredict the jet growth rate, whilst the H-L model slightly overpredicts the growth rate. The 'hybrid' mixing length model was found to perform much better than the fully modified model. Switching from the unmodified to the modified mixing length model after ten slot widths resulted in much better agreement in the 4mm slot case, and little difference in the 2mm slot case. The standard mixing length model performed better than the modified model in the case of the 8mm, due to the large potential core. To summarise, the H-L form of the $k-\epsilon$ model appears to give the best overall performance in this pressure ratio range.

The results for all the CFD tests were consistent, although there are certain discrepancies between the predicted and experimental results. The magnitude of the positive normal velocity component gives an indication of the amount of mixing in the jet, which should increase with the amount of radial out-flow. Higher levels of mixing in the jet are indicated by higher eddy viscosity levels, higher turbulent kinetic energy, and a greater jet growth rate and more rapid velocity decay. The consistency of the CFD predictions may be illustrated by considering the results for the 4mm slot. The H-L model was shown in figure 7.41 to predict higher radial out-flow velocities (i.e. to have a more positive normal velocity component) than the standard $k-\epsilon$ model. The turbulent kinetic energy and eddy viscosities, shown in figures 7.44 and 7.47, were also predicted to be higher by the H-L model. These differences are all reflected in the jet growth rate and velocity decay plots (figures 7.31 and 7.32) which show the H-L model predicts greater entrainment and mixing than the standard $k-\epsilon$ model. The predictions of the standard mixing length and standard $k-\epsilon$ model for the normal velocity, turbulent kinetic energy and eddy viscosity profiles were found to be very similar, and so not surprisingly were the growth rate and velocity decay plots. Finally, the modified mixing length model was found to predict positive normal velocities which were in excess of those predicted using the H-L model. The turbulent kinetic energy and eddy viscosities were also found to be greatest with this model. In accordance with this, the modified mixing length model can be seen in figures 7.31 and 7.32 to predict the greatest jet growth and velocity decay rates.

A discrepancy is apparent when the experimental data is compared to the CFD predictions. The magnitude of the measured normal velocities is in excess of the greatest CFD prediction, given by the modified mixing length model. However the trend does not extend to the turbulent kinetic energy profiles and the eddy viscosities, both of which are smaller than any of the CFD predictions. This discrepancy may largely be due to errors in the experimental data, since the scatter in the normal velocity profiles and the \overline{uv} Reynolds shear stress (and hence eddy viscosity) suggest the error in these components is significant. However, none of the turbulence models studied take accurate account of the effects of streamwise curvature, and all assume incorrectly, that the eddy viscosity is isotropic. It would appear that the mean flow can be predicted with reasonable confidence using relatively simple turbulence models, however improvements in the predictions may be possible if a more complex model, such as the Reynolds stress model, is used. Such models take account of eddy viscosity anisotropy, and the effects of pressure reflections from the wall. The errors associated with the mean flow calculation are far less than those for the fluctuating components, so it is feasible that the discrepancy between the CFD results and the experimental findings is largely due to experimental error.

8.3.3 Jet breakaway predictions

The mechanism of breakaway, as previously explained, is highly dependent on the shock cell structure, and the prediction of flow separation. The Chen Kim and the RNG model were both found to perform best in these circumstances. The standard $k-\epsilon$ model is notoriously poor at predicting separation, and showed no signs of separation at pressures well in excess of the experimentally determined breakaway pressures. Using the standard numerical scheme, the RNG and the Chen Kim models both predicted the jet issuing from the 4mm slot would breakaway at a pressure of 4.8 bar. The breakaway pressure recorded by Senior was in fact only 4 bar. The CFD predictions were greatly improved by the use of the higher order numerical scheme, which resulted in a large region of recirculating flow on the Coanda surface at a pressure of 4.15 bar, and total jet breakaway at a pressure of 4.3 bar. This overprediction of the jet breakaway was attributed to the use of wall functions, which assumes the boundary layer is turbulent and therefore less susceptible to separation than the laminar boundary layer which exists in the real flow.

Chapter 9

Conclusions and future work

9.1 Conclusions

- An increase in slot width results in a jet with a larger potential core. A jet becomes fully developed when this potential core no longer exists, due to the growth of the outer shear layer. The potential core from the 8mm slot persists for a greater distance round the surface than that of the 2mm slot, hence the jet growth rate for the larger slot appears less than that for a smaller slot early on round the Coanda surface.
- The Reynolds number effects have been found to be negligible in the range of pressure ratios studied, i.e. 0.85 to 0.7.
- A modified version of the mixing length model (which takes account of the effects of streamline curvature and divergence) has been found to give reasonable predictions for the incompressible, axisymmetric wall jet. However, the model greatly over-predicts the effects of curvature in compressible flows.
- The Hanjalic-Launder modification to the $k-\epsilon$ model gives reasonable predictions for the mean flow in incompressible and compressible flows. The best agreement was achieved with the 2mm slot which rapidly forms a fully developed jet, however agreement deteriorates as the slot width increases due to the prolonged existence of the potential core.
- All the turbulence models studied predicted the levels of turbulent kinetic energy and eddy viscosity incorrectly. The relatively simple nature of the model formulations cannot accurately account for the full effects of curvature on the turbulence structure.
- The predictions of the underexpanded compressible jet have been assessed using the surface pressure predictions. The standard $k-\epsilon$ model has been found to predict the shock cell structure with greatest accuracy. The Chen-Kim and RNG forms of the $k-\epsilon$ model both resulted in high numerical diffusion, and the mixing length model

greatly over-predicts the mixing rate in the jet which leads to the early elimination of the inviscid core. The shock cell structure predictions of all the models were improved by using a higher order numerical scheme.

- Artificial Schlieren images have successfully been generated, showing the salient features of the first two shock cells round the flare surface. The fine details of the real flow cannot be resolved without much finer grid refinement, which can lead to convergence problems.
- The Chen-Kim and RNG $k-\epsilon$ models were found to give the best jet breakaway predictions. The shock structure has a strong influence on the mechanism of jet breakaway, hence predictions were further improved by using the higher order numerical scheme.
- No one turbulence model has been found to give accurate predictions under all flow conditions. Each turbulence model has strengths and weaknesses, depending on the flow situation. The performance of each model is dependent on the differencing scheme used to discretise the equations. The turbulence models described in this thesis have been used on versions 2.0 and 2.1 of PHOENICS using the standard hybrid differencing scheme, and a higher second order scheme of Roe (1982). The results which may be obtained using more recent versions of the CFD code may differ slightly from these reported here, and further improvements in the predictions may be made using more sophisticated differencing schemes which may become available in later versions.

9.2 Suggestions for further work

There is a great deal of scope for future research work in this field, however a number of problems would need to be addressed before further work could be conducted on the present rig. The greatest problem which prevented more extensive work being performed in this project was the cleanliness of the air supply. The oil vapours entering the atmosphere through leaks in the pipework, and the calibration nozzle and flare outlets were a health hazard. The filters currently present in the line should be sufficient, however a thorough clean of all the pipework downstream of the compressor and the filters would be recommended to remove the extensive oil and particulates which have amassed in the pipework through rusting and oil carry over from the compressor. The pipework carrying the filters is currently in the same room as the Coanda flare. Isolation of this pipework from the experimental laboratory would reduce the oil vapour problem. The introduction of a ventilation system in the experimental laboratory would also ease the situation by extracting the air vented from the flare and the calibration nozzle.

The experimental tests in this work were limited to pressure ratios of no less than 0.7. However, if the above measures are taken to improve the cleanliness of the air and the supply pipework, it should be possible to extend the experimental tests down to choked flow conditions. The problems of strain gauging of the hot film sensors (discussed in chapter 4) may also need to be addressed at higher operating velocities. Prato *et al* (1998) used miniature platinum hot film probes to which they applied Epoxy at the base of the sensor prongs to damp out the flow induced vibrations. A similar technique may also be required for the high speed Coanda flow field.

The experimental measurements presented in this thesis were all obtained from a planar model of the Coanda flare. The next obvious step would be to extend this work to turbulence measurements on an axisymmetric model of the Coanda flare, to study the additional effects of divergence on the turbulence structure. These results could then be compared directly to those of Morrison and Hawkins who both studied incompressible flow over axisymmetric models of the Coanda flare.

The method of traversing the hot film anemometer could be changed for both the planar and axisymmetric models to allow measurements in the early part of the jet development,

between the slot and 32° . The changes to the traverse gear would be minimal, and the analysis software would require only minor changes. The probe would be introduced facing into the flow instead of perpendicular to the jet, as illustrated in figure 3.2. Introducing the probe end on into the flow should also reduce the problems associated with strain gauging, and the problems of prong resonance.

There is also a great deal of scope for further work on the computational side. The CFD results at high speeds have highlighted a number of issues which could be investigated in the future. Further work is necessary to obtain stable solutions at the high speeds using finer and finer grids, to confirm the grid density required to provide a grid independent solution.. This may require the use of different numerical schemes, and / or turbulence models. The use of other higher order numerical schemes could also yield improvements in the shock cell structure, and hence the breakaway predictions.

All the CFD predictions of the Coanda flare have involved grids which extend only from the slot exit. The velocity is therefore assumed to be uniform across the slot. It may be beneficial in the future to model the flow upstream of the slot to see if non-uniformity of the flow at the slot exit has a significant effect on the downstream flow predictions.

A further drawback of the CFD work described in this thesis is as a result of the use of wall functions. These assume that the boundary layer is fully turbulent. The high accelerations of the flow at exit result in an initially laminar boundary layer which is more susceptible to separation than a turbulent one. Further work could involve the use of a low Reynolds number turbulence model which dispenses with the use of wall functions, which have the potential for predicting the transition between a laminar and turbulent boundary layer, such as the two equation model of Jones and Launder (1972). Higher order models, such as the Reynolds stress model, could also improve on the predictions of the Coanda flow field by taking account of the anisotropy of the eddy viscosity.

Bibliography

- ALCARAZ, E. (1977) 'Contribution à l'étude d'un jet plan turbulent évoluant le long d'une paroi convexe à faible courbure', Thèse d'Etat, Université Claude Bernard, Lyon
- ALCARAZ, E., CHARNAY, G. & MATHIEU, J. (1976) 'Measurements in a wall jet over a convex surface', *Physics of Fluids*, Vol.20, pp.203-210
- BOUSSINESQ, J. (1877) 'Theorie de l'écoulement tourbillant', *Mem. Pre. par. div. Sav.* 23, Paris
- BRADSHAW, P. (1969) 'The analogy between streamline curvature and buoyancy in turbulent shear flow', *J. Fluid Mechs.* Vol.36, pp.177
- BRADSHAW, P. (1973) 'Effect of streamline curvature on turbulent flow', *AGARDograph* No. 169
- BRADSHAW, P. (1975) *An introduction to turbulence and its measurement*, Pergamon Press Ltd., Oxford
- BRADSHAW, P., FERRIS, D. H. & ATWELL, D. H. (1967) 'Calculation of boundary layer development using the turbulent energy equation', *J. Fluid Mechs.*, Vol.28, p.593
- BRADSHAW, P. & GEE, M. T. (1960) 'Turbulent wall jets with and without an external stream', National Physical Laboratory, Aeronautical Research Council Report 22008, FM 2971
- BRUUN, H. H. (1971) 'Linearisation and hot wire anemometry', *Journal of Physics E : Sci. Instrum.* Vol. 4, pp. 815-820

Bibliography

- BRUUN, H. H. (1995) *Hot Wire Anemometry - Principles and Signal Analysis*, Oxford University Press
- CEBICI, T. & SMITH, A. M. O. (1974) *Analysis of turbulent boundary layers*, Academic, New York
- CHAMPAGNE, F. H., SLEICHER, C. A. & WEHRMANN, O. H. (1967) 'Turbulence measurements with inclined hot wires', *J. Fluid Mechs.*, Vol.28, Part 1, pp.153-175
- CHEN, Y. S. & KIM, S. W. (1987) 'Computation of turbulent flows using an extended k- ϵ turbulence closure model', N.A.S.A. CR-179204
- CHENG, G. C. & FAROKHI, S. (1992) 'On turbulent flows dominated by curvature effects', *J. Fluids Engng. - Trans. of ASME*, Vol.114, No.1, pp.52-57
- DAKOS, T., VERRIOPOULOS, C. A. & GIBSON, M. M. (1984) 'Turbulent flow with heat transfer in plane and curved wall jets', *J. Fluid Mechs.* Vol. 145, pp. 339-360
- ESKINAZI, S. & YEH, H. (1956) 'An investigation on fully developed turbulent flows in a curved channel', *J. Aero. Sci.*, Vol.23 p.23
- FAN, S. & LAKSHMINARAYANA, B. (1993) 'Low Reynolds number k- ϵ model for unsteady turbulent boundary layer flows', *AIAA J.*, Vol.31, No.10, pp.1777-1784
- FEKETE, G. I. 'Coanda flow of a two-dimensional wall jet on the outside of a circular cylinder', McGill University, Dept. of Mech. Eng., Rept. 63-11
- FINGERSON, L. M. & FREYMUTH, P. 'Thermal Anemometers', Technical paper, TSI Manual
- FREYMUTH, P. (1968) 'Noise in hot wire anemometers', *Rev. Sci. Instrum.*, Vol.39, No.4, pp.550-557

- FREYMUTH, P. (1977) 'Frequency response and electronic testing for constant temperature hot wire anemometers', *J. Phys. E : Sci. Instrum.*, Vol.10, pp.705-710
- FUJISAWA, N. & KOBAYASHI, R. (1987) 'Turbulence characteristics of wall jets along strong convex surfaces', *Int. J. Mech. Sci.*, Vol.29, pp.311-320
- GIBSON, M. M., JONES, W. P. & YOUNIS, B. A. (1981) 'Calculation of turbulent boundary layers on curved surfaces', *Phys. Fluids*, Vol.24, pp.386-395
- GIBSON, M. M. & RODI, W. (1981) 'A Reynolds stress closure model of turbulence applied to the calculation of a highly curved mixing layer', *J. Fluid Mech.*, Vol.103, pp.161-182
- GIBSON, M. M. & YOUNIS, B. A. (1982) 'Modelling the curved turbulent wall jet', *A.I.A.A. J.*, Vol.20, No.12, pp.1707-1712
- GILCHRIST, A. R. (1985) 'The development and breakaway of a compressible air jet with streamline curvature and its application to the Coanda flares', Ph.D. Thesis, Univ. of Durham
- GILCHRIST, A. R. & GREGORY-SMITH, D. G. (1988) 'Compressible Coanda wall jet : Predictions of jet structure and comparison with experiment', *Int. J. Heat and Fluid Flow*, Vol. 9, No. 3
- GILLIS, J. C. & JOHNSTON, J. P. (1980) 'Experiments on the turbulent boundary layer over convex curved walls, and its recovery to flat wall conditions', *Papers from the 2nd Symp. on Turbulent Shear Flows*, Springer
- GILLIS, J. C. & JOHNSTON, J. P. (1983) 'Turbulent boundary-layer flow and structure on a convex wall and its redevelopment on a flat wall', *J. Fluid Mech.* Vol.135, pp.123-153
- GLAUERT, M. B. (1956) 'The wall jet', *J. Fluid Mech.* Vol. 1, p. 625

- GREGORY-SMITH, D. G., GILCHRIST, A. R. & SENIOR, P. (1990) 'A combined system for measurements of high speed flow by interferometry, Schlieren and shadowgraph', *Meas. Sci. Technol.* Vol. 1, pp.363-367
- GREGORY-SMITH, D. G. & GILCHRIST, A. R. (1987) 'The compressible Coanda wall jet - an experimental study of jet structure and breakaway', *Heat and Fluid Flow*, Vol. 8, No. 2
- GREGORY-SMITH, D. G. & HAWKINS, M. J. (1989) 'Modelling an axisymmetric curved wall jet with application to the Coanda flare', 3rd Int. PHOENICS Users Conf., Dubrovnik
- GREGORY-SMITH, D. G. & SENIOR, P. (1994) 'The effects of base steps and axisymmetry on supersonic jets over Coanda surfaces', *Int. J. Heat and Fluid Flow*, Vol.15, No.4, pp.291-298
- GUITTON, D. E. (1964) 'Two dimensional turbulent wall jets over curved surfaces', McGill Univ. MERL Rep. No. 64-7
- GUITTON, D. E. (1967) Corrigendum and addendum to report no. 64-7, McGill Univ. MERL Rep. No. 67-1
- GUITTON, D. E. (1970) 'Some contributions to the study of equilibrium and non-equilibrium wall jets over curved surfaces', Ph.D. Thesis, McGill University
- GUITTON, D. E. & NEWMAN, B. G. (1976) 'Self-preserving turbulent wall jets over convex surfaces', Dept. Mech. Engng., McGill University, Montreal
- HANJALIC, K. (1994) 'Advanced turbulence closure models - A view of current status and future prospects', *Int. J. heat and fluid flow*, Vol.15, No.3, pp.178-203
- HANJALIC, K. & LAUNDER, B. E. (1972) 'A Reynolds stress model of turbulence and its application to thin shear flows', *J. Fluid Mechs.*, Vol.52, p.609

Bibliography

- HANJALIC, K. & LAUNDER, B. E. (1980) 'Sensitising the dissipation equation to irrotational strains', A.S.M.E. J. Fluids Engng., Vol.102, pp.34-40
- HANJALIC, K. (1982) Proceedings of the 1980-81 AFOSR/HTTM Stanford Conference on Complex Turbulent Flows
- HARLOW, F. H. & NAKAYAMA, P. I. (1968) 'Transport of turbulence energy decay rate', LA-3854, Los Alamos Science Lab., Univ. California, USA
- HAWKINS, M. J. (1988) 'A study of turbulent flows and curved jets including application of the laser Doppler anemometry technique', Ph.D. Thesis, Univ. of Durham
- HENAU, V., RAITHBY, G. D. & THOMPSON, B. E. (1990) 'Prediction of flows with strong curvature and pressure gradient using the k- ϵ turbulence model', J. Fluids Engng., Vol.114, pp.40-47
- HINZE, J. (1975) Turbulence, McGraw-Hill, Inc.
- IRWIN, H. P. A. (1973) 'Measurements in a self-preserving plane wall jet in a positive pressure gradient', J. Fluid Mechs., Vol.61, p.33
- IRWIN, H. P. A. H. & SMITH, P. A. (1975) 'Prediction of the effect of streamline curvature on turbulence', Phys. Fluids Vol. 18, p. 624
- ISSA, R. I. & LOCKWOOD, F. C. (1977) 'On the prediction of two-dimensional supersonic viscous interactions near walls', AIAA J. Vol.15, No.2, pp.182-188
- JONES, W. P. & LAUNDER, B. E. (1972) 'Prediction of laminarisation with a 2-equation model of turbulence', Int. J. Heat and Mass Transfer, Vol.15, p.301
- JØRGENSEN, F. E. (1971) 'Directional Sensitivity of wire and fibre film probes', DISA Info., No.11

- KÁRMÁN, T. VON (1934) 'Some aspects of the turbulence problem', Proc. 4th Int. Congr. Appl. Mech., Cambridge, p.54
- KELLER, J. B. (1957) 'Teapot effect', J. of Applied Physics, Vol.28, No.8, pp.859-864
- KOPMELS, M. & SMITH, A. G. (1993) 'Prediction of Coanda effect flow fields', The PHOENICS J. of Comp. Fluid Dynamics and its Applications, Vol.6, No.9, pp.408-426
- KING, L. V. (1914) 'On the convection of heat from small cylinders in a free stream of fluid', Phil. Trans. Royal Soc., Vol.214A, p.373
- LAM, C. K. & BREMHORST, K. (1981) 'Modified form of the k- ϵ model for predicting wall turbulence', J. Fluids Engng., Vol.103, pp.465-460
- LAUNDER, B. E., PRIDDEN, C. H. & SHARMA, B. I. (1977) 'The calculation of turbulent boundary layers on spinning and curved surfaces', J. Fluids Engng., Vol.99, pp.231-239
- LAUNDER, B. E., REESE, G. J. & RODI, W. (1975) 'Progress in the development of a Reynolds stress turbulence closure', J. Fluid Mech. Vol.68, p.537
- LAUNDER, B. E. & RODI, W. (1981) 'The turbulent wall jet', Prog. Aerospace Sci., Vol.19, pp.81-128
- LAUNDER, B. E. & RODI, W. (1983) 'The turbulent wall jet - measurements and modelling', Ann. Rev. Fluid Mech., Vol.15, pp. 429-459
- LAUNDER, B. E. & SPALDING, D. B. (1974) 'The numerical computation of turbulent flows', Comp. Methods in Appl. Mech. and Engng, Vol.3, pp.269-289
- LEES, L. & REEVES, L. R. (1964) 'Supersonic separated and reattaching laminar flows : I. General theory and application to adiabatic boundary layer / shock wave interactions', A.I.A.A. J., Vol.2, No.11, pp.1907-1920

- LIEN, F. S. & LESCHZINER, M. A. (1993) 'A pressure-velocity solution strategy for compressible flow and its application to shock boundary layer interaction using 2nd moment turbulence closure', *J. Fluids Engng.-Trans. ASME*, Vol.115, No.4, pp.717-725
- LOMAS, C. G. (1986) *Fundamentals of hot wire anemometry*, Cambridge Univ. Press
- MASSEY, B. (1989) *Mechanics of fluids*, Sixth Edition, Van Nostrand Reinhold
- MATHIEU, J. (1959) 'Contribution à l'étude aérothermique d'un jet plan évoluant en présence d'une paroi', Thèse de Docteur es Sciences, Université de Grenoble
- McGUIRK, J. J. & PAGE, G. J. (1990) 'Shock capturing using a pressure correction method', *AIAA J.* Vol.28, No.10, pp.1751-1757
- MERONEY, R. N. and BRADSHAW, P (1975) 'Turbulent boundary layer growth over a longitudinally curved surface', *A.I.A.A. J.* Vol.13, pp.1448-1453
- METRAL, A. & ZERNER, F. (1948) 'The Coanda effect', British TIL/4207 translation of French Pub. Sci. et Tech. du Min. de L'Air, p.218
- MOORE, H. (1995) 'Experiments in a turbine cascade for the validation of turbulence and transition models', Ph.D. Thesis, Univ. of Durham
- MORRISON, J. F. & GREGORY-SMITH, D. G. (1984) 'Calculation of an axisymmetric turbulent wall jet over a surface of convex curvature', *Int. J. Heat and Fluid Flow*, Vol.5, No.3, pp.139-148
- MORRISON, J. F. (1982) 'A study of an axisymmetric wall jet with streamline curvature and its application to the Coanda flare', Ph.D. Thesis, Univ. of Durham
- MORROW, T. B. (1972) 'Effects of dirt accumulation on hot wire and hot film sensors', *Proceedings of the DISA Conference*, Vol.1, pp.122-124

Bibliography

- MOTALLEBI, F. (1994) 'A review of the hot wire technique in 2-D compressible flows', Prog. Aerospace Sci. Vol.30, pp.267-294
- MUCK, K. C., HOFFMANN, P. H. & BRADSHAW, P. (1985) 'The effect of convex surface curvature on turbulent boundary layers', J. Fluid Mechs., Vol.161, pp.347-369
- MYERS, G. E., SCHAUER, J. J. & EUSTIS, R. H. (1963) 'Plane turbulent wall jet flow development and friction factor', J. Basic Engineering, Vol.85, p.47
- NAGANO, Y. & HISHIDA, M. (1987) 'Improved form of the k- ϵ model for turbulent shear flows', Trans. A.S.M.E. Vol.109, pp.156-160
- NEWMAN, B. G. (1961) 'The deflection of plane jets by adjacent boundaries - Coanda Effect', Boundary Layer and Flow Control, Pergamon Press, Vol.1, p.232
- NEWMAN, B. G. (1969) 'The prediction of turbulent jets and wall jets', Canadian Aero. and Space J., pp.288-305
- OSWATITSCH, K. (1958) 'Die Ablosungsbedingung von Grenzschichten', Symposium on Boundary Layer Research, pp.357-367
- PATANKAR, S. V. (1980) Numerical heat transfer and fluid flow, Hemisphere, McGraw Hill, New York
- PATANKAR, S. V. & SPALDING, D. B. (1967) 'Heat and mass transfer in boundary layers', London: Morgan-Grampian
- PATEL, V. C., RODI, W. & SCHEUERER, G. (1985) 'Turbulence models for near wall and low Reynolds number flows : A review', AIAA J., Vol.23, No.4, pp.1308-1319
- PERDICHIZZI, A., UBALDI, M. & ZUNINO, P. (1990) 'A hot wire measuring technique for mean velocity and Reynolds stress components in compressible flow', Proceedings of the 10th Symposium, V.K.I. paper 8

PERRY, A. E. (1982) Hot wire anemometry, Clarendon Press Oxford

PRANDTL (1945) 'Über ein neues formalsystem für die ausgebildete turbulenz',
Nachrichten von der Akad. der Wissenschaft in Göttingen

PRATO, J., LAKSHMINARAYANA, B. & SURYAVAMSHI, N. (1998), to be
published

RASTOGI, A. K. (1972) 'Effectiveness and heat transfer downstream of three
dimensional film cooling slots', Ph.D. Thesis, Univ. London

RAYLEIGH, LORD (1917) 'On the dynamics of revolving fluids', Proc. R. Soc. London,
A93, No.148

RODERICK, W. E. B. (1961) 'Use of the Coanda effect for the deflection of jet sheets
over smoothly curved surfaces. Part II - Some tests with supersonic over and under
expanded jet sheets', U.T.I.A., T.N. No.51

ROE, P. L. (1982) 'Numerical modelling of shockwaves and other discontinuities',
Numerical Methods, pp.211-243

SAWYER, R. A. (1963) 'Two dimensional reattaching jet flows including the effects of
curvature on entrainment', J. Fluid Mechs. Vol.17, p.481

SCHLICHTING, H. (1979) Boundary layer theory, 7th Edition, McGraw Hill, New
York

SCHWARZ, W. H. & COSART, W. P. (1960) 'Two dimensional turbulent wall jet', J.
Fluid Mechs., Vol.10, p.48

SENIOR, P. (1991) 'The aerodynamics of curved jets and breakaway in Coanda flares',
Ph.D. Thesis, Univ. of Durham

Bibliography

- SIMON, T. W. (1981) 'Turbulent boundary layer heat transfer experiments : convex curvature effects, including introduction and recovery' Rep. HMT-31, Thermosci. Div., Dept. Mechs. Engng, Stanford
- SO, R. M. C. & MELLOR, G. L. (1972) 'An experimental investigation of turbulent boundary layers along curved surfaces', NASA-CR-1940
- SPALDING, D. B. (1972) 'A novel finite difference formulation for differential expressions involving both first and second derivatives', Int. J. Numer. Methods in Engng., Vol.4, p.551
- THOMANN, H. (1968) 'Effect of streamwise wall curvature on heat transfer in a turbulent boundary layer', J. Fluid Mechs., Vol.33, pp.283-292
- TOWNSEND, A. A. (1956) The structure of turbulent shear flow, Cambridge University Press
- VERSTEEG. H. K. & MALALASEKERA, W. (1995) An introduction to Computational Fluid Dynamics, Longman Scientific & Technical
- WILLE, R. & FERNHOLZ, H. (1965) 'Report on the first European Mechanics Colloquium, on the Coanda effect', J. Fluid Mechs., Vol.23, part 4, pp.801-819
- WILKINS, J., WITHERIDGE, R. E., DESTY, D. H., MASON, J. T. H. & NEWBY, N. (1977) 'The design, development and performance of Indair and Mardair flares', Paper 2822, Offshore Technology Conference, Houston
- WILSON, D. J. & GOLDSTEIN, R. J. (1976) 'Turbulent wall jets with cylindrical streamwise surface curvature', A.S.M.E. J. Fluids Engng, Vol.98, pp. 550-557
- YAKHOT, V. & ORSZAG, S. A. (1986) 'Renormalization group analysis of turbulence', J. Sci. Comput., Vol.1, p3

Bibliography

YAKHOT, V. & SMITH, L. M. (1992) 'The Renormalization group, the ϵ -expansion and derivation of turbulence models', *J. Sci. Comput.*, Vol.7, No.1

Appendix A

A.1 Determining the governing equations

A brief explanation of the derivation of the governing equations will be given here, including an explanation of the differences between the conservation and non-conservation forms of the equations. The final set of equations are presented in the general format used by the CFD code PHOENICS and other finite volume packages.

A control volume analysis is used when determining the governing equations. This control volume may either be stationary with the fluid moving through it, or it may move with the fluid along a streamline, so it always contains the same fluid particles. The conservation form of the governing equations are obtained by considering the stationary control volume, and the non-conservation form of the equations are obtained when the control volume is considered to move with the fluid.

The equations may be converted simply between the two forms. In most theoretical aerodynamics it makes little difference whether the conservation or non-conservation form of the equations are used. However, in CFD, the form used can make a difference, and the most useful is the conservation form.

A.1.1 Continuity equation

The mass conservation equation requires that the increase of mass in the element must equal the net rate of flow of mass into the fluid element. The conservation equation may be determined by considering the control volume shown in figure A.1, which shows the mass flows of fluid in and out of the fluid element control volume.

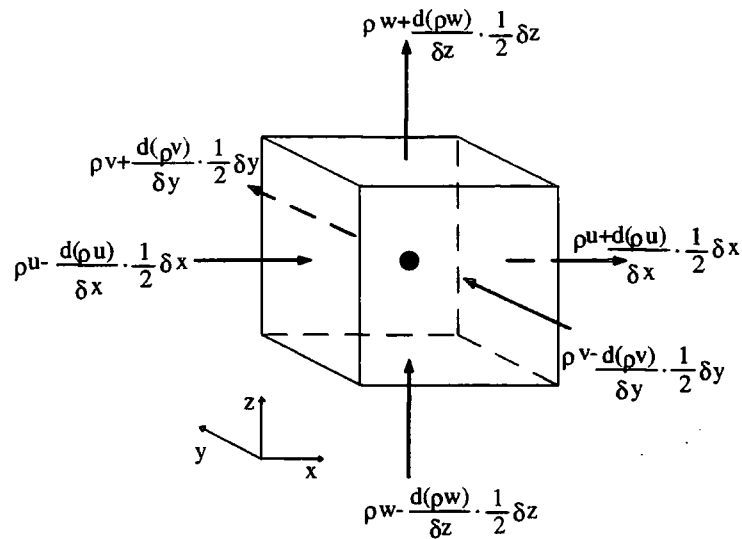


Figure A.1 : Mass flows in and out of fluid element control volume

The continuity equation for compressible, unsteady flow is given in equation (A.1).

$$\frac{\partial \rho}{\partial t} + \frac{\partial(\rho U)}{\partial x} + \frac{\partial(\rho V)}{\partial y} + \frac{\partial(\rho W)}{\partial z} = 0 \quad \text{or} \quad \frac{\partial \rho}{\partial t} + \text{div}(\rho \mathbf{U}) = 0 \quad (\text{A.1})$$

Conservative and non-conservative forms

The substantive (or total) derivative for a variable, ϕ , is $D\phi/Dt$. This is the time rate of change of a variable ϕ per unit mass *for a fluid particle as it moves through space*. The substantial derivative may be written in full as :

$$\begin{aligned} \frac{D\phi}{Dt} &= \frac{\partial \phi}{\partial t} + U \frac{\partial \phi}{\partial x} + V \frac{\partial \phi}{\partial y} + W \frac{\partial \phi}{\partial z} \\ &= \frac{\partial \phi}{\partial t} + \mathbf{U} \cdot \text{grad } \phi \end{aligned} \quad (\text{A.2})$$

A more useful expression is the time rate of change of variable ϕ per unit volume. For the moving particle, this is given by the product of $D\phi/Dt$ and density, as shown in equation (A.3)

$$\rho \frac{D\phi}{Dt} = \rho \left(\frac{\partial\phi}{\partial t} + \mathbf{U} \cdot \text{grad } \phi \right) \quad (\text{A.3})$$

The rate of change of a variable ϕ per unit volume for a *fluid element which is stationary* (i.e. the conservation form) is given by equation (A.4).

$$\frac{\partial(\rho\phi)}{\partial t} + \text{div}(\rho\phi\mathbf{U}) \quad (\text{A.4})$$

Equation (A.4) may be expanded, and from this expansion shown in (A.5), the link between the conservation form, and the substantive derivative may clearly be seen.

$$\begin{aligned} \frac{\partial(\rho\phi)}{\partial t} + \text{div}(\rho\phi\mathbf{U}) &= \rho \left[\frac{\partial\phi}{\partial t} + \mathbf{U} \cdot \text{grad } \phi \right] + \phi \underbrace{\left[\frac{\partial\rho}{\partial t} + \text{div}(\rho\mathbf{U}) \right]}_{\text{Term equals zero from conservation of mass}} \\ \text{so } \frac{\partial(\rho\phi)}{\partial t} + \text{div}(\rho\phi\mathbf{U}) &= \rho \frac{D\phi}{Dt} \end{aligned} \quad (\text{A.5})$$

Hence also :

$$\begin{aligned} \rho \frac{DU}{Dt} &= \frac{\partial(\rho U)}{\partial t} + \text{div}(\rho U\mathbf{U}) \\ \rho \frac{DV}{Dt} &= \frac{\partial(\rho V)}{\partial t} + \text{div}(\rho V\mathbf{U}) \\ \rho \frac{DW}{Dt} &= \frac{\partial(\rho W)}{\partial t} + \text{div}(\rho W\mathbf{U}) \end{aligned} \quad (\text{A.6})$$

A.1.2 The momentum equations

Newton's second law must be applied when deriving the three momentum equations. Here the rate of change of momentum within the control volume must be equal to the rate at which momentum enters the volume, plus the sum of the forces acting on the volume. The two types of forces which may act are body forces and surface forces. Body forces act directly on the mass of the fluid element, such as gravitational, electric or magnetic forces. Surface forces, which act directly on the surface of the fluid element, are due to two sources. Firstly, the pressure distribution which acts on the surface imposed by the surrounding fluid, and secondly, normal and shear stresses which act on the surface caused by frictional movement of the surrounding fluid.

The rates of increase of the x-, y- and z- momentum per unit volume of a fluid particle have been given in equation (A.6). In general, the contributions due to the various surface forces appear as separate terms in the momentum equations, whilst the effects of body forces appear as source terms.

The nine viscous stresses are denoted by τ_{ij} , with the suffix notation indicating the direction of the viscous stress. The suffices i and j indicate the stress component acts in the j -direction on a surface normal to the i -direction. The pressure force acts as a compressive normal stress and is denoted by p (tensile stresses are taken as positive).

The x-component of the momentum equation is formed by setting the rate of change of x-momentum of the fluid particle equal to the total force in the x-direction on the element due to the surface stresses, plus the rate of increase of x-momentum due to the sources. The y- and z- components of the momentum equation are formed in a similar way. The three momentum equations are given in (A.7-A.9).

$$\rho \frac{DU}{Dt} = \frac{\partial(-P + \tau_{xx})}{\partial x} + \frac{\partial \tau_{yx}}{\partial y} + \frac{\partial \tau_{zx}}{\partial z} + S_{Mx} \quad (\text{A.7})$$

$$\rho \frac{DV}{Dt} = \frac{\tau_{xy}}{\partial x} + \frac{\partial(-P + \tau_{yy})}{\partial y} + \frac{\tau_{zy}}{\partial z} + S_{My} \quad (\text{A.8})$$

$$\rho \frac{DW}{Dt} = \frac{\partial \tau_{xz}}{\partial x} + \frac{\partial \tau_{yz}}{\partial y} + \frac{(-P + \tau_{zz})}{\partial z} + S_{Mz} \quad (\text{A.9})$$

where the source terms S_{Mx} , S_{My} and S_{Mz} include the contributions due to the body forces.

A.1.3 The energy equation

The final fundamental governing equation is that of energy, which must be conserved. Thus, the rate of change of energy of a fluid particle must be equal to the rate of heat addition to the fluid particle, plus the rate of work done on the particle. The rate of increase of energy of a fluid particle per unit volume is given by $\rho \frac{DE}{Dt}$, where E is equal to the sum of internal energy, e , and kinetic energy, $0.5(U^2 + V^2 + W^2)$. The energy equation is given in (A.10)

$$\begin{aligned} \rho \frac{DE}{Dt} = & -div(p\mathbf{U}) + \left[\frac{\partial(U\tau_{xx})}{\partial x} + \frac{\partial(U\tau_{yx})}{\partial y} + \frac{\partial(U\tau_{zx})}{\partial z} + \frac{\partial(V\tau_{xy})}{\partial x} \right. \\ & \left. + \frac{\partial(V\tau_{yy})}{\partial y} + \frac{\partial(V\tau_{zy})}{\partial z} + \frac{\partial(W\tau_{xz})}{\partial x} + \frac{\partial(W\tau_{yz})}{\partial y} + \frac{\partial(W\tau_{zz})}{\partial z} \right] \\ & + div(k \text{ grad } T) + S_E \end{aligned} \quad (\text{A.10})$$

where the term $div(k \text{ grad } T)$ is equal to the rate of heat addition to the fluid particle due to heat conduction (where k here is the thermal conductivity of the fluid), and changes in the gravitational potential energy are considered in the source term, S_E .

The motion of a fluid has been described above using 5 partial differential equations - conservation of mass, three momentum equations, and an energy equation. There are however four unknown thermodynamic variables, ρ , P , e and T . Assuming a perfect gas, the equations of state given in (A.11) and (A.12) provide the necessary relationships for these variables to be solved.

$$P = \rho RT \quad (\text{A.11})$$

$$e = C_v T \quad (A.12)$$

where R is the specific gas constant, and C_v is the specific heat at constant volume.

A.2 The Navier-Stokes equations

The governing equations presented so far contain unknown viscous stress components, τ_{ij} , however, the equations are more useful if suitable models are introduced for these stresses. For a Newtonian fluid, the viscous stresses are proportional to the rates of deformation. For compressible flow, Newton's law of viscosity involves two constants of proportionality. The first is dynamic viscosity, μ , which relates the stresses to linear deformations, and the second is the bulk viscosity, λ , which relates the stresses to volumetric deformations. Schlichting (1979) suggests $\lambda = -\frac{2}{3}\mu$ for gases. The resulting approximations for the viscous stresses are given in equation (A.13).

$$\begin{aligned} \tau_{xx} &= 2\mu \frac{\partial U}{\partial x} + \lambda \operatorname{div} \mathbf{U} & \tau_{yy} &= 2\mu \frac{\partial V}{\partial y} + \lambda \operatorname{div} \mathbf{U} & \tau_{zz} &= 2\mu \frac{\partial W}{\partial z} + \lambda \operatorname{div} \mathbf{U} \\ \tau_{xy} = \tau_{yx} &= \mu \left(\frac{\partial U}{\partial y} + \frac{\partial V}{\partial x} \right) & \tau_{xz} = \tau_{zx} &= \mu \left(\frac{\partial U}{\partial z} + \frac{\partial W}{\partial x} \right) & & \\ \tau_{yz} = \tau_{zy} &= \mu \left(\frac{\partial V}{\partial z} + \frac{\partial W}{\partial y} \right) & & & & \end{aligned} \quad (A.13)$$

Substituting these approximations into the momentum equations results in the following set of equations :

$$\begin{aligned} \frac{DU}{Dt} &= -\frac{\partial P}{\partial x} + \frac{\partial}{\partial x} \left[2\mu \frac{\partial U}{\partial x} + \lambda \operatorname{div} \mathbf{U} \right] + \frac{\partial}{\partial y} \left[\mu \left(\frac{\partial U}{\partial y} + \frac{\partial V}{\partial x} \right) \right] \\ &+ \frac{\partial}{\partial z} \left[\mu \left(\frac{\partial U}{\partial z} + \frac{\partial W}{\partial x} \right) \right] + S_{Mx} \end{aligned} \quad (A.14(a))$$

$$\begin{aligned} \frac{DV}{Dt} = & -\frac{\partial P}{\partial x} + \frac{\partial}{\partial x} \left[\mu \left(\frac{\partial U}{\partial y} + \frac{\partial V}{\partial x} \right) \right] + \frac{\partial}{\partial y} \left[2\mu \frac{\partial V}{\partial y} + \lambda \operatorname{div} \mathbf{U} \right] \\ & + \frac{\partial}{\partial z} \left[\mu \left(\frac{\partial V}{\partial z} + \frac{\partial W}{\partial y} \right) \right] + S_{My} \end{aligned} \quad (\text{A.14(b)})$$

$$\begin{aligned} \frac{DW}{Dt} = & -\frac{\partial P}{\partial x} + \frac{\partial}{\partial x} \left[\mu \left(\frac{\partial U}{\partial z} + \frac{\partial W}{\partial x} \right) \right] + \frac{\partial}{\partial y} \left[\mu \left(\frac{\partial V}{\partial z} + \frac{\partial W}{\partial y} \right) \right] \\ & + \frac{\partial}{\partial z} \left[2\mu \frac{\partial W}{\partial z} + \lambda \operatorname{div} \mathbf{U} \right] + S_{Mz} \end{aligned} \quad (\text{A.14(c)})$$

The energy equation may also be written with these substitutions, and is given below.

$$\begin{aligned} \frac{DE}{Dt} = & -\operatorname{div}(P\mathbf{U}) + \lambda(\operatorname{div} \mathbf{U})^2 + \mu \left[2 \left(\frac{\partial U}{\partial x} \right)^2 + 2 \left(\frac{\partial V}{\partial y} \right)^2 + 2 \left(\frac{\partial W}{\partial z} \right)^2 \right. \\ & \left. + \left(\frac{\partial U}{\partial y} + \frac{\partial V}{\partial x} \right)^2 + \left(\frac{\partial U}{\partial z} + \frac{\partial W}{\partial x} \right)^2 + \left(\frac{\partial V}{\partial z} + \frac{\partial W}{\partial y} \right)^2 \right] + \operatorname{div}(k \operatorname{grad} T) + S_E \end{aligned} \quad (\text{A.15})$$

A.2.1 Simplified form of the Navier Stokes equations

The momentum equations may be expressed in a simpler form by effectively 'hiding' the two smaller contributions to the viscous stress terms in the momentum source term, resulting in the use of a new source term, S'_M . The energy equation may also be simplified by replacing the terms due to the viscous stresses with a dissipation function, Φ . The full set of governing equations, expressed in their simplest *conservation* forms, are given in (A.16(a)-(f)).

$$\text{Mass} \quad \frac{\partial \rho}{\partial t} + \operatorname{div}(\rho \mathbf{U}) = 0 \quad (\text{A.16 (a)})$$

$$\text{x - momentum} \quad \frac{\partial(\rho U)}{\partial t} + \operatorname{div}(\rho U \mathbf{U}) = -\frac{\partial P}{\partial x} + \operatorname{div}(\mu \operatorname{grad} U) + S'_{Mx} \quad (\text{b})$$

$$\text{y - momentum} \quad \frac{\partial(\rho V)}{\partial t} + \text{div}(\rho V\mathbf{U}) = -\frac{\partial P}{\partial x} + \text{div}(\mu \text{ grad } V) + S'_{M_y} \quad (\text{c})$$

$$\text{z - momentum} \quad \frac{\partial(\rho W)}{\partial t} + \text{div}(\rho W\mathbf{U}) = -\frac{\partial P}{\partial x} + \text{div}(\mu \text{ grad } W) + S'_{M_z} \quad (\text{d})$$

$$\text{internal energy} \quad \frac{\partial(\rho e)}{\partial t} + \text{div}(\rho e\mathbf{U}) = -P \text{ div } \mathbf{U} + \text{div}(k \text{ grad } T) + \Phi + S_e \quad (\text{e})$$

$$\text{Equations of state} \quad P = \rho RT \quad e = C_v T \quad (\text{A.16 (f)})$$

where

$$\Phi = \left[2\left(\frac{\partial U}{\partial x}\right)^2 + 2\left(\frac{\partial V}{\partial y}\right)^2 + 2\left(\frac{\partial W}{\partial z}\right)^2 + \left(\frac{\partial U}{\partial y} + \frac{\partial V}{\partial x}\right)^2 + \left(\frac{\partial U}{\partial z} + \frac{\partial W}{\partial x}\right)^2 + \left(\frac{\partial V}{\partial z} + \frac{\partial W}{\partial y}\right)^2 \right]$$

The dissipation function, Φ is always positive due to the squared terms. It represents a source of internal energy due to deformation work done on the fluid element.

Appendix B

B.1 The Reynolds averaged Navier Stokes equations

Flow becomes turbulent beyond a critical Reynolds number, and the instantaneous variables of the governing equations comprise of a mean and a fluctuating component, as shown on equation (B.1).

$$U = \bar{U} + u \quad V = \bar{V} + v \quad W = \bar{W} + w \quad P = \bar{P} + p \quad (B.1)$$

Substitution of these terms into the Navier Stokes equations given in Appendix A results in a highly complex system of equations which cannot be solved using a direct numerical solution. As a consequence, to simplify the equations they are time averaged to produce the Reynolds averaged Navier Stokes equations.

For simplicity, incompressible, constant viscosity flow is considered here. Following the above substitutions, and time averaging, the continuity equation may be written :

$$\text{div } \mathbf{U} = 0 \quad (B.2)$$

The terms of the x-momentum equation are examined individually to see the effects of substituting the mean and fluctuating components, and time averaging.

- 'rate of change' term : $\frac{\partial(\overline{\bar{U} + u})}{\partial t} = \frac{\partial \bar{U}}{\partial t}$ (B.3)

- 'convective' term : $\overline{\text{div}(UU)} = \text{div}(\overline{U\bar{U}}) + \text{div}(\overline{u\mathbf{u}})$ (B.4)

since, $\text{div}(UU) = \frac{\partial U^2}{\partial x} + \frac{\partial UV}{\partial y} + \frac{\partial UW}{\partial z}$, and substituting the mean and fluctuating components into the terms for ρU^2 , ρUV and ρUW and time averaging results in the appearance of additional mean values containing the fluctuating velocity components, as shown by equations (B.5).

$$\begin{aligned}
 \overline{U^2} &= \overline{(\overline{U} + u)(\overline{U} + u)} = \overline{U^2} + \overline{u^2} \\
 \overline{UV} &= \overline{(\overline{U} + u)(\overline{V} + v)} = \overline{UV} + \overline{uv} \\
 \overline{UW} &= \overline{(\overline{U} + u)(\overline{W} + w)} = \overline{UW} + \overline{uw}
 \end{aligned}
 \tag{B.5}$$

- 'pressure' term :
$$-\frac{1}{\rho} \frac{\partial P}{\partial x} = -\frac{1}{\rho} \frac{\partial \overline{P}}{\partial x} \tag{B.6}$$

- 'diffusive' term :
$$\overline{\frac{\mu}{\rho} \operatorname{div} \operatorname{grad} U} = \frac{\mu}{\rho} \operatorname{div} \operatorname{grad} \overline{U} \tag{B.7}$$

The additional terms which result from the time-averaging of the convective term are transferred to the right hand side of the momentum equation to reflect their role as additional turbulent stresses on the mean velocity components, \overline{U} , \overline{V} and \overline{W} . Similar time-averaging of the y- and z-component momentum equations result in the appearance of six extra stress terms which are known as the *Reynolds stresses*, given in equation (B.8). The time-averaged momentum equations, containing the Reynolds stresses, are known as the Reynolds equations.

$$\begin{aligned}
 \tau_{xx} &= -\rho \overline{u^2} & \tau_{yy} &= -\rho \overline{v^2} & \tau_{zz} &= -\rho \overline{w^2} \\
 \tau_{xy} &= \tau_{yx} = -\rho \overline{uv} & \tau_{xz} &= \tau_{zx} = -\rho \overline{uw} & \tau_{yz} &= \tau_{zy} = -\rho \overline{vw}
 \end{aligned}
 \tag{B.8}$$

B.1.1 Full set of turbulent flow equations

The full set of turbulent flow equations for compressible flow are given in (B.9(a)-(d)).

Continuity

$$\frac{\partial \rho}{\partial t} + \text{div}(\rho \bar{\mathbf{U}}) = 0 \quad (\text{B.9(a)})$$

Reynolds equations

$$\begin{aligned} \frac{\partial(\rho \bar{U})}{\partial t} + \text{div}(\rho \bar{U} \bar{\mathbf{U}}) = & -\frac{\partial \bar{P}}{\partial x} + \left[-\frac{\partial(\rho \bar{u}^2)}{\partial x} - \frac{\partial(\rho \bar{u} \bar{v})}{\partial y} - \frac{\partial(\rho \bar{u} \bar{w})}{\partial z} \right] \\ & + \text{div}(\mu \text{grad } \bar{U}) + S'_{Mx} \end{aligned} \quad (\text{B.9(b)})$$

$$\begin{aligned} \frac{\partial(\rho \bar{V})}{\partial t} + \text{div}(\rho \bar{V} \bar{\mathbf{U}}) = & -\frac{\partial \bar{P}}{\partial y} + \left[-\frac{\partial(\rho \bar{u} \bar{v})}{\partial x} - \frac{\partial(\rho \bar{v}^2)}{\partial y} - \frac{\partial(\rho \bar{v} \bar{w})}{\partial z} \right] \\ & + \text{div}(\mu \text{grad } \bar{V}) + S'_{My} \end{aligned} \quad (\text{B.9(c)})$$

$$\begin{aligned} \frac{\partial(\rho \bar{W})}{\partial t} + \text{div}(\rho \bar{W} \bar{\mathbf{U}}) = & -\frac{\partial \bar{P}}{\partial z} + \left[-\frac{\partial(\rho \bar{u} \bar{w})}{\partial x} - \frac{\partial(\rho \bar{v} \bar{w})}{\partial y} - \frac{\partial(\rho \bar{w}^2)}{\partial z} \right] \\ & + \text{div}(\mu \text{grad } \bar{W}) + S'_{Mz} \end{aligned} \quad (\text{B.9(d)})$$

Time averaging a general transport equation, e.g. equation (A.17), for a scalar quantity ϕ , which comprises of a mean component Φ and fluctuating component ϕ' , results in the following typical transport equation.

$$\frac{\partial(\rho \Phi)}{\partial t} + \text{div}(\rho \Phi \bar{\mathbf{U}}) = \text{div}(\Gamma_{\Phi} \text{grad } \Phi) + \left[-\frac{\partial(\rho \bar{u} \Phi)}{\partial x} - \frac{\partial(\rho \bar{v} \Phi)}{\partial y} - \frac{\partial(\rho \bar{w} \Phi)}{\partial z} \right] + S_{\Phi} \quad (\text{B.10})$$

Appendix C

C.1 The mathematical basis of PHOENICS

The variables used within PHOENICS may be thought of as either dependent or auxiliary. Dependent variables are the subject of a conservation equation, whereas auxiliary variables are either constant, or derived from an algebraic expression. In each case they may be subdivided into scalar and vector quantities. The distinction between scalar and vector quantities is important since each is stored at a different location in space. Scalars are stored at the centre points of six-sided cells, with values supposed to be typical of the whole cell. Vectors are stored at the centre points of the six cell faces.

The grid cell nomenclature is shown below in figure 6.1. Temperatures and pressures are evaluated within the cells, at the points denoted by P, N, S, E, W. West to east velocities are calculated at cell-wall locations e.g. w and e. South-to-north velocities are calculated at cell-wall locations e.g. s and n.

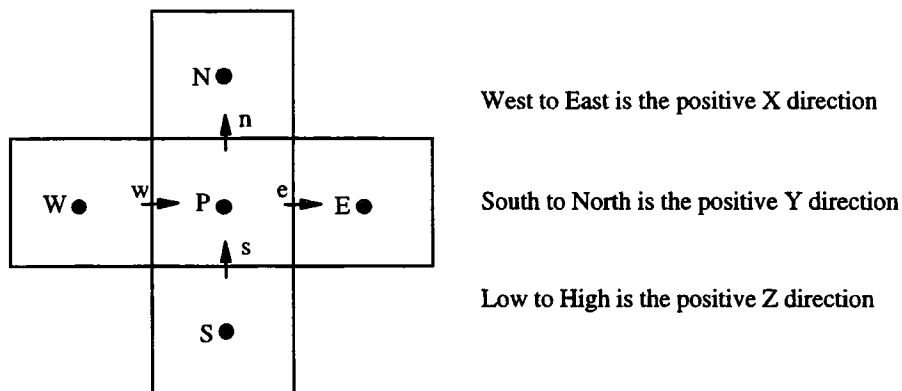


Figure C.1 : Grid cell nomenclature

PHOENICS grids are structured and may be either Cartesian, cylindrical-polar, or body fitted. In all cases, the grid distribution can be non-uniform in all co-ordinate directions, and the grid definitions are as follows :-

- x measures distance (or angle) in west-to-east direction
- y measures distance in south-to-north direction
- z measures distance in low-to high direction.

The basic balance equation is given below in equation (C.1). The quantities balanced are the dependent variables, examples of which include the mass of a phase, energy, momentum, and turbulence quantities.

$$\text{Outflow from cell} - \text{Inflow into cell} = \text{net source within cell} \quad (\text{C.1})$$

The terms which appear in the balance equation are convection (i.e. directed mass flow), diffusion (i.e. random motion of electrons, molecules or larger structures, e.g. eddies), time variation and sources (e.g. pressure gradients or body forces for momentum).

PHOENICS provides solutions to the discretized versions of sets of differential equations having the following general form, for single phase flow :

$$\frac{\partial(\rho\Phi)}{\partial t} + \text{div}(\rho\mathbf{U}\Phi - \Gamma_{\Phi} \cdot \text{grad}(\Phi)) = S_{\Phi} \quad (\text{C.2})$$

where :- Φ - any conserved property, e.g. enthalpy, momentum per unit mass
 Γ_{Φ} - exchange coefficient of the entity Φ
 S_{Φ} - source rate of Φ

When time-averaged values of the quantities are involved, as is the case with turbulent flows, special expressions may have to be introduced for Γ and S , to account for the correlations between velocity, density, Φ 's and other quantities of the fluid flow.

Typically, many equations of the above type have to be solved simultaneously since they are linked in various ways. For turbulent flows, PHOENICS can solve equations that are time-averaged. It is presumed that the time over which the averaging is made is long compared with the time scale of the turbulent motion.

Some particular forms of the balance equation are given below. The mass continuity equation is obtained by setting Φ to unity in the above equation which yields the following :-

$$\frac{\partial\rho}{\partial t} + \text{div}(\rho\mathbf{U}) = S \quad (\text{C.3})$$

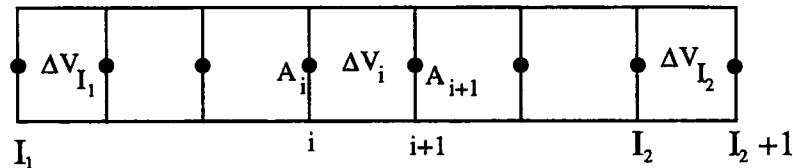
where S is the mass inflow rate per unit volume of space from some external domain.

The momentum equations are obtained when Φ is set to U , V or W and the exchange coefficient and sources have the following values :-

$$\Gamma_{\Phi} = \rho(\mu_t + \mu_l) \quad \text{and} \quad S_{\Phi} = -\text{grad}(p) + \text{gravity} + \text{friction} + \dots \quad (\text{C.4})$$

These balance equations cannot be solved numerically in differential form. Transforming them into a solvable form is known as discretisation, and PHOENICS performs this process using the finite volume method. This is the most commonly used discretisation method, and bears many similarities to the finite difference method. The technique was developed specifically to solve equations of heat transfer and fluid flow and is described in detail in Patankar (1980).

The technique is based on the discretisation of integrals (rather than differentials) for each finite control volume, ΔV_i , as illustrated below :



$$\text{Continuous Integral} \quad : \quad \int_{\Delta V_i} \frac{\partial \rho}{\partial t} dVol = \int_i \rho \underline{U} \cdot \underline{dA}$$

$$\text{Discrete Model} \quad : \quad \frac{\Delta \rho}{\Delta t} = (\text{Flux}_{in})_i - (\text{Flux}_{out})_i = (\rho U)_i A_i - (\rho U)_{i+1} A_{i+1}$$

$$\text{so} \quad : \quad \sum_i^{I_2} \frac{\Delta \rho}{\Delta t} \Delta V_i = (\text{Flux}_{in})_{I_1} - (\text{Flux}_{out})_{I_2}$$

The flux based finite volume approach exactly mimics conservation at the discrete level, and errors are as a result of truncation errors at the boundaries.

Before solution of these equations, interpolation assumptions are required to obtain scalar values at cell faces and vector quantities at the cell centres. A wide variety of interpolation assumptions are available, but the fully implicit upwind set is used by default. Whatever scheme is used, the result after integration is likely to be a set of equations of the following form :-

$$\Phi_P = \frac{a_E \Phi_E + a_W \Phi_W + a_N \Phi_N + a_S \Phi_S + a_H \Phi_H + a_L \Phi_L + a_T \Phi_T + S}{a_E + a_W + a_N + a_S + a_H + a_L + a_T + a_P} \quad (C.5)$$

where Φ represents the relevant dependent variable, and the subscripts P, E, W, N, H and L denote the locations at which this variable is computed, in accordance with the north-south-east-west-high-low convention described earlier. The subscript T denotes the earlier time value.

The a 's are coefficients which are temporarily treated as constant. Those with subscripts N, S, E, W, H and L express the interactions between neighbouring cells by way of diffusion and bulk motion (i.e. convection), while a_T expresses the time dependence effect. These coefficients have the following form :-

$$\underbrace{(Area \times V \times \rho)}_{convection} + \underbrace{\frac{(Area \times \Gamma)}{Dist.}}_{diffusion} + \underbrace{\frac{Vol. \times \rho}{\partial t}}_{transient} \quad (C.6)$$

The balance equations are cast into correction form before solution. In this form, the sources are replaced by the errors in the real equation, and the coefficients may be only approximate. The corrections tend to zero as convergence is approached, reducing the possibility of round-off errors affecting the solution.

To close the equation set, auxiliary variables and the boundary conditions need to be specified. Auxiliary equations must be provided for thermodynamic properties (e.g. density, enthalpy and entropy), transport properties (e.g. viscosity, diffusivity, conductivity), source terms (e.g. viscous dissipation), interphase transport (e.g. of momentum, energy, mass). There may also be 'artificial' auxiliary equations, such as those for false transients and boundary conditions. Boundary conditions are represented as linearised sources for cells adjacent to boundaries and have the following form :

$$S_{\Phi} = a_{BC} \times (\Phi_{BC} - \Phi_P) \quad (C.7)$$

Where : a_{BC} is termed the COEFFICIENT
 Φ_{BC} is termed the VALUE

and the equation for Φ_P becomes :

$$\Phi_P = \frac{a_E \Phi_E + a_W \Phi_W + a_N \Phi_N + a_S \Phi_S + a_H \Phi_H + a_L \Phi_L + a_T \Phi_T + a_{BC} \Phi_{BC} + S}{a_E + a_W + a_N + a_S + a_H + a_L + a_T + a_P + a_{BC}} \quad (C.8)$$

For each dependent variable Φ , there are as many algebraic equations as there are cells in the integration domain. Thus the number of equations to be solved are numerous and they are often strongly coupled. They are solved using an iterative 'guess-and-correct' method. The algorithm is known as SIMPLEST, which is a pressure correction algorithm for finite volume calculations.

